UNIVERSITÀ DEGLI STUDI DI PAVIA
DIPARTIMENTO DI FISICA

Corso di Laurea Magistrale in Scienze Fisiche

Studies of eco-friendly gas mixtures for RPC detectors at CERN LHC experiments

Tesi per la Laurea Magistrale di:
Mattia Verzeroli

Relatore: Prof. Paolo Vitulo
Correlatori: Dott. Roberto Guida
Dott.ssa Beatrice Mandelli

Anno Accademico 2020-2021

Contents

Summary

Several gaseous detectors are operated at the CERN LHC experiments. In particular, Resistive Plate Chambers (RPCs) can be found in the ALICE, ATLAS, and CMS Muon Systems. RPCs detectors are operated with a freon-based gas mixture containing $C_2H_2F_4$ and SF_6, both greenhouse gases (GHGs) with a very high global warming potential (GWP), 1430 and 22800 respectively. These gases, together with CF_4 and C_4F_{10}, are responsible for 70% of CERN operation's direct greenhouse gas emission. Moreover, the European Union defines a set of regulations aiming at reducing the GHG emissions from fluorinated gases. This regulation could bring to have lower availability and higher costs in the future. The present work is related to one of the strategies delineated by the CERN gas group to reduce GHG emissions: the search for eco-friendly gas mixtures for RPCs detectors. The first part of the thesis is focused on the study and characterization of RPC performances with these new gas mixtures in the laboratory environment. Some alternative to $C_2H_2F_4$ were tested, such as CO_2, He and HFO1234ze. This last one is a molecule in the family of HydroFluoroOlefins with a GWP of 7. Furthermore, Novec 4710 was tested as a substitution of SF_6 since it presents a good electronegativity and a GWP of 2100. The RPC performances were evaluated by studying the detector's efficiency, currents, streamer probability, prompt charge, cluster size, and time resolution. The second part of this thesis deals with RPC detectors tested at the CERN Gamma Irradiation Facility with some of the alternative gas mixtures. Here the RPC performances were studied under a similar LHC experiment radiation background, thanks to a 12 TBq ^{137}Cs source and a muon beam, provided by the SPS accelerator. This studies also allow to investigate the behavior of the single gas component of the mixtures. The main outcome is that substituting 30% R134a concentration with He or CO_2 does not imply any change in RPC performance with respect to the standard gas mixture. Moreover, it is possible to see that an increase of the SF_6 concentration together with a decrease of the ratio between R134a and HFO1234ze brings to an increase in the currents and to a drop in the efficiency with respect to the standard gas mixture, in a condition of gamma rates of about 600 Hz/cm^2. The Novec 4710 seems promising as a SF_6 substitute with 0.1% concentration although it is known that it can react with water. Studies of the production of possible compounds is ongoing as well as validation tests both in laboratory condition and in test beams with high particle rate environment.

Sommario

Presso gli esperimenti LHC del CERN sono in funzione diversi rivelatori a gas. In particolare possiamo trovare gli Resistive Plate Chambers (RPC) nei rivelatori di muoni di ALICE, ATLAS e CMS. I rivelatori RPC funzionano con una miscela di gas a base di freon che contiene il $C_2H_2F_4$ e il SF_6, entrambi gas serra (GHG) con un potenziale di riscaldamento globale (GWP) molto alto: 1430 e 22800 rispettivamente. Questi gas sono responsabili, insieme al CF_4 e al C_4F_{10}, del 70% delle emissioni dirette di gas serra del CERN. Inoltre l'UE ha definito un insieme di norme che mirano a ridurre le emissioni di gas serra dovute ai gas fluorinati. Queste norme potrebbero portare in futuro ad una minore reperibilità e a maggiori costi. Questo lavoro di tesi riguarda una delle strategie adottate dal CERN per ridurre le emissioni di gas serra, ovvero la ricerca di gas sostenibili a livello ambientale per le RPC. La prima parte della tesi si concentra sullo studio e sulla caratterizzazione delle *performance* delle RPC operate con queste nuove miscele di gas nell'ambiente controllato del laboratorio. Sono state testate alcune alternative al $C_2H_2F_4$, come la CO_2, l'He e l'HFO1234ze. Quest'ultimo è una molecola appartenente alla famiglia degli *HydroFluoroOlefin* con un GWP pari a 7. Inoltre il Novec 4710 è stato testato come alternativa all'SF_6, dal momento che presenta una buona elettronegatività e un GWP di 2100. Le *performance* degli RPC è stata valutata studiandone l'efficienza, le correnti, la *streamer probability*, la *prompt charge*, la *cluster size* e la risoluzione temporale. La seconda parte della tesi si concentra sugli RPC testati, con alcune miscele di gas alternative, alla *Gamma Irradiation Facility* del CERN. Qui le *performance* degli RPC sono state studiate sotto un fondo di radiazione simile a quello degli esperimenti di LHC. Questa condizione di irraggiamento è ottenuta grazie a una sorgente di ^{137}Cs con un'attività di 12 TBq e da un fascio di muoni, fornito dall'acceleratore SPS. Questi studi permettono di indagare il comportamento dei singoli gas che compongono le miscele. Il risultato principale è che la sostituzione del 30% di R134a con He o CO_2 non produce nessun cambiamento nel comportamento degli RPC rispetto alla miscela standard. Inoltre è possibile notare che un aumento della concentrazione di SF_6 insieme alla diminuzione del rapporto tra R134a e HFO1234ze comporta un aumento delle correnti e una diminuzione dell'efficienza rispetto alla miscela standard, in una condizione di irraggiamento circa pari a 600 Hz/cm^2. Il gas Novec 4710 sembra promettente come sostituto dell'SF_6 in una concentrazione dello 0.1% anche se è noto che possa reagire con l'acqua. Si stanno attualmente svolgendo studi sulla possibile produzione di composti dovuti a questa reazione, come anche si stanno continuando i test di validazione sia nelle condizioni di laboratorio che al test beam, ovvero in un ambiente con un'alta radiazione di fondo.

Chapter 1

Introduction

The European Organization for Nuclear Research (CERN) is an European research organization that provides particle accelerators and the infrastructure needed for high-energy physics research. In particular, it hosts the Large Hadron Collider (LHC), designed to collide proton beams with a center-of-mass energy of 14 TeV, with a nominal luminosity of $10^{34}\,\mathrm{cm}^{-2}\mathrm{s}^{-1}$. CMS, ATLAS, LHCb and ALICE are the four main experiments that are located along the collider. The Muon System, that allows to detect muons, is part of their detectors. It is made up of several types of gaseous detectors, among which Resistive Plate Chambers (RPCs) can be found in the ALICE, ATLAS and CMS experiments. RPCs detectors are operated with a freon-based gas mixture containing $C_2H_2F_4$ and SF_6, both greenhouse gases (GHGs) with a very high global warming potential (GWP). The European Union defined a set of regulations aiming at reducing the GHG emissions from fluorinated gases [29], such as:

- Restrict the placing on the market by reducing products availability of fluorinated GHGs;
- Ban the use of GHGs where eco-friendly alternatives are already available;
- Require regular and certified check controls on leaks for existing equipments;
- Require a recovery of the gases at the end of the equipment life.

The CERN EP-DT-FS Gas Team group deals with the maintenance, operation and development of gas systems for particle detectors at LHC and not LHC experiments. In particular, the group R&D is focused on the reduction of the GHGs emissions from particle detection and gas systems. The ATLAS and CMS RPC systems account for 50% of the CERN GHG emissions due to the presence of leaks at detector levels. The CERN Gas Team developed different strategies in order to reduce GHG emissions:

- Optimization of current gas system technologies (including gas recirculation);
- Development of gas recuperation systems;
- Research on alternative gases.

This thesis focuses on the search for alternative gases for RPCs detectors. In particular, the aim of this work is to study and characterize RPC performances with new eco-friendly gas mixtures. The present work is structured in three different chapters. The first one is dedicated to the description of RPC detectors. In particular, it is divided in different sections concerning the RPC systems in the LHC experiment, the historical development of the RPCs, their main characteristics and a description of the current gas mixture used. The second chapter concerns the systematic studies about the detector performances with alternative gas mixtures in the laboratory environment. The last chapter is dedicated to the studies performed at the Gamma Irradiation Facility (GIF++), in which RPCs operated with some selected gas mixtures were tested under a similar LHC experiments radiation background.

Chapter 2

RPC detectors at LHC experiments

2.1 The Large Hadron Collider

The Large Hadron Collider (LHC) is a particle accelerator and collider of the European Organization of Nuclear Research (CERN), placed in the already existing 26.7 km tunnel that was built for the LEP machine [1, 2, 3]. LHC is designed to collide proton beams with a center-of-mass energy of 14 TeV, with nominal luminosity of $10^{34}\,\mathrm{cm}^{-2}\mathrm{s}^{-1}$. However, it can also be operated in heavy ions (Pb) mode, with an energy of 2.8 TeV and a luminosity of $10^{27}\,\mathrm{cm}^{-2}\mathrm{s}^{-1}$.

By colliding antiparallel high-energy and high-intensity beams, LHC allows to explore the TeV scale allowing the experiments to probe deeper inside matter and providing further understanding of processes that occurred at the very early history of the Universe. The main goal of the LHC research is the study of the nature of electroweak symmetry breaking, which brought to the discover of Higgs bosons in 2012 [4, 5], as well as the search of new physics.

LHC is the last element in the CERN accelerator complex. It starts with the Linear Accelerator 4 (Linac4) that accelerates negative hydrogen ions to 160 MeV to prepare them to enter in the Proton Synchrotron Booster. Then, ions are stripped of their electrons during injection from Linac4 into the PSB, leaving only protons. These are accelerated to 2 GeV for injection into the Proton Synchrotron (PS) which pushes the beam up to 26 GeV. Protons are then sent to the Super Proton Synchrotron (SPS), where they are accelerated up to 450 GeV before to be sent to LHC. Here the two beams are brought into collision inside four detectors (ALICE, ATLAS, CMS, LHCb).

2.2 LHC experiments: Muon detectors

The four main experiments present different goals, but they required about the same characteristics. In particular, the detectors capability of identifying charged particle and measuring particles momentum with high resolution are of fundamental importance. The detectors also need high granularity, in order to reduce the influence of overlapping events,

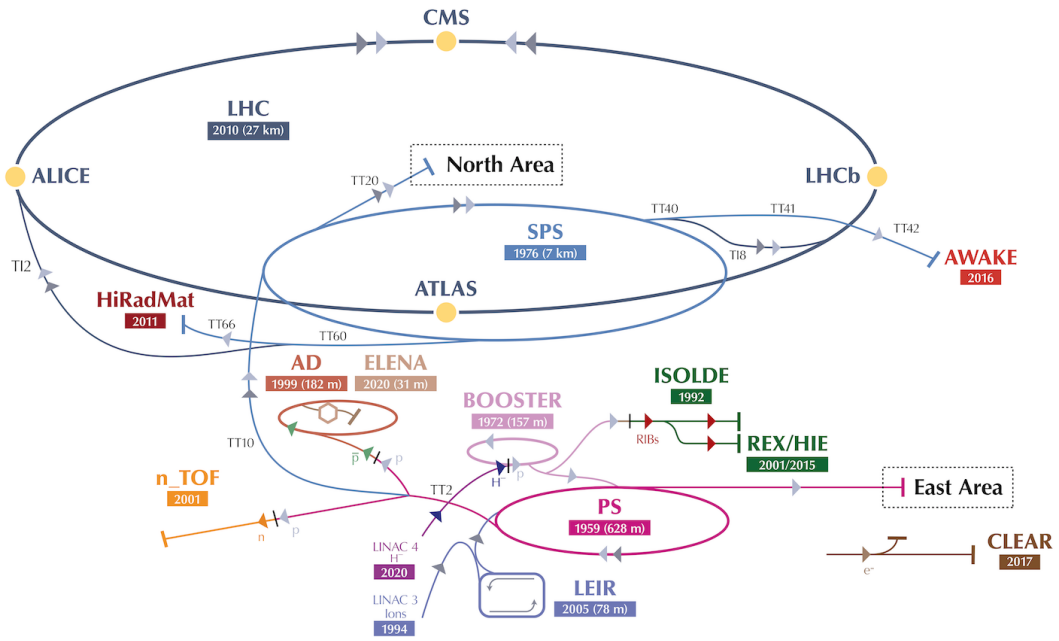

Figure 2.1: CERN accelerators complex [6].

and fast radiation-tolerant electronics for data acquisition [7, 8, 9, 10]. The general structure of LHC experiments could be divided into three different subparts:

- Inner Detectors:

  They are located close to the collision point. They allow the charged particles tracking and momentum measurements, as well as vertices reconstructions;

- Hadronic and Electromagnetic Calorimeter:

  They measure energy of hadrons, photons and electrons;

- Muon Systems:

  Since muons interact little with the electromagnetic calorimeter, a dedicated Muon System to detect them is needed. This system is in the outermost layers of the experiments and is composed by gaseous detectors. Muon detection is fundamental for a complete identification and characterization of collision, since muons are a very clean probe for many events of interest.

Since this thesis is focused on gaseous detectors, in particular RPCs, in the following section is reported a brief description about the design and layout of Muon Systems in the main LHC experiments.

2.2.1 CMS

The CMS (Compact Muon Solenoid) experiment structure is based on a super-conductive solenoid that produces a 3.8 T magnetic field. Figure 2.2 reports the experiment structure.

The tracker, the electromagnetic and hadronic calorimeters are located within the magnetic field volume. The iron yoke is equipped with a muons spectrometer for identification, triggering and momentum measurement. The system is divided into five separate wheels in the barrel, with four concentric layers of detectors. Both positive and negative endcaps are instead instrumented with four independent disks. Three different gaseous detector technologies are employed:

- Drift Tubes (DT): they are used to detect muons up to pseudo-rapidity $|\eta| < 1.2$[1];
- Catode Strip Chambers (CSC): they are in the endcaps region ($0.9 < |\eta| < 2.4$). They allow the handling of higher rate and non-uniform magnetic field;
- Resistive Plate Chambers (RPC): they are employed in both barrel and endcaps region ($|\eta| < 1.6$).

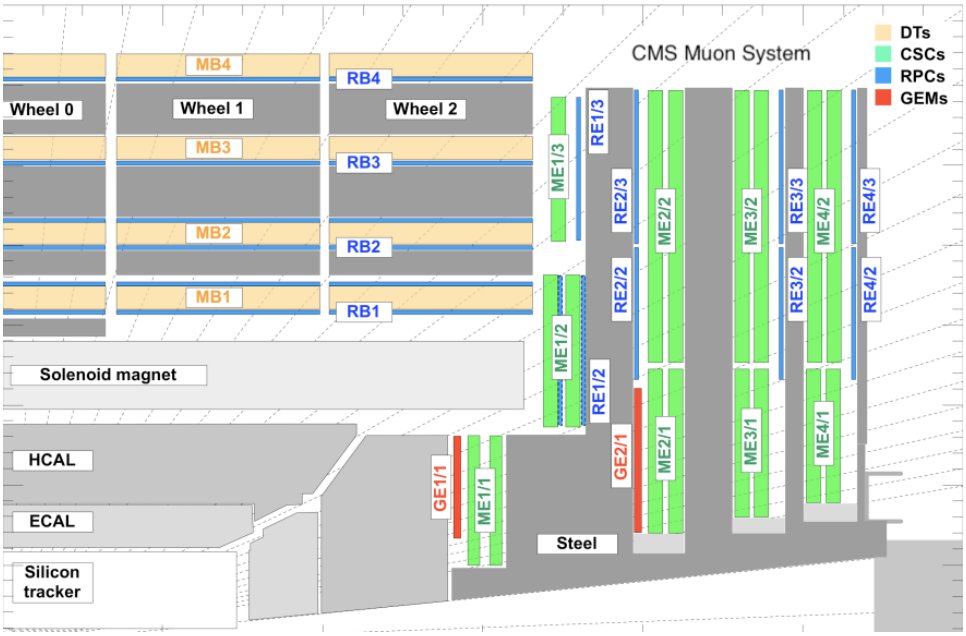

Figure 2.2: Quadrant of the CMS detector showing the Muon System [11].

2.2.2 ATLAS

The physics program of the ATLAS (A Toroidal LHC Apparatus) experiment requires high performance over the large range in trasverse momentum p_T. The experiment structure

[1]The pseudo-rapidity η is defined by:

$$\eta = -\log\left(\tan\left(\frac{\theta}{2}\right)\right)$$

where θ is the angle between the particle momentum and beam ax.

is reported in Figure 2.3. Its muon system includes three large superconducting air-core toroids, precision tracking chambers for accurate momentum resolution and an effective trigger system. The latter is realized with two different detector technologies: RPCs are used in the barrel, with two layers of chambers installed in the middle station and a third layer on the outer chamber station. The endcap trigger system is instead composed of Thin Gap Chamber (TGC), multi-wire chambers operated in saturated mode. Three multi layers are in the middle tracking station, while some others are part of the inner station. Precise p_T measurements are instead made possible by Monitored Drift Tube (MDT). Moreover, the use of sTGC and MicroMegas detectors in the inner station of the endcap allows to have optimal performances regardless the high background rate in this region.

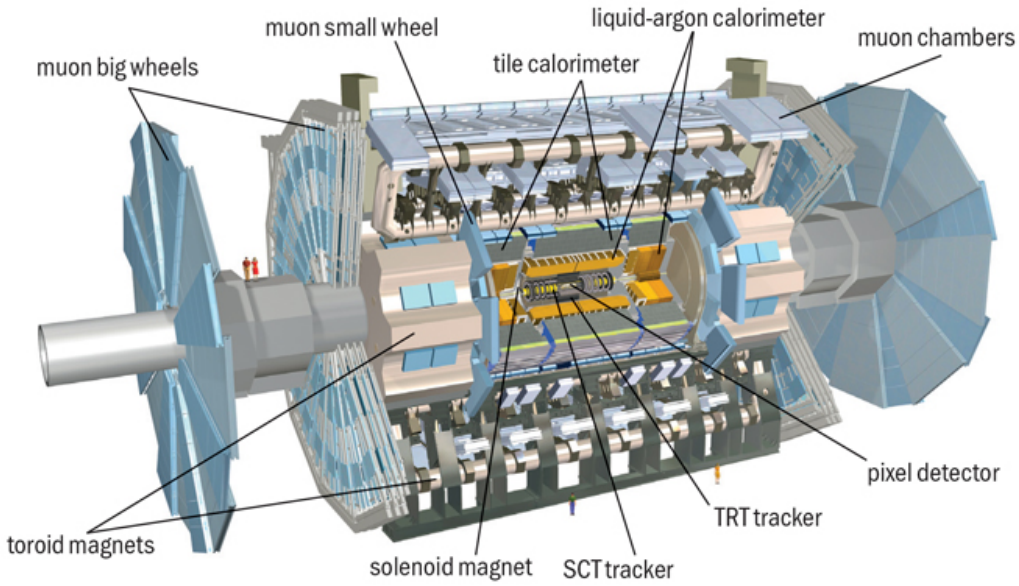

Figure 2.3: ATLAS structure[12].

2.2.3 ALICE

Since ALICE (A Large Ion Collider Experiment) is fully dedicated to heavy ion physics, its muon spectrometer needs to measure very low p_T in a large rapidity range ($-4 < \eta < -2.5$). The experiment structure is reported in Figure 2.4. Its tracking system is made of five stations with two detectors planes each, consisting of cathode pad chambers. These detectors are multi-wire proportional chambers with a segmented cathode plane. The system is also capable of highly efficient triggering, with four planes of 18 RPCs, operating in saturated avalanche mode.

2.2.4 LHCb

LHCb is a single-arm spectrometer with a forward angular coverage from 10 mrad to 300 mrad in the bending plane, to best exploit the statistics of the b and $\bar{b}$ production,

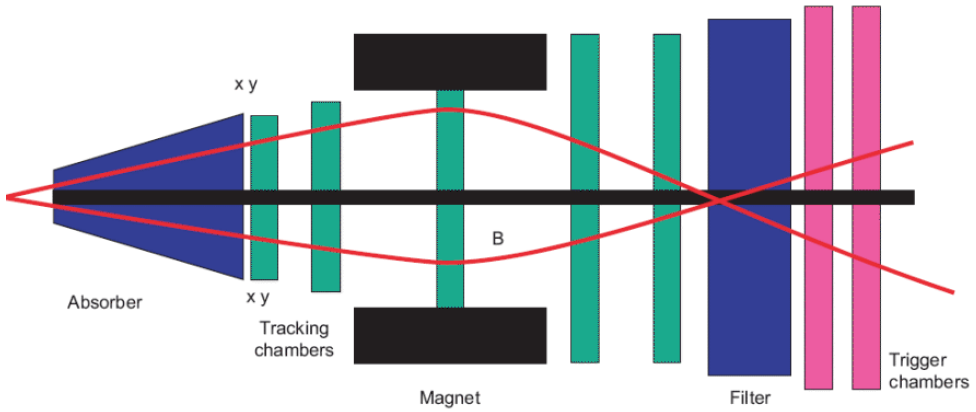

Figure 2.4: ALICE Muon Systems layout [13].

which predominantly happens in the same forward or backward region. The experiment structure is reported in Figure 2.5. The muon detection system is fundamental in the LHCb experiment since muons are present in the final state of many CP-sensitive B decay. The muon system is mainly composed of Multi Wire Proportional Chamber (MWPC). Lastly, the outmost layer hosts the Outer Tracker, a gaseous detector with twelve double layers of straw tubes.

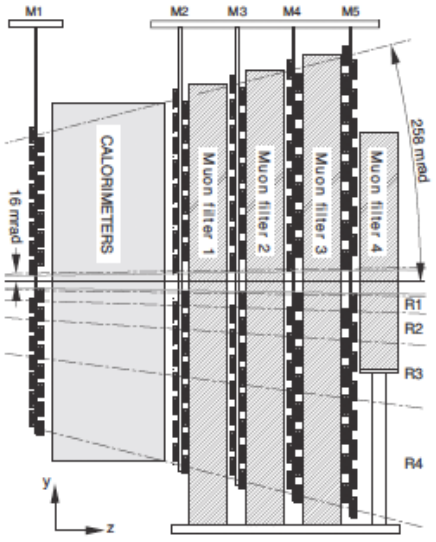

Figure 2.5: LHCb Muon Systems layout [10].

2.3 Resistive Plate Chambers

2.3.1 Historical Developments

All the gaseous detectors are based on the physical process of gas ionization, but the charge multiplication and collection can be very different from one detector to another [14, 18, 19, 20]. The ion-electron pairs, produced by the passage of a charged particle through the gas, are accelerated by the electric field and if they have enough energy, they could produce a secondary ionization. The continuous ionization brings to a multiplication of the free electrons and ions and the charge distribution acquires the typical avalanche shape.

Resistive Gaseous Detectors are a family of detectors of charged particles, energetic photons and neutrons, whose active medium is a gas and which are characterized by having at least one of the electrodes made of resistive materials.

First gaseous detectors were based on a cylindrical geometry and they were developed in the 1940s: the primary electrons created by the crossing ionizing particle were collected at a central wire and the avalanche processes occurred in the region immediately surrounding it. In fact, in such detectors the electric field decreases inversely with the distance from the central wire. Since the electron avalanche process needs the electric field to be intense enough, the consequence is that multiplication phenomena in a central wire gaseous detector can take place only at very small distances from the wire, where the electric field is above the multiplication threshold.

The planar resistive gaseous detectors were developed later than cylindrical ones. In parallel-plate detectors, the whole volume is available for multiplication and no region of the detector is privileged for this process.

However, in both cases, primary ionizations can be produced at any point of the gas volume. This means that in a cylindrical detector, primary electrons will have to drift for a variable time, depending on the position they were generated at, before reaching the region around the wire where they can start an avalanche, and give rise to a detectable signal. The time between the creation of the primary electrons and the generation of the output signal will be intrinsically affected by fluctuations, since different primary electrons will have to travel different distances depending on where they were generated. It is important to stress out that the drift velocity is highly dependent on the type of gas. This could lead to a time resolution of a few hundreds of nanoseconds.
On the contrary, in planar geometry a primary electron can give origin to an avalanche immediately after it was generated. In this case there is no separation between drift and multiplication region, and this drastically reduces the timing fluctuations described. Moreover, the resulting signal is the sum of the signals produced by the various avalanches and this further reduced timing fluctuations. Therefore, planar detectors are the only ones in the family of gaseous detectors to reach time resolutions for charged particles better than 1 ns.

The results of the first Parallel-Plate Counter were presented by J. W. Keuffel in 1948 [15, 16]. The first prototype consisted of two molybdenum disks, separated by a 3.0 mm gap and with a 3.1 cm^2 area. Later, Keuffel built counters made out of two copper plates kept at 2.5 mm distance and with a 35 cm^2 area. Across the two electrodes, put at a potential difference variable between 1 and 3 kV, xylene vapors ($C_6H_{12}(CH_3)_2$) were

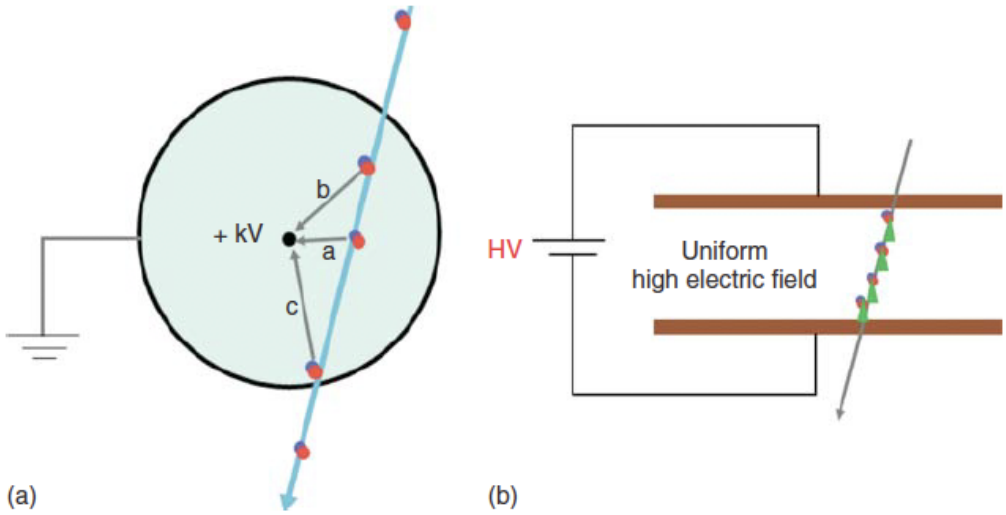

Figure 2.6: The effect of the different geometry on the charge development between a wire detector (a) and a parallel plate detector (b), [14].

flowed, at a partial pressure around 6 mmHg plus Ar, for a total pressure of 3800 mmHg. These devices were operated in spark mode, with output pulses around 100 V and with 50 Ω of impedance. Efficiency, measured with cosmic rays, was on the order of 90% in the plateau region, and time resolution from 5 ns up to 18 ns, depending on the applied high voltage. Despite these promising results, this detector remained extremely complicated and delicate to build.

During the 1950s several works were published in this field, both for what concerns the development of the detector itself, and for the electronics necessary for its rapid switch-off after the passage of an ionizing particle. Some interesting variations of the basic principle were developed. One of them is the flash chamber developed in Pisa by M. Conversi's group, which exploited the fact that a discharge inside these devices is usually accompanied by the emission of visible photons [17]. Basically, it consisted of a plane capacitor filled with a network of glass tube, without any central wire covered with black paper to shield them against external light and filled with argon or neon at 0.5 atm. However, this device could not be operated continuously. According to Conversi, these studies were at the origin of the development of spark chambers, which played such an important role in high energy particle detection.

Later, some researchers studied and tried to exploit in some practical devices avalanche mode of operation in parallel-plate detectors (called parallel-plate avalanche counters, PPAC). The high voltage applied to these detectors was constant, continuous in time and was sufficiently low so that avalanches did not transit to sparks. The signal from the avalanche detector was correspondingly small, but important advantages were that it could be operate at much higher counting rates, than spark counters, and could also handle many events simultaneously. Note that the electrodes used were metallic, sometimes solid and sometimes in the form of meshes.

In the '70-'80s a very important change was introduced in the development of parallel

plate detectors: the metal electrodes were substituted by resistive ones. One of the first modern RPCs was the Y. N. Pestov's Planar Spark Chambers (PSC). It had a copper cathode and the anode made of a special glass contained iron Fe^+ which allowed electronic conduction. The outer surface of the glass was coated with a conductive layer. The gap between the electrodes was 0.1 mm and the gas mixture was composed mainly of Ar or Ne with an addition of organic gases to ensure the UV light absorption. With these modifications, the time resolution was better than 1 ns.

At the beginning of the 1980s, R. Santonico and R. Cardarelli built in Rome the first prototype of the modern RPCs, using phenolic laminate compressed at high pressure. They operated at atmospheric pressure and did not require processes to prepare the electrodes as long and complex as those necessary for Pestov's counters [19]. The most important features of those RPCs were:

- Planar geometry that allowed a good time resolution;
- Resistive materials for the electrodes that prevented the discharge from propagating through the whole gas;
- Application of the HV to the electrodes via a signal-transparent resistive layer;
- Easiness of production.

Electrodes were built using two high-pressure laminates (HPL) sheets separated by a button like spacers of width 2 mm and laterally sealed by a frame of PVC which act as a good insulator.

2.3.2 Signal Development

When a single-gap RPC is traversed by an ionizing particle, n_{cl} ion-electron clusters are generated along its path. For "cluster" it is intended a primary ion-electron pair, directly generated by the impinging particle, plus the additional pairs that can be generated by the primary electron in case it has enough kinetic energy to further ionize the atoms or molecules in the gas mixture. Note that the number of clusters n_{cl} following the passage of an ionizing particle is not fixed, but its actual value changes from event to event according to a certain probability distribution. In the case of RPC, it is possible to assume that it follows a Poisson distribution and that it depends linearly on the gas gap g. Values for the average value of the number of clusters per unit length, which here will be indicated with λ, have been measured experimentally for many gases and can be found in literature. In case of gas mixture, the value for λ is the weighted average of the ones corresponding to the gas mixture components.

Given these assumptions, the probability P_{cl} that k ion-electron clusters are generated in the gas gap by an ionizing particle can be computed by simple Poissonian statistics[2]:

[2]In case the particle is crossing the RPC gas gap not perpendicularly, we will also define:

$$\lambda_{eff} = \frac{\lambda}{\cos(\phi)}$$

$$P_{cl}(n_{cl} = k) = \frac{(g\lambda)^k}{k!} e^{-g\lambda} \tag{2.1}$$

and the average value of this probability is $g\lambda$. The probability that not one single cluster is generated in the gas gap is given by:

$$P_{cl}(n_{cl} = 0) = e^{-g\lambda}$$

This equation is important since it expresses the intrinsic inefficiency of the detector, so its value imposes limits on the thickness of the gas layer.

It is possible to consider the effect of a uniform electric field in the gas gap, due to an applied external voltage. If the electric field is intense enough, electrons contained in the cluster will acquire enough kinetic energy to start avalanching. The simple model of an avalanche is a pure exponential development. In this case, the charge contained in the avalanches at a certain position x, with respect to the cathode, will be given by:

$$q(x) = q_e e^{\alpha^* v_d t} \sum_{j=1}^{n_{cl}} n_0^j M_j, \qquad 0 < t \leq \frac{g - x_0^{n_{cl}}}{v_d}$$

where n_0^j is the number of primary electrons contained in the jth cluster, α^* is the effective first Townsend coefficient, q_e is the elementary electron charge, v_d is the electron drift velocity ([14], p. 70). M_j is introduced to consider stochastic fluctuations in the avalanche processes and it is a random number extracted from a Polya distribution, describing the stochastic effects that take place in the avalanche development.

The signal of the RPC is usually read on copper strips placed close to the electrodes. Using the Shockley-Ramo theorem which states that the induced charge on the strip depends on the instantaneous change in the line flux of the electromagnetic field it is possible to describe the induced current with the expression:

$$i_{ind} = q v_d E_w$$

where v_d is the electrons drift velocity and E_w is the weighting field, that in case of the RPC can be assumed uniform across the gap and can be expressed in terms of the gas gap and the thickness of the electrodes by the formula:

$$E_w = \frac{\epsilon_r}{\epsilon_r g + 2d} = \frac{1}{g + 2\frac{2d}{\epsilon_r}}$$

where ϵ_r is the electrodes dielectric permittivity and d is the electrode thickness. The induced current over time caused by the avalanche process takes then the following expression:

$$i_{ind} = v_d E_w q_e e^{\alpha^* v_d t} \sum_{j=1}^{n_{cl}} n_0^j M_j$$

---

where ϕ is the azimuthal angle of the track if the incident particle and we will substitute λ_{eff} to λ in following equations.

$i_{ind}(t)$ contains basically most of the information coming out from an RPC. The charge induced on the external pickup electrodes can be computed by direct integration of the previous formula and is given by:

$$q_{ind} = \frac{\epsilon_r g}{\epsilon_r g + 2d\alpha^* g} \sum_{j=1}^{n_{cl}} n_0^j M_j \left[e^{\alpha^*(g - x_0^j) - 1} \right] \tag{2.2}$$

where x_0^j is the initial position of the jth cluster.

RPCs can work in two different modes: avalanche or streamer. The transition between these two modalities was studied and summarized by H. Raether [21]. One of the main conclusions is that sparks appear when the total charge in the avalanche is close to or exceeds 10^8 electrons (the so-called Raether limit).

The discharge of the RPC is a sequence of stages and the streamer is not a direct evolution of the first avalanche, but rather a late discharge stage that develops via gas photoionization processes after the first avalanche is extinguished. In a RPC at low voltage range the growth of the charge is exponential, that is typical of the proportional mode. At higher voltage, multiple pulsed signals start to appear: the avalanche to streamer transition occurs. The new pulses are late and the signals are much larger than the avalanches. As an example, in the waveform shown in Figure 2.7 an avalanche signal is followed by a streamer after-pulse.

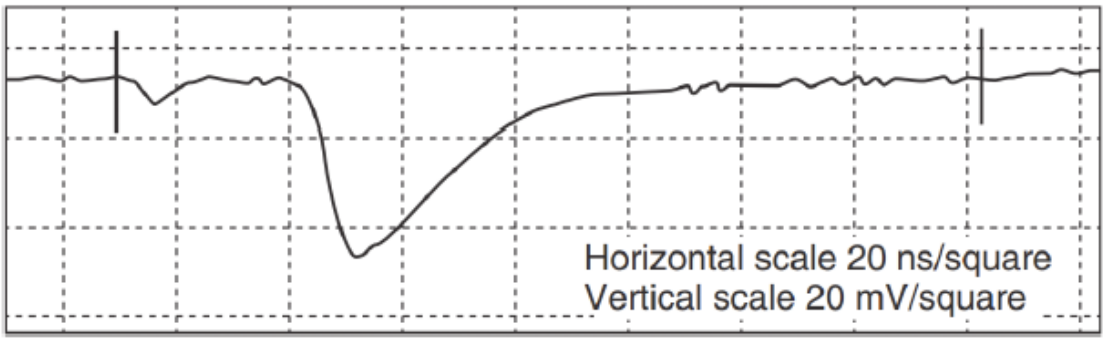

Figure 2.7: Example of a RPC signal at 9.4 kV showing an avalanche precursor followed by a streamer pulse [20].

Both operation modes have advantages and disadvantages. The streamer mode allows to obtain good detection efficiency (greater than 95%) and time resolution ($\simeq$ ns), when a low flux of incident particle is involved. At higher flux $\left(200 \frac{\text{Hz}}{\text{cm}^2}\right)$, as in LHC, RPCs begin to lose their efficiency, due to the fact that, after the streamer development, the area of the electrodes plates involved in the discharge needs a certain time, in the order of 10 ms, to get charged again. To solve the problem one can operate the detector in avalanche mode. In this case lower gains are used to reduce the size and charge of the avalanches and therefore to avoid the discharge.

In the following sections is reported a description of some fundamental aspects of RPC performance.

2.3.3 Charge distribution

Equation 2.2 allows one to predict the shape of the charge distribution. However, since in this equation there are many stochastic variables, it is preferred to follow a Monte Carlo approach. Figure 2.8 shows the simulations of the charge distributions for a 2 mm and 9 mm gap chamber. For this simulation, λ was assumed to be 5.5 clusters/mm in both cases, and the product $\alpha^* g = 9$.

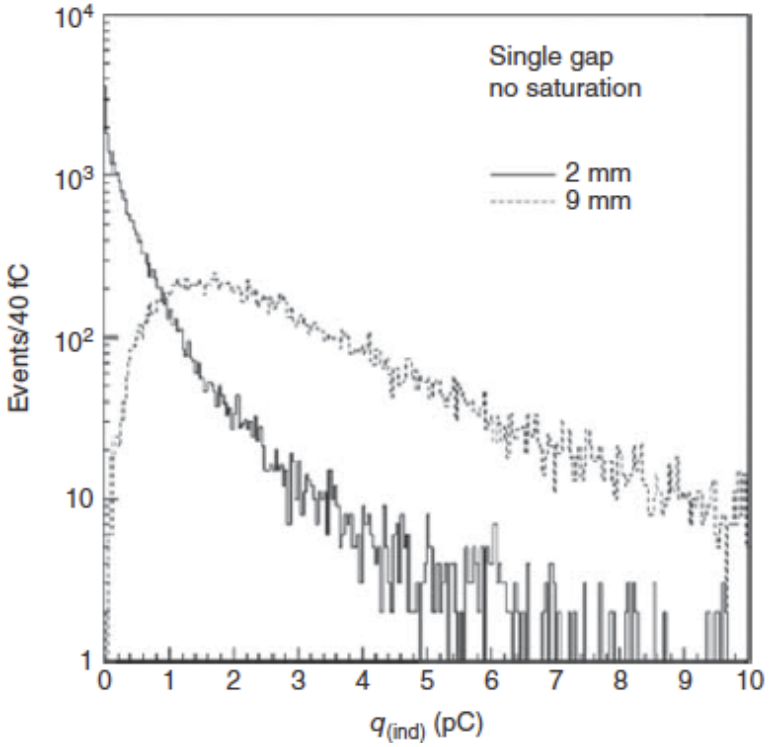

Figure 2.8: Simulation of charge distribution for 2mm and 9mm gap [22].

The two sets of distributions differ significantly: in the 2 mm gap, the curves tend to diverge for $q_{ind} \to 0$, while in the 9 mm gap they tend to vanish. Even if the average induced charge is roughly the same, the number of events characterized by small charges is greater in the 2 mm gap with respect to the 9 mm gap. There is also an excess of events in the right tail of the distribution, counterbalanced by less events in the central part. On the contrary, the curves for the 9 mm gap case vanish for charges close to zero. Essentially, the events with a charge less than certain electronic thresholds are the ones which are bound not to be detected and confused with the electronic noise. This implies that the shape of the charge distribution close to zero is fundamental to predict the efficiency the device will be able to reach given certain operating conditions.

If the fluctuation in the number of electrons n_0^j contained in each cluster and in the gain gas are neglected, it is possible to obtain an analytical expression for the charge probability distribution. If the case in which the cluster is closest to the cathode is considered, it is possible to obtain the following expression:

$$P(q) = S_n q^{\frac{\lambda}{\alpha^*}-1}$$

where in the last expression S_n is a normalization factor that absorbs all the constant values for a given operating voltage and gas used [14]. In this case the charge distribution depends just on the $\frac{\lambda}{\alpha^*}$ ratio. There are three cases of interest:

- $\frac{\lambda}{\alpha*} < 1$: the resulting distribution is strictly decreasing and it diverges for $q_{ind} \to 0$. This is the typical situation of a 2 mm gap;
- $\frac{\lambda}{\alpha^*} \simeq 1$: $P(q)$ is constant;
- $\frac{\lambda}{\alpha^*} > 1$: the resulting distribution is strictly increasing, and it starts at 0 for $q_{ind} = 0$. This is typical for a wide-gap RPC where, thanks to the large value of gap width g, α^* can be set conveniently low.

The reason of the two parameters having effect on the distribution depends on the fact that the Poisson probability of finding a particular number of clusters n_{cl}, Equation 2.1, depends on λ, while α^* is a fundamental parameter in the avalanche multiplication process. However, when the gain in the gas is large enough, deviations from the exponential multiplications appear. The effects are due to the electric fields between the ions and the electrons in the avalanche locally modifying the electric field across the gap, thus making the electron in the avalanche see a distorted field. This effect is also known as the space-charge effect.

2.3.4 Efficiency

RPC efficiency can be computed by looking at the charge distribution close to zero, so counting the fraction of events which are under a certain electronic threshold. For simplicity, it is possible to consider Equation 2.2 for only one cluster ($j = 1$). In this case, the charge induced on an external pickup electrode has a simplified expression and is given by:

$$q^1_{ind} = \frac{q_e}{\alpha^* g} \Delta V_w n^1_0 M_1 \left[e^{\alpha^*(g-x_0)} - 1 \right]$$

where ΔV_w is the weighting potential. For an event to be revealed, *i.e.* distinguished with respect to the intrinsic noise of the system, its induced charge q^1_{ind} must be greater than a certain electronic threshold q_{thr}, characteristic of the readout electronics. Only these events will account for the efficiency of the detector. Inverting the previous equation, it is possible to obtain that to satisfy this condition, the cluster has to be originated at a distance of the cathode less than:

$$x^1_0 < g - \frac{1}{\alpha^*} \log\left(\frac{q_{thr}}{A_1} + 1 \right)$$

where:

$$A_1 = \frac{q_e \Delta V_w M_1 n^1_0}{\alpha^* g}$$

If it is assumed that the clusters contain only one electron and the avalanche fluctuations are neglected, the efficiency can be computed by:

$$\epsilon_C = 1 - e^{-\left(1-\frac{\eta}{\alpha}\right)g\lambda}\left[1 + \Delta V_W \frac{\alpha - \eta}{q_e} q_{thr}\right]^{\frac{\lambda}{\alpha}}$$

where β is the electronegativity attachment and η is the attachment coefficient[3]. The efficiency of the detector depends on the gas gap and on the choice of the gas mixture.

2.3.5 Time resolution

Starting from the signal of a single primary electron somewhere in the RPC, it is possible to compute the time resolution:

$$i_{ind}(t) = I_s e^{\alpha^* v_d t}$$

where I_s is the signal current amplitude, different from event to event, exponentially distributed around some average amplitude. The time t where the signal crosses a certain threshold I_{thr} is then given by:

$$t = \frac{1}{\alpha^* v_d} \log\left(\frac{I_{thr}}{I_S}\right)$$

Starting from this equation, one can obtain that the fluctuations on the crossing time t, so RPC time resolution, is given by:

$$\sigma_t = \frac{1.28}{\alpha^* v_d}$$

Intrinsic time resolution of RPCs is therefore dominated by the magnitudes of the effective Townsend coefficient and the drift velocity and it is independent of the primary ionization parameters, at least for the first order. With a more accurate study, it is possible to show that the timing variance at first order is a decreasing function of the average number of initiated avalanches.

2.3.6 Bulk resistivity

The RPC resistive electrodes are usually made of HPL plates covered with a thin layer of melamine. The bakelite plates are made of several compressed layers of kraft paper imbued with resin, then heated and finally cut. Different types of cooking cycles and maximum cooking temperature carry a different bulk resistivity, a very important parameter since the rate capability is strongly dependent on it. Indeed, the time constant of an RPC involved in an avalanche process is smaller at lower resistivity and at a very high particle rate a drop of voltage V_d occurs across the plates because of the high current flow between them [23]. This voltage drop can be estimated to be:

[3]The attachment coefficient is the probability that an electron drifting through a gas under the influence of a uniform electric field will undergo electron attachment in a unit distance of drift.

$$V_d = 2\bar{Q}_e r s \rho$$

where $\bar{Q}_e$ is the average electronic charge, r is the particle rate normalized to the area, s is the electrode thickness and ρ is the bulk resistivity.

The quality of the bakelite is very important and it is crucial to monitor the environmental conditions in which the RPC is located. As a matter of fact the resistivity is strongly dependent on temperature and humidity conditions. For example, works done by many groups [24] have shown that the resistivity is correlated with the environmental temperature by the following empirical relation:

$$\rho_{20} = \rho_T \, e^{0.128(T-20)}$$

where ρ_T is the measured value at the temperature T, ρ_{20} is the corrected value for a temperature $T = 20°\mathrm{C}$. Other works [26] show that the temperature and humidity dependence of bulk resistivity of bakelite for RPCs.

2.3.7 RPCs at LHC

RPC detectors are currently used in several experiments around the world. At LHC, RPCs are present in three of the four main experiments: ATLAS, CMS and ALICE. Thanks to their fast time resolution (1 ns) and suitable space resolution (1 cm) they are widely used for the muon trigger systems. The main difference between the ATLAS and CMS RPCs is the layout: the former has single-gap while the latter has double-gap RPCs. On the other hand, the ALICE experiment has two kinds of RPCs: the single-gap and the multi-gap. The differences between the two systems are considerable. The single gap are made of HPL and are used as a trigger while the multi-gap are made of glass and are employed for particle identification by using time of flight techniques [25]. In the three experiments, the RPCs are mainly operated with a three components gas mixture made of $C_2H_2F_4$ (R134a), iC_4H_{10} and SF_6. Even if the geometry of each experiment is slightly different, the experimental apparatus conception is the same.

2.4 RPC and greenhouse gases

2.4.1 Greenhouse gases and Global Warming Potential

A greenhouse gas (GHG) is any gas that has the property of absorbing infrared radiation (net heat energy) emitted from Earth's surface and reradiating it back to Earth's surface, thus contributing to the greenhouse effect. Carbon dioxide, methane and water vapor are the most important greenhouse gases in the atmosphere. GHGs have a profound effect on the energy budget of the Earth system despite making up only a fraction of all atmospheric gases. Several processes influence greenhouse gas concentrations. Some, such as tectonic activities, operate at timescales of millions of years, whereas others, such as vegetation, soil, wetland and ocean sources operate at timescales of hundreds to thousands of years. Human activities, especially fossil-fuel combustion since the Industrial Revolution, are responsible for steady increases in atmospheric concentration of various greenhouse gases, especially carbon dioxide, methane, ozone and chlorofluorocarbons (CFCs). The

effect of each greenhouse gas on Earth's climate depends on its chemical nature and its relative concentration in the atmosphere. Some gases have a high capacity of absorbing infrared radiation or occur in significant quantities, whereas others have considerably lower capacities for absorption or occur only in trace amounts. Radiative forcing, as defined by the Intergovernmental Panel on Climate Change (IPCC), is a measure of the influence a given greenhouse gas or other climate factors have on the amount of radiant energy impinging upon Earth's surface [27].

A measure of how much heat a GHG traps in the atmosphere in a fixed time span is given by the Global Warming Potential (GWP). It is the time-integrated radiative forcing due to a pulse emission, representing a mass, of a given gas, over some given time period (or horizon) relative to a pulse emission of carbon dioxide. Emission targets are set in terms of equivalent emissions of carbon dioxide, where the carbon dioxide equivalence of emissions of other greenhouse gases is determined using the GWP with a 100-years time horizon (GWP_{100}) [28].

The GWP of a gas strongly depends both on its radiation absorption in the infrared spectra (also known as radiative activity) and on the atmospheric lifetime of the gas. In particular, hydrofluorocarbons (HFCs), hydrochlorofluorocarbons (HCFCs), and sulfur hexafluoride (SF_6) are called high-GWP gases because, for a given amount of mass, they trap substantially more heat than CO2. (The GWPs for these gases can be in the thousands or tens of thousands).

Due to their environmental risk, a "F-gas regulations" started to appear in many countries. As concerns the EU, the F-gas regulation aims to reduce emission from industry to 70% below 1990 levels by 2030 [29]. The new provisions aim to decrease the EU's emissions of fluorinated greenhouse gases by 70 million tonnes (Mton) of CO_2 equivalent to 35 Mton by 2030. Three main regulatory approaches are used to effect a reduction of fluorinated greenhouse gas emission:

- Introduction of a gradual phase-down of quantities of hydrofluorocarbons (HFCs) available on the market;
- Prohibitions on use and placement on the market, insofar as technically feasible and more climate friendly alternatives are available;
- Continuation and expansion of the scope of regulations concerning leak tests, certification and disposal.

The new F- gas regulation will create incentives to use alternatives to F-gases.

2.4.2 RPC gas mixture

For efficient operation, RPCs require the use of gas mixtures with a somewhat demanding combination of characteristics [14]:

- High density of primary ion-electron clusters, to assure high detection efficiency;
- Relevant quenching properties, since the mixture should be characterized by low photon emission and transmission, to reduce the photon feedback phenomena;

- Being electronegative, to reduce the transversal side of the discharges and improve its localization;
- Possibly, it should not be dangerous for human health.

In addition, desirable characteristics include the following:

- The chemistry process which take place during electron multiplication should have reasonable limits in the production of the following species:
  - Aggressive chemicals such as hydrofluoric acid, which may attack the RPC electrode's surface and gas system components;
  - Polymerization materials, which may form depositions of extraneous material on the plates
- The gas mixture should be eco-friendly. This implies that it should be characterized by a negligible Ozone Depletion Power[4] (ODP) and low GWP to reduce damage to the ozone layer and the greenhouse effect.

As previously mentioned, a crucial parameter to understand the performance of an RPC detector is the cluster density λ. In principle, λ should be as large as possible to maximize the signal and to achieve high efficiency and its value changes with the gas mixture. With a high percentage of $C_2H_2F_4$, in addition to a high value of λ, RPCs have excellent timing properties due to higher electron drift velocity compared to that of other gases. Even in low percentage with respect to $C_2H_2F_4$, polyatomic molecules acting as a quencher, like iC_4H_{10}, are necessary to absorb photons in a wide energy range. In fact such molecules have a large number of non-radiative excited states and therefore they avoid that the UV photons produce secondary avalanches.
It has been demonstrated [31, 32] that adding a small quantity of SF_6 to a $C_2H_2F_4/iC_4H_{10}$ gas mixture helps to suppress the streamer as it can be seen in Figure 2.9. Without SF_6 there is a clear streamer peak well separated from the avalanche one while in the mixture with SF_6 the streamer peak seems to move to lower values. The specific mechanism by which the SF_6 molecule is so effective in reducing the streamer probability should be related to its electron affinity ($1.05 \pm 0.10\,\text{eV}$).

2.4.3 RPC gas system in LHC experiments

The RPC systems at the LHC are mainly operated with a $C_2H_2F_4/iC_4H_10/SF_6$ gas mixture and the total volume of the chambers approaches a value of $15\,\text{m}^3$ each, covering a surface of $\simeq 4000\,\text{m}^2$. Due to the large size of the systems, the cost of the mixture and the use of greenhouse gases, the RPCs are operated using recirculating gas systems, with a recirculation fraction up to 90% [34]. The recirculation fraction has been validated for a

[4]The ODP of a compound is defined as the ratio of the total amount of ozone destroyed by that compound with respect to the amount of the ozone destroyed by the same mass of CFC-11. The ODP of CFC-11 is defined to be 1 [30].

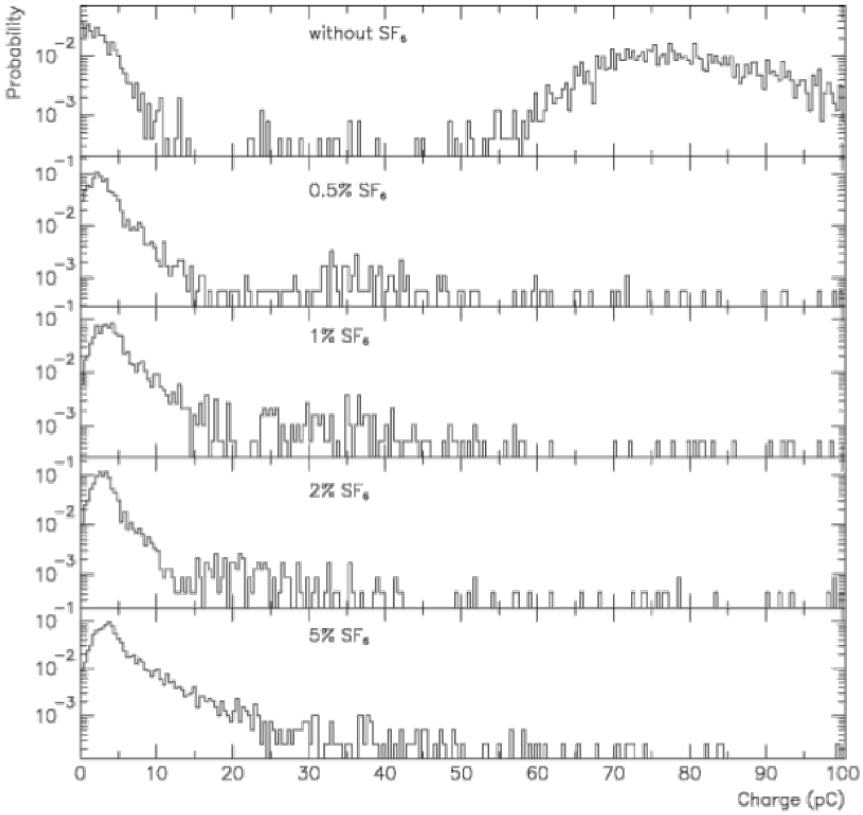

Figure 2.9: Experimental charge distribution as a function of SF_6 concentration added to the baseline mixture [31].

safe operation of the detectors and purifier cartridges are required on the return lines to clean the gas from accumulated impurities that can compromise RPCs performance. It is however not possible to operate the detectors to higher recirculation fractions due to the presence of leaks at the detector level. For this reason, fresh gas mixture must be continuously injected into the system. The main responsible for greenhouse gas emissions is the $C_2H_2F_4$. The GWP of the $C_2H_2F_4$ calculated over a period of 100 years is 1430 and its production is subject to the European Regulation [29]. It is therefore advisable to search for new environmentally friendly gases with a lower GWP that can be used as an alternative to $C_2H_2F_4$ to reduce the emissions and contain the operational costs. The alternative gases should also optimize, where possible, the RPCs performance and aging issues. Several gases with similar properties of $C_2H_2F_4$ are already available on the market and used for specific industrial application as replacements for the $C_2H_2F_4$. For example, gases in the family of the HydroFluoroOlefin (HFO) have already been identified by the refrigeration industry as a low GWP (4-6 over 100 years) alternatives and are used nowadays in refrigerating systems. Since the relevant properties for particle detectors operation are not available for such new gases, a simulation of the detector with the desired gas mixture can be hardly achieved. Thus, the search for new $C_2H_2F_4$ alternatives requires an experimental setup where RPC performance can be tested with these new eco-friendly gases.

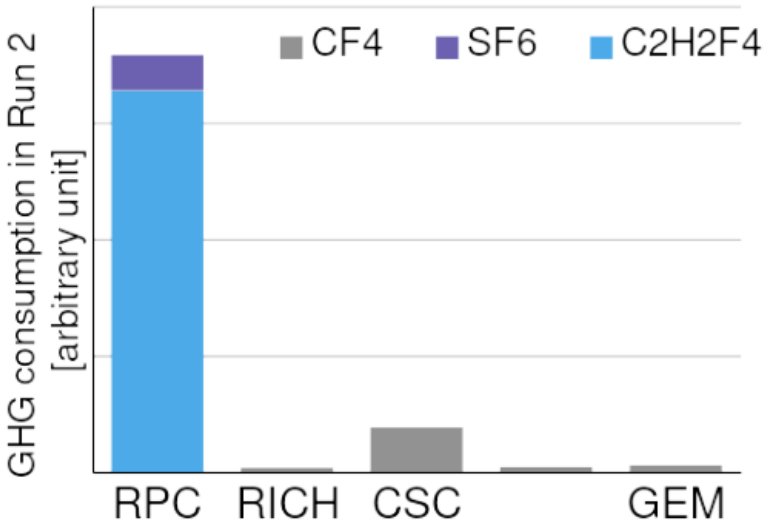

Figure 2.10: GHG emissions from gas systems. The main contribution is due to the $C_2H_2F_4$.

2.5 Gamma Irradiation Facility

The GIF++ (Gamma Irradiation Facility) is located in the *Experimental Hall North Area* (EHN1) on the CERN Prevessin site in France and it houses a radioactive ^{137}Cs source with an activity of 12.15 TBq in September 2020 (initially 14.9 TBq in November 2011) [35]. As it can be seen from Figure 2.11, the GIF++ area is mainly composed by the actual irradiation area (100 m^2), a preparation zone and a two-floor area that hosts the gas systems and the electronic service. The bunker is delimited by 1.6 m thick concrete blocks, creating a shielded area that is accessible from two sides. The roof of the bunker, made as well of concrete blocks, can be removed when necessary. Outside the main bunker entrance, a preparation area is available for preliminary tests on detectors before moving them into the irradiation area.

This facility is positioned directly in the H4 beam line from SPS, allowing it to have a high-energy muon beam under high adjustable background radiation from the ^{137}Cs source. To deliver a uniform flux of the 662 keV photons at each distance from the radiator, an angular correction filter is installed, which modifies the $\propto \frac{1}{r^2}$ dependence of the γ-ray flux. The simulation of the radiation field with a $\pm 37°$ opening angle is reported in Figure 2.12.

The irradiation rate can be modified remotely by selecting different attenuation filters combinations according to the matrix reported in Table 2.1.

Currently, more than ten setups are under test in the facility, covering different gaseous detector technologies: Drift Tubes (DT), Cathode Strip Chambers (CSC), MicroMegas (MM), Resistive Plate Chambers (RPC), small-Strip Thin Gas Chamber (sTGC). The different setups come from the four LHC experiments, which make use of the GIF++ facility for both R&D studies as well as for validation and detector aging purposes.

Table 2.1: Matrix of available GIF++ radiation attenuation factors. The attenuation factors 1, 2, 3 of filters A, B, C have to be multiplied.

	A	B	C
1	1.0	1.0	1.0
2	10.0	1.5	2.2
3	100.0	100.0	4.6

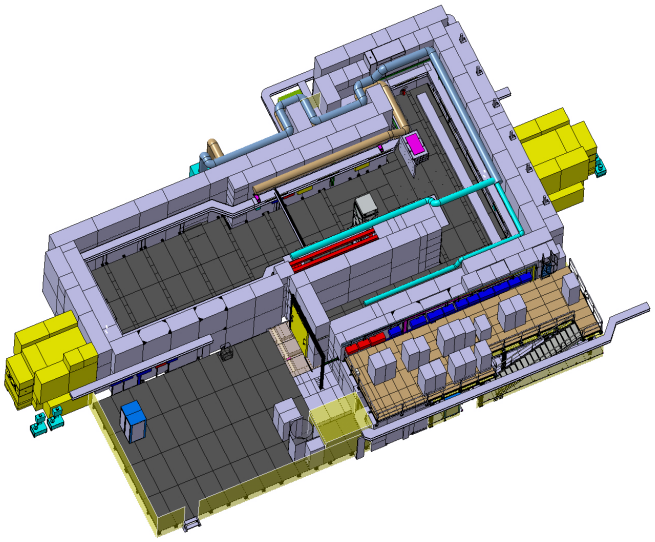

Figure 2.11: Floor plan of the GIF++ facility [35].

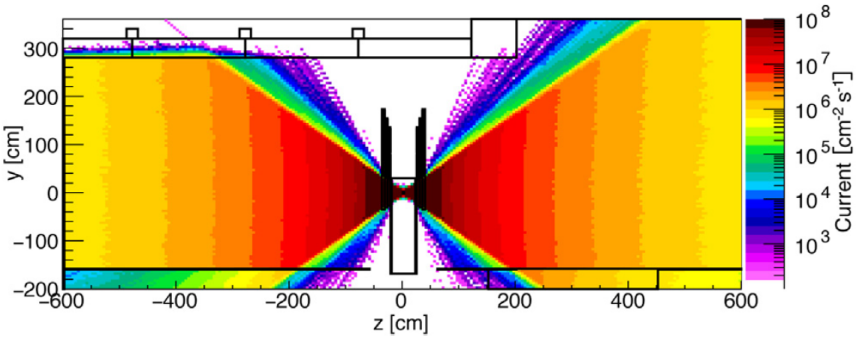

Figure 2.12: Photon current in the vertical plane through the source at $x = 0.65$ m [35].

Chapter 3

Gas Related Studies on RPC Performance

The aim of the present study was to characterize, with cosmic muons, different gas mixtures in terms of their GWP and test the performances of RPC detectors using these mixtures. The gas mixtures tested were chosen with the goal to reduce the GWP with respect to the standard gas mixture, actually used in LHC experiments. The RPC performance with the new gas mixtures must have an almost identical behavior with respect to the standard gas mixture since in the LHC experiments it will not be possible to replace Front-End electronics, high voltage connectors, *etc.* In some cases, new mixtures were tested with the only purpose of understanding better the effect of a gas component in the gas mixture, so without worrying about its GWP or its compatibility with LHC electronics.

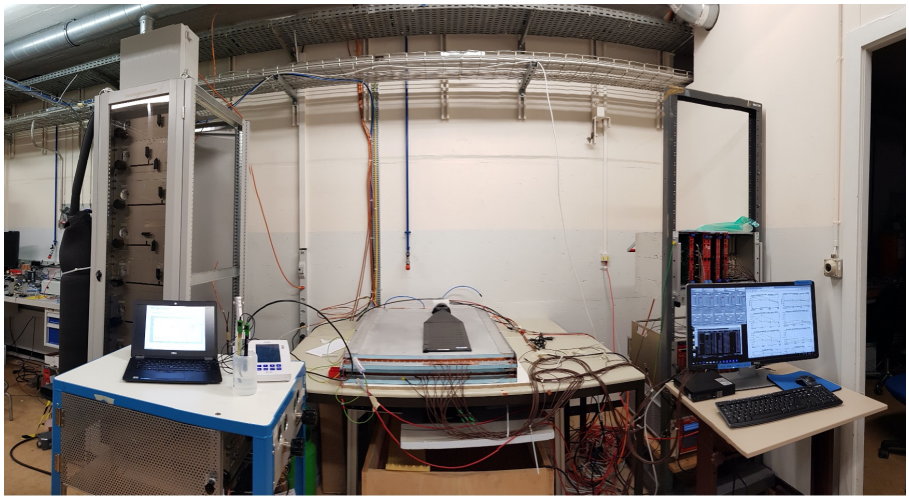

Figure 3.1: Experimental setup. Starting from the left: gas mixing unit, gas analysis, detectors, electronics.

Such studies were done with the setup shown in Figure 3.1. In the following sections the experimental setup, the analysis methodology and the results of the study are shown.

3.1 Experimental setup

A scheme of the experimental setup is shown in Figure 3.2. It is composed of three different parts: gas supply, detectors and readout. In the following sections each part will be described.

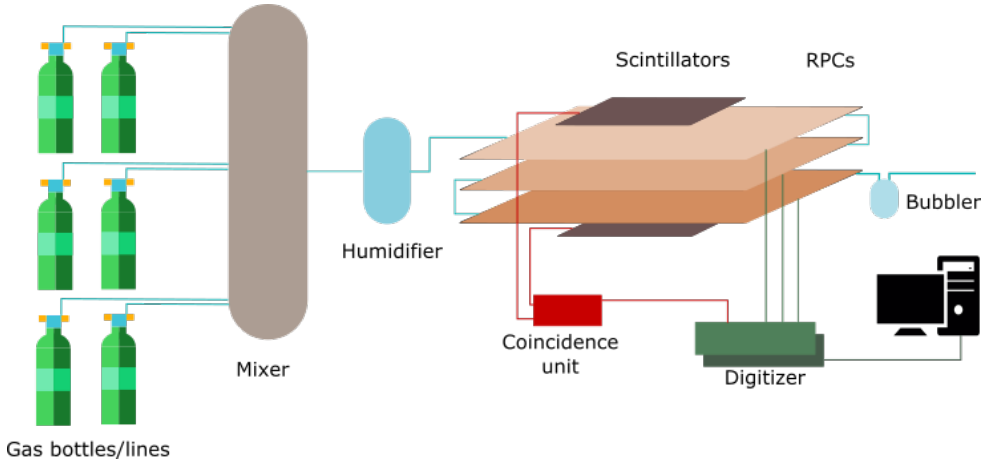

Figure 3.2: Experimental setup scheme.

3.1.1 Gas supply

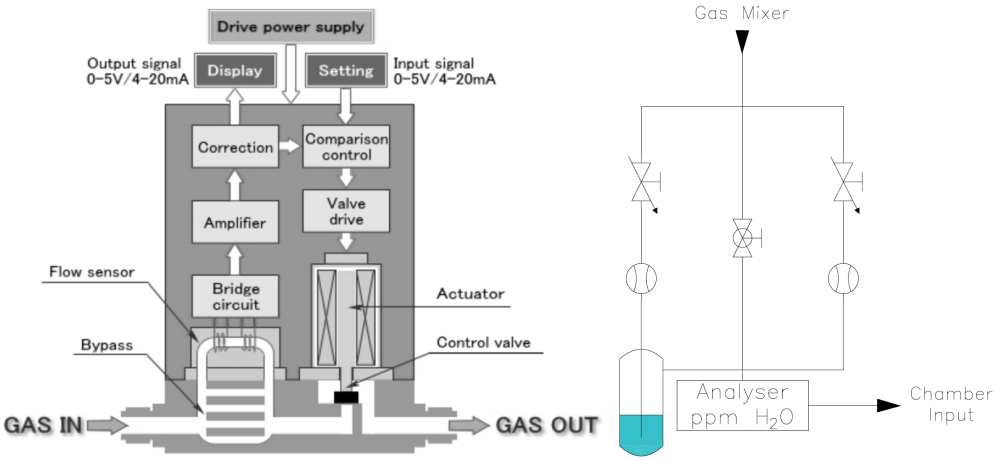

Figure 3.3: a) Mass Flow Controller scheme [36]; b) Humidifier scheme.

The gas bottles and gas lines were connected to a gas mixer. On each line a Mass Flow Controller (MFC) was installed that allowed to adjust the flow of each gas component and the total flow injected into the detectors. MFCs are composed of a flow sensor, a bypass, a valve and a control circuit, as shown in Figure 3.3a. In the flow sensor, two resistors are wounded on the upstream side and the downstream side, around the capillary tube.

When no gas is flowing in the capillary, the heat of the upstream and downstream sides of the resistors is kept at equilibrium and the flow rate output signal shows zero. The input gas is divided into the sensor and a bypass. When the gas begins to flow into the sensor, a temperature difference occurs between the upstream and the downstream resistors and the thermal balance is lost. This change is captured by the bridge circuit as a flow rate output signal. The flow control valve performs PID operation (proportional, integral, derivative) to match the signal level between the external flow rate setting signal and the flow rate output signal. Since the valve opening is fine tuned and adjusted automatically, it is possible to control the flow rate under the setting condition [36]. MFCs were remotely connected to a PC and controlled via dedicated software.

The different gas lines were flushed into a 2 l volume, allowing the gas to mix before going to the input of the detectors. Between the gas mixer and the chamber input a humidifier was installed, shown in Figure 3.3b, to control the dew point of the gas, usually kept between 2 °C and 4 °C. A return line connected to the chambers output and terminating into a bubbler was installed that ensure to visibly check if the detector was under the correct flushing condition.

3.1.2 Detectors

Plastic scintillators

As concerns the cosmic muons trigger, a set of two plastic scintillators was used. The scintillators had the same size (17 cm x 60 cm) and they were located above (namely SCTOP) and below (namely SCBOT) the RPC chambers, in correspondence of the seven strips used for the readout as shown in Figure 3.2.

In order to find the scintillators voltage working point, a complete characterization of both of them was done. The two scintillators were aligned by placing them one above the other. The scintillators were powered with a NIM power supply module[1] and the muon counts and coincidences between the scintillators were obtained with a NIM discriminator module[2], a NIM coincidence module[3] and a NIM scaler module[4].

First, the signal of both the scintillators were observed with an oscilloscope[5] in order to determine the starting voltage and the signal threshold. A 35 mV threshold and a starting applied voltage of 1500 V were chosen. The voltage of the first scintillator was kept fixed at the mentioned value while the second one was tested with different applied voltages. For each voltage value, the number of coincidences between the two scintillators in 120 s was recorded. Then the coincidence rate with respect to the applied voltage was plotted. A sigmoid function was used to fit the data and to obtain the maximum coincidence value. From this value the working point was computed as the voltage value that gives the 95% of the maximum coincidence value added to 150 V. The results for the two scintillators

[1] CAEN N470.

[2] LeCroy 4608.

[3] LeCroy 465.

[4] CAEN N145.

[5] Tektronix TDS2024B.

are shown in Figure 3.4. The working point values are a little bit different between the two scintillators, but for simplicity a value of 1550 V is chosen as working point. At this voltage, the scintillator currents are the same and correspond to 384 μA.

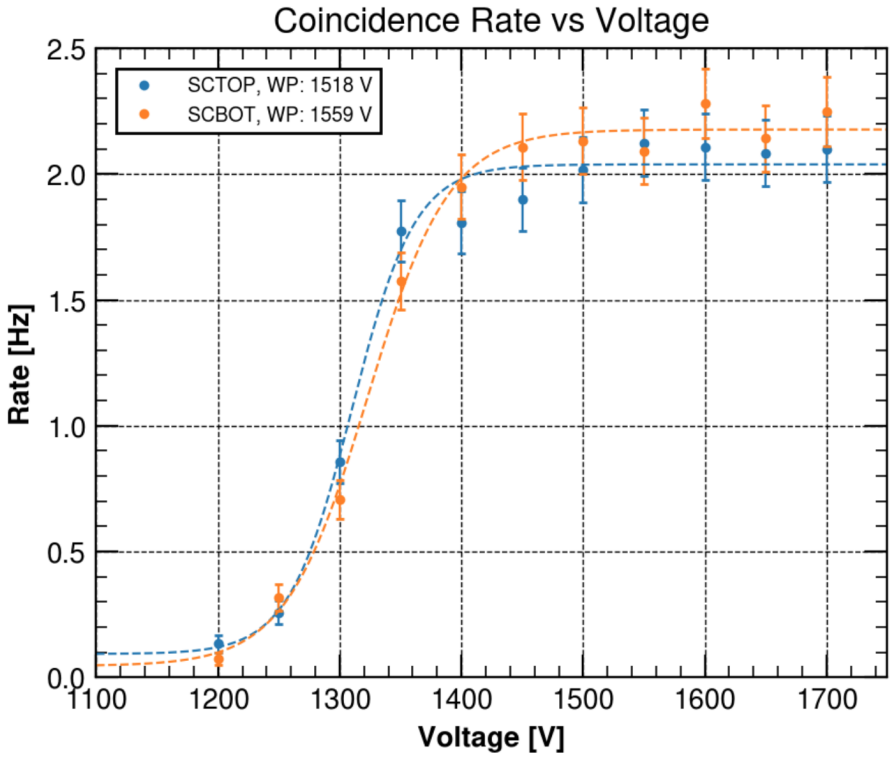

Figure 3.4: Results of scintillators characterization.

RPCs

Two standard 2 mm gap wide, 70 cm x 100 cm HPL RPCs (namely RPC 9 and 11) were used. They were aligned between the scintillators and they were powered by a HV power supply[6]. The signal readout was done on seven, 2.6 cm wide copper strips for each RPC. The sensitive area of these strips corresponded approximately to the sensitive area of the scintillators. All the strips, even those that are not used, were terminated using 50 Ω resistances on one side, and only the signal strips were welded to LEMO cables with MCX connectors on the other side. Each RPCs was located in an aluminum frame that was connected to the ground. In order to be sure that every part of the frame was connected to the ground, some copper tape with a conductive glue was used applied between every different aluminum piece.

In order to characterize the RPC detectors, it is important to know the bulk resistivity that can affect the rate capability of the detector. To measure the bakelite resistivity, the

[6]Mainframe: CAEN SY5527, board: CAEN A1526N.

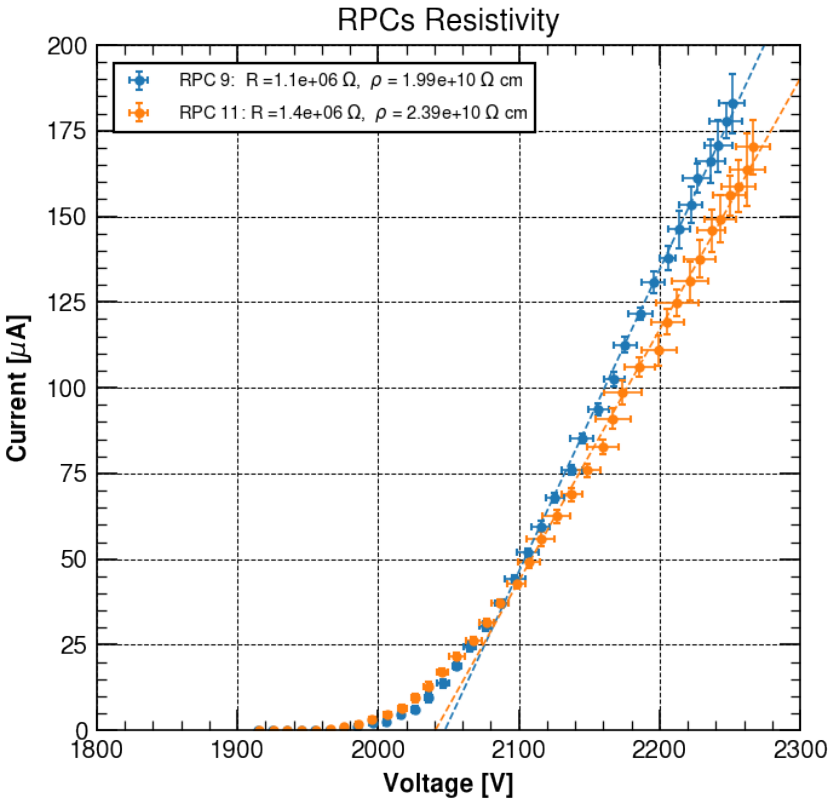

Figure 3.5: Results of resistivity characterization. The dashed line represents the linear fit result.

creation of a breakdown condition in the gas gap is fundamental in order that the resistance will be nearly zero and the total resistance of the chamber is given only by the electrodes. In this condition, obtained by using pure argon gas, it is possible to record several values of the current for different applied voltages in the range between 1000 V and 2500 V. For each applied voltage, the mean current of one minute of data is recorded as current value and the mean standard deviation is considered as uncertainty. Then, the resistance value could be extrapolated by fitting the I-V curve in the region of the breakdown. Figure 3.5 shows the resistance and the resistivity of the two RPCs. This data were taken with a not humidified argon gas. The resistivity of the two chambers are in agreement with the expected resistivity values of the HPL, that should be in the range of $10^{10}\,\Omega\,\mathrm{cm}$ to $10^{11}\,\Omega\,\mathrm{cm}$.

3.1.3 Readout

The LEMO cables soldered on the RPC strips were connected directly in a CAEN VME digitizer that allowed to record a voltage signal in ADC units, sampled over time. The

different types of used digitizer are shown in Table 3.1.

Table 3.1: Digitizers used in this work.

Model	**Resolution [bit]**	**V_{pp} [V]**	**Sampling Frequency [MSample/s]**	**ADC to mV [mV]**
v1720	12	2	250	0.488
v1730	14	2	500	0.122
v1730SB	14	2	500	0.122
v1742	12	1	1000	0.244
DT5730SB	14	2	500	0.122

The digitizers were then connected via USB bridge to a PC. One digitizer channel was dedicated to the acquisition of the trigger signal, produced by the coincidence between the two scintillators[7]. The smallest charge that a digitizer can measure on a strip with an impedance R is given by:

$$\Delta Q = \frac{\Delta V}{R}\Delta T$$

where ΔT is the inverse of the sampling frequency and ΔV is the ADC to mV conversion. The induced signal measured on the strips is a drop of voltage on the chambers gap: the peak of an event has a negative voltage with respect to the baseline. Sometimes the presence of reflections or overshoots due to non perfect impedance matching and strip crosstalk can be seen during the recording of a signal. For this reason it is important to analyze the shape of the signal in order to discriminate the signal from any electronic noise.

3.2 Data taking and analysis

The data was fully analyzed with the Python library `olefin` [37]. In order to understand the functioning of the library analysis, it is important to show the methodology of a typical data acquisition. The first step it to have the right gas mixture inside the detector. Every time a new gas mixture is used, a certain amount of time is needed before switching on the chambers, to allow a complete replacement of the previous gas mixture. This amount of time depend on the gas flow. In particular, 6 chamber volumes of gas are flushed before switching on the detectors. When the chambers are ready, the high voltage steps to use and the number of trigger events to record are decided. The first parameter is determined by the type of gas mixture, since different gas mixtures can give different chambers working points. The second parameter is determined by the level of statistics that is needed. For example, if a new gas mixture is under test, it is possible to start with the voltage values of a known gas mixture, for example the standard one, and a very low statistic, like 100 trigger events. This allows to do a fine tuning of the correct voltage steps that it is needed for the analysis. Then, it is possible to do an acquisition with the voltage steps selected and with high statistics, like 8000-10000 trigger events.

[7]Coincidence was obtained in the same way as described in Section 3.1.2.

The data were taken with the digitizer, that allows to record in a `wave<n>.txt` the raw waveform data, where `<n>` is the number of the digitizer channel, corresponding to a chamber strip. The acquisition usually recorded 520 samples over time for each event. These files were then collected in some folders, each one representing an applied voltage value. During the acquisition, a `olefin_config.yml` file was created. This file contained all the information about the specific data acquisition, and it was structured in the following way:

- `acquisition`: it contained the dictionary that allowed to match the `wave<n>.txt` files to the corresponding RPC and strips;
- `digitizer`: it contained information about the digitizer used (model, resolution...);
- `run`: it contained the dictionary with the fit initial parameters of the sigmoid function used to model the efficiency, the composition of the gas mixture and the temperature and pressure values;
- `signal`: it contained information about the different thresholds that were used in the Signal Analysis, which will be discussed in Section 3.2.1.

Temperature and pressure values were measured in the laboratory room with a sensor connected to the PC[8]. It is important to stress out that the applied voltage to the chamber doesn't correspond to the effective voltage within the gap. Indeed, the data was acquired in different periods, for which the atmospheric conditions, even in the laboratory environment, could change. The temperature and pressure affect the RPC operation in a relevant way [38]. In the first instance, the temperature affects the resistivity of the HPL. HPL resistivity usually decreases with the temperature increase. Moreover, temperature and pressure have a direct relationship with the gas density. Generally speaking, drift velocity and multiplication parameters depend on the ratio $\frac{E}{\rho_{gas}}$ and therefore any change in the temperature T or in the pressure p is affecting these parameters as well. It is useful to introduce the concept of effective applied voltage when comparing data from the same RPC, defined as:

$$HV_{eff} = HV_{app} \frac{p_0}{p} \frac{T}{T_0}$$

where p_0 and T_0 are the reference values, HV_{app} is the voltage set by the HV module. The reference values are taken to be $p_0 = 965$ mbar and $T_0 = 20\,^{\circ}\mathrm{C}$.

The structure of `olefin` library follows the structure of the data analysis: Signal Analysis, Event Analysis, Acquisition Analysis and Run Analysis. The general scheme is reported in Figure 3.6 and in the following section the different parts of the library are described.

3.2.1 Signal Analysis

The analysis starts with the Signal Analysis, that is the lowest level analysis at signal level. It analyses data from a single signal and it extracts the physical variables, called features. The most important features at this level are described in the following list:

[8] Yoctopuce Yocto-Meteo-V2.

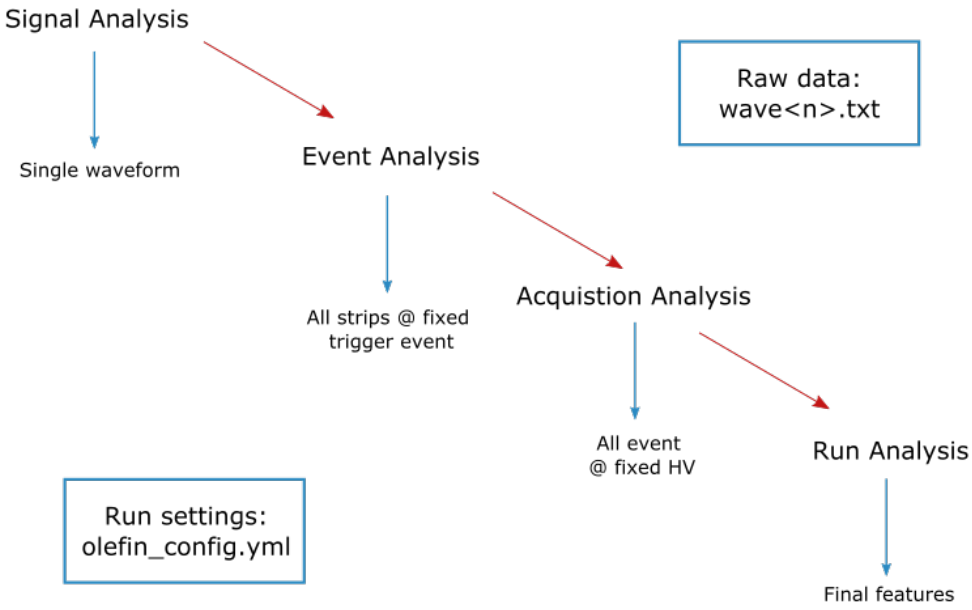

Figure 3.6: `olefin` library scheme.

- `baseline`: usually it is calculated over the first 150 samples and it allows to work on the pedestal subtracted signals;
- `time_peak`: it is the time, expressed in samples, where the earlier peak is found and it is calculated as a subtraction between the actual signal time and the trigger time. The trigger time is computed as the crossing falling edge of the trigger signal. If two trigger signals are present, only the time of the falling edge of the first one is considered.
- `height`: it is the height of the peak expressed in mV;
- `inverse_height`: it is the absolute value of the height undershoot of the signal expressed in mV;
- `charge`: It is the cumulative sum of the ADC samples that crosses a charge threshold, usually set at 9 samples, divided by a factor that takes into account the ADC range of the digitizer, its time resolution and the resistance termination of the strips.

In addition to these features, other useful variables are computed. These variables are used in order to characterize the signal and to allow an easy selection of the signal data. These are reported in the following list:

- `height_ratio`: it is the ratio between the absolute value of the height and the absolute value of the inverse height;
- `reflections_count` It is the number of ADC samples crossing the noise threshold, usually set at 9 samples. This variable is useful to distinguish a real signal from the cross talking noise or the dark noise that might be present;

- `fired`: it is a boolean value and it indicates if the height crosses the height threshold, usually set at 2 mV;
- `isin_time_window`: it is a boolean value and it indicates if the time peak is inside the temporal window set in the `olefin_config.yml` file. This time window mainly depends on the readout set up and it needs to be checked and corrected every time there is a change in the set up;
- `might_be_noise`: it it a boolean value and it indicates if the reflection count crosses the threshold of noise count, usually set at 2 counts;
- `is_signal`: it is a boolean value and it indicates if the variables `fired` and `isin_time_window` are `true`;
- `is_fat_signal`: it is a boolean value and it indicates if `is_signal` is true and if `height_ratio` is less than the height ratio threshold, usually set at 1;
- `is_detected`: this is a boolean value and it indicates if `is_signal` is `true` and `is_fat_signal` is `false`;
- `signal_type`: it is an integer that indicate the type of the signal:
  - -2: it indicates something not categorized. A signal is classified in this way if the variable `is_detected` is `false`;
  - 3: it indicates a streamer signal. A signal is classified in this way if the variable `is_detected` is `true`, if the value of the feature `charge` exceeds the charge avalanche threshold, usually set at 16 pC, and if the value of the feature `height` exceeds the height avalanche threshold, usually set at 12 mV;
  - 1: it indicates an avalanche signal. A signal is classified in this way if it is not classifiable in the previous types.

3.2.2 Event Analysis

An event is defined as the simultaneously captured signal from different strips on the same RPC and corresponding to a trigger coincidence. This means that one event will contain features from different channels of the digitizer. These features are described in the following list:

- `event_charge`: this is the sum of the collected charge by all the strips;
- `cluster_size`: it is the biggest cluster of fired events, so the number of consecutive strips fired;
- `is_detected`: this variable is `true` if there is at least one `is_detected` signal;
- `time_peak`: it is the minimum time over which a peak is found, *e.g.* if the signal is composed by an avalanche followed by a streamer, the time of the avalanche is considered;
- `event_type`: this is the type of the biggest signal.

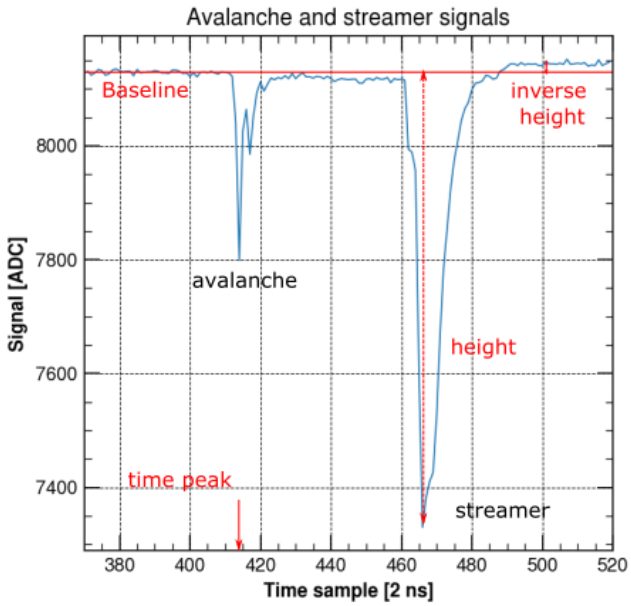

Figure 3.7: Example of an avalanche signal followed by a streamer signal.

3.2.3 Acquisition Analysis

The Acquisition Analysis considers all the events at one fixed applied high voltage. The features computed in this step are reported in the next list:

- `efficiency`: it is the number of the detected events over the total recorded ones. It is calculated by computing the ratio of the events where at least one strip has an event that `is_detected` over the total number of trigger events recorded:

$$\epsilon = \frac{\text{triple coincidence}}{\text{double coincidence}}$$

  where ϵ is the efficiency and double coincidence is the single trigger signal;

- `efficiency_error`: it is the error on the computed efficiency. It is given by the error of a binomial distribution:

$$\epsilon_{err} = \sqrt{\frac{\epsilon(1-\epsilon)}{N_{counts}}}$$

  where N_{counts} is the number of events recorded;

- `streamer_probability`: it is the number of streamer events over the total trigger;

- `streamer_probability_error`: this is the error on the computed streamer probability, calculated as the error of a binomial distribution.

3.2.4 Run Analysis

A run is a collection of acquisitions, so with different high voltages applied, done on one or more RPCs. It contains the final and more general features. To obtain those features, it is necessary to consider the efficiency values obtained in the Acquisition Analysis as a function of the voltage applied to the chambers. This efficiency curve can be fitted by a sigmoid function. A sigmoid function is a mathematical function with an "S" shape, continuous and with all its derivatives continuous, used in many different contexts. For fitting the RPC efficiency curve, it was used in the following form:

$$\epsilon(HV_{eff}) = \frac{\epsilon_{max}}{1 + e^{\gamma(HV_{eff} - HV_{50})}}$$

where ϵ is the efficiency measured at a certain value of the effective operating voltage HV_{eff}, ϵ_{max} is the asymptotic efficiency for $HV_{eff} \to +\infty$, γ is a coefficient proportional to the inflection point of the sigmoid and HV_{50} is the point for which 50% of ϵ_{max} is reached. The use of the sigmoid provides a uniform way to compare performance of different chambers and different gas mixtures.

Then, the features computed in this step are the following:

- `knee`: it is the voltage where the efficiency reach 95% of its maximal value;
- `working_point`: it is usually defined as the knee plus 150 V (WP);
- `streamer_probability_wp`: this represents the streamer probability computed at the working point. This value is extrapolated from a sigmoid function model;
- `streamer_probability_error_wp`: it is the streamer probability error at working point. The error value is extrapolated by a linear interpolation.

3.3 Characterization of RPCs with different gas mixtures

The analysis and the results of several gas mixtures tested in the laboratory are reported in the following sections. First, a complete characterization with the standard gas mixture was done. Then, part of R134a concentration was substituted with other gases with lower GWP, such as He, CO_2 and HFO1234ze. 3M^{TM} NOVEC^{TM} 4710 was tested as a substitute for the SF_6, since it has a lower GWP, as reported in Table 3.2.

The use of He as a component of the RPC gas mixture was already studied [39]. From this study, it is possible to see that He has a higher ionization potential with respect to R134a and the effect is to reduce the effective pressure inside the gap. This also leads to a reduction of the working point. Historically the CO_2 was used in gaseous detectors, in particular in wire chambers, as a quencher. So, the use of CO_2 could bring to a reduction of available electrons for the ionization and as a consequence to bring a limitation of streamers production. However, this behavior is different between the wire chambers and the RPCs since the CO_2 hasn't the same quenching properties as iC_4H_{10}. He and CO_2 are available on the market in addition to being stable gases and already used in gaseous detectors. However, at the moment, He can't be used in the experimental cavern of LHC

experiments, since it could damage the photomultipliers (*e.g.* see [41]). The HFO1234ze was already tested in the last years as a component for the RPC gas mixtures [42, 43]. The results show that when HFO1234ze is used as a complete replacement of R134a, the detector is not efficient below 15 kV. It needs to be used with another gas that effectively reduces the gas density, resulting in a lower voltage required to operate the detector. In recent years, the CERN gas team group has been testing the NOVEC 4710 as a component of the RPC gas mixture [45, 46]. It presents a high electronegativity that allows to use it as a SF_6 substitute.

The GWP_{100} of the gases used in this work are shown in Table 3.2.

Table 3.2: GWP_{100} of gases considered in this work.

Gas	**GWP_{100}**
R134a	1430
HFO1234ze	6
SF_6	22800
CO_2	1
He	0
iC_4H_{10}	3.3
NOVEC 4710	7000
HFO1224YD	0

3.3.1 RPC performance with the standard gas mixture

First the RPCs were characterized with the standard CMS gas mixture (named STD in the following). This is a three components gas mixture made of 95.2% R134a, 4.5% iC_4H_{10} and 0.3% SF_6. It is the gas mixture mainly used in the RPC detectors in the CMS experiment (in ATLAS the iC_4H_{10} is set to 5%). The STD will be used as reference for comparison with all the gas mixtures tested. This allows also to compare results of different RPCs tested with the same gas mixture, since different detectors usually present slightly different behaviors. This can be seen in Figure 3.8, where the results of the efficiency scan for the two different RPCs are reported. From this analysis it is possible to obtain the main chamber and gas mixture features, that are reported in Table 3.3.

Charge distributions are shown in Figure 3.9a and Figure 3.9b. In this figure only detected events are considered and the graph shows the prompt charge distribution for each applied high voltage. It is possible to observe the distribution of the avalanche population at lower charges and the streamers one at charges greater than 16 pC. The red line represents the charge threshold used in the analysis (16 pC), that allows to distinguish an avalanche from a streamer. The streamers presence is higher with higher applied voltages. If the mean prompt charge as a function of the effective voltage is considered, it is possible to see that the charge increases together with the voltage applied (Figure 3.9c and Figure 3.9d). However, variations in this trend for streamer signals may be due to a low statistic, since the streamers are very few, or due to random sparks that could increase locally the charge.

Time spectrums are shown in Figure 3.10a and Figure 3.10b. Also in this case, only detected events are considered and the graph shows one time arrival distribution for each

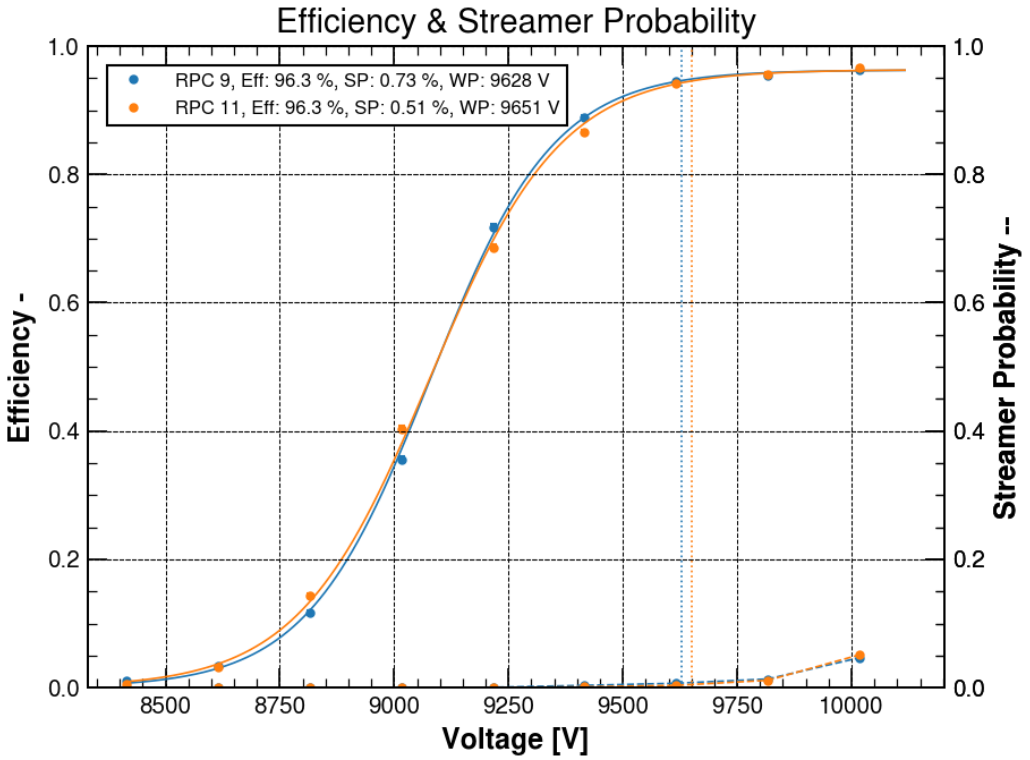

Figure 3.8: STD gas mixture: efficiency (continuous line) and streamer probability (dashed line) for RPC 9 and 11. Vertical lines represent the working point values. The voltage values are already corrected for pressure and temperature and errors are inside the marks.

applied voltage. The time resolution is defined as the standard deviation of the gaussian fitted to the main peak of the histogram. The time resolution is intrinsically affected by the maximum sampling rate of the electronic device, that depends on the digitizer used[9]. It is possible to see that as the voltage increases, the arrival time decreases. This effect is due to the fact that the drift velocity increases when the electric field increases [40]. It is also possible to see a decrease of the time resolution as the applied voltage increases (Figure 3.10c and Figure 3.10d).

Cluster size distributions are shown in Figure 3.11a and Figure 3.11b. The cluster size is defined as the number of adjacent strips fired for a single trigger event. High cluster size increases occupancy and may deteriorate the detector spatial resolution. A low cluster size is essential when triggering and tracking capability is required. As the voltage increases, the number of streamer increases and the space-charge effects become more important. This leads to a signal that is distributed among several strips, with a consequent increase of the cluster size (Figure 3.11c and Figure 3.11d).

It is possible to compute the GWP_{100} of the standard gas mixture starting from the GWP_{100} of the single component shown in Table 3.2. This gas mixture presents a GWP_{100}

[9]In this case, digitizer v1730SB was used.

value about 3384, calculated over 100 years. The main contribution is given by the R134a, that represents the main concentration of the gas mixture.

Table 3.3: Main STD gas mixture features

	RPC 9	**RPC 11**
Working point [V]	9628 $\pm$ 4	9651 $\pm$ 4
Maximum efficiency [%]	96.3 $\pm$ 0.1	96.3 $\pm$ 0.1
Streamer probability at WP [%]	0.73 $\pm$ 0.08	0.51 $\pm$ 0.07
Mean avalanche charge at WP [pC]	2.21 $\pm$ 0.02	2.24 $\pm$ 0.02
Mean streamer charge at WP [pC]	112 $\pm$ 1	141 $\pm$ 3
Mean time resolution at WP [ns]	2.223 $\pm$ 0.002	2.139 $\pm$ 0.002
Mean cluster size at WP [N. strips]	1.47 $\pm$ 0.01	1.53 $\pm$ 0.01
Currents at WP [μA]	0.03 $\pm$ 0.01	0.00 $\pm$ 0.01

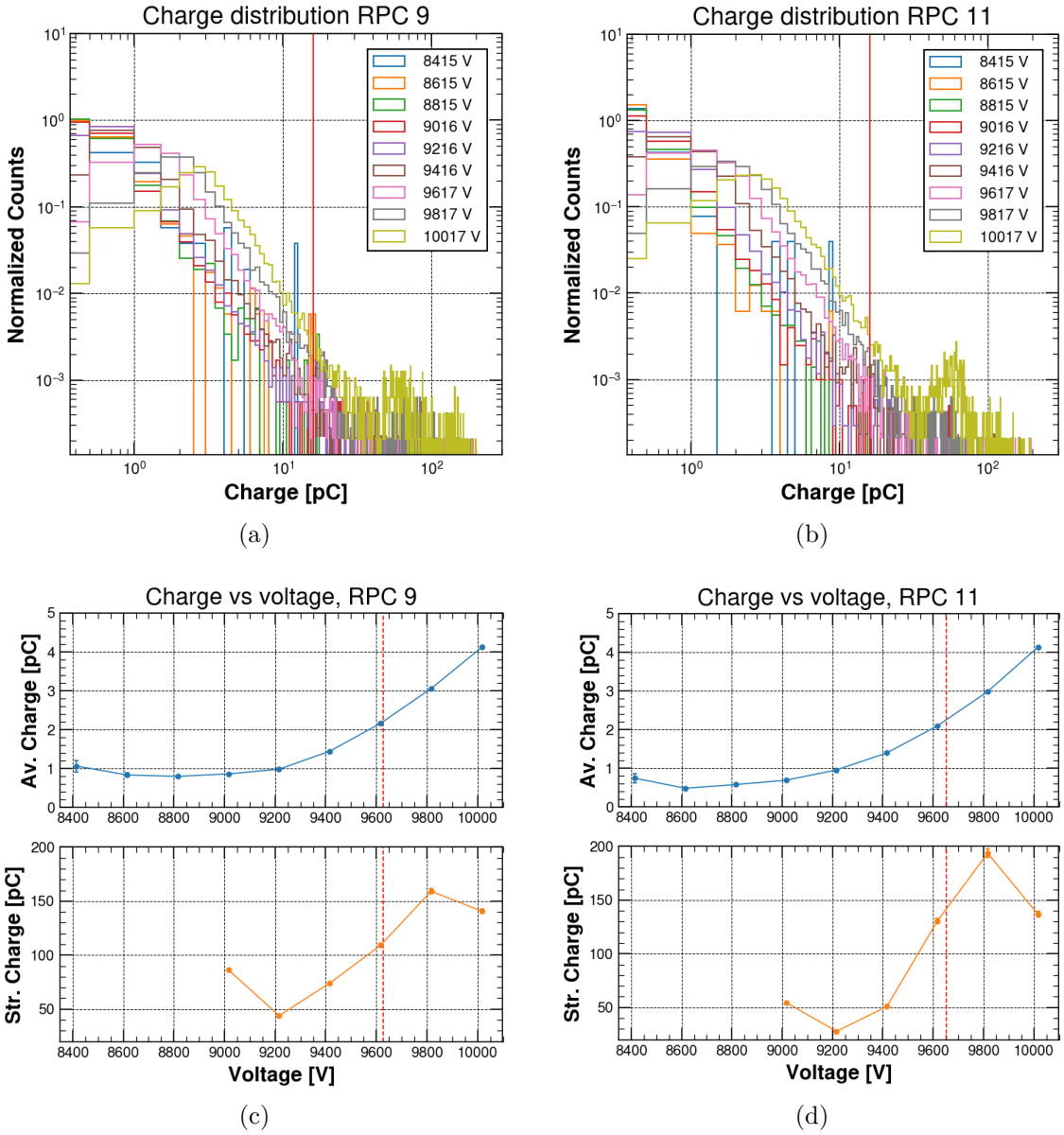

Figure 3.9: STD gas mixture: Charge distributions for different applied voltages for RPC 9 (a) and RPC 11 (b); Mean avalanche charge and streamer charge values for different applied voltage for RPC 9 (c) and RPC 11 (d). In (a) and (b) the vertical lines represent the charge threshold (16 pC) that allows to distinguish an avalanche signal from a streamer signal. In (c) and (d) the red lines represent the RPC working point.

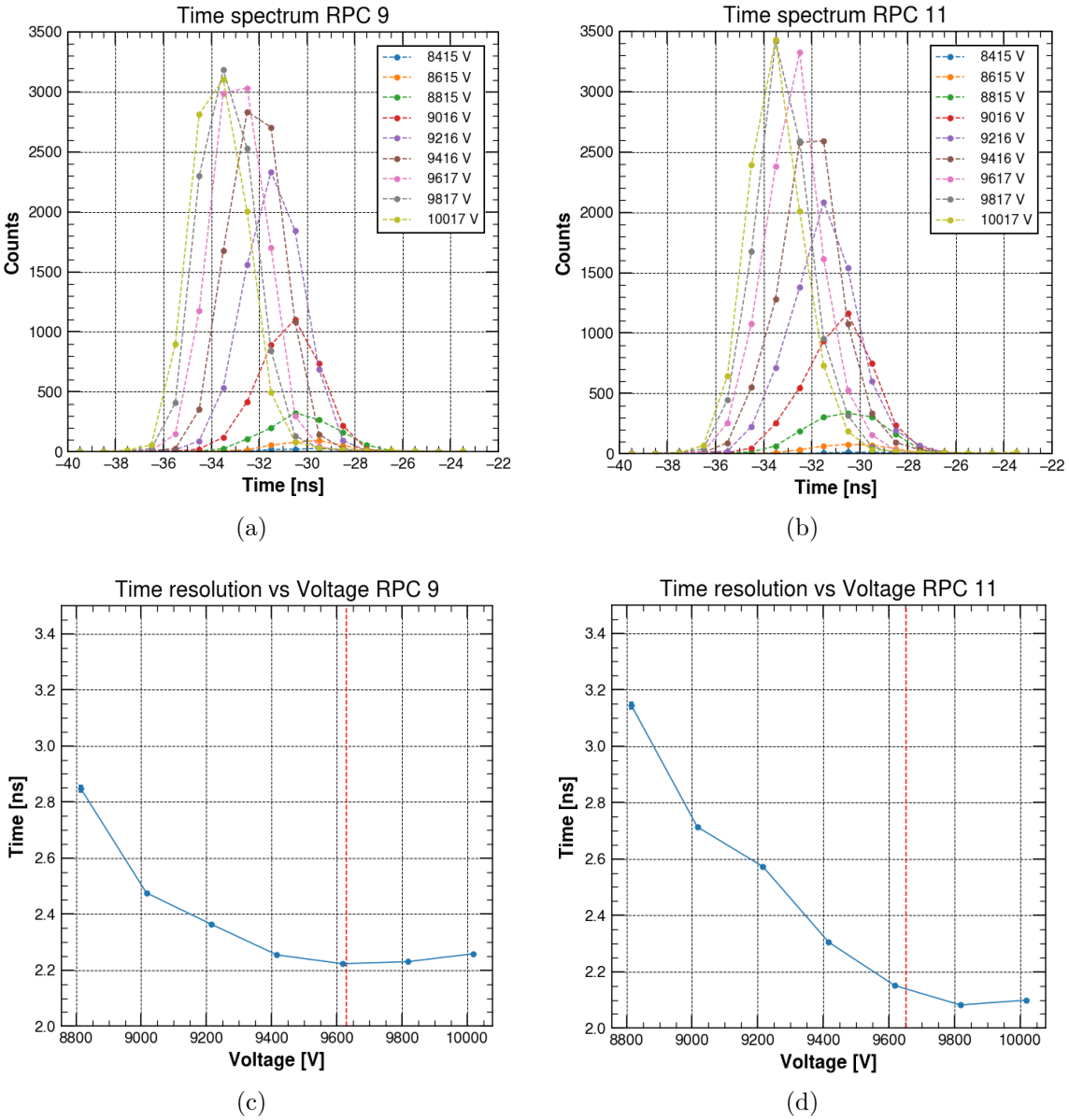

Figure 3.10: STD gas mixture: (a) Time spectrums for different applied voltages for RPC 9 (a) and RPC 11(b); Mean time resolution values for different applied voltages for RPC 9 (c) and RPC 11 (d). In (c) and (d) the red lines represent the RPC working point.

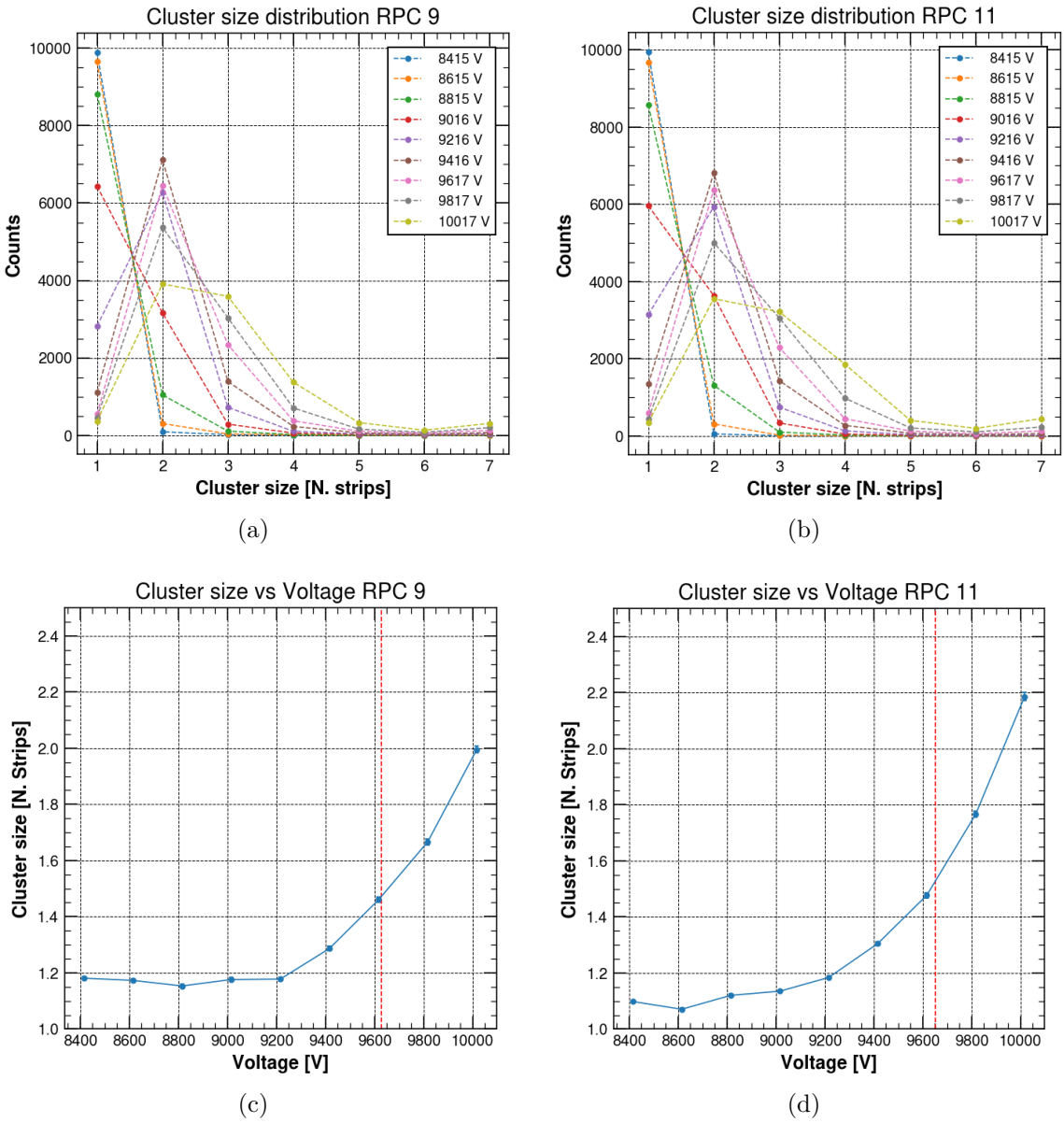

Figure 3.11: STD gas mixture: Cluster size distribution for different applied voltages for RPC 9 (a) and RPC 11 (b); Mean cluster size values for different applied voltages for RPC 9 (c) and RPC 11 (d). In (c) and (d) the red lines represent the RPC working point.

3.3.2 Addition of He to the standard gas mixture

The first attempt to reduce the GWP of the STD gas mixture consisted in replacing 30% of R134a with 30% He. With this substitution, different concentrations of SF_6 were tested, in order to find the lower concentration that allows to have a similar behavior with respect to the STD gas mixture. The gas mixtures tested are listed in Table 3.4, with the relative GWP_{100}.

Table 3.4: GWP_{100} for He 30% gas mixtures.

	R134a [%]	**He** [%]	**SF_6** [%]	**iC_4H_{10}** [%]	**GWP_{100}**
STD	95.2	0	0.3	4.5	3384
SF_6 0.3%	65.2	30	0.3	4.5	2389
SF_6 0.45%	65.05	30	0.45	4.5	2498
SF_6 0.6%	64.9	30	0.6	4.5	2606
SF_6 0.8%	64.7	30	0.8	4.5	2751
SF_6 1%	64.5	30	1	4.5	2895

The efficiency curves for both the chambers are shown in Figure 3.12. Current, charge, cluster size and time resolution are shown in Figure 3.13 and Figure 3.14 as a function of the effective voltage subtracted from the detectors working point. Figure 3.15 shows the streamer probability, working point and maximum efficiency for both RPCs as a function of the SF_6 concentration. Figure 3.16 shows the charge distribution at the working point for both RPCs. The main features are reported in Table 3.5 and Table 3.7. Instead, Table 3.6 and Table 3.8 show the comparison with respect to the features of the STD gas mixture.

The comparison between Table 3.6 and Table 3.8 is used to validate the quality of the acquired data. It was already shown that the two chambers present a slightly different behavior for the same gas mixture. However, it is possible to compare the chambers for the features difference of the gas mixture under test with respect to the STD gas mixture, since it should remove, at least partially, the dependence on the chambers characteristics. In fact, the difference of the maximum efficiency with respect to the STD gas mixture is compatible between the two chambers. Instead, the difference of the working point with respect to the STD gas mixture is not perfectly compatible but with a low discrepancy ($\sim$ 20 V). This discrepancy is not that relevant since it can be produced by a slight underestimation of the error. The other features shown in the table depend on the resistivity of the chambers, and this makes comparison difficult. For example, RPC 9 has a lower resistivity respect to RPC 11, and this is reflected in the fact that RPC 9 has bigger mean charges with respect to RPC 11.

It is possible to consider the comparison between the He 30% gas mixtures and the STD gas mixture. The working point values of all He 30% gas mixtures are significantly lower with respect to the STD gas mixture. For both the chambers, there is a difference in the working point between 1850 V and 1450 V. The He 30% gas mixtures also allow the chambers to reach the maximum efficiency, since they present the same values of the STD gas mixture. The streamer probability is higher for the SF_6 0.3% gas mixture and it reaches a plateau after a SF_6 concentration of 0.45%, as we can see from Table 3.6 and

Table 3.8. The plateau value is compatible with the standard gas mixture only for RPC 9, while for RPC 11 there is a maximum discrepancy of 0.4%. The avalanche charges of He 30% gas mixtures are very similar to the STD gas mixture for RPC 11, while RPC 9 seems to have a higher charge. For RPC 9 there is a difference in the avalanche charge between 0.4 pC and 0.3 pC with respect to the STD gas mixture. RPC 9 is more sensitive to the charge variation since it has a lower resistivity, and that could justify why RPC 11 seems to see no variation. From the streamer charge data it seems that there is a decrease of the streamer charge for both the chamber and for all the He 30% gas mixtures with respect to the STD. For RPC 9 this difference is between 15 pC and 60 pC, while for RPC 11 it is between 80 and 100 pC. This could be a good result since the development of higher charges can produce greater aging effects. However, this improvement could have been produced by a pure statistical issue, since the streamers are few in the STD gas mixture (streamer probability less than 1% at the working point) and this could produce distributions that do not reflect the real behavior of the gas mixture. Cluster size and time resolution seem to be identical as the STD gas mixture for RPC 9. However, RPC 11 seems to have a little increase of the cluster size and a little decrease of the time resolution with respect to the STD gas mixture. These differences are not very large and can still be related to the different resistivity of the two chambers. The currents are the same as the STD gas mixtures for all the He 30% gas mixture and RPCs. They start to increase a little only for voltage values 500 V greater than the working point.

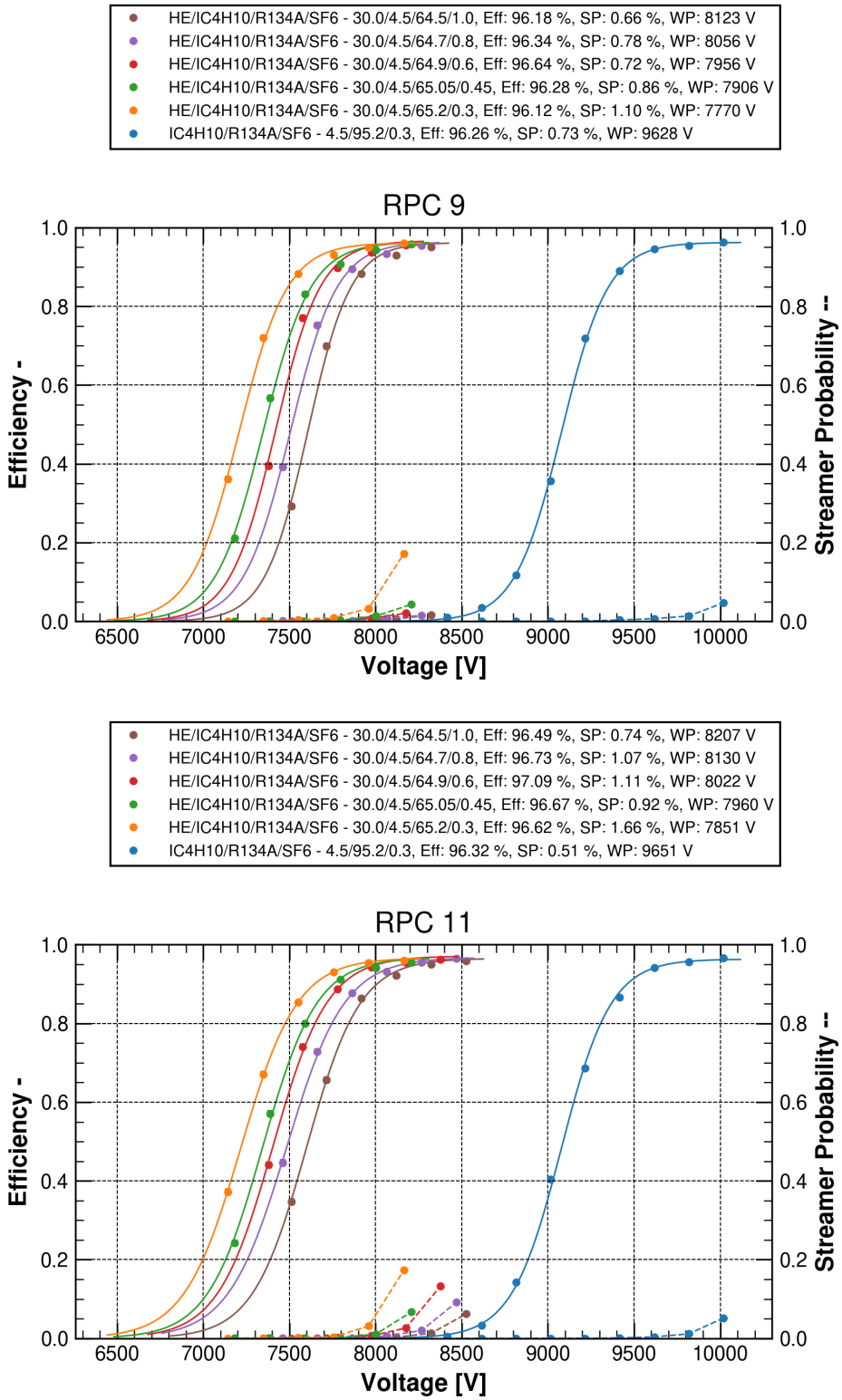

Figure 3.12: Comparison between He 30% gas mixtures and the STD gas mixture: efficiency (continuous line) and streamer probability (dashed line).

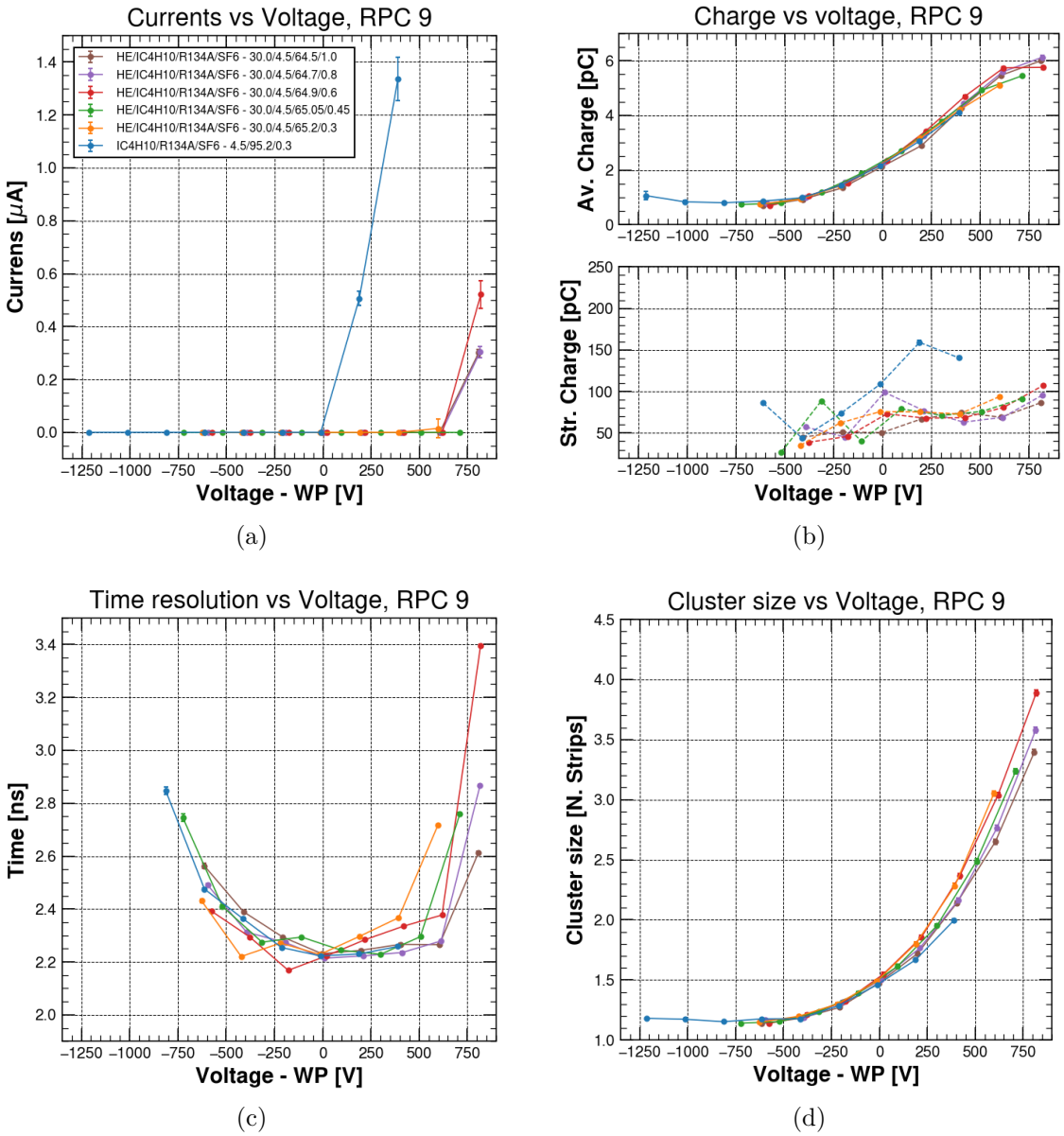

Figure 3.13: Comparison between He 30% gas mixtures and the STD gas mixture for RPC 9: (a) Currents for different applied voltages; (b) Avalanche charge and streamer charge for different applied voltages; (c) Cluster size for different applied voltages; (d) Time resolution for different applied voltages.

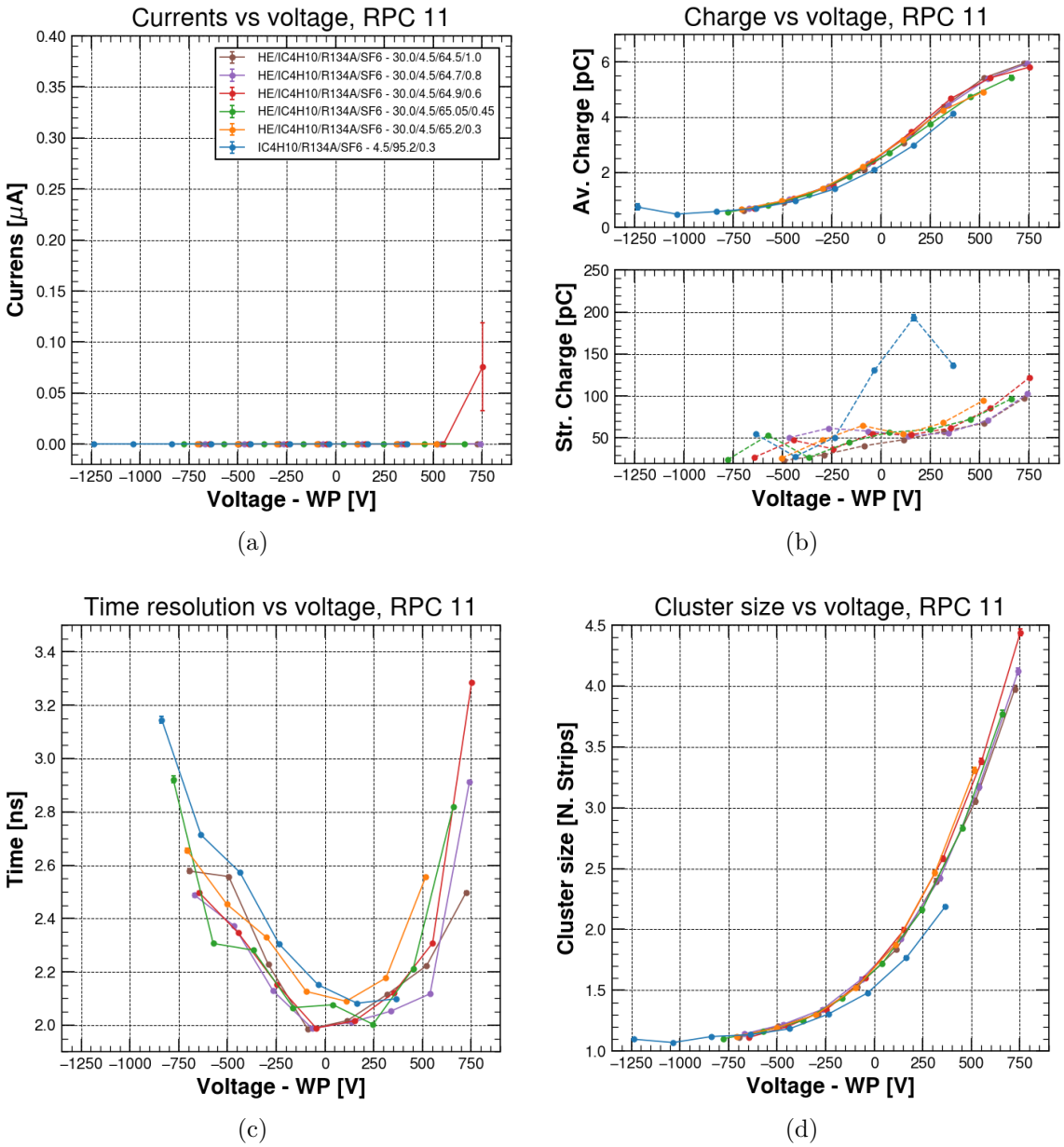

Figure 3.14: Comparison between He 30% gas mixtures and the STD gas mixture for RPC 11: (a) Currents for different applied voltages; (b) Avalanche charge and streamer charge for different applied voltages; (c) Cluster size for different applied voltages; (d) Time resolution for different applied voltages.

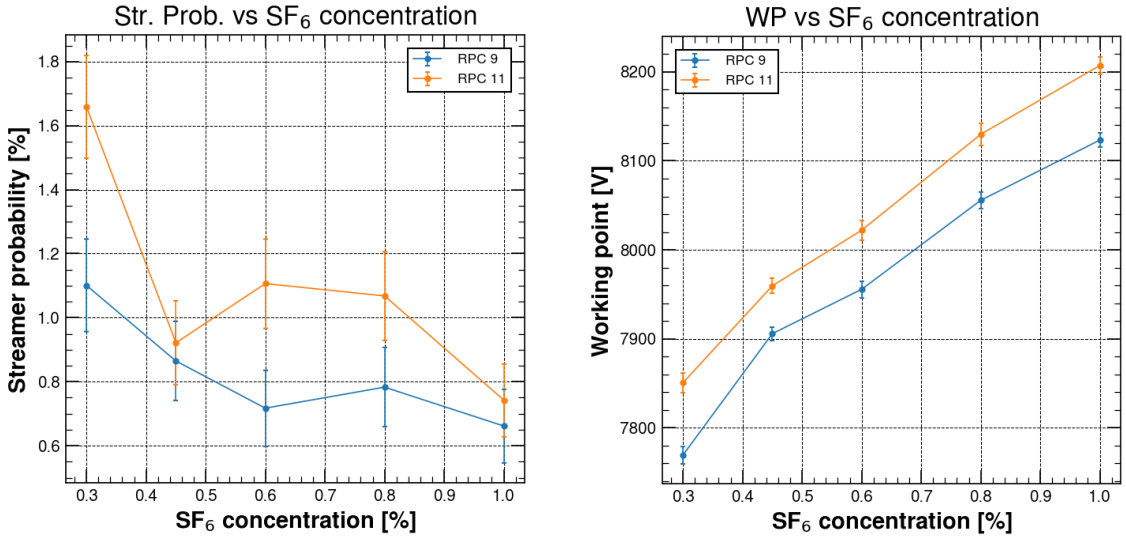

(a)

(b)

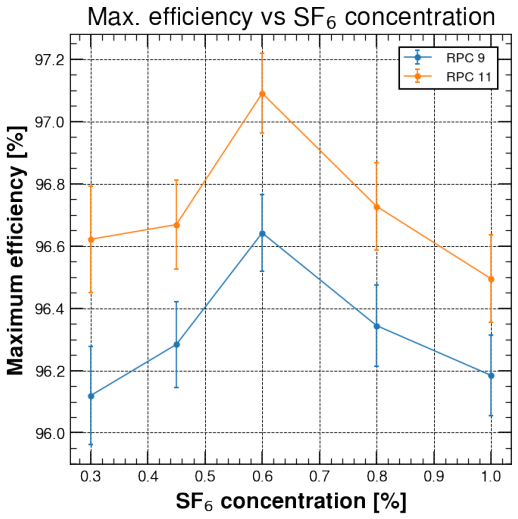

(c)

Figure 3.15: He 30% gas mixtures: (a) Streamer probability as a function of SF_6 concentration; (b) Working point as a function of SF_6 concentration; (c) Maximum efficiency as a function of SF_6 concentration.

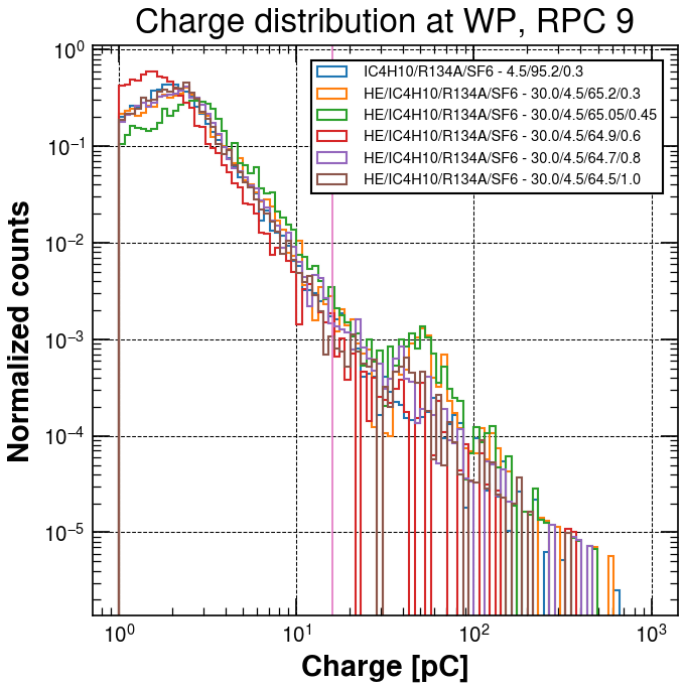

(a)

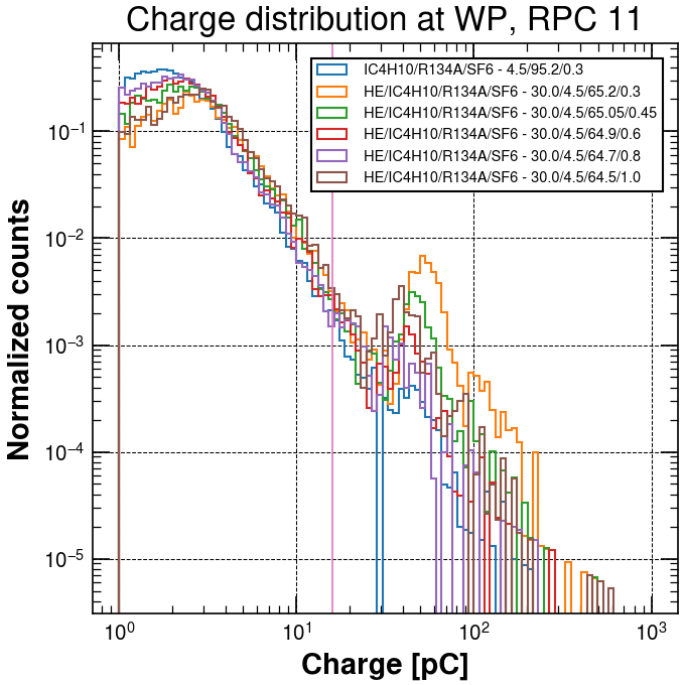

(b)

Figure 3.16: He 30% gas mixtures: (a) Charge distribution at working point for RPC 9; (b) Charge distribution at working point for RPC 11. The vertical line represents the charge threshold (16 pC) that allows to distinguish an avalanche signal from a streamer signal.

Table 3.5: RPC 9 feature values computed for He 30% gas mixtures.

RPC 9	**SF_6 0.3%**	**SF_6 0.45%**	**SF_6 0.6%**	**SF_6 0.8%**	**SF_6 1%**
Working point [V]	7770 ± 10	7906 ± 8	7956 ± 9	8056 ± 10	8123 ± 8
Maximum efficiency [%]	96.1 ± 0.2	96.3 ± 0.1	96.6 ± 0.1	96.3 ± 0.1	496.2 ± 0.1
Streamer probability at WP [%]	1.1 ± 0.1	0.9 ± 0.1	0.7 ± 0.1	0.8 ± 0.1	0.7 ± 0.1
Mean avalanche charge at WP [pC]	2.23 ± 0.03	2.32 ± 0.03	2.25 ± 0.03	2.25 ± 0.03	2.13 ± 0.03
Mean streamer charge at WP [pC]	75.7 ± 0.7	60.9 ± 0.6	70.2 ± 0.7	97 ± 1	50.8 ± 0.3
Mean time resolution at WP [ns]	2.233 ± 0.003	2.268 ± 0.003	2.217 ± 0.003	2.217 ± 0.003	2.231 ± 0.003
Mean cluster size at WP [N. strips]	1.51 ± 0.01	1.51 ± 0.01	1.52 ± 0.01	1.49 ± 0.01	1.48 ± 0.01
Currents at WP [μA]	0.02 ± 0.01	0.00 ± 0.01	0.00 ± 0.01	0.00 ± 0.01	0.00 ± 0.01

Table 3.6: RPC 9 difference between the feature values computed for He 30% gas mixtures and the STD gas mixture.

RPC 9	**ΔSF_6 0.3%**	**ΔSF_6 0.45%**	**ΔSF_6 0.6%**	**ΔSF_6 0.8%**	**ΔSF_6 1%**
Working point [V]	−1858 ± 14	−1722 ± 12	−1672 ± 13	−1572 ± 14	−1505 ± 12
Maximum efficiency [%]	−0.1 ± 0.3	0.0 ± 0.3	0.4 ± 0.3	0.1 ± 0.3	−0.1 ± 0.3
Streamer probability at WP [%]	0.4 ± 0.2	0.1 ± 0.2	0.0 ± 0.2	0.0 ± 0.2	−0.1 ± 0.2
Mean avalanche charge at WP [pC]	0.02 ± 0.04	0.11 ± 0.05	0.03 ± 0.04	0.03 ± 0.05	−0.08 ± 0.05
Mean streamer charge at WP [pC]	−36 ± 2	−51 ± 2	−42 ± 2	−15 ± 3	−61 ± 2
Mean time resolution at WP [ns]	0.010 ± 0.005	0.044 ± 0.005	−0.006 ± 0.005	−0.006 ± 0.005	0.008 ± 0.005
Mean cluster size at WP [N. strips]	0.04 ± 0.02	0.04 ± 0.02	0.05 ± 0.02	0.02 ± 0.02	0.01 ± 0.02
Currents at WP [μA]	−0.03 ± 0.01	−0.03 ± 0.01	−0.03 ± 0.01	−0.03 ± 0.01	−0.03 ± 0.01

Table 3.7: RPC 11 feature values computed for He 30% gas mixtures.

RPC 11	**SF_6 0.3%**	**SF_6 0.45%**	**SF_6 0.6%**	**SF_6 0.8%**	**SF_6 1%**
Working point [V]	7851 ± 11	7960 ± 9	8022 ± 11	8130 ± 12	8207 ± 10
Maximum efficiency [%]	96.6 ± 0.2	96.7 ± 0.1	97.1 ± 0.1	96.7 ± 0.1	96.5 ± 0.1
Streamer probability at WP [%]	1.7 ± 0.2	0.9 ± 0.1	1.1 ± 0.1	1.1 ± 0.1	0.7 ± 0.1
Mean avalanche charge at WP [pC]	2.66 ± 0.03	2.54 ± 0.03	2.64 ± 0.03	2.63 ± 0.03	2.52 ± 0.03
Mean streamer charge at WP [pC]	59.9 ± 0.4	54.3 ± 0.4	54.9 ± 0.4	56.3 ± 0.6	43.8 ± 0.3
Mean time resolution at WP [ns]	2.109 ± 0.003	2.074 ± 0.003	1.995 ± 0.003	1.995 ± 0.003	1.998 ± 0.003
Mean cluster size at WP [N. strips]	1.68 ± 0.02	1.66 ± 0.02	1.69 ± 0.02	1.70 ± 0.02	1.66 ± 0.02
Currents at WP [μA]	0.00 ± 0.01	0.00 ± 0.01	0.00 ± 0.01	0.00 ± 0.01	0.00 ± 0.01

Table 3.8: RPC 11 difference between the feature values computed for He 30% gas mixtures and the STD gas mixture.

RPC 11	**ΔSF_6 0.3%**	**ΔSF_6 0.45%**	**ΔSF_6 0.6%**	**ΔSF_6 0.8%**	**ΔSF_6 1%**
Working point [V]	−1800 ± 15	−1692 ± 13	−1629 ± 15	−1521 ± 16	−1444 ± 14
Maximum efficiency [%]	0.3 ± 0.3	0.3 ± 0.3	0.8 ± 0.3	0.4 ± 0.3	0.2 ± 0.3
Streamer probability at WP [%]	1.2 ± 0.2	0.4 ± 0.2	0.6 ± 0.2	0.6 ± 0.2	0.2 ± 0.2
Mean avalanche charge at WP [pC]	0.41 ± 0.05	0.29 ± 0.05	0.40 ± 0.05	0.38 ± 0.05	0.27 ± 0.05
Mean streamer charge at WP [pC]	−81 ± 3	−87 ± 3	−86 ± 3	−85 ± 3	−97 ± 3
Mean time resolution at WP [ns]	−0.030 ± 0.005	−0.065 ± 0.005	−0.144 ± 0.005	−0.144 ± 0.005	0.141 ± 0.005
Mean cluster size at WP [N. strips]	0.16 ± 0.03	0.13 ± 0.03	0.16 ± 0.03	0.17 ± 0.03	0.13 ± 0.03
Currents at WP [μA]	0.00 ± 0.02	0.00 ± 0.02	0.00 ± 0.02	0.00 ± 0.02	0.00 ± 0.02

3.3.3 Addition of CO_2 to the standard gas mixture

A second alternative to reduce the GWP of the STD gas mixture could be the addition of CO_2. The study is also interesting to understand the difference in adding He or CO_2 to the RPC STD gas mixture. 30% of R134a was substitute with 30% of CO_2 and different concentrations of SF_6 were tested, in order to find the lower concentration that allows to have a similar behavior with respect to the STD gas mixture. The gas mixtures tested are listed in Table 3.9, with the relative GWP_{100}.

Table 3.9: GWP_{100} for CO_2 30% gas mixtures.

	R134A [%]	**CO_2** [%]	**SF_6** [%]	**iC_4H_{10}** [%]	**GWP_{100}**
STD	95.2	0	0.3	4.5	3384
SF_6 0.3%	65.2	30	0.3	4.5	2390
SF_6 0.45%	65.05	30	0.45	4.5	2498
SF_6 0.6%	64.9	30	0.6	4.5	2607
SF_6 0.8%	64.7	30	0.8	4.5	2751
SF_6 1%	64.5	30	1	4.5	2896

The efficiency curves for both the chambers are shown in Figure 3.17. Current, charge, cluster size and time resolution are shown in Figure 3.18 and Figure 3.19 as a function of the effective voltage subtracted by the chambers working point. Figure 3.20 shows the streamer probability, working point and maximum efficiency for both RPCs as a function of the SF_6 concentration. Figure 3.21 shows the charge distribution at the working point for both RPCs. The main features are reported in Table 3.11 and Table 3.13. Instead, Table 3.12 and Table 3.14 show the comparison with respect to the features of the STD gas mixture.

For this set of measurements, a new STD gas mixture calibration of the chambers was performed, since it has been a long time since the previous calibration. For completeness, Table 3.10 shows the features of the new calibration for the two detectors.

Table 3.10: New STD gas mixture characterization.

	RPC 9	**RPC 11**
Working point [V]	9523 $\pm$ 4	9603 $\pm$ 5
Maximum efficiency [%]	96.8 $\pm$ 0.1	97.4 $\pm$ 0.1
Streamer probability at WP [%]	0.4 $\pm$ 0.1	0.7 $\pm$ 0.1
Mean avalanche charge at WP [pC]	1.89 $\pm$ 0.02	2.37 $\pm$ 0.02
Mean streamer charge at WP [pC]	76.1 $\pm$ 1	55.4 $\pm$ 0.1
Mean time resolution at WP [ns]	2.576 $\pm$ 0.002	2.184 $\pm$ 0.002
Mean cluster size at WP [N. strips]	1.38 $\pm$ 0.01	1.56 $\pm$ 0.01
Currents at WP [μA]	0.00 $\pm$ 0.01	0.00 $\pm$ 0.01

The new run with the STD gas mixture presents some differences with respect to the old one. This is probably due to the fact that the first STD gas mixture calibration was done

immediately after the end of the conditioning phase of the detectors. So it is possible that the chambers had not yet reached perfect operating stability and consequently changed slightly over time. Since all the gas mixtures, except for CO_2 30% gas mixtures, were tested right after the conditioning phase, the first STD gas mixture calibration was used for all of them. In fact it is safe to assume that the behavior of the chamber remains constant over a short period of time.

First, it is possible to compare Table 3.12 and Table 3.14. The difference of the working point and maximum efficiency with respect to the STD gas mixture are compatible for all the gas mixture tested except for the working point of the SF_6 0.3% gas mixture that has a little discrepancy ($\sim$ 9 V).

Then it is possible to consider the comparison between the CO_2 30% gas mixture and the STD. The working point values of all CO_2 30% gas mixtures are lower with respect to the STD. For both chambers there is a difference in the working point between 570 V and 100 V. Both the chambers reach the maximum efficiency, although there appears to be a slight decrease, around 0.4%, compared to the STD gas mixture and the He 30% gas mixtures. The streamer probability is significantly higher with respect to the STD gas mixture, especially for lower concentrations of SF_6. In this case, the streamer probability seems to reach a plateau values after a SF_6 concentration of 0.8% since the streamer probability values are compatible between the 0.8% and 1% SF_6 gas mixture for both the chambers. However, it remains higher than the STD gas mixture. The avalanche charges of CO_2 30% gas mixture seems to be slightly higher with respect to the STD gas mixture and for both the chambers. Also the mean streamer charge has higher values with respect to the STD gas mixture. As previously mentioned, this worsening could be due to a pure statistical effect, since the streamers are few in the STD gas mixture (streamer probability less than 1% at the working point) and this could produce distributions that do not reflect the real behavior of the gas mixture. The cluster size seems to be a little higher with respect to the STD gas mixture, but the difference is neglectable. However, an improvement of the time resolution is evident.

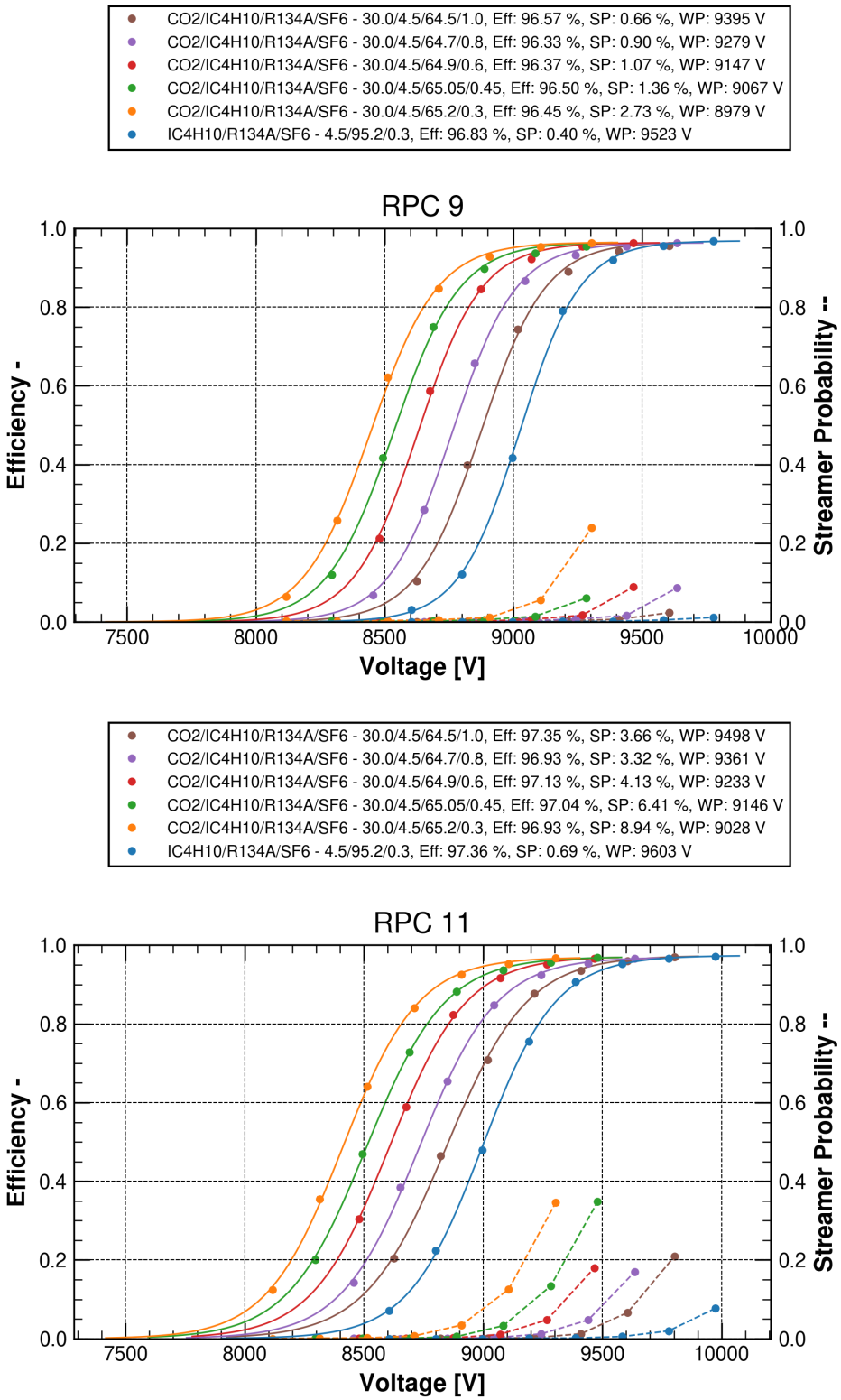

Figure 3.17: Comparison between CO_2 30% gas mixtures and the STD gas mixture: efficiency (continuous line) and streamer probability (dashed line).

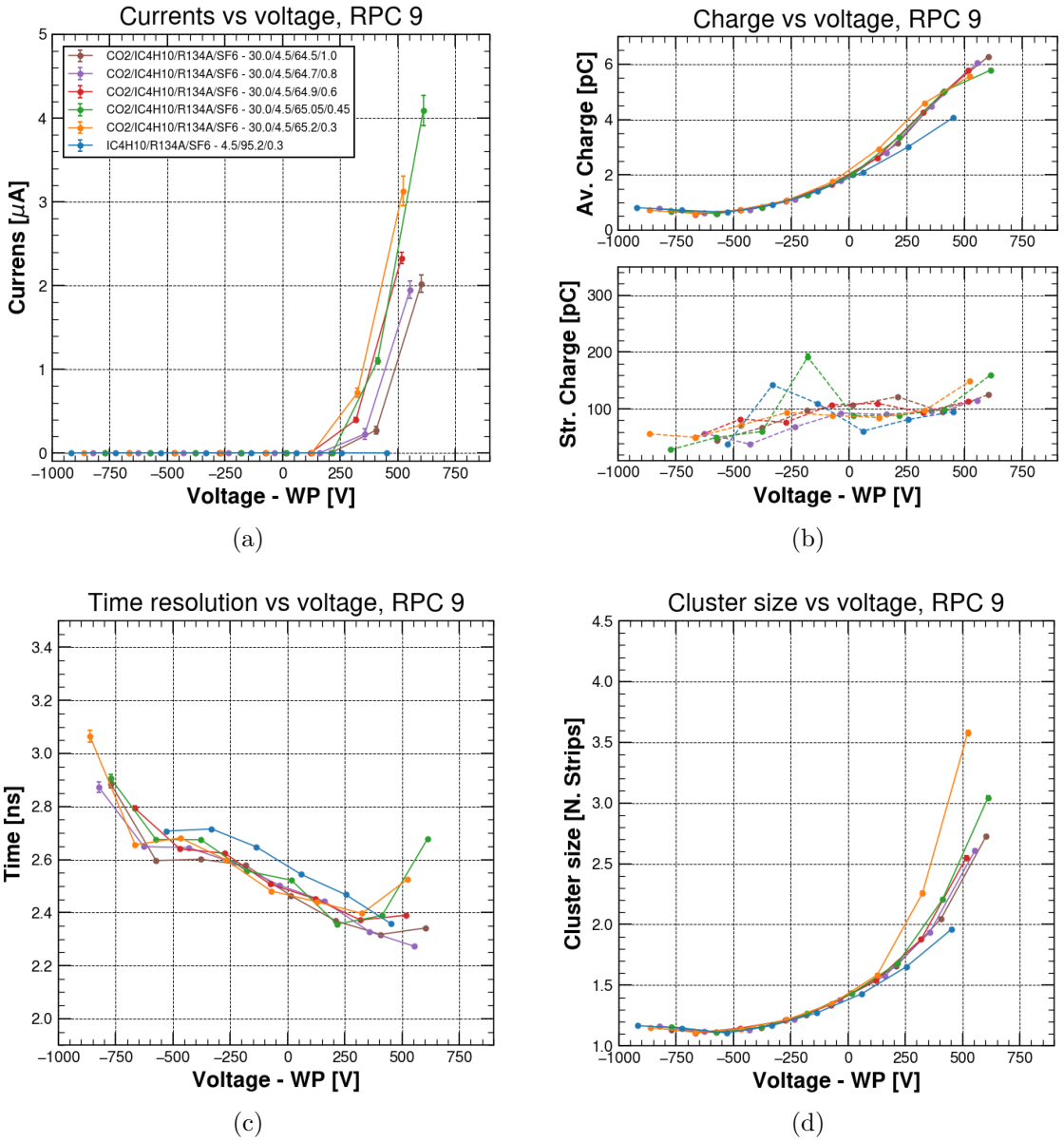

Figure 3.18: Comparison between CO_2 30% gas mixtures and the STD gas mixture for RPC 9: (a) Currents for different applied voltages; (b) Avalanche charge and streamer charge for different applied voltages; (c) Cluster size for different applied voltages; (d) Time resolution for different applied voltages.

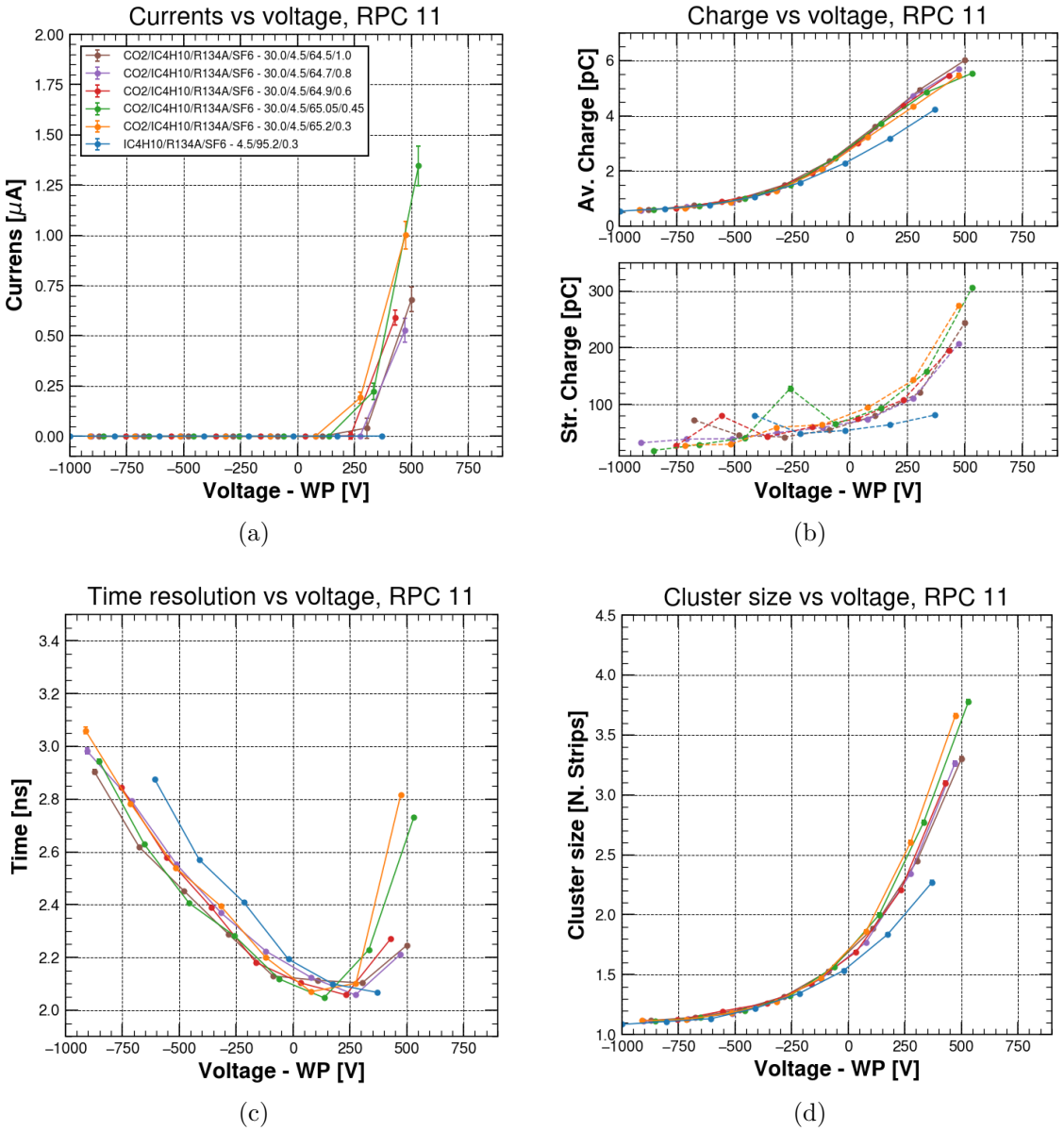

Figure 3.19: Comparison between CO_2 30% gas mixtures and the STD gas mixture for RPC 11: (a) Currents for different applied voltages; (b) Avalanche charge and streamer charge for different applied voltages; (c) Cluster size for different applied voltages; (d) Time resolution for different applied voltages.

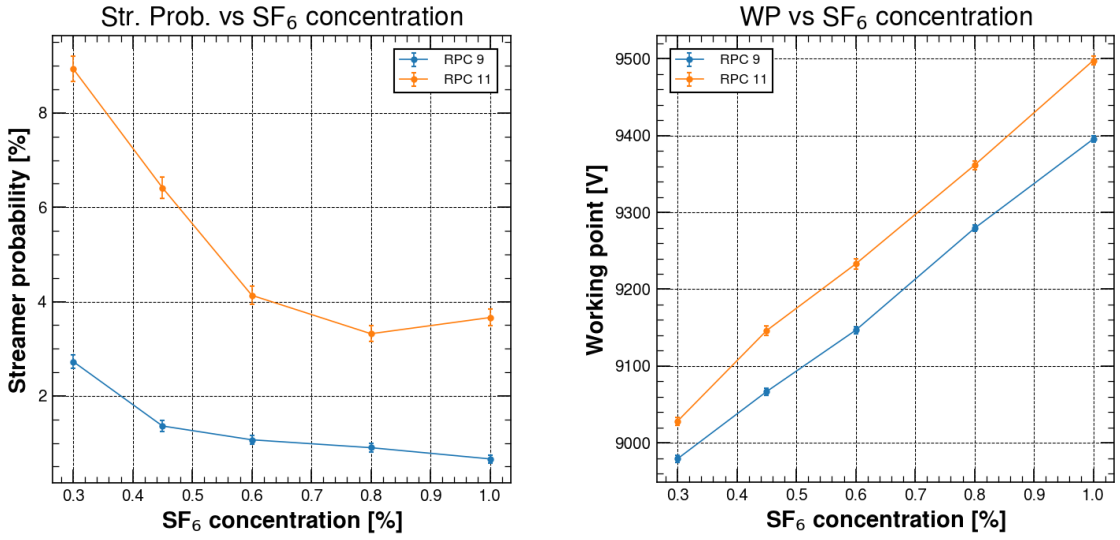

(a)

(b)

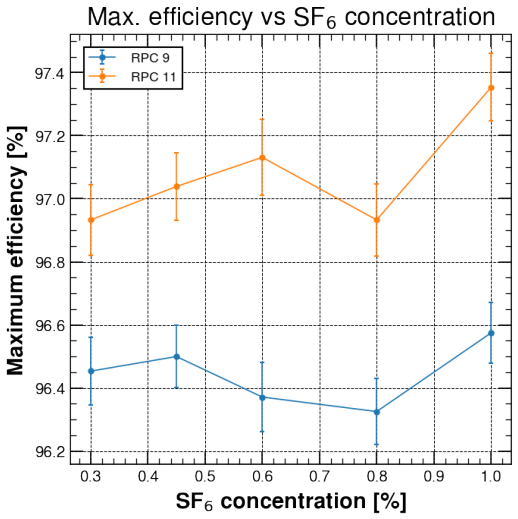

(c)

Figure 3.20: CO_2 30% gas mixtures: (a) Streamer probability as a function of SF_6 concentration; (b) Working point as a function of SF_6 concentration; (c) Maximum efficiency as a function of SF_6 concentration.

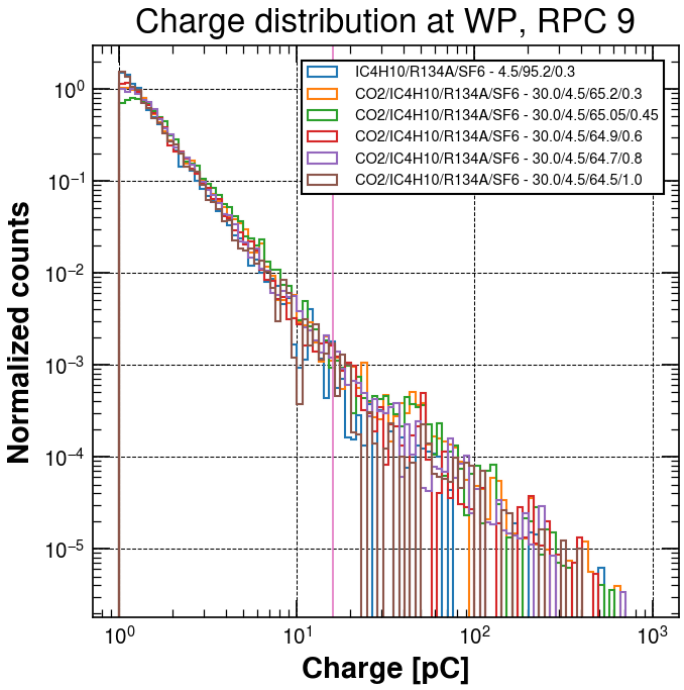

(a)

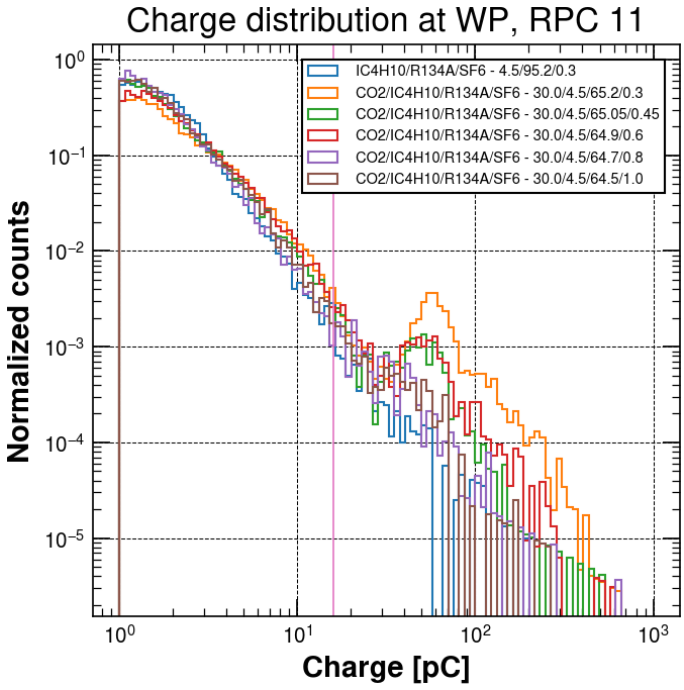

(b)

Figure 3.21: CO_2 30% gas mixtures: (a) Charge distribution at working point for RPC 9; (b) Charge distribution at working point for RPC 11. The vertical line represents the charge threshold (16 pC) that allows to distinguish an avalanche signal from a streamer signal.

Table 3.11: RPC 9 feature values computed for CO_2 30% gas mixtures.

RPC 9	**SF_6 0.3%**	**SF_6 0.45%**	**SF_6 0.6%**	**SF_6 0.8%**	**SF_6 1%**
Working point [V]	8979 ± 4	9067 ± 4	9147 ± 5	9279 ± 4	9395 ± 4
Maximum efficiency [%]	96.5 ± 0.1	96.5 ± 0.1	96.4 ± 0.1	96.3 ± 0.1	96.6 ± 0.1
Streamer probability [%]	2.7 ± 0.2	1.4 ± 0.1	1.1 ± 0.1	0.9 ± 0.1	0.7 ± 0.1
Mean avalanche charge [pC]	2.17 ± 0.02	1.97 ± 0.02	2.02 ± 0.02	1.98 ± 0.02	1.95 ± 0.02
Mean streamer charge [pC]	87.5 ± 0.7	98 ± 1	108.4 ± 0.9	92.7 ± 0.8	106.5 ± 0.8
Mean time resolution [ns]	2.467 ± 0.002	2.525 ± 0.002	2.486 ± 0.002	2.492 ± 0.002	2.472 ± 0.002
Mean cluster size [N. strips]	1.43 ± 0.01	1.42 ± 0.01	1.41 ± 0.01	1.42 ± 0.01	1.42 ± 0.01
Currents [μA]	0.00 ± 0.01	0.00 ± 0.01	0.00 ± 0.01	0.00 ± 0.01	0.00 ± 0.01

Table 3.12: RPC 9 difference between the feature values obtained for CO_2 30% gas mixtures and the STD gas mixture.

RPC 9	**ΔSF_6 0.3%**	**ΔSF_6 0.45%**	**ΔSF_6 0.6%**	**ΔSF_6 0.8%**	**ΔSF_6 1%**
Working point [V]	−544 ± 8	−456 ± 8	−377 ± 9	−244 ± 9	−128 ± 9
Maximum efficiency [%]	−0.4 ± 0.2	−0.3 ± 0.2	−0.5 ± 0.2	−0.5 ± 0.2	−0.3 ± 0.2
Streamer probability [%]	2.3 ± 0.3	1.0 ± 0.2	0.7 ± 0.2	0.5 ± 0.2	0.3 ± 0.1
Mean avalanche charge [pC]	0.28 ± 0.04	0.08 ± 0.03	0.14 ± 0.04	0.10 ± 0.04	0.06 ± 0.03
Mean streamer charge [pC]	11 ± 1	22 ± 1	32 ± 1	17 ± 1	30 ± 1
Mean time resolution [ns]	−0.109 ± 0.004	−0.051 ± 0.004	−0.090 ± 0.004	−0.083 ± 0.004	−0.103 ± 0.004
Mean cluster size [N. strips]	0.05 ± 0.02	0.04 ± 0.02	0.03 ± 0.02	0.04 ± 0.02	0.04 ± 0.02
Currents [μA]	0.0 ± 0.2	0.0 ± 0.2	0.0 ± 0.2	0.0 ± 0.2	0.0 ± 0.2

Table 3.13: RPC 11 feature values obtained for CO_2 30% gas mixture.

RPC 11	**SF_6 0.3%**	**SF_6 0.45%**	**SF_6 0.6%**	**SF_6 0.8%**	**SF_6 1%**
Working point [V]	9028 ± 5	9146 ± 6	9233 ± 7	9361 ± 5	9498 ± 6
Maximum efficiency [%]	96.9 ± 0.1	97.0 ± 0.1	97.1 ± 0.1	96.9 ± 0.1	97.4 ± 0.1
Streamer probability [%]	8.9 ± 0.3	6.4 ± 0.2	4.1 ± 0.2	3.3 ± 0.2	3.7 ± 0.2
Mean avalanche charge [pC]	2.75 ± 0.02	2.86 ± 0.02	2.82 ± 0.02	2.80 ± 0.02	2.91 ± 0.02
Mean streamer charge [pC]	82.6 ± 0.5	74.6 ± 0.6	72.8 ± 0.4	68.2 ± 0.6	66.6 ± 0.5
Mean time resolution [ns]	2.122 ± 0.002	2.096 ± 0.002	2.117 ± 0.002	2.164 ± 0.002	2.122 ± 0.002
Mean cluster size [N. strips]	1.71 ± 0.01	1.70 ± 0.01	1.64 ± 0.01	1.65 ± 0.01	1.69 ± 0.01
Currents [μA]	0.0 ± 0.1	0.0 ± 0.1	0.0 ± 0.1	0.0 ± 0.1	0.0 ± 0.1

Table 3.14: RPC 11 difference between the feature values obtained for CO_2 30% gas mixture and the STD gas mixture.

RPC 11	**ΔSF_6 0.3%**	**ΔSF_6 0.45%**	**ΔSF_6 0.6%**	**ΔSF_6 0.8%**	**ΔSF_6 1%**
Working point [V]	−575 ± 10	−457 ± 11	−370 ± 12	−242 ± 10	−106 ± 11
Maximum efficiency [%]	−0.4 ± 0.2	−0.3 ± 0.2	−0.2 ± 0.2	−0.4 ± 0.2	0.0 ± 0.2
Streamer probability [%]	8.2 ± 0.4	5.7 ± 0.3	3.4 ± 0.3	2.6 ± 0.3	3.0 ± 0.3
Mean avalanche charge [pC]	0.38 ± 0.04	0.49 ± 0.04	0.45 ± 0.04	0.43 ± 0.04	0.54 ± 0.04
Mean streamer charge [pC]	27.2 ± 0.8	19.2 ± 0.9	17.4 ± 0.7	12.7 ± 0.9	11.2 ± 0.8
Mean time resolution [ns]	−0.062 ± 0.003	−0.087 ± 0.003	−0.067 ± 0.03	−0.020 ± 0.003	−0.061 ± 0.003
Mean cluster size [N. strips]	0.14 ± 0.02	0.14 ± 0.02	0.08 ± 0.02	0.08 ± 0.02	0.12 ± 0.02
Currents [μA]	0.0 ± 0.2	0.0 ± 0.2	0.0 ± 0.2	0.0 ± 0.2	0.0 ± 0.2

3.3.4 Comparison between the best CO_2 and He 30% gas mixtures

In this section, the best CO_2 and He 30% gas mixtures are compared. In particular, the 1% SF_6 concentration is selected, due to the better streamer probability with respect to the other SF_6 concentrations. As a reference, the second characterization with the STD gas mixture, reported in Section 3.3.3, was used. The efficiency and streamer probability curves are reported in Figure 3.22, while currents, charges, time resolution and cluster size are shown in Figure 3.23 and Figure 3.24 as a function of the voltage subtracted by the RPC working point. Figure 3.25 shows the charge distribution at the working point for both RPCs.

As previously reported, the main difference between the two gas mixtures is the working point. In both cases, it is lower with respect to the STD gas mixture, about 150 V for the CO_2 gas mixture and about 1400 V for the He gas mixture. Both the mixtures reach the same maximum efficiency of the STD gas mixture. The streamer probability is higher for the CO_2 gas mixture, in particular for RPC 11. If Figure 3.23a and Figure 3.24a are considered, it is possible to see that the CO_2 gas mixture has higher currents with respect to the He and STD gas mixtures. Also the avalanche charge has a faster rise as voltage increases for the CO_2 gas mixture as compared to the He and STD ones. The time resolution is less than the STD gas mixture value for both the gas mixtures under test. As concerns the cluster size, the difference between the three gas mixtures are negligible.

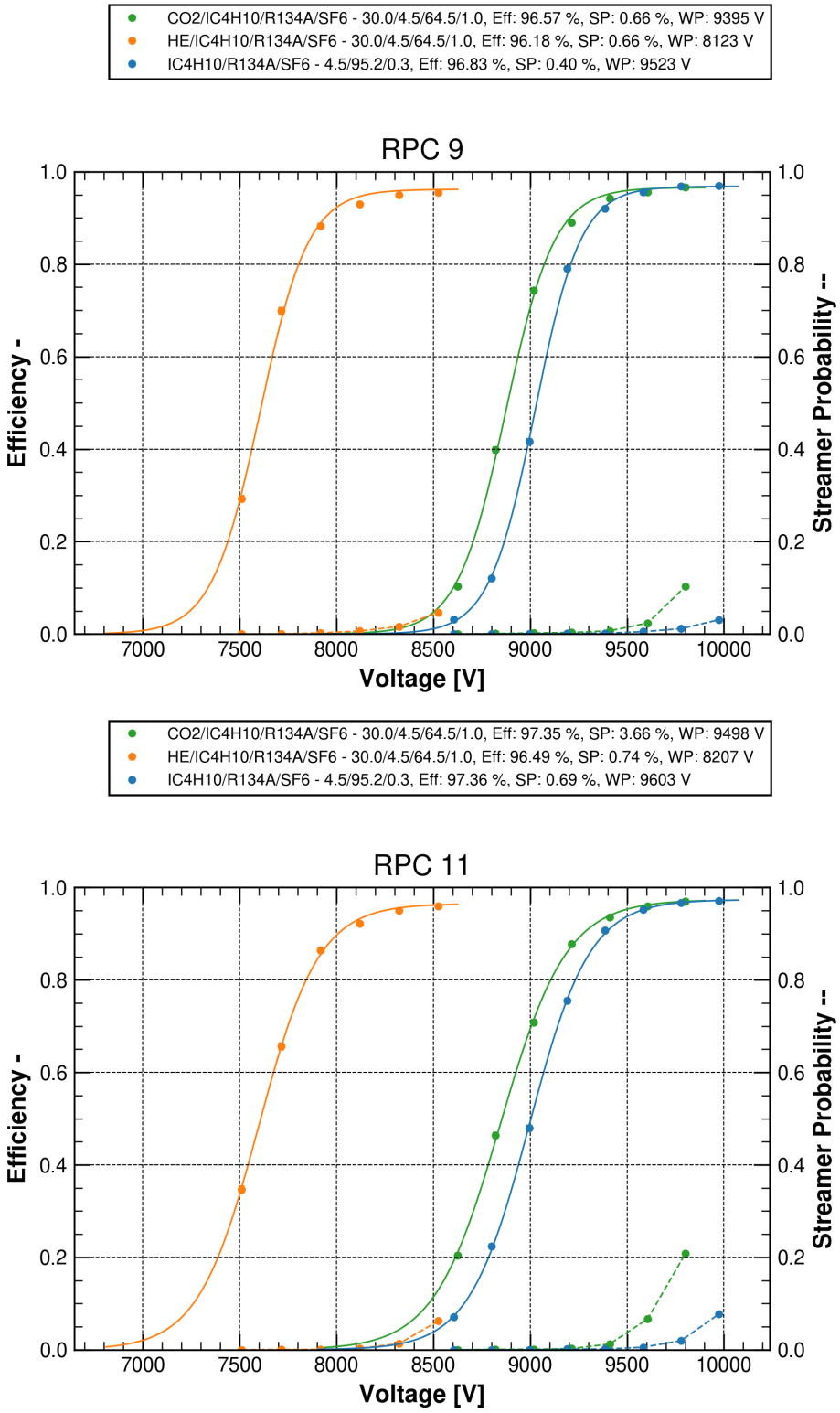

Figure 3.22: Comparison between the best of CO_2 30% and He 30% gas mixtures and the STD gas mixture: efficiency (continuous line) and streamer probability (dashed line).

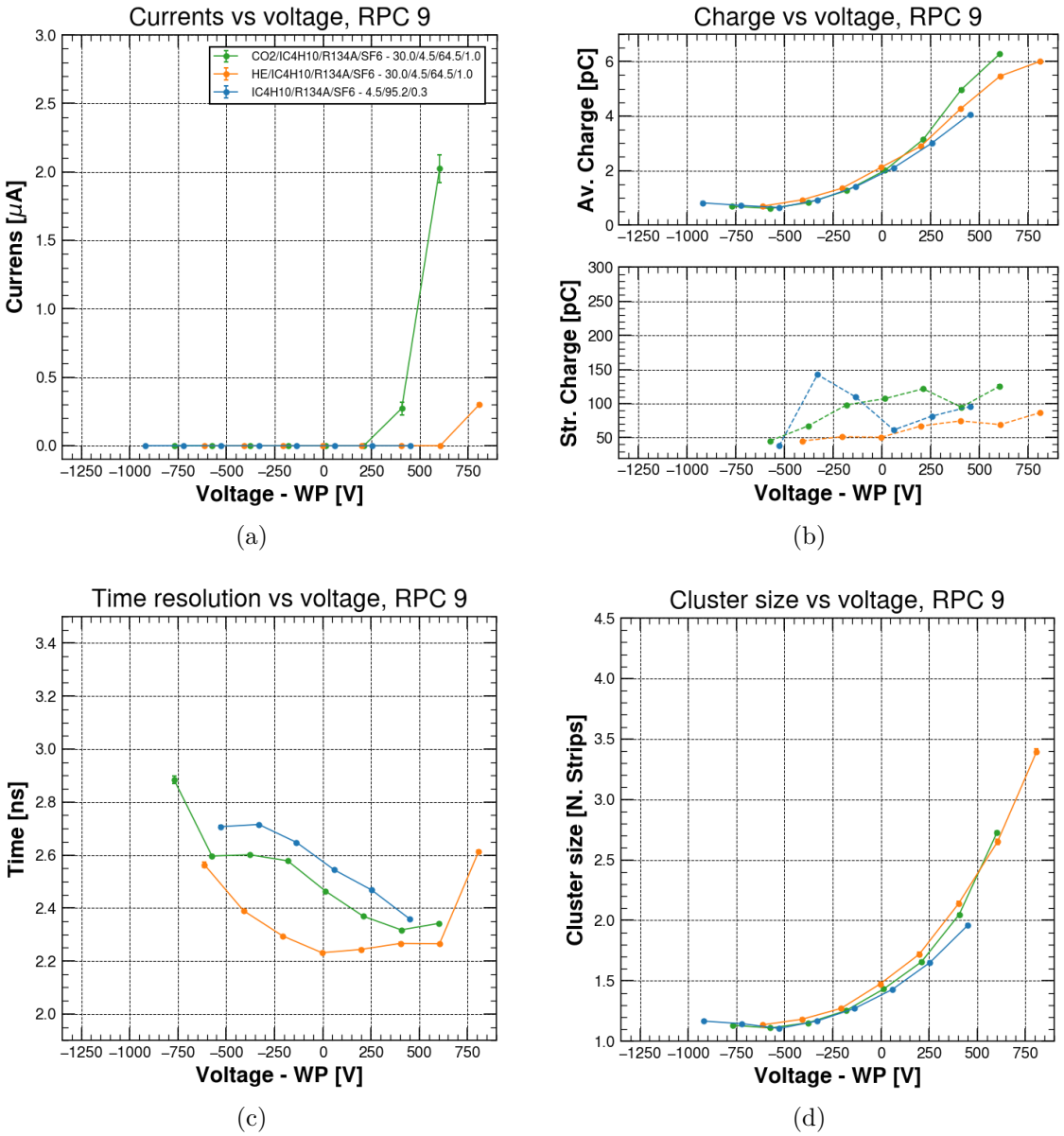

Figure 3.23: Comparison between the best of CO_2 30% and He 30% gas mixtures and the STD gas mixture for RPC 9: (a) Currents for different applied voltages; (b) Avalanche charge and streamer charge for different applied voltages; (c) Cluster size for different applied voltages; (d) Time resolution for different applied voltages.

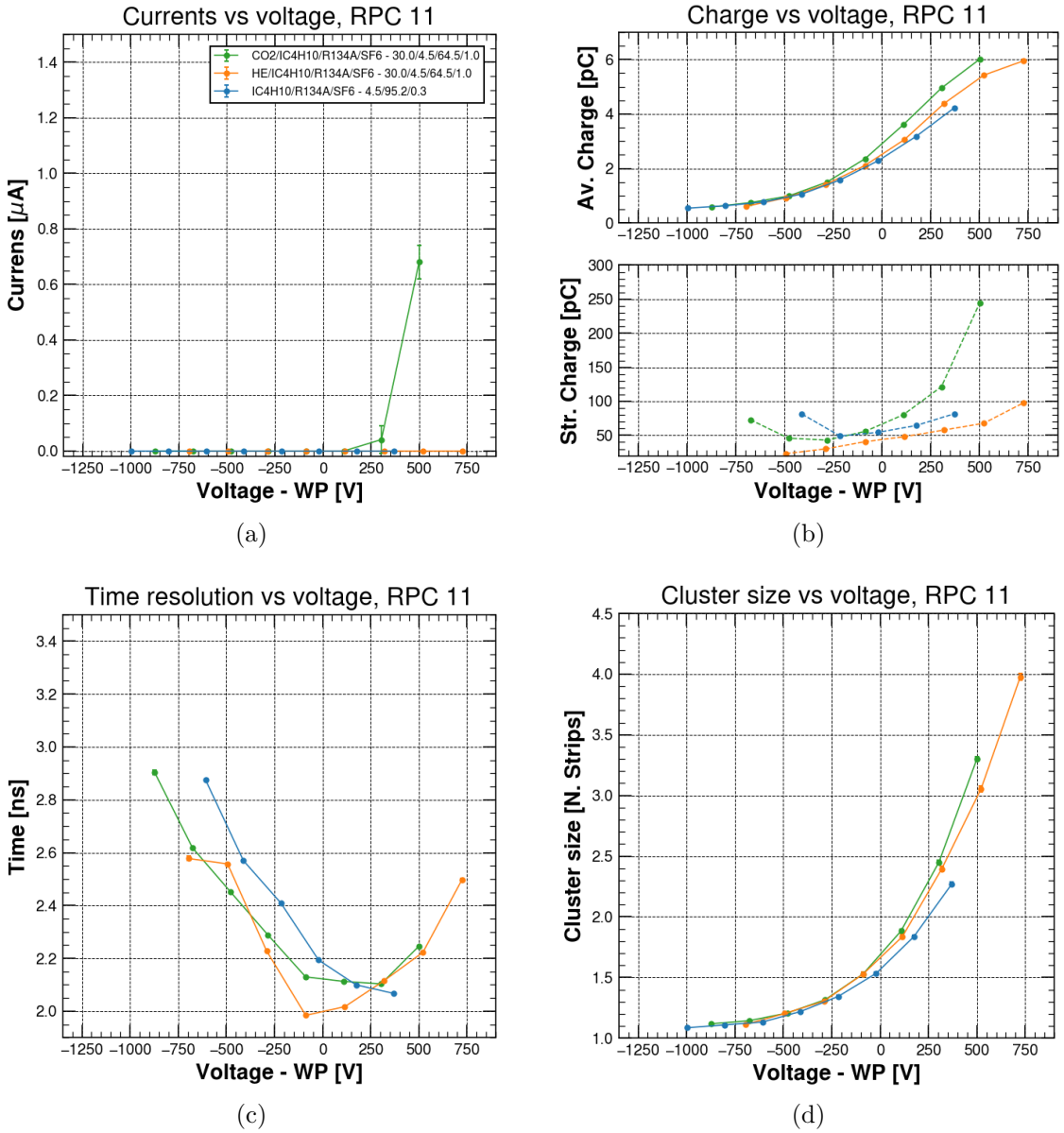

Figure 3.24: Comparison between the best of CO_2 30% and He 30% gas mixtures and the STD gas mixture for RPC 11: (a) Currents for different applied voltages; (b) Avalanche charge and streamer charge for different applied voltages; (c) Cluster size for different applied voltages; (d) Time resolution for different applied voltages.

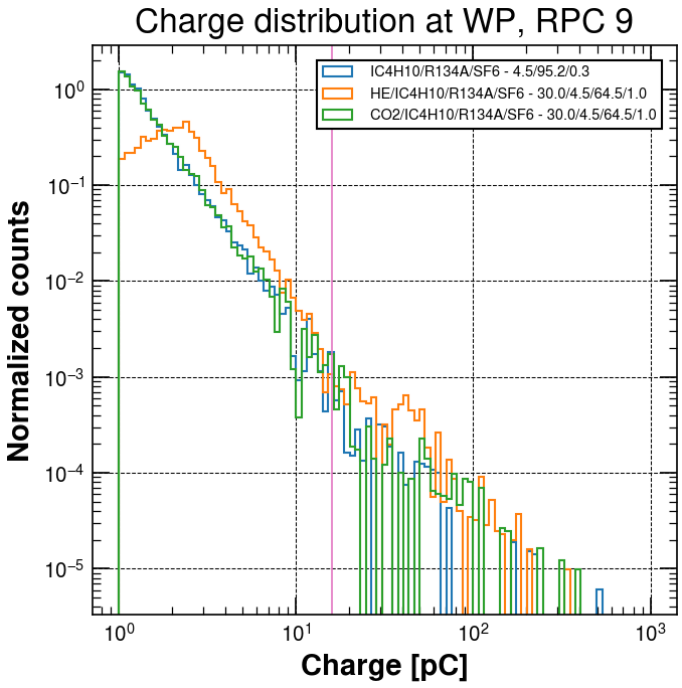

(a)

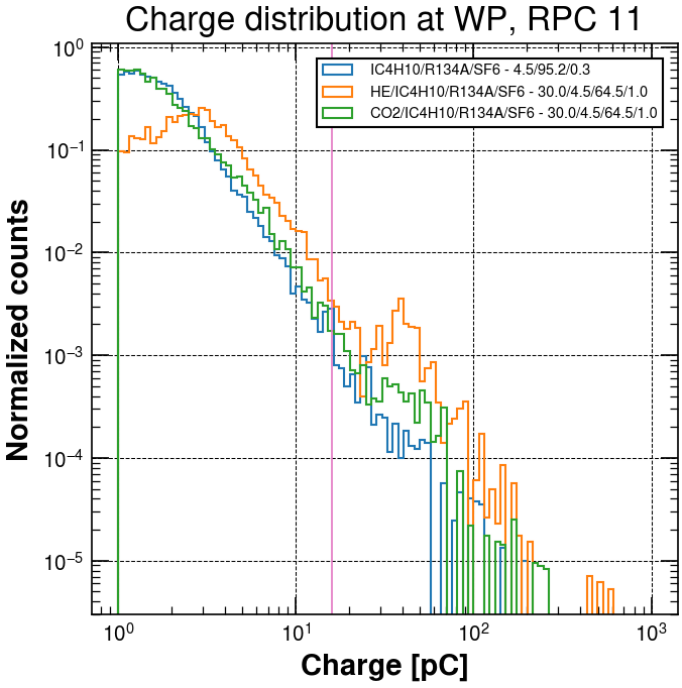

(b)

Figure 3.25: Best of CO_2 30% and He 30% gas mixtures (a) Charge distribution at working point for RPC 9; (b) Charge distribution at working point for RPC 11. The vertical line represents the charge threshold (16 pC) that allows to distinguish an avalanche signal from a streamer signal.

3.3.5 Addition of CO_2 and HFO1234ze to the standard gas mixture

Another way to reduce the GWP of the standard gas mixture is to substitute part of R134a with a gas of the HydroFluoroOlefin family. In particular, the tetrafluoropropene has a molecule $C_3H_2F_4$ which differs from only one atom from the R134a whose molecule is $C_2H_2F_4$. The HFO isomer used in this work is the HFO1234ze. Several tests were performed in the last years and different mixtures have been tested to understand how HFO1234ze could replace the R134a [42, 43]. The results showed that when HFO1234ze is used as a complete replacement of the R134a, the detector is not efficient below 15 kV. The idea was then to use a gas that effectively reduces the gas density, in this case CO_2, resulting in a lower voltage required to operate the detector. In order to deeply understand the behavior of HFO1234ze and CO_2 mixtures, several gas mixtures were tested, reported in Table 3.15 with their respective GWP_{100}.

Table 3.15: GWP_{100} for HFO1234ze gas mixtures.

	HFO1234ze [%]	**R134A** [%]	**CO_2** [%]	**SF_6** [%]	**iC_4H_{10}** [%]	**GWP_{100}**
STD	0	95.2	0	0.3	4.5	3384
CO_2 69%-HFO	25	0	69	1	5	762
CO_2 67%-HFO	25	0	67	1	7	762
CO_2 69%-R134a	0	25	69	1	5	1587

The efficiency curves for both the chambers are shown in Figure 3.26. Current, charge, cluster size and time resolution are shown in Figure 3.27 and Figure 3.28 as a function of the effective voltage subtracted by the chambers working point. Figure 3.29 shows the charge distribution at the working point for both RPCs. The main features are reported in Table 3.16 and Table 3.18. Instead, Table 3.17 and Table 3.19 show the comparison with respect to the features of the STD gas mixture.

First, it is possible to consider the comparison between CO_2 69%-HFO and CO_2 67%-HFO gas mixtures with respect to the STD gas mixture, referring to Table 3.17 and Table 3.19. The working points for these gas mixtures are very similar to each other. In particular, for CO_2 69%-HFO they are, respectively for RPC 9 and RPC 11, 260 V and 250 V higher compared to the STD gas mixture; for CO_2 67%-HFO they are, respectively for RPC 9 and RPC 11, 270 V and 230 V higher with respect to the STD gas mixture. Also the streamer probability has higher values: for CO_2 69%-HFO there is an increase of about 11% and 23% for RPC 9 and RPC 11 respectively; for CO_2 67%-HFO there is an increase of about 8% and 16% for RPC 9 and RPC 11 respectively. There is a big difference in these values for the two RPCs, but the trend is the same for both the chambers. Such increase of the streamer probability may lead to a detector with higher aging effects. If the time resolution is considered, there is a significant increment, of about 0.2 ns, for both the detectors and both the gas mixtures with respect to the STD one. It is possible to consider the efficiency curve shown in Figure 3.26. It can be seen that the fit done by the sigmoid function for CO_2 69%-HFO and CO_2 67%-HFO gas mixtures present a knee that deviates significantly from the data and the fit has a different shape with respect to the

fit of the STD gas mixture. In fact, if the maximum efficiency reached by the detectors is considered, there is a difference of about 2% for RPC 9 and about 3% for RPC 11, with respect to the STD gas mixture. This could not be explained by a misalignment of the scintillators as the experimental set up did not change between the measurements for the He 30% gas mixtures and these measurements and this issue is not present in the He 30% gas mixtures results. Therefore this problem is probably due to this type of gas mixture and perhaps linked to the high presence of CO_2, as this issue is present also in the CO_2 69%-R134a gas mixture. It is possible to see that the avalanche charge is bigger for both gas mixtures when compared to the STD one, with an increase of about 2 pC for both chambers. Instead, the streamer charge is significantly smaller: for CO_2 69%-HFO there is a decrease of about 25 pC and 50 pC for RPC 9 and RPC 11 respectively; for CO_2 67%-HFO a decrease of about 35 pC and 70 pC for RPC 9 and RPC 11 respectively. The charge distributions for both the detectors are reported in Figure 3.29. However, also in this case it is difficult to determine whether this improvement is due to the mixture or to a statistical problem. The higher avalanche charge can partially justify the increase in the mean cluster size. The most critical parameters for these gas mixtures are surely the currents being their values much larger than the STD gas mixture, as it can be seen from Figure 3.27 and Figure 3.28. This currents increase with respect to the STD gas mixture is caused by the increased charge developed inside the detector. Higher charge inside the gas gap can affect the rate capability of the chamber, a parameter that is really important when the detectors are located in a high irradiation environment, such as in the LHC experiments. Higher currents can also accelerate the chambers aging effects.

It is possible to consider the CO_2 69%-R134a gas mixture, in which all the HFO1234ze is substituted by R134a. From Table 3.17 and Table 3.19 it is possible to see that the increase of the streamer probability with respect to the STD gas mixture is the same as the CO_2 69%-HFO gas mixture. The avalanche charge remains 1 pC higher with respect to the STD gas mixture, but this variation is smaller with respect to the CO_2 69%-HFO gas mixture. However, the streamer charge has the opposite behavior since, with respect to the STD gas mixture, it increases by 30 pC for both chambers. Also in this case, it is difficult to determine whether this improvement is due to the mixture or to a statistical problem. The chambers don't reach the same maximum efficiency of the STD gas mixture. It is interesting to notice that also the current curves present a different shape. The currents value at the working point is higher with respect to the STD gas mixture but smaller with respect to CO_2 69%-HFO and CO_2 67%-HFO. From this data, we can see that the current increase of CO_2 69%-HFO and CO_2 67%-HFO gas mixture is not generated only by the presence of the HFO1234ze, but also by the high concentration of CO_2.

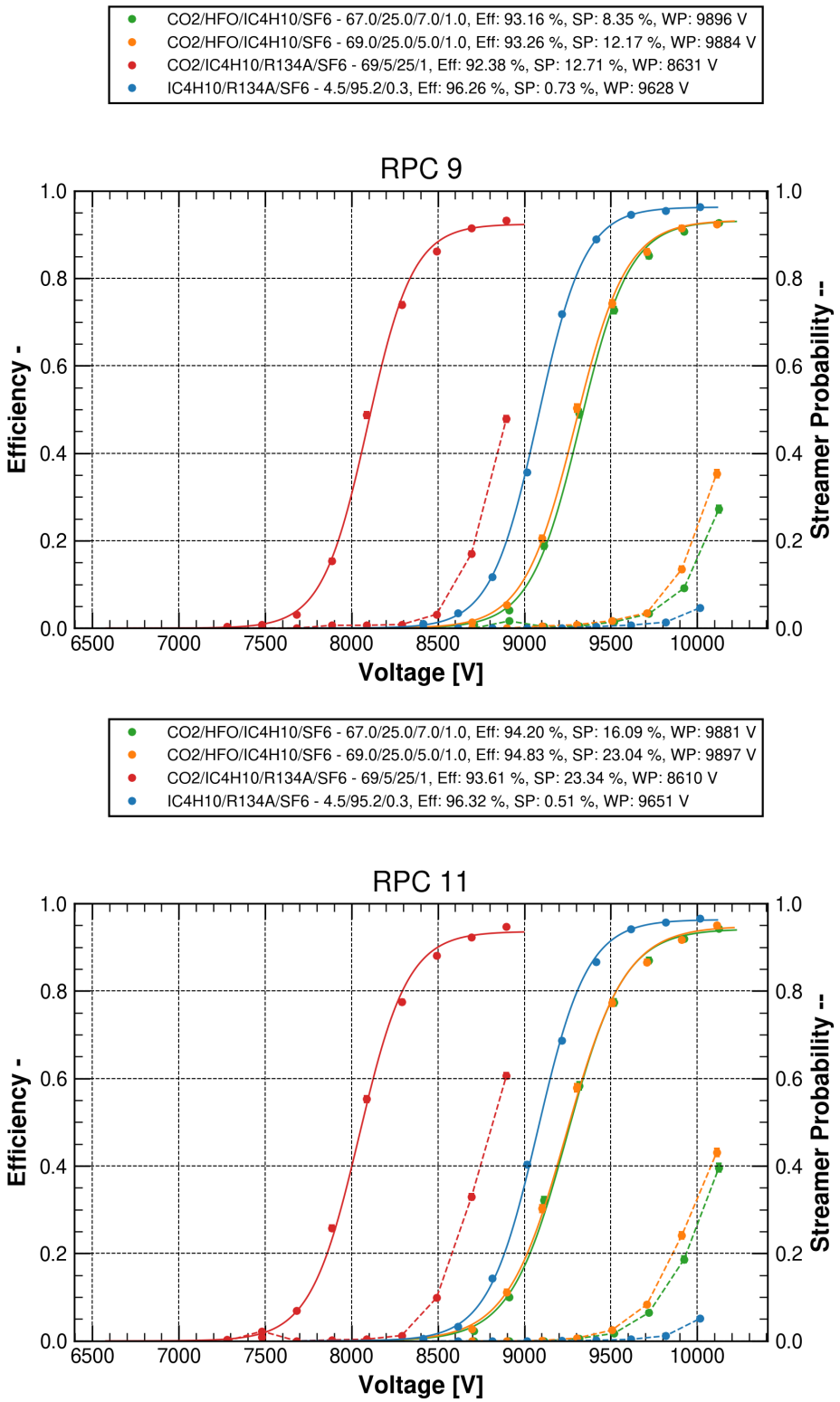

Figure 3.26: Comparison between HFO1234ze gas mixtures and the STD gas mixture: efficiency (continuous line) and streamer probability (dashed line).

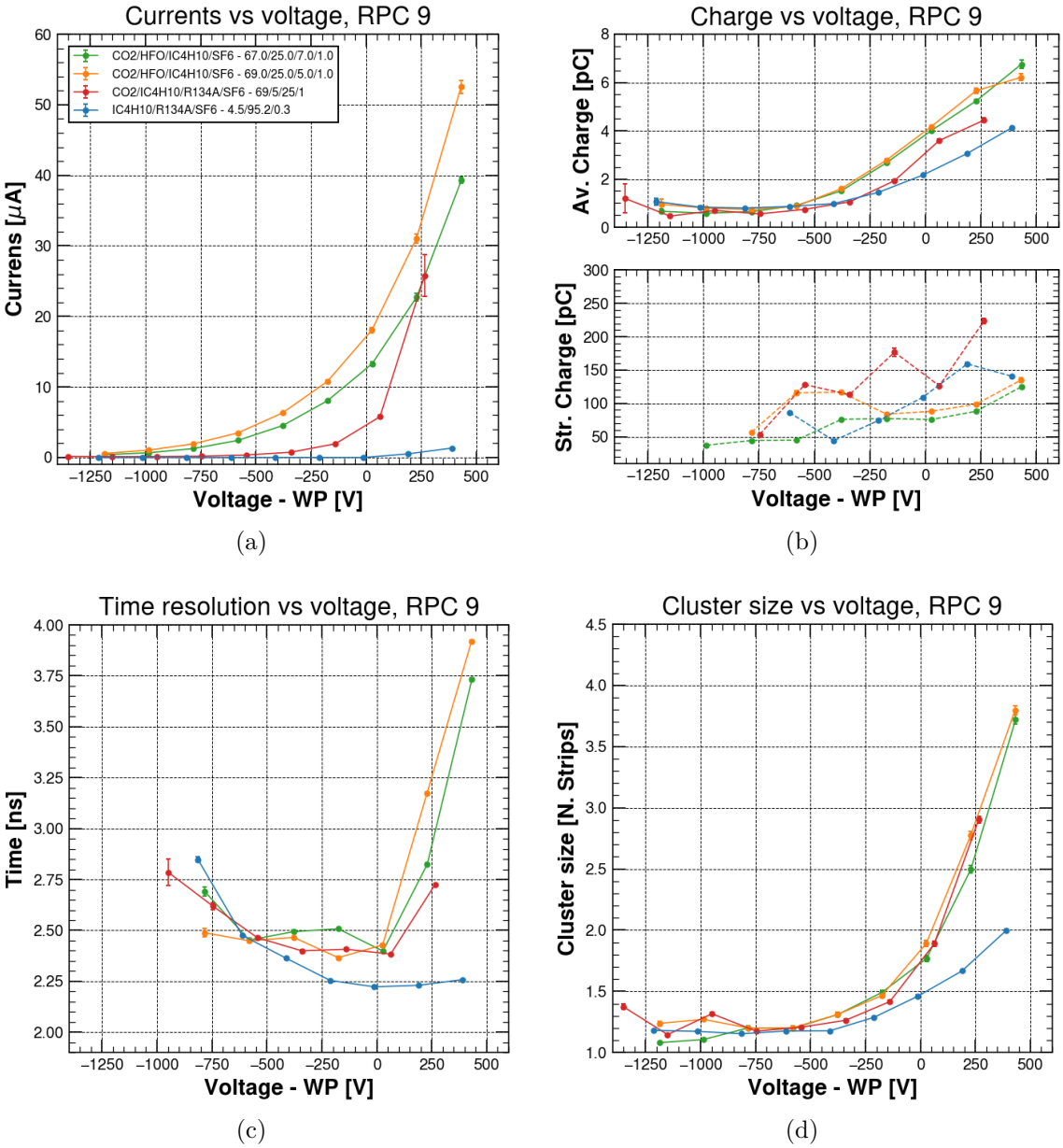

Figure 3.27: Comparison between HFO1234ze gas mixtures and the STD gas mixture for RPC 9: (a) Currents for different applied voltages; (b) Avalanche charge and streamer charge for different applied voltages; (c) Cluster size for different applied voltages; (d) Time resolution for different applied voltages.

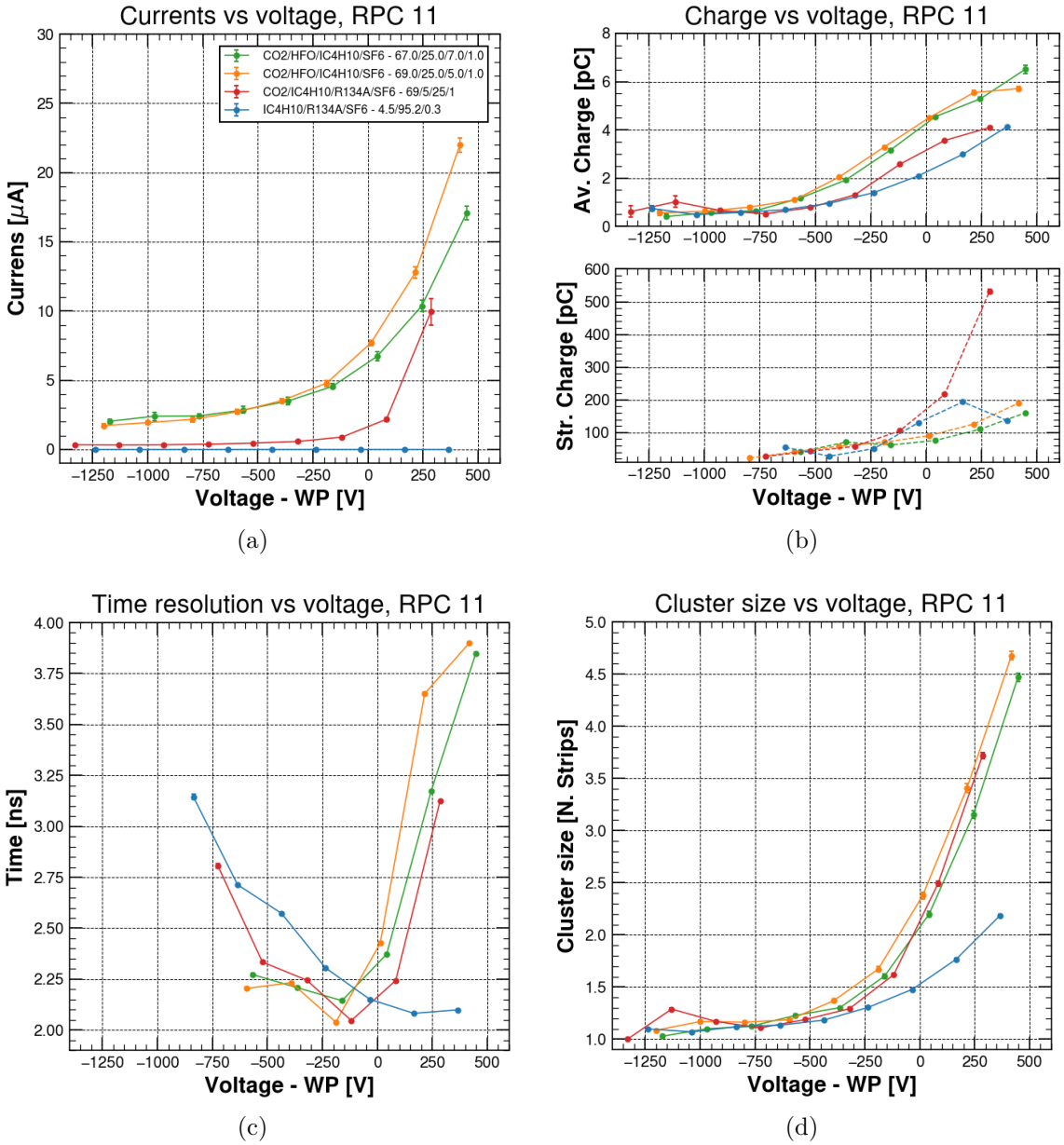

Figure 3.28: Comparison between HFO1234ze gas mixtures and the STD gas mixture for RPC 11: (a) Currents for different applied voltages; (b) Avalanche charge and streamer charge for different applied voltages; (c) Cluster size for different applied voltages; (d) Time resolution for different applied voltages.

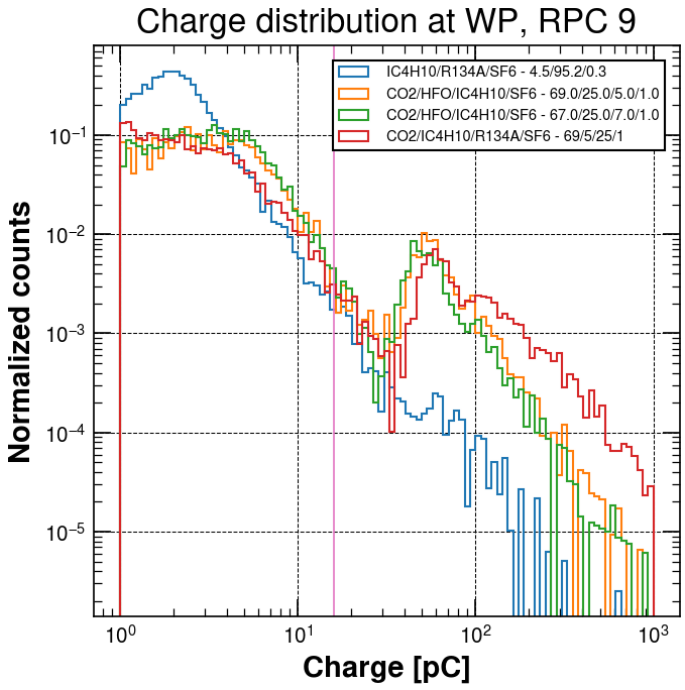

(a)

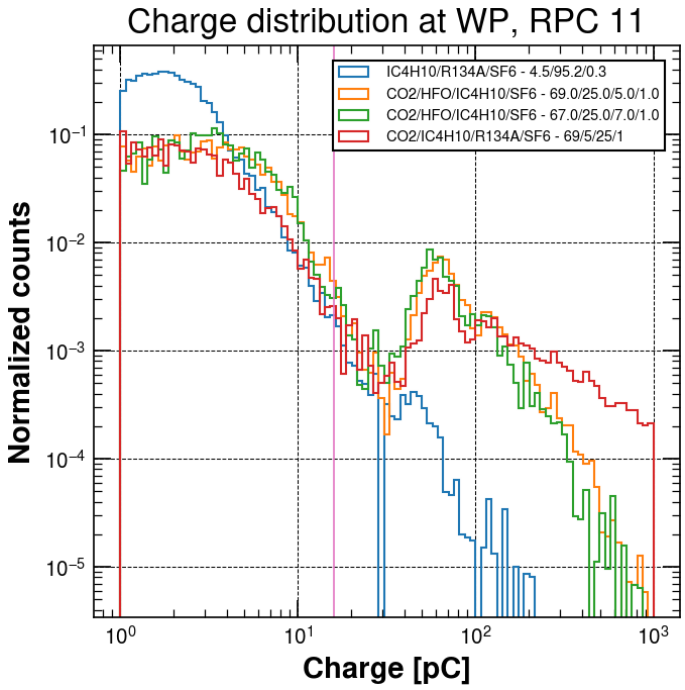

(b)

Figure 3.29: HFO1234ze gas mixtures (a) Charge distribution at working point for RPC 9; (b) Charge distribution at working point for RPC 11. The vertical line represents the charge threshold (16 pC) that allows to distinguish an avalanche signal from a streamer signal.

Table 3.16: RPC 9 feature values obtained for HFO1234ze gas mixtures.

RPC 9	**CO_2 69%-HFO**	**CO_2 67%-HFO**	**CO_2 69%-R134a**
Working point [V]	9884 ± 8	9896 ± 8	8631 ± 6
Maximum efficiency [%]	93.3 ± 0.3	93.2 ± 0.3	92.4 ± 0.3
Streamer probability at WP [%]	12.2 ± 0.6	8.3 ± 0.5	12.7 ± 0.4
Mean avalanche charge at WP [pC]	3.99 ± 0.06	3.82 ± 0.05	3.07 ± 0.04
Mean streamer charge at WP [pC]	87 ± 2	76 ± 1	142 ± 4
Mean time resolution at WP [ns]	2.420 ± 0.005	2.413 ± 0.005	2.391 ± 0.004
Mean cluster size at WP [N. strips]	1.83 ± 0.03	1.73 ± 0.02	1.74 ± 0.02
Currents at WP [μA]	17.1 ± 0.3	12.6 ± 0.3	4.6 ± 0.2

Table 3.17: RPC 9 difference between the feature values obtained for HFO1234ze gas mixture and the STD gas mixture.

RPC 9	**ΔCO_2 69%-HFO**	**ΔCO_2 67%-HFO**	**ΔCO_2 69%-R134a**
Working point [V]	257 ± 13	268 ± 12	−997 ± 10
Maximum efficiency [%]	−3.0 ± 0.4	−3.1 ± 0.4	−3.9 ± 0.4
Streamer probability at WP [%]	11.4 ± 0.7	7.6 ± 0.6	12.0 ± 0.5
Mean avalanche charge at WP [pC]	1.78 ± 0.08	1.61 ± 0.07	0.86 ± 0.06
Mean streamer charge at WP [pC]	−24 ± 3	−36 ± 3	30 ± 5
Mean time resolution at WP [ns]	0.197 ± 0.007	0.190 ± 0.007	0.168 ± 0.005
Mean cluster size at WP [N. strips]	0.36 ± 0.03	0.26 ± 0.03	0.27 ± 0.03
Currents at WP [μA]	17.1 ± 0.3	12.5 ± 0.3	4.6 ± 0.2

Table 3.18: RPC 11 feature values obtained for HFO1234ze gas mixtures.

RPC 11	**CO_2 69%-HFO**	**CO_2 67%-HFO**	**CO_2 69%-R134a**
Working point [V]	9897 ± 9	9881 ± 9	8610 ± 6
Maximum efficiency [%]	94.8 ± 0.3	94.2 ± 0.3	93.6 ± 0.2
Streamer probability at WP [%]	23.0 ± 0.8	16.1 ± 0.7	23.3 ± 0.6
Mean avalanche charge at WP [pC]	4.42 ± 0.06	4.26 ± 0.06	3.15 ± 0.04
Mean streamer charge at WP [pC]	89 ± 1	73 ± 1	171 ± 3
Mean time resolution at WP [ns]	2.400 ± 0.005	2.325 ± 0.005	2.162 ± 0.003
Mean cluster size at WP [N. strips]	2.33 ± 0.03	2.07 ± 0.03	2.13 ± 0.02
Currents at WP [μA]	7.5 ± 0.2	6.3 ± 0.3	1.6 ± 0.1

Table 3.19: RPC 11 difference between the feature values obtained for HFO1234ze gas mixtures and the STD gas mixture.

RPC 11	**ΔCO_2 69%-HFO**	**ΔCO_2 67%-HFO**	**ΔCO_2 69%-R134a**
Working point [V]	246 ± 13	230 ± 13	−1041 ± 10
Maximum efficiency [%]	−1.5 ± 0.4	−2.1 ± 0.4	−2.7 ± 0.4
Streamer probability at WP [%]	22.5 ± 0.8	15.6 ± 0.8	22.8 ± 0.7
Mean avalanche charge at WP [pC]	2.17 ± 0.08	2.01 ± 0.07	0.90 ± 0.06
Mean streamer charge at WP [pC]	−52 ± 4	−68 ± 3	29 ± 6
Mean time resolution at WP [ns]	0.261 ± 0.007	0.185 ± 0.007	0.022 ± 0.005
Mean cluster size at WP [N. strips]	0.80 ± 0.04	0.55 ± 0.04	0.60 ± 0.03
Currents at WP [μA]	7.5 ± 0.2	6.3 ± 0.3	1.6 ± 0.1

3.3.6 Addition of Novec^{TM} 4710, CO_2 and He to the standard gas mixture

Another way to reduce the GWP of the STD is to find a substitute for the SF_6. In fact, this gas has the highest GWP in the standard gas mixture, even if it is used in the smallest concentration. 3M^{TM} Novec^{TM} 4710 is a sustainable alternative to SF_6 for electrical equipment insulation [44]. It offers excellent dielectric properties, a wide range of operating temperatures and significant reductions in environmental impact compared to SF_6 (GWP_{100} of 2100 instead of 22800). This gas also has a high electronegativity. The CERN's gas group tested different concentrations of this gas as a substitute of the SF_6 in the standard gas mixture [45]. From this data it is possible to see that it is possible to obtain a performance similar to the standard gas mixture if a concentration of 0.1% of Novec 4710 is used. In order to confirm this data, the STD gas mixture in which we used 0.1% and 0.3% Novec 4710 concentration instead of the 0.3% SF_6 concentration was tested.

Later, from the He 30% and CO_2 30% gas mixtures, analyzed in Section 3.3.2 and Section 3.3.3, the gas mixtures with the 1% SF_6 concentration were selected. Since 0.1% Novec 4710 concentration is very similar to a 0.3% SF_6 concentration, it is possible to estimate the Novec 4710 concentration that corresponds to a 1% SF_6 concentration. To do so, the following proportion was used:

$$0.1\%\ \text{Novec 4710} : 0.3\%\ SF_6 = x\%\ \text{Novec 4710} : 1\%\ SF_6$$

which gives 0.35% of Novec 4710. Then the gas mixtures tested in Section 3.3.2 and Section 3.3.3 were considered and the 1% of SF_6 was replaced with 0.35% of Novec 4710. Table 3.20 reports all the gas mixtures tested with the respective GWP_{100}.

Table 3.20: GWP_{100} for Novec 4710 gas mixtures.

	R134a [%]	**CO_2** [%]	**He** [%]	**iC_4H_{10}** [%]	**SF_6** [%]	**Novec 4710** [%]	**GWP_{100}**
STD	95.2	0	0	4.5	0.3	0	3384
Novec 0.1%	95.4	0	0	4.5	0	0.1	3250
Novec 0.3%	95.2	0	0	4.5	0	0.3	3194
N-He 30%	65.15	0	30	4.5	0	0.35	2269
N-CO_2 30%	65.15	30	0	4.5	0	0.35	2269

The efficiency curves for both the chambers are shown in Figure 3.30. Current, charge, cluster size and time resolution are shown in Figure 3.31 and Figure 3.32 as a function of the effective voltage subtracted by the chambers working point. Figure 3.33 shows the charge distribution at the working point for both RPCs. The main features are reported in Table 3.21 and Table 3.23. Instead, Table 3.22 and Table 3.24 show the comparison with respect to the features of the STD gas mixture.

First, it is possible to compare the Novec 0.1% and Novec 0.3% with respect to the STD gas mixture. For both chambers, the working point of the Novec 0.3% gas mixture is about 450 V higher. This effect indicates that the Novec 4710 has a strong electronic

affinity. Instead, the working point for the Novec 0.1% gas mixture is very similar to the STD gas mixture. Indeed it is compatible with the STD gas mixture values for RPC 9 and it presents a little discrepancy of 20 V for RPC 11. Both the chambers reach the same maximum efficiency of the STD and present the same streamer probability. The avalanche charges are compatible with the STD gas mixture for RPC 11, while they are smaller for RPC 9. This is probably due to the lower resistivity of RPC 9, which makes the chamber more sensitive to charge. The mean streamer charge is lower with respect to the STD gas mixture, except for RPC 9 with Novec 0.1 % gas mixture. However, if the streamer charge as a function of the voltage is considered, reported in Figure 3.31, it is possible to see that the value of the streamer charge for the data near the working point is out of the trend. This can be produced by low statistics or other effects that could have affected the data, like the development of a random discharge. The time resolution is similar with respect to the STD gas mixture for RPC 11, while it is 0.3 ns higher for RPC 9, for both the gas mixtures. Instead, the cluster size is the same as the STD gas mixture for both the chambers and both the gas mixtures tested.

Then the N-He 30% and N-CO_2 30% were compared to the STD gas mixture. The working point is about 1400 V smaller for N-He 30% and it is about 50 V higher for the N-CO_2 30% gas mixture. The chambers reach the same maximum efficiency of the standard gas mixture. The streamer probability of the N-He 30% gas mixture is the same of the standard gas mixture for both the chambers. Instead, The streamer probability of the N-CO_2 30% is the same as the standard gas mixture only for RPC 9, while for RPC 11 is about 2% bigger. For the gas mixture N-He 30%, both chambers have an avalanche charge similar to the STD, while for the N-CO_2 30% only RPC 9 presents a value compatible with the STD one and for RPC 11 the avalanche charge is 0.4 pC bigger with respect to the STD. In all the cases, the streamer charge is lower than the STD, but once again it is difficult to know if this result is due only to the few statistics. Both gas mixtures present a time resolution 0.3 ns higher only for RPC 9, while it is the same for RPC 11. The cluster size is the same as the STD for both the chambers and both the gas mixture tested.

Then it is possible to compare the N-He 30% and N-CO_2 30% with the respectively He 30% and CO_2 30% gas mixtures. In Table 3.25 and Table 3.26 the main features subtracted by the STD values are reported. First, it is possible to compare the two He mixtures. The working point difference with respect to the STD gas mixture is about the same for the two gas mixtures, with a difference of about 1500 V. The values are compatible for RPC 11, instead for RPC 9 there is a little discrepancy. However, the maximum efficiency and streamer probability differences are compatible between the two gas mixtures, and they are also compatible with the STD gas mixture. The avalanche charge is very similar to the STD gas mixture for both the gas mixtures. Instead, the streamer charge is smaller than the STD gas mixture one in all the cases, and it is also very similar between the two gas mixtures tested for a fixed RPC. Also for the time resolution and the cluster size there are no relevant differences between the two mixtures and compared to the standard one. The only relevant difference between the two mixtures is the current. In fact it is higher in the N-He 30% gas mixture than in the He 30% gas mixture: for RPC 9, 1 μA difference at the working point; for RPC 11, 2.6 μA difference at the working point.

It is possible to compare the two CO_2 gas mixtures. For the CO_2 30% gas mixture and both RPCs the working point is about 130 V less than the STD gas mixture one, while for N-CO_2 30% it is about 50 V higher. However, for both the gas mixture and for both the

RPCs, the maximum efficiency is reached and it is similar to the STD. For the RPC 9 there is no difference between the two gas mixtures for what concerns the streamer probability, that is also very similar to the STD. However, for RPC 11 the streamer probability is different for both the gas mixtures when compared to the STD gas mixture. In particular, for CO_2 30% it is 3% higher and for N-CO_2 30% it is 1.7% higher. Also the avalanche charge is higher for RPC 11 and for both the mixture with respect to the STD gas mixture, while for RPC 9 there are no relevant differences. Both the chambers have the same behavior for what concerns the streamer charge. In particular, it seems higher with respect the STD gas mixture for the CO_2 gas mixtures and it is lower for the N-CO_2 30% gas mixture. The time resolution is the same of the STD gas mixture except for RPC 9 and N-CO_2 30% it is 1.7% gas mixture, but this difference seems to be not so relevant. For both the gas mixture and both RPCs, the cluster size is slightly bigger with respect to the STD gas mixture, but also in this case it is a small difference: 0.05 n. strips for RPC 9 and 0.12 n. strips for RPC 11.

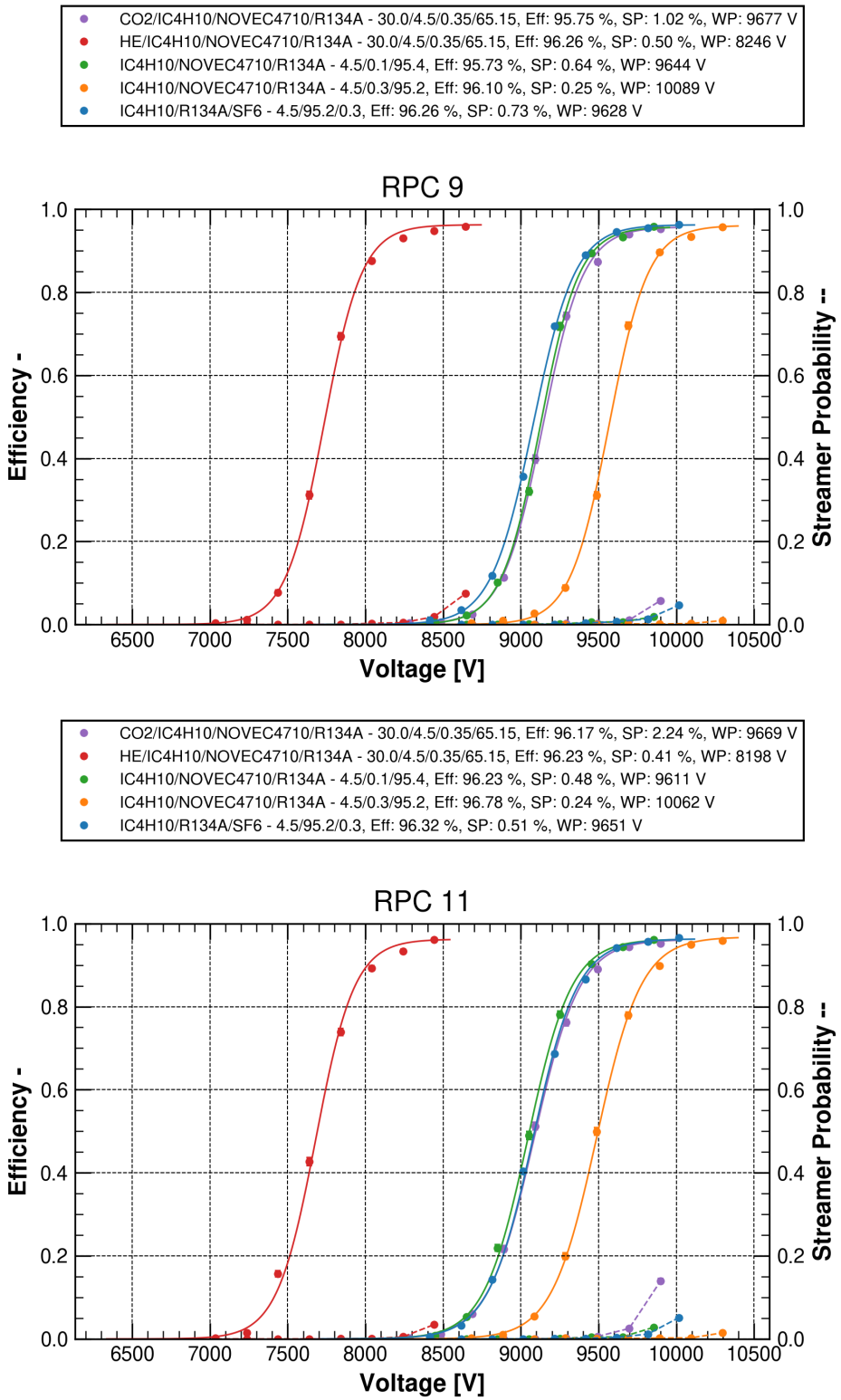

Figure 3.30: Comparison between Novec 4710 gas mixtures and the STD gas mixture: efficiency (continuous line) and streamer probability (dashed line).

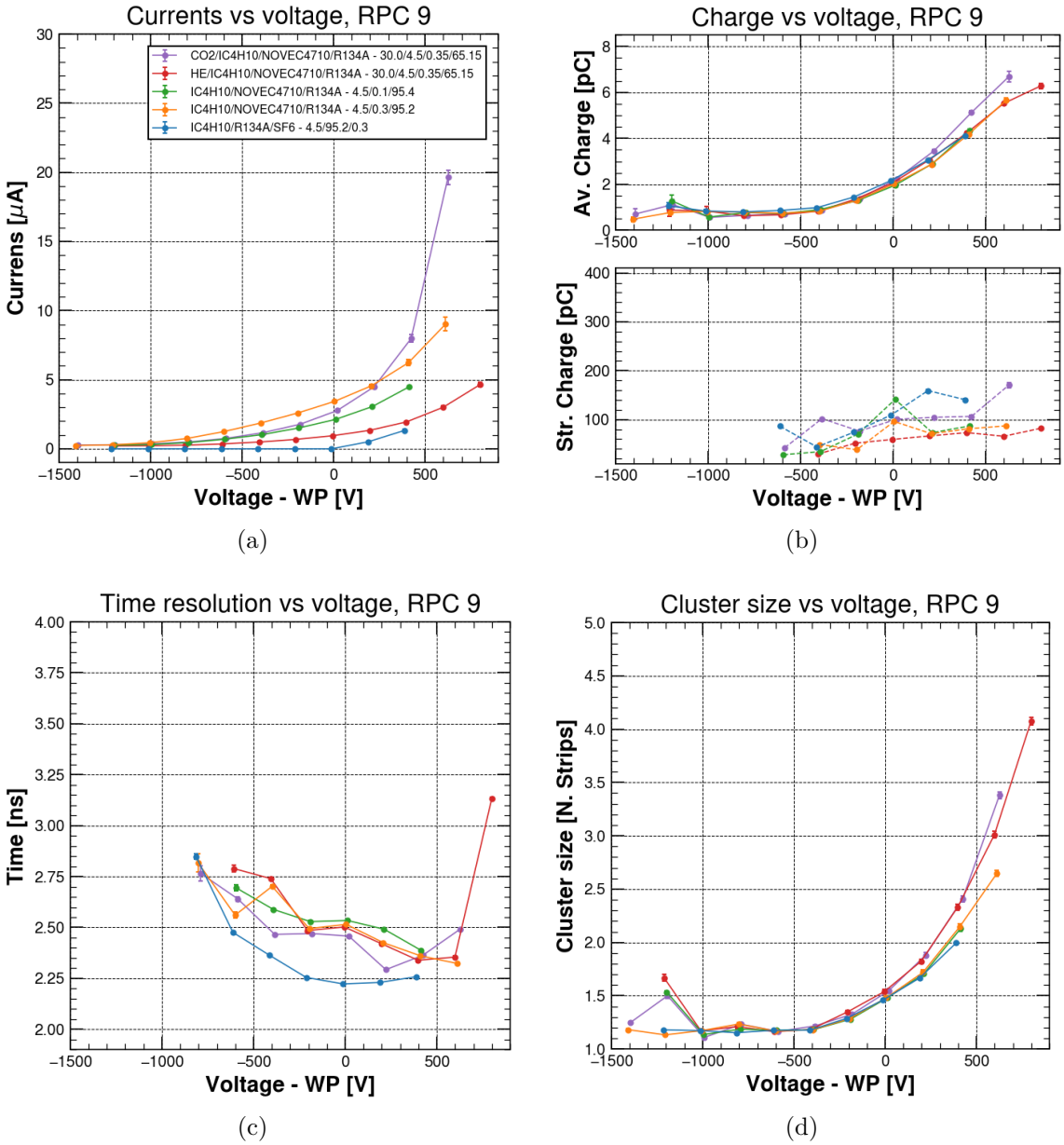

Figure 3.31: Comparison between Novec 4710 gas mixtures and the STD gas mixture for RPC 9: (a) Currents for different applied voltages; (b) Avalanche charge and streamer charge for different applied voltages; (c) Cluster size for different applied voltages; (d) Time resolution for different applied voltages.

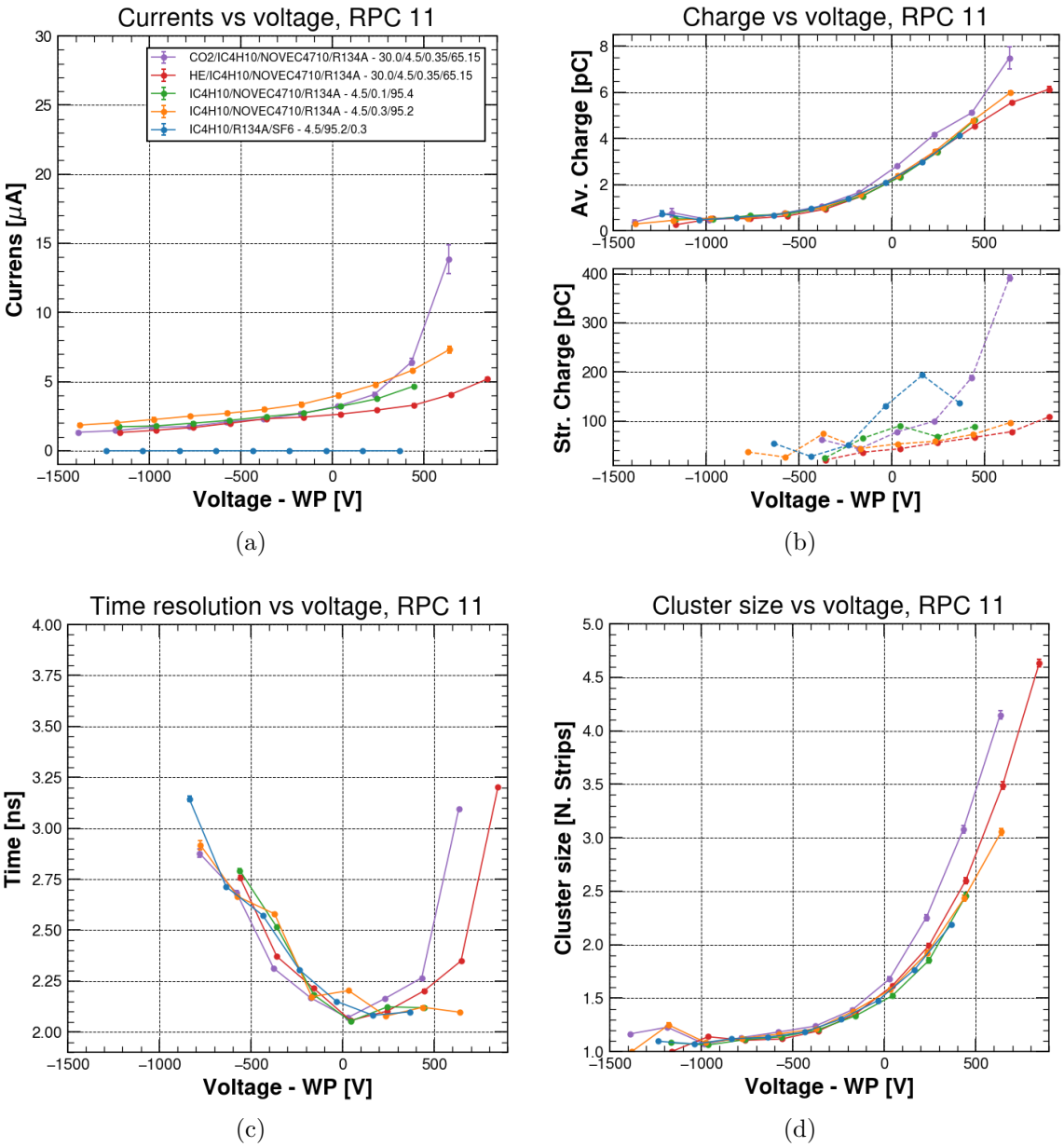

Figure 3.32: Comparison between Novec 4710 gas mixtures and the STD gas mixture for RPC 11: (a) Currents for different applied voltages; (b) Avalanche charge and streamer charge for different applied voltages; (c) Cluster size for different applied voltages; (d) Time resolution for different applied voltages.

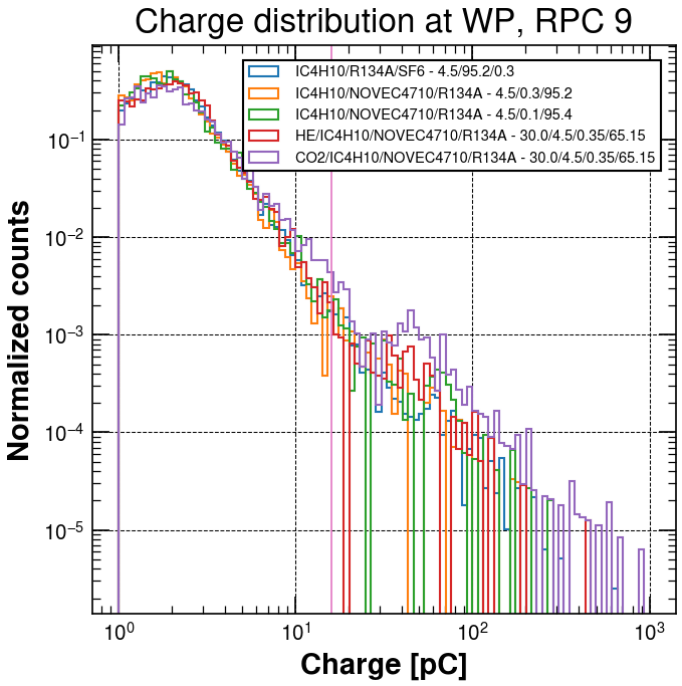

(a)

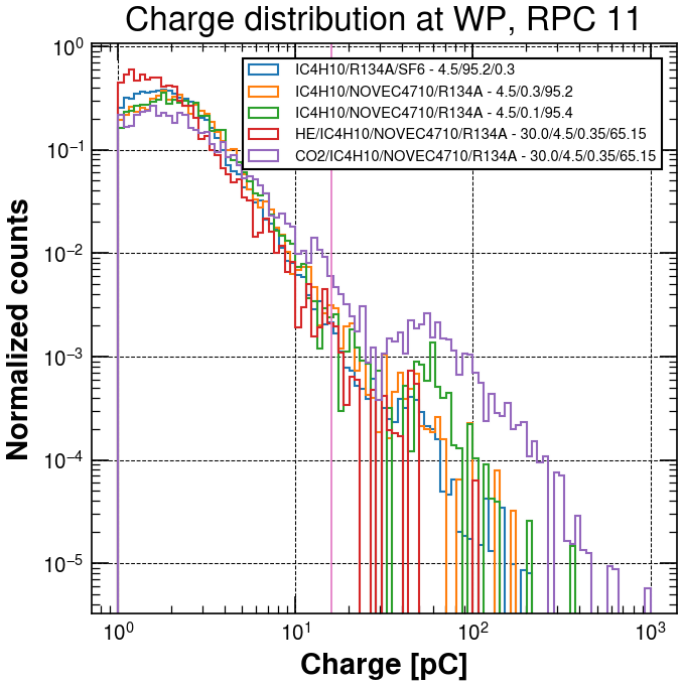

(b)

Figure 3.33: Novec 4710 gas mixtures (a) Charge distribution at working point for RPC 9; (b) Charge distribution at working point for RPC 11. The vertical line represents the charge threshold (16 pC) that allows to distinguish an avalanche signal from a streamer signal.

Table 3.21: RPC 9 feature values obtained for Novec 4710 gas mixtures.

RPC 9	**Novec 0.3%**	**Novec 0.1%**	**N-He 30%**	**N-CO_2 30%**
Working point [V]	10089 ± 7	9644 ± 7	8246 ± 7	9677 ± 7
Maximum efficiency [%]	96.1 ± 0.2	95.7 ± 0.2	96.3 ± 0.2	95.7 ± 0.2
Streamer probability at WP [%]	0.2 ± 0.1	0.6 ± 0.1	0.5 ± 0.1	1.0 ± 0.2
Mean avalanche charge at WP [pC]	1.99 ± 0.04	1.92 ± 0.03	2.07 ± 0.03	2.15 ± 0.04
Mean streamer charge at WP [pC]	94.4 ± 0.7	137 ± 2	59.4 ± 0.4	98 ± 1
Mean time resolution at WP [ns]	2.515 ± 0.005	2.534 ± 0.005	2.500 ± 0.005	2.459 ± 0.005
Mean cluster size at WP [N. strips]	1.47 ± 0.02	1.47 ± 0.02	1.55 ± 0.02	1.53 ± 0.02
Currents at WP [μA]	3.41 ± 0.04	2.09 ± 0.03	0.95 ± 0.01	2.67 ± 0.06

Table 3.22: RPC 9 difference between the feature values obtained for Novec 4710 gas mixtures and the STD gas mixture.

RPC 9	**ΔNovec 0.3%**	**ΔNovec 0.1%**	**ΔN-He 30%**	**ΔN-CO_2 30%**
Working point [V]	461 ± 11	16 ± 11	-1382 ± 11	49 ± 11
Maximum efficiency [%]	-0.2 ± 0.3	-0.5 ± 0.4	0.0 ± 0.3	-0.5 ± 0.3
Streamer probability at WP [%]	-0.5 ± 0.2	-0.1 ± 0.2	-0.2 ± 0.2	0.3 ± 0.3
Mean avalanche charge at WP [pC]	-0.22 ± 0.06	-0.29 ± 0.05	-0.15 ± 0.05	-0.06 ± 0.06
Mean streamer charge at WP [pC]	-17 ± 2	25 ± 5	-52 ± 2	-14 ± 2
Mean time resolution at WP [ns]	0.291 ± 0.007	0.311 ± 0.007	0.277 ± 0.007	0.235 ± 0.007
Mean cluster size at WP [N. strips]	0.00 ± 0.03	0.00 ± 0.03	0.07 ± 0.03	0.05 ± 0.03
Currents at WP [μA]	3.4 ± 0.1	2.1 ± 0.1	0.9 ± 0.1	2.6 ± 0.1

Table 3.23: RPC 11 feature values obtained for Novec 4710 gas mixtures.

RPC 11	**Novec 0.3%**	**Novec 0.1%**	**N-He 30%**	**N-CO_2 30%**
Working point [V]	10062 ± 7	9611 ± 7	8198 ± 6	9669 ± 7
Maximum efficiency [%]	96.8 ± 0.2	96.2 ± 0.2	96.2 ± 0.2	96.2 ± 0.2
Streamer probability at WP [%]	0.2 ± 0.1	0.5 ± 0.1	0.4 ± 0.1	2.2 ± 0.3
Mean avalanche charge at WP [pC]	2.26 ± 0.04	2.15 ± 0.03	2.17 ± 0.03	2.65 ± 0.04
Mean streamer charge at WP [pC]	51.9 ± 0.5	85 ± 1	42.0 ± 0.2	72.9 ± 0.9
Mean time resolution at WP [ns]	2.198 ± 0.005	2.081 ± 0.005	2.091 ± 0.005	2.084 ± 0.005
Mean cluster size at WP [N. strips]	1.54 ± 0.02	1.48 ± 0.02	1.56 ± 0.02	1.64 ± 0.02
Currents at WP [μA]	3.9 ± 0.2	3.10 ± 0.07	2.6 ± 0.1	3.13 ± 0.08

Table 3.24: RPC 11 difference between the feature values obtained for Novec 4710 gas mixtures and the STD gas mixture.

RPC 11	**ΔNovec 0.3%**	**ΔNovec 0.1%**	**ΔN-He 30%**	**ΔN-CO_2 30%**
Working point [V]	410 ± 11	-40 ± 11	-1453 ± 10	18 ± 11
Maximum efficiency [%]	0.5 ± 0.3	-0.1 ± 0.3	-0.1 ± 0.3	-0.2 ± 0.3
Streamer probability at WP [%]	-0.3 ± 0.2	0.0 ± 0.2	-0.1 ± 0.2	1.7 ± 0.3
Mean avalanche charge at WP [pC]	0.02 ± 0.06	-0.09 ± 0.05	-0.07 ± 0.05	0.40 ± 0.06
Mean streamer charge at WP [pC]	-89 ± 3	-56 ± 4	-99 ± 3	-68 ± 4
Mean time resolution at WP [ns]	0.059 ± 0.006	-0.058 ± 0.006	-0.048 ± 0.006	-0.055 ± 0.006
Mean cluster size at WP [N. strips]	0.02 ± 0.03	-0.05 ± 0.03	0.03 ± 0.03	0.11 ± 0.03
Currents at WP [μA]	3.9 ± 0.2	3.10 ± 0.07	2.6 ± 0.1	3.13 ± 0.08

Table 3.25: RPC 9 difference between the feature values obtained for He and CO_2 gas mixtures and the STD gas mixture.

RPC 9	**ΔHe 30%**	**ΔN-He 30%**	**ΔCO_2 30%**	**ΔN-CO_2 30%**
Working point [V]	-1505 ± 12	-1382 ± 11	-128 ± 9	49 ± 11
Maximum efficiency [%]	-0.1 ± 0.3	0.0 ± 0.3	-0.3 ± 0.2	-0.5 ± 0.3
Streamer probability at WP [%]	-0.1 ± 0.2	-0.2 ± 0.2	0.3 ± 0.1	0.3 ± 0.3
Mean avalanche charge at WP [pC]	-0.08 ± 0.05	-0.15 ± 0.05	0.06 ± 0.03	-0.06 ± 0.06
Mean streamer charge at WP [pC]	-61 ± 2	-52 ± 2	30 ± 1	-14 ± 2
Mean time resolution at WP [ns]	0.008 ± 0.005	0.277 ± 0.007	-0.103 ± 0.004	0.235 ± 0.007
Mean cluster size at WP [N. strips]	0.01 ± 0.02	0.07 ± 0.03	0.04 ± 0.02	0.05 ± 0.03
Currents at WP[μA]	-0.03 ± 0.01	0.9 ± 0.1	0.0 ± 0.2	2.6 ± 0.1

Table 3.26: RPC 11 difference between the feature values obtained for He and CO_2 gas mixtures and the STD gas mixture.

RPC 11	**ΔHe 30%**	**ΔN-He 30%**	**ΔCO_2 30%**	**ΔN-CO_2 30%**
Working point [V]	-1404 ± 14	-1453 ± 10	-106 ± 11	18 ± 11
Maximum efficiency [%]	0.2 ± 0.3	-0.1 ± 0.3	0.0 ± 0.2	-0.2 ± 0.3
Streamer probability at WP [%]	0.2 ± 0.2	-0.1 ± 0.2	3.0 ± 0.3	1.7 ± 0.4
Mean avalanche charge at WP [pC]	0.27 ± 0.05	-0.07 ± 0.05	0.54 ± 0.04	0.40 ± 0.06
Mean streamer charge at WP [pC]	-97 ± 3	-99 ± 3	11.2 ± 0.8	-68 ± 4
Mean time resolution at WP [ns]	0.141 ± 0.005	-0.048 ± 0.006	-0.061 ± 0.003	-0.055 ± 0.006
Mean cluster size at WP [N. strips]	0.13 ± 0.03	0.03 ± 0.03	0.12 ± 0.02	0.11 ± 0.03
Currents at WP [μA]	0.00 ± 0.02	2.6 ± 0.1	0.0 ± 0.2	3.13 ± 0.08

3.4 Summary results

It is possible to resume the results found in the previous sections. The main features as a function of the RPCs and of the gas mixture are reported in Figure 3.34, Figure 3.35, Figure 3.36 and Figure 3.37[10].

First, it is possible to consider the working point for the different gas mixtures. The majority of the tested gas mixtures present a lower or comparable working point with respect to the STD gas mixture. CO_2 69%-HFO, CO_2 67%-HFO and Novec 0.3% are the only exceptions. It is possible to see that all the HFO1234ze gas mixtures reach a lower maximum efficiency with respect to the STD gas mixture. Since CO_2 69%-R134a differs mainly from the STD for the replacement of 69% of R134a with the same concentration of CO_2, it is possible to affirm that the lower maximum efficiency is caused by the change in the ratio between CO_2 and R134a. If the streamer probability is considered, it is possible to see that its values increases as the CO_2 concentration increases. Indeed, the value of the streamer probability is slightly higher than the STD gas mixture one in the CO_2 30% and in the N-CO_2 30%,with an increase for the CO_2 67%-HFO gas mixture, that has the 67% of CO_2, and a maximum value for CO_2 69%-HFO and CO_2 69%-R134a where a 69% of CO_2 concentration is present.

As for the avalanche charge, all the HFO1234ze gas mixtures present higher values with respect to the STD gas mixture. If the CO_2 69%-R134a gas mixture is considered it is possible to see a relevant increase of the charge, and that could be related to the high presence of CO_2. Moreover, if CO_2 69%-R134a is compared to CO_2 69%-HFO gas mixture, in which 25% of R134a is substituted by 25% of HFO1234ze, it is possible to see a further increase in the charge. This allows to affirm that also HFO1234ze contributes in charge increasing.

The mean streamer charge data are not so relevant, since they are mainly influenced by the statistics. Also the time resolution seems to vary between 2 and 2.7 ns without a clear trend. However, there is a clear increase in the cluster size for all the HFO1234ze gas mixtures. This could be related to the high CO_2 concentration in the gas mixture. Probably, unlike wire chambers, the CO_2 is not sufficient to contain the lateral dispersion of the avalanche since it can't absorb the UV photons produced in the gap. Moreover, the R134a reduction produces also a reduction also of the electronegativity of the gas mixture that could increase the cluster size. The currents present higher values with respect to the STD gas mixture for all the HFO1234ze and Novec gas mixtures. From the HFO1234ze gas mixtures it is possible to see that the main contribution of the currents increase is due to the HFO1234ze, together with the CO_2, since the currents are higher in the CO_2 69%-HFO and CO_2 67%-HFO gas mixture respect to the CO_2 69%-R134a gas mixture.

The He 30% gas mixture family is the one with the most similar behavior with respect to the standard gas mixture, in particular for SF_6 concentration greater than 0.45%. Despite these excellent results, it must be remembered that the use of He is, at the moment, prohibited in the experimental cavern. Also the CO_2 30% gas mixture family has good results, in particular for SF_6 concentration greater than 0.8%. The Novec 0.1% gas mixture performances are identical to the STD, except for the currents that are higher.

[10]For the STD gas mixture, we use the data set reported in Section 3.3.1.

The HFO1234ze gas mixtures seem to be not promising, due to the lower efficiency, higher working point, higher streamer probability, higher charge and higher currents.

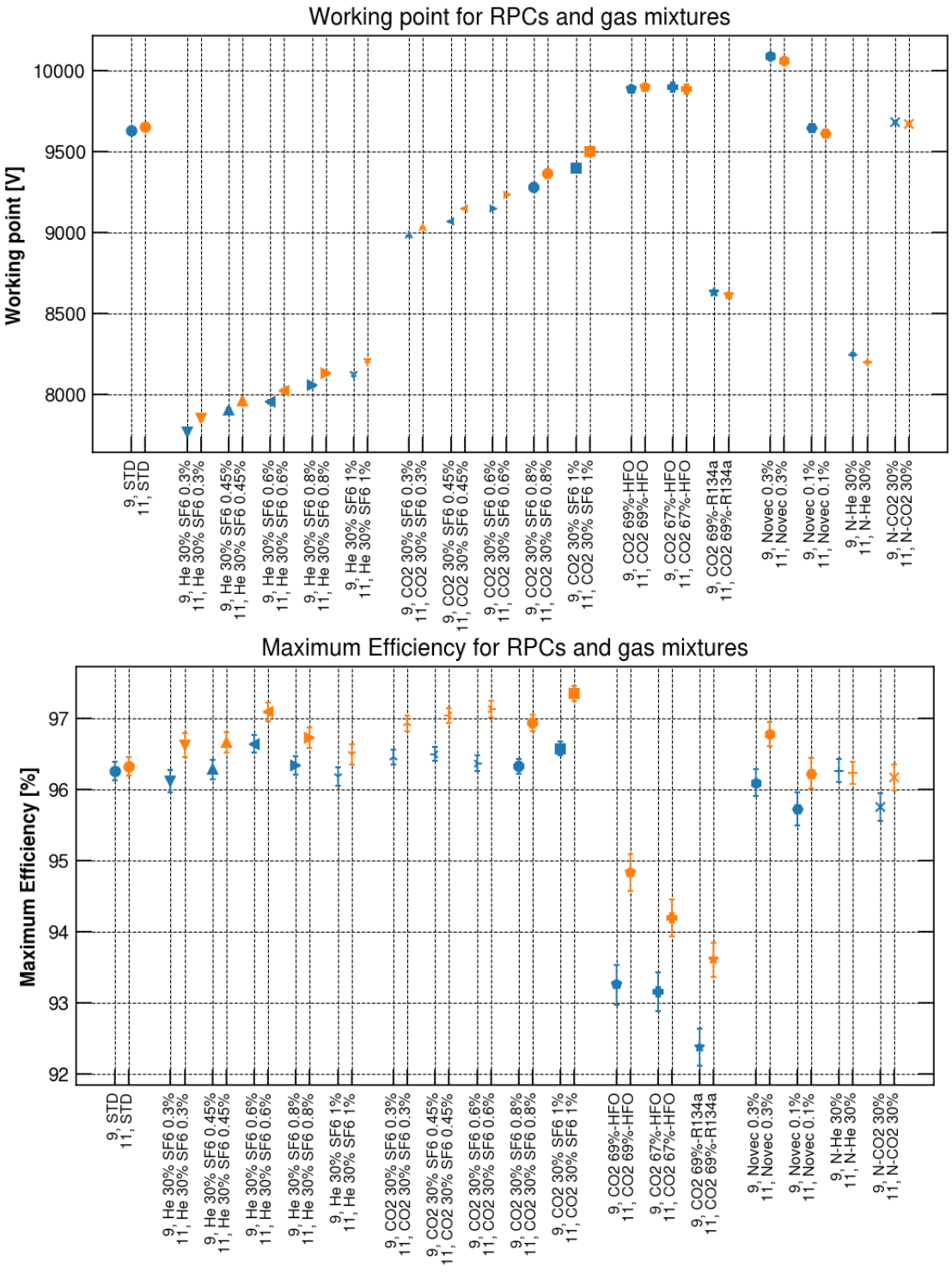

Figure 3.34: Working point and maximum efficiency at working point for all the RPCs and gas mixtures.

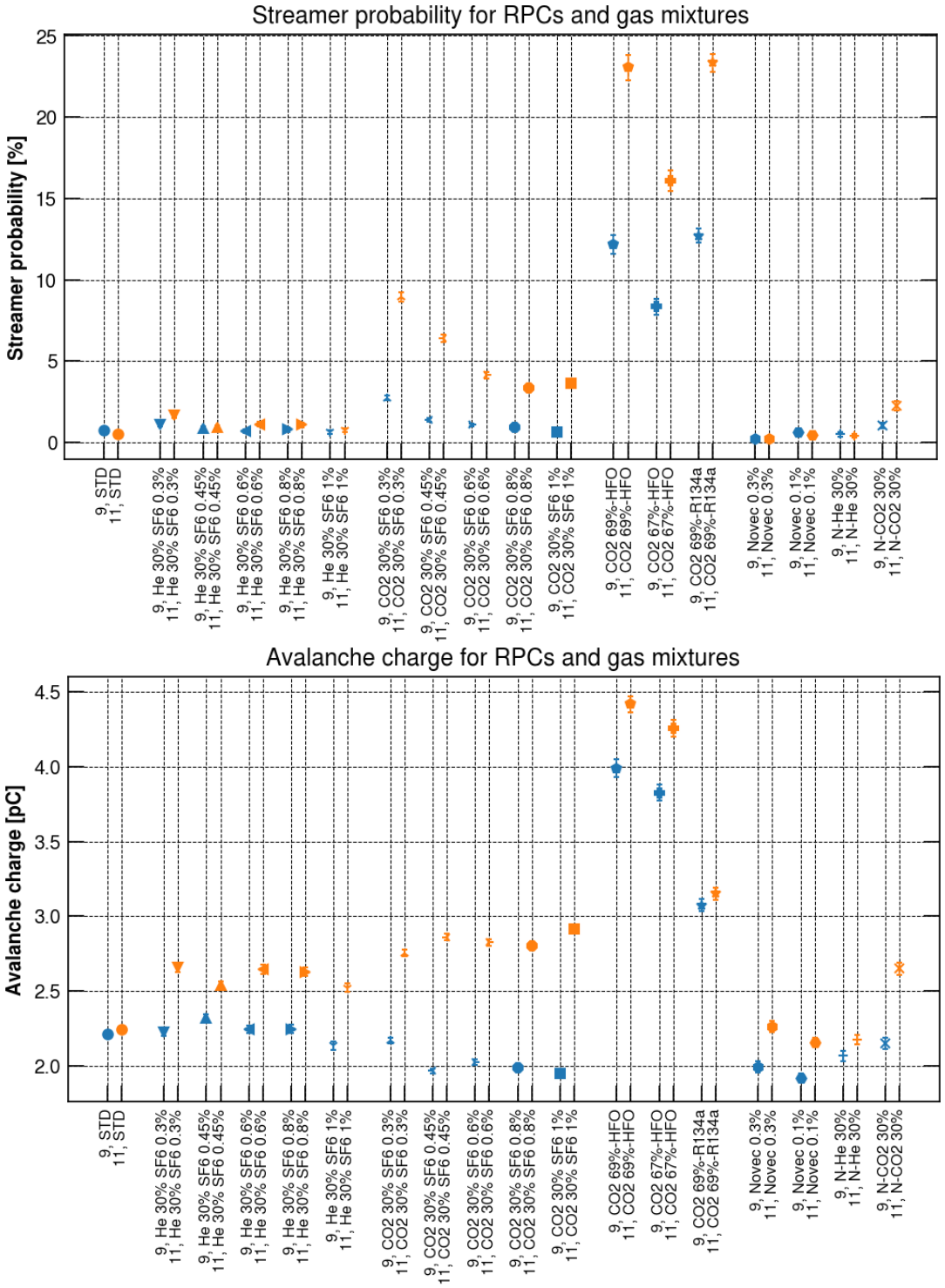

Figure 3.35: Streamer probability and avalanche charge at working point for all the RPCs and gas mixtures.

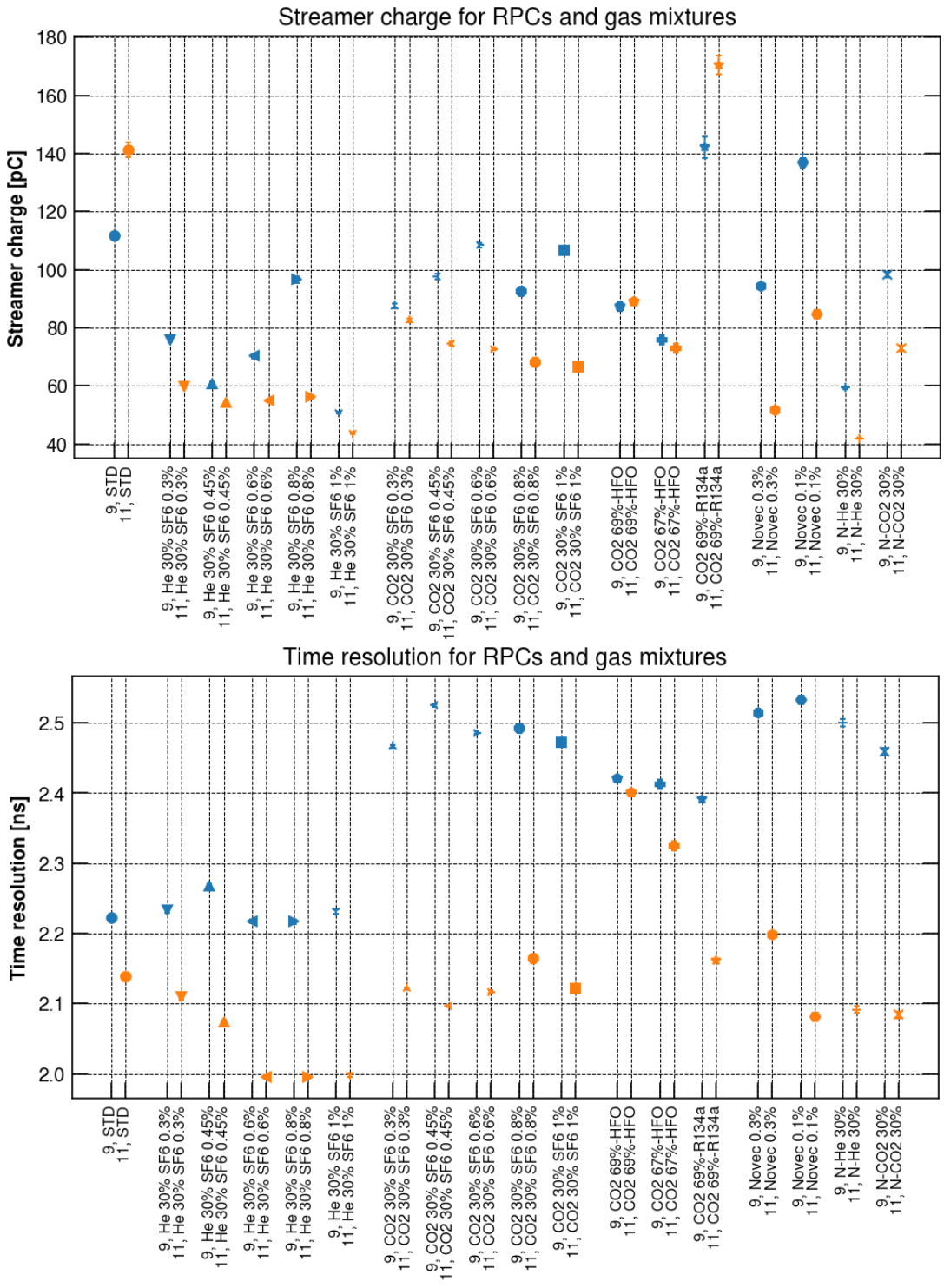

Figure 3.36: Streamer charge and time resolution at working point for all the RPCs and gas mixtures.

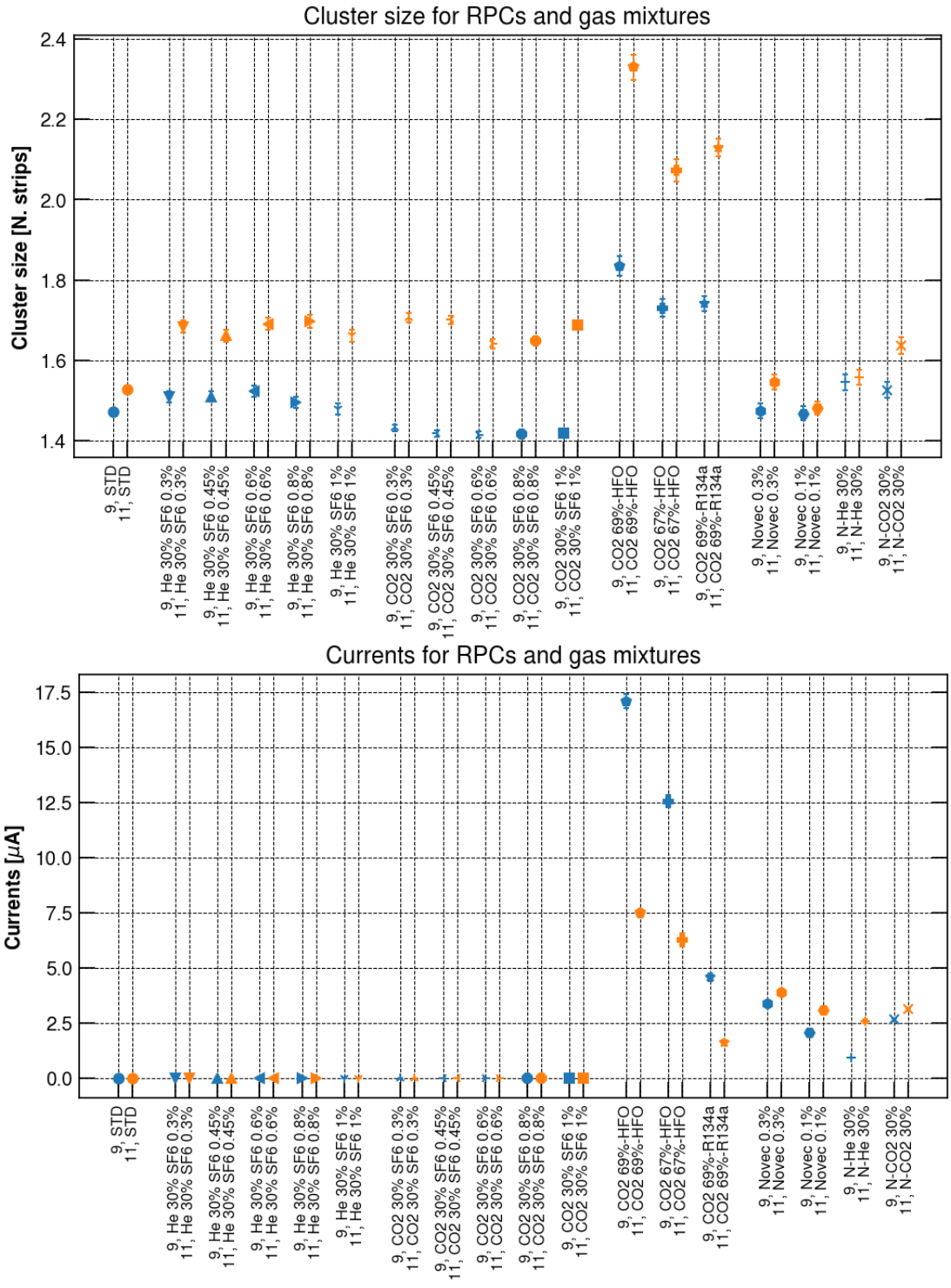

Figure 3.37: Cluster size and currents at working point for all the RPCs and gas mixtures.

Chapter 4

Test Beam Studies at GIF++

The aim of the study is to validate the eco-friendly gas mixtures, tested in laboratory, under high particle irradiation flux. At the GIF++ facility two different tests were performed. In the first one, we selected a particular gas mixture, previously tested in the laboratory, and we used it in RPCs detectors located in a high gamma irradiation environment. This allows us to estimate possible detector aging effects due to the tested gas mixture. As for the second test we used the muon beam from the SPS, in combination with ^{137}Cs gamma background, in order to understand if the RPC performances with the selected eco-gas mixture were similar to the STD gas mixture, in irradiation conditions similar to LHC experiments.

In the following sections the description of the experimental setup and the results obtained from the test beam studies are reported.

4.1 Experimental setup

Figure 4.1 shows the scheme of the experimental setup. The setup was located in three different areas: the gas room, the GIF++ bunker and the electronic room. These areas represent the three parts of which the set up was composed: gas supply, detectors and electronic/readout. In the following section each part will be described.

4.1.1 Gas supply

The scheme of the gas system is shown in Figure 4.2. First, the gas mixture under test was created in a dedicated gas rack, inside the gas room located above the electronic room. Using MFCs it was possible to create a mixture from 3 up to 5 components, in the same way done in the laboratory setup. The gases were initially flushed into a volume of 5 liters in the mixer. Then the gas were flushed into another ATEX[1] rack where iC_4H_{10} was added to the mixture. Then the gas was flushed to the close loop rack. Three of the four lines were used to flush the gas to three chamber installed inside the bunker. The flow could be

[1]The ATEX directives are two EU directives describing the minimum safety requirements for workplaces and equipment used in explosive atmospheres.

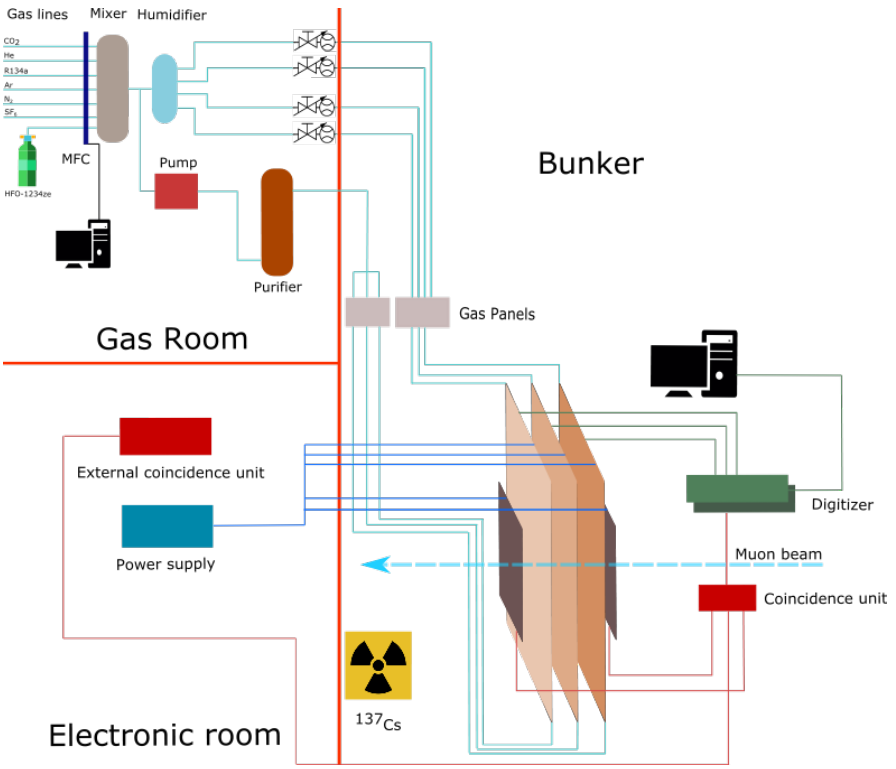

Figure 4.1: Scheme of the GIF++ experimental setup.

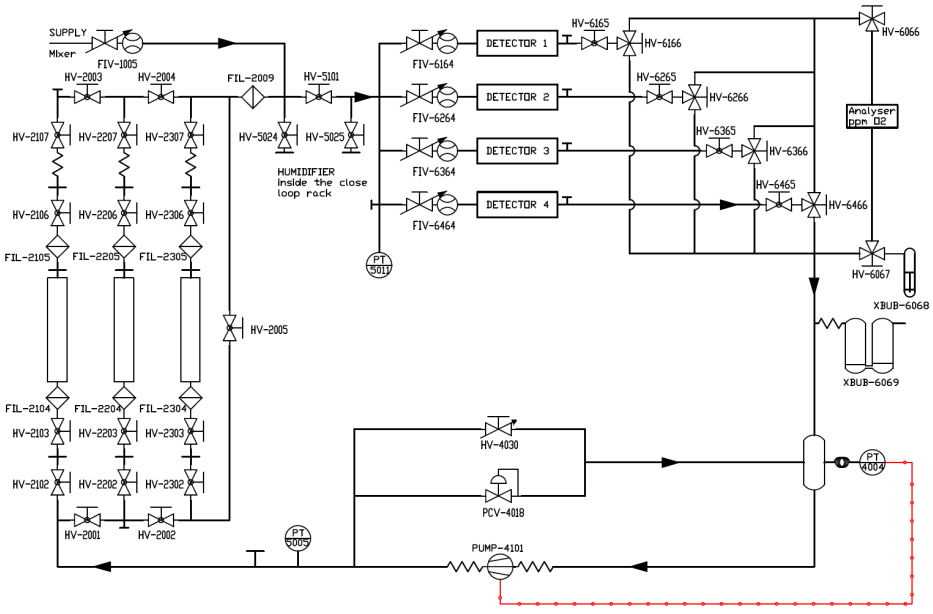

Figure 4.2: Scheme of the gas system [47].

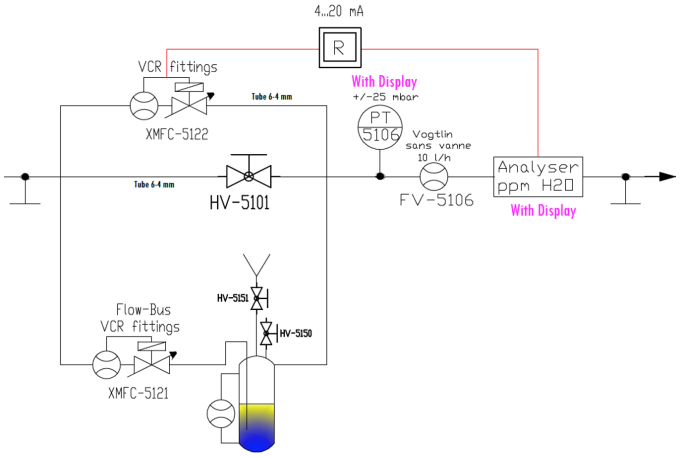

Figure 4.3: Scheme of the humidifier system.

regulated via dedicated software by setting the flow of the MFCs. In addition, a manual rotameter was installed for each line, allowing to further tune the gas flow sent to each chamber. Between the output of the mixer and the distribution lines there is an humidifier module that allows to inject some water vapor to reach a dew point of about 4 °C, that corresponds to a relative humidity of 40%. The module itself, which scheme is reported in Figure 4.3, consisted of two different lines: the first sent the gas from the mixer to the chambers without any change. This line was also referred to as the dry one. A second parallel gas line makes the gas bubble into a water volume, and it was referred to as the wet one. Both the dry and the wet lines were controlled by dedicated MFCs. The wet line was usually put to a 100% set point while the dry line was controlled through the Siemens LOGO! PLC software [47] and it was able to regulate the set point of the MFC by using a Proportional Integrative (PI) algorithm. On the return lines a gas analysis module could be used to measure the concentration of oxygen and water in the mixture. The presence of oxygen might indicate an air leak in some point of the gas distribution module. Instead, the water vapor level was constantly monitored to regulate the flow of the dry line in the humidifier module. To allow gas recirculation it was necessary to pump the gas back at the input point of the line. To do so, a pump module was installed inside the gas rack, that could be managed thanks to the logic module Siemens LOGO!. The pump adapt its speed in a way to maintain the system stable at the pressure set. Before being injected again into the loop, the gas could be sent into the purifier module. The module could be bypassed and it was made of three different cartridges, each one able to filter O_2 and H_2O from the mixture.

4.1.2 Detectors

Plastic scintillators

Plastic scintillators were used as a trigger for the muon beam. The GIF++ facility already had a combination of two scintillators (Figure 4.4) located on the beam line at the beginning and at the end of the bunker. However, the area covered by these scintillators was greater

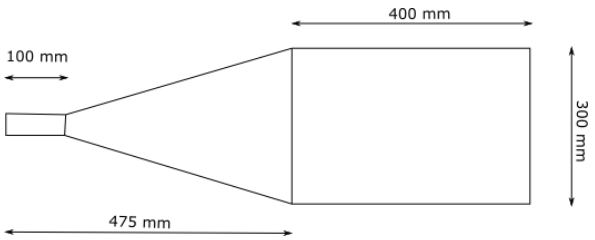

Figure 4.4: GIF++ facility scintillators.

than the sensitivity area of our RPCs, where the seven strips used for the readout were located. This could produce a decrease of the chamber efficiency due to a geometrical factor. To solve this problem, two other plastic scintillators (namely SCTOPG and SCBOTG, with an area of 20 cm x 42 cm) were used, aligned with the sensitive strips and located on the same trolley of RPCs. Then the coincidence of all the four scintillators was considered, being careful to check and correct the delay between all them. Finally, this coincidence was used as a trigger signal for the digitizer.

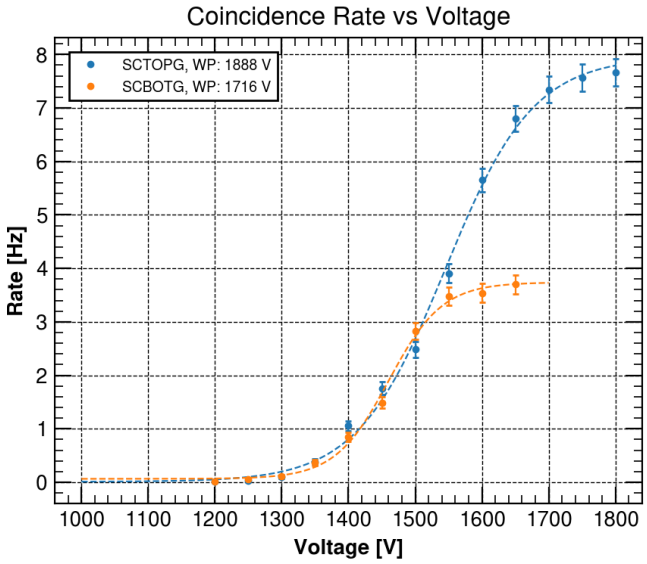

Figure 4.5: Results of scintillators characterization.

In order to find the working point for our scintillators, a complete characterization was done. The same approach and the same electronics reported in Section 3.1.2 were used. The signal of both the scintillators was observed with an oscilloscope in order to determine the starting voltage and the signal threshold. A threshold of 35 mV and the starting applied voltage of 1500 V were selected. The results obtained for the two scintillators are shown in Figure 4.5. The two scintillators present a different behavior. In particular, it is possible to notice that SCTOPG presents, at the working point, a double rate with respect to SCBOTG. This is probably due to an aging effect since these scintillators have been in

use for several years. However, for the purposes of the study this is not a big issue, since the spurious coincidences were removed thanks to the use of coincidences between the four scintillators. A working point value of 1700 V was choose for SCTOPG. This value was selected in order to avoid too high currents that could further damage this detector. For the same reason, for SCBOTG a working point value of 1600 V was selected. The currents at these working points are 374 μA and 351 μA, respectively for SCTOPG and SCBOTG.

RPCs

Figure 4.6: Different configurations of the chambers trolley.

Table 4.1: RPC 7, 8 and 10 characteristics.

RPC	**Length** [cm]	**Height** [cm]	**Strips pitch** [cm]	**Producer**	**Year**
7	70	100	2.1	General Tecnica	2019
8	70	100	2.6	Kodel University	2021
10	70	100	2.6	Kodel University	2021

Three different HPL RPCs (namely RPC 7, 8 and 10) were used. The characteristics of these detectors are reported in Table 4.1. These were vertically aligned between the scintillators and powered by a voltage supply[2]. The RPCs and the scintillators were located on a trolley that allowed to change the detectors orientation starting from a vertical position, used for the test beam and the long term study, to an horizontal position, used for data acquisition with cosmic rays. The two different configurations are shown in Figure 4.6. The signal readout was composed of seven copper strips for each RPC. All the strips, even those that were not used, are terminated with 50 Ω resistor on one side, and only the

[2]Mainframe: CAEN SY5527LC, RPCs board: CAEN A1526N, Scintillators board: AG7236DN.

signal strips were welded to LEMO cables with MCX connectors on the other side. Each RPCs was located in an aluminum frame that was connected to the ground. In order to be sure that every part of the frame was connected to the ground, we used a copper tape with a conductive glue applied between each different aluminum piece.

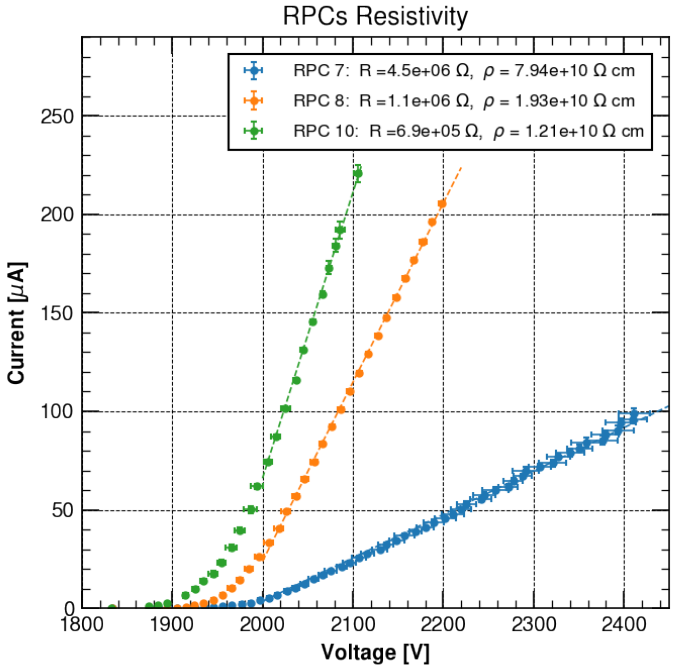

Figure 4.7: Results of resistivity characterization. The dashed line represents the linear fit result.

In order to characterize the RPCs, the HPL resistivity was measured with the same procedure reported in Section 3.1.2 by flushing the chambers with pure argon and recording several values of the current for different applied voltages in the range between 1000 V and 2500 V. For each applied voltage, the current mean value over one minute of data acquisition was taken as current value and the uncertainty given by the mean standard deviation. Then, the resistance value could be extrapolated by fitting the I-V curve in the region of the breakdown. Figure 4.7 shows the resistance and resistivity for the three RPCs, performed in September 2021. These data were taken in a dry argon gas configuration. Also in this case, the resistivity of the three chambers are in agreement with the expected resistivity values of the HPL, that should be in the range of $10^{10}\,\Omega$cm to $10^{11}\,\Omega$cm.

During the year, different resistivity measurements were done. This is important since a variation in the detector resistivity could bring a variation in the detector performance, *e.g.* in the working point, in the currents, in the charges produced or in the rate capability. All the measurements are reported in Table 4.2. The January measurements present higher resistivity values for RPC 8 and 10. This is probably due to a reduction of HPL humidity since during December all the chambers were opened to the air for the Christmas shutdown.

The resistivity of RPC 7 remained quite stable during all these months.

Table 4.2: RPC 7, 8 and 10 resistivity.

RPC	**August 2021** ρ [MΩ/cm^2]	**September 2021** ρ [MΩ/cm^2]	**January 2022** ρ [MΩ/cm^2]
7	77068 $\pm$ 1	79390 $\pm$ 2	77694 $\pm$ 6
8	21448 $\pm$ 1	19258 $\pm$ 1	32655 $\pm$ 2
10	13383 $\pm$ 40	12072 $\pm$ 20	14345 $\pm$ 40

4.1.3 Readout

LEMO cables were connected directly to a CAEN VME digitizer, in the same way as reported in Section 3.1.3. Usually RPC 7 was connected to the digitizer DT5730SB, while RPC 8 and RPC 10 were connected to the digitizer v1730. The coincidence between the four scintillators was used as a trigger signal and connected to one channel of each digitizer. The coincidence signal was duplicated by a FAN-IN FAN-OUT NIM module[3]. The digitizer was then connected via USB bridge to a pc. All this electronics were located inside the bunker, where a concrete alcove was present to minimize the length of cables and therefore the distortion of signals.

4.2 Data taking and analysis

The goal of test beam studies is to understand if the gas mixture under test has a similar behavior with respect to the STD one, also in a high gamma rate environment. In the laboratory several gas mixtures with a cosmic muons characterization were selected. During the muon beam time, three RPCs were flushed with one gas mixture at time and different attenuation factors for the ^{137}Cs source were set. This allows to control the gamma rate seen by the detectors and to study the efficiency of the gas mixture as a function of different gamma rays condition. Usually a cycle of several attenuation factors (between ABS 1.5 and ABS 220) was chosen and it is repeated for each gas mixture under test. Concerning the data taking, the working point of all the gas mixtures under test was already known from the laboratory studies. Then, the high voltage steps to use and the number of trigger events to record for each step were decided. For the purpose of this study, 5000-10000 trigger events were sufficient to study the behavior of the gas mixture.

The data were recorded by the digitizer and analyzed by `olefin` library in the same way as reported in Section 3.2. The only difference is related to the rate computation, not used in the laboratory analysis. For the rate computation, for each voltage step the largest time window (622340 samples) allowed by the digitizer was recorded. Then, the raw data were smoothed by a Savitzky-Golay filter in order to not consider the noise as peaks. The function `find_peaks`, present in the `scipy` library, allows to find the peaks and the heights

[3]LECROY 430.

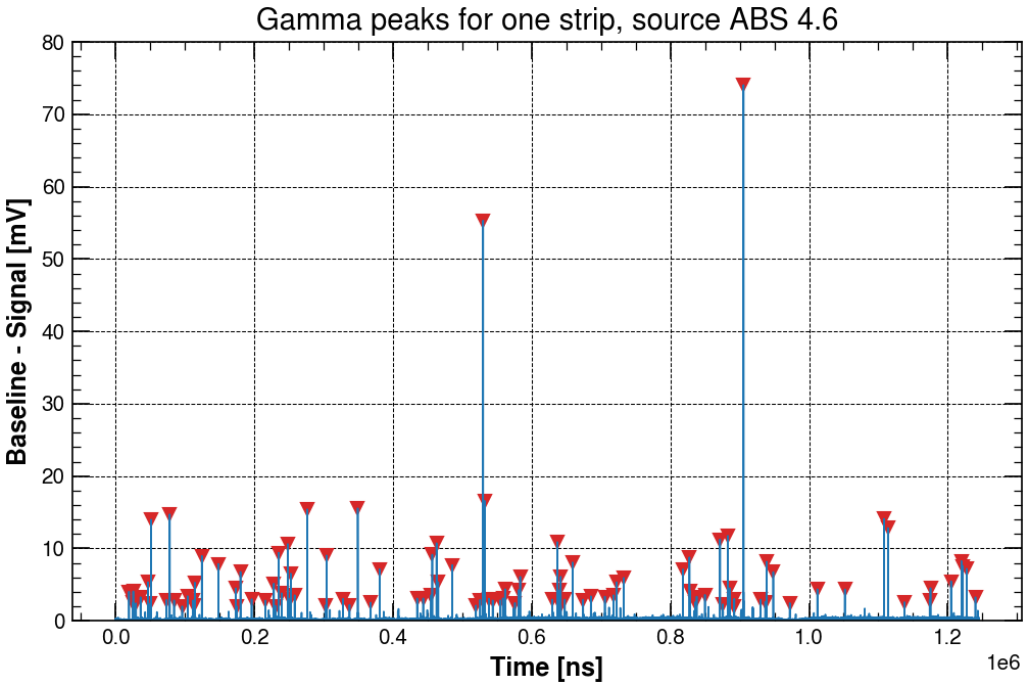

Figure 4.8: Example of rate analysis result. Red markers show the position of the detected peaks.

for each peak produced by the gamma rays. From the number of peaks, it is possible to find the rate simply dividing it for the area of the strips and for the time resolution of the digitizer and the record length of the time window. The rate uncertainty is calculated as the error on a Poissonian distribution with the bootstrap technique. Figure 4.8 shows an example of the rate analysis results.

4.3 Gas mixture characterization at the Test Beam

During the four muon beam time, eleven eco-friendly gas mixtures were tested. The different test beam will be identified by the name of the month in which they took place: July, September, October and November 2021. For each test beam, a RPCs characterization with the STD gas mixture was done. Not in all the test beams it was possible to take data with all the three RPCs, due to some problems that occurred. In particular, in the test beam of July, only RPC 7 was ready to take data. Different attenuation factors of the gamma source were used. Moreover between the test beams there were some changes in the set up position. In fact, all the main features were presented as a function of the detector rate, that is directly connected to the level of the detector irradiation.

It is important to notice that the chamber rate depends not only on the gamma irradiation level, but also on the gas mixture and detector sensitivity to this irradiation. This issue was investigated in the October and November test beams. To do so, data about

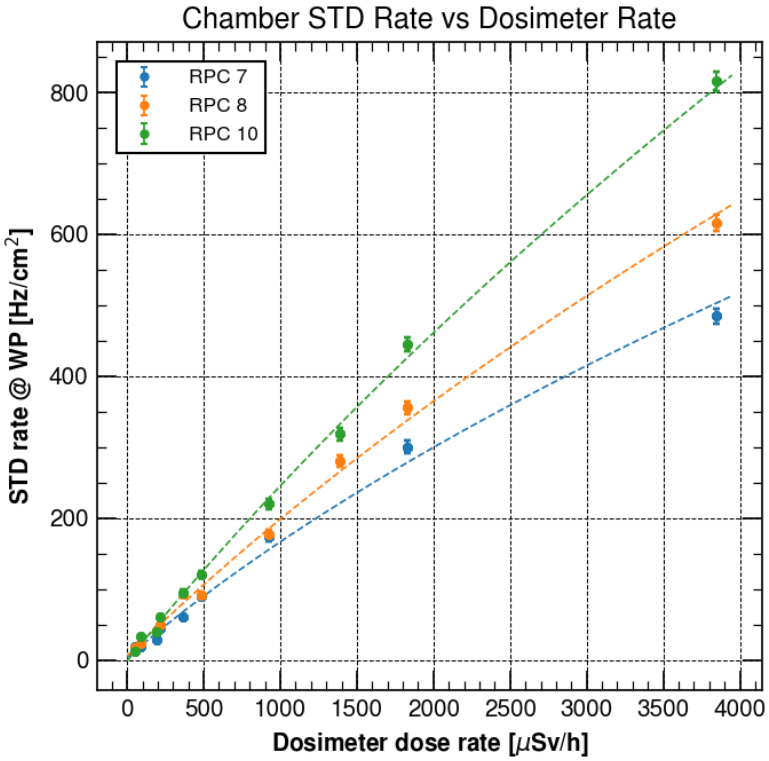

Figure 4.9: RPC gamma rate for the STD gas mixture as a function of the dosimeter dose rate. The fit is represented by the dashed line.

the gamma dose rate were collected with a dosimeter[4] located on the detectors trolley. The dosimeter data are independent from the RPC gamma rates, so it depends only on the irradiation level and not on the gas mixture or the RPC. The gamma dose rate was collected for each combination of upstream and downstream filter attenuations used during our data taking. After that, It was possible to find a match between the dosimeter rate and the RPC gamma rate for the STD gas mixture, which was used as a reference. To do so, the RPC gamma rate for the STD gas mixture was plotted as a function of the dosimeter dose rate, for all the three chambers, as shown in Figure 4.9. Then the following fit function was used in order to modeling the data:

$$f(x) = \sqrt{ax + b} + c$$

Finally, for each RPC the inverse fit function was used in order to convert, for each tested gas mixture, the dosimeter dose rates into the standard gas mixture rate, that is now independent from the specific gas mixture. These studies are ongoing and from the initial results the difference that this correction brings to the data analysis is negligible. For this reason, in the next sections only the RPC gamma rate not corrected will be considered.

[4]Mirion RDS-31ITX.

In the following sections the results and the analysis of the different gas mixtures tested were reported.

4.3.1 Standard gas mixture characterization

For all the test beams a characterization of the RPCs with the STD gas mixture was done and it was used for comparison with the other gas mixtures. Several attenuation factors for the gamma source were used ranging from 0 Hz/cm^2 to 800 Hz/cm^2. Figure 4.10, Figure 4.11 and Figure 4.12 show the efficiency and the streamer probability curves as a function of the effective voltage. From these plots it is possible to see that there is a decrease in maximum efficiency as the intensity of the source increases. Moreover the efficiency curves are shifted to higher effective voltage. This is a well known effect due to the high currents that flows inside the chambers gap. Increasing currents correspond to a more significant voltage drop across the resistive electrodes. This voltage drop decreases the effective electric field inside the gap, leading to a smaller efficiency of the detector:

$$HV_{gap} = HV_{applied} - R_{electrodes}\, I_{gap} \tag{4.1}$$

Inverting this formula and knowing the value of the HPL resistivity, it is possible to apply a correction on the data.

From Figure 4.10, Figure 4.11 and Figure 4.12, it is possible to see that the three detectors behavior changed a bit over time. This is the same issue of the laboratory detectors (RPC 9 and 11) since all the three RPCs were new and the commissioning had just finished. The detector that presents the biggest change is RPC 7, in particular as concerns the working point, shown in figure 4.13. RPC 7 was initially tested in the laboratory without the humidifier module that was under construction. When this detector started ti be used at GIF++ , it was always used in combination with humidified gas mixtures, which may have resulted in a reduction over time in its resistivity. However, RPC 9 and 10 show no significant changes between the various test beams.

In order to analyze the data, it is useful to consider the main features as a function of the detector gamma rate. In Figure 4.13-4.18, all these data for the STD gas mixture are shown. It is possible to start considering the working point as a function of the detector gamma rate, shown in Figure 4.13. It is possible to see that there is a dependence on the chamber resistivity, due to the voltage drop reported in Equation 4.1. The greater the resistivity of the chamber, the more the working point seems to increase linearly as a function of the chamber rate. RPC 7 has a perfectly linear trend, while it is only slightly visible in RPC 8 and absent in RPC 10. Concerning the maximum efficiency, shown in Figure 4.14, it has the same behavior for the three RPCs and for all the test beams, since it decreases when the gamma rays intensity increases. From Figure 4.10-4.12 it is possible to see that the streamer probability decrease when the gamma rays intensity increases. This is not a real physical effect but it is an artifact due to data analysis. In fact it is difficult to distinguish between a gamma signal and an avalanche signal, and this brings to a wrong computation of the streamer probability. For this reason, in the following sections the streamer probability will be not considered. The avalanche charge has a linear trend as a function of the detector rate, as Figure 4.15 shows, for all the three RPCs but with some differences between the test beams for RPC 7. This difference can be related with the decreasing of RPC 7 resistivity due to the use of the humidifier. Indeed, it is possible to see

that the more time this detector spends in the facility, hence connected to the humidifier module, the greater the charges become. The time resolution, shown in Figure 4.16, is the same for all the test beams and for all the RPCs. It is around 2 ns at the working point. The difference in the bulk resistivity brings to a different behavior for different RPCs as concerns the cluster size. However, its values stay below 1.5 strips in all the cases and this is the results expected from the standard gas mixture. Figure 4.18 shows the currents as a function of the rate. It is possible to see that the currents increase linearly as the rate increase.

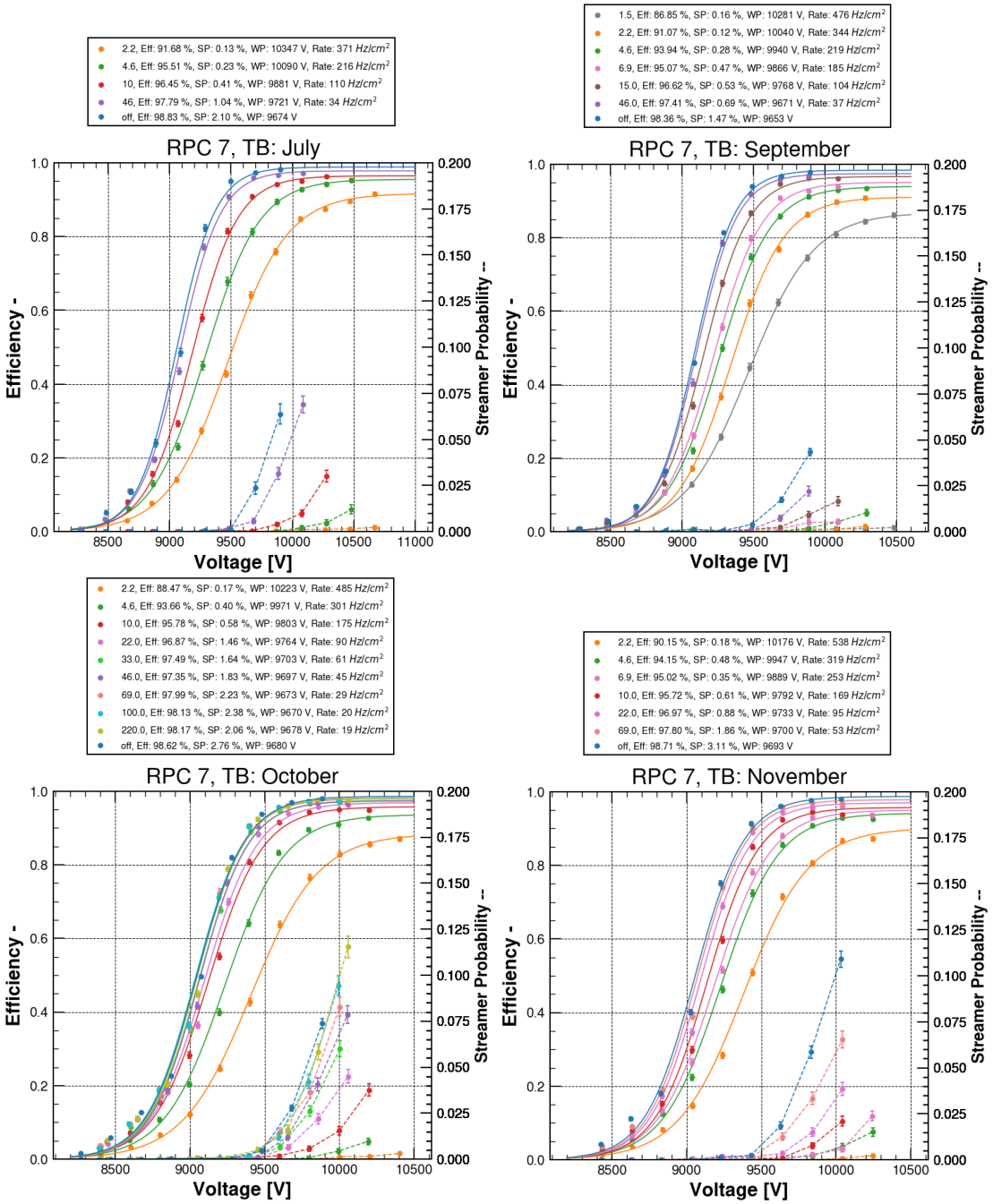

Figure 4.10: STD gas mixture and RPC 7: efficiency (continuous line) and streamer probability at source off (dashed line) for all the test beam.

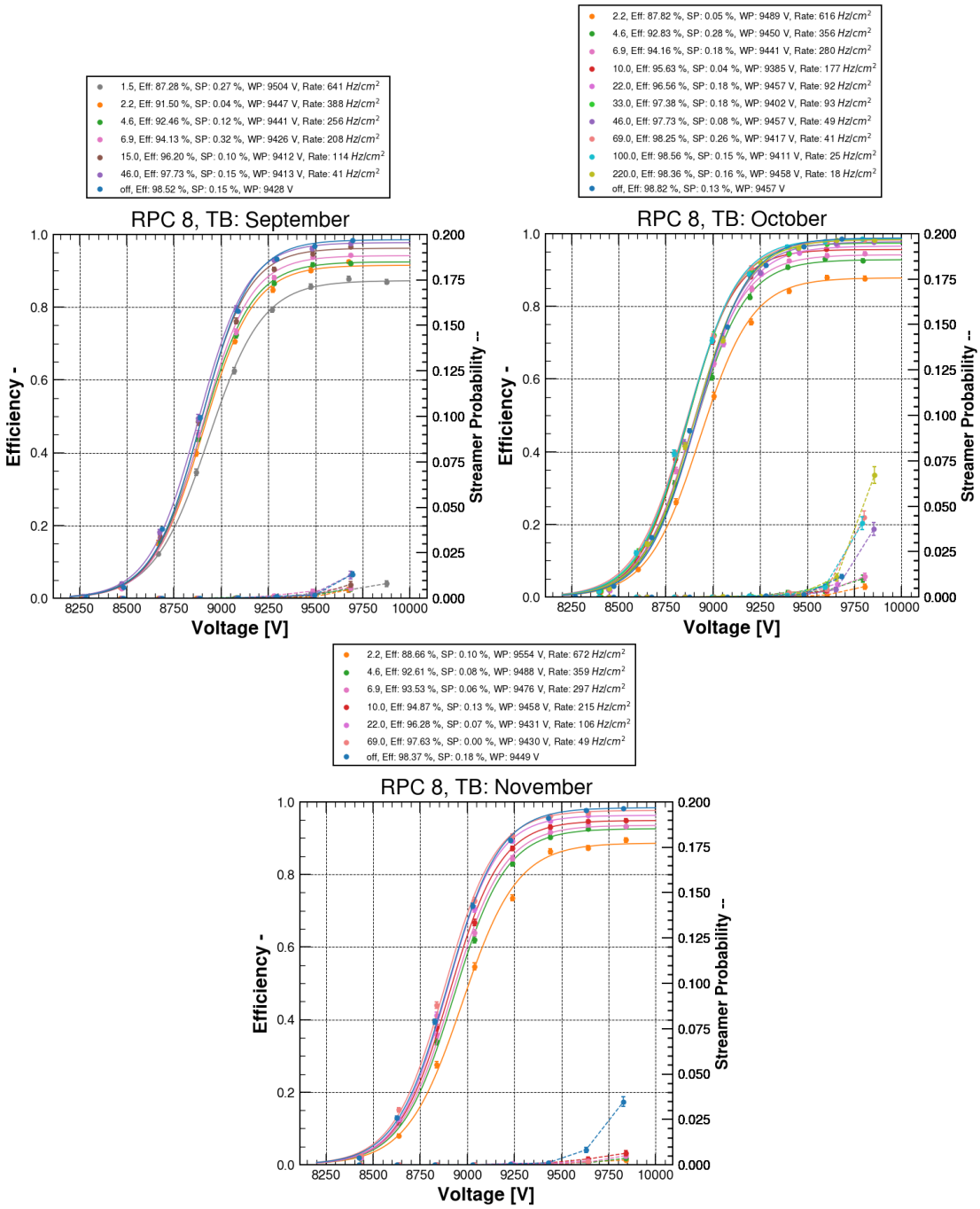

Figure 4.11: STD gas mixture and RPC 8: efficiency (continuous line) and streamer probability at source off (dashed line) for all the test beam.

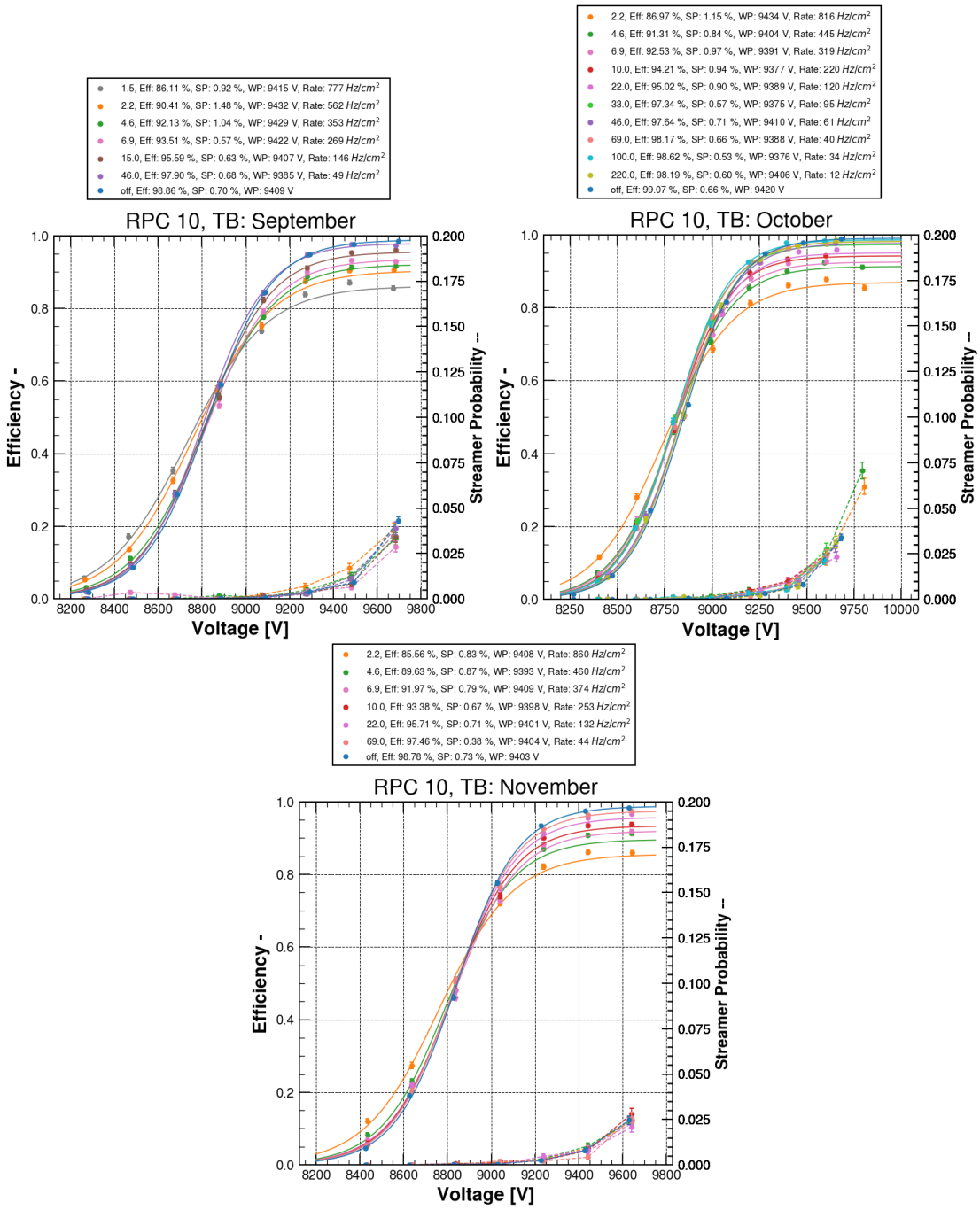

Figure 4.12: STD gas mixture and RPC 10: efficiency (continuous line) and streamer probability at source off (dashed line) for all the test beam.

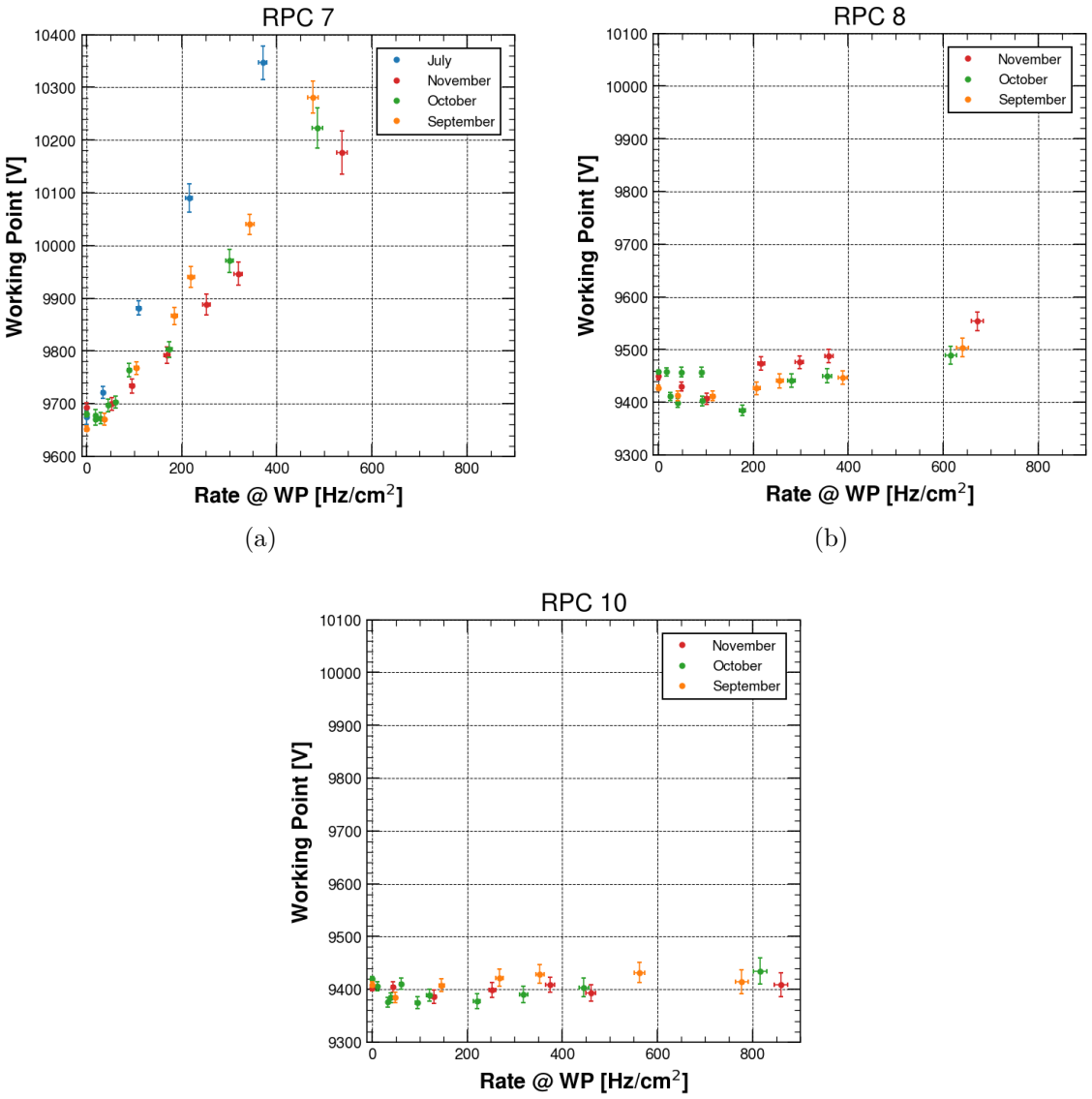

Figure 4.13: Working point as a function of the detector rate for RPC 7 (a), RPC 8 (b) and RPC 10 (c) operated with STD gas mixture in the four test period periods.

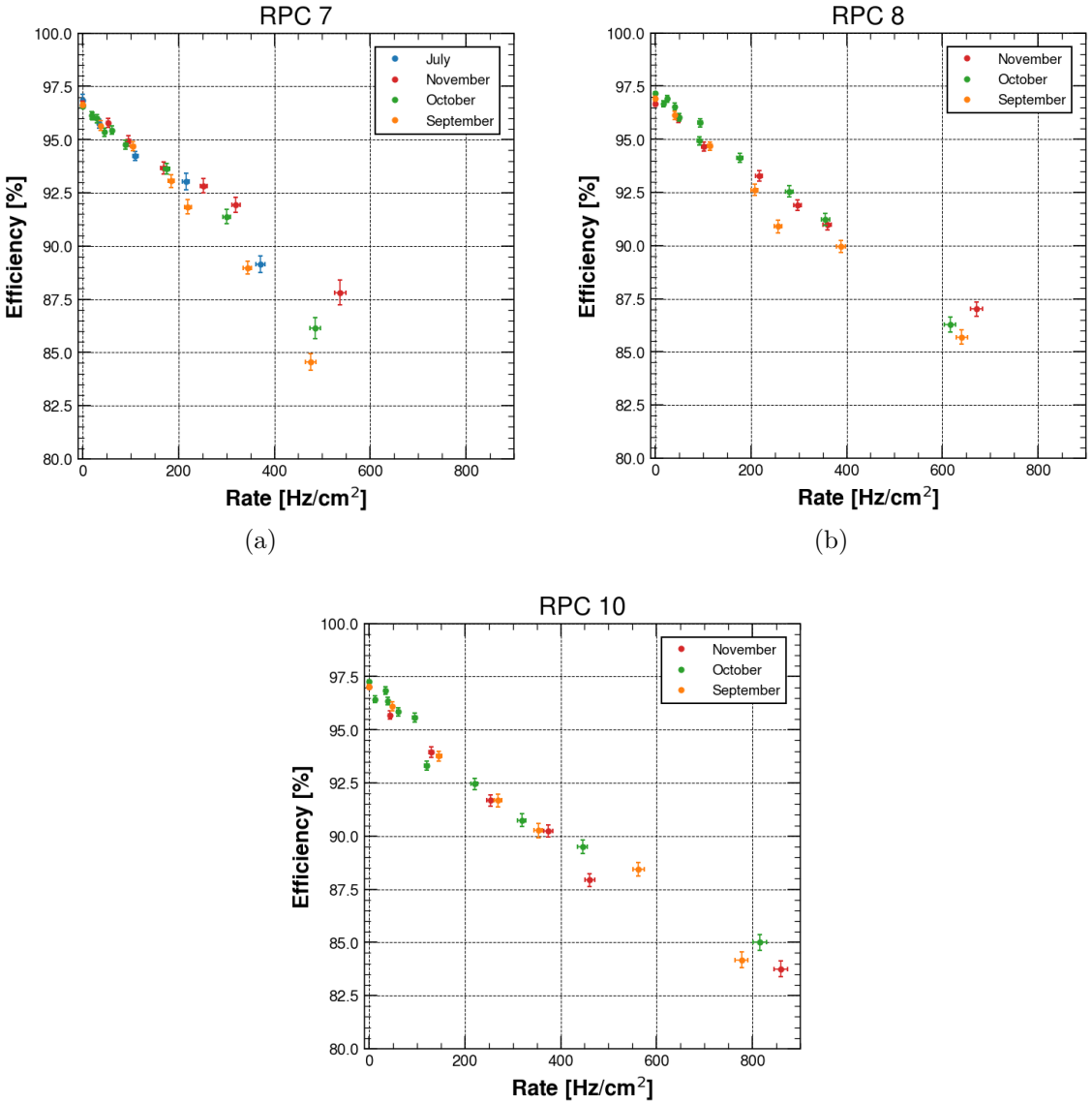

Figure 4.14: Maximum efficiency as a function of the detector rate for RPC 7 (a), RPC 8 (b) and RPC 10 (c) operated with STD gas mixture in the four test period periods.

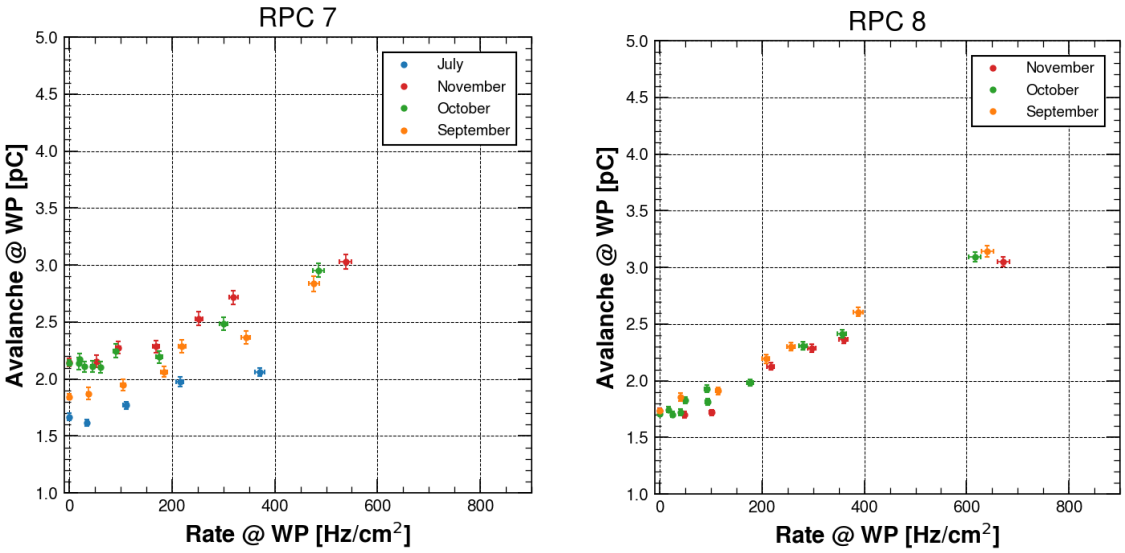

(a)

(b)

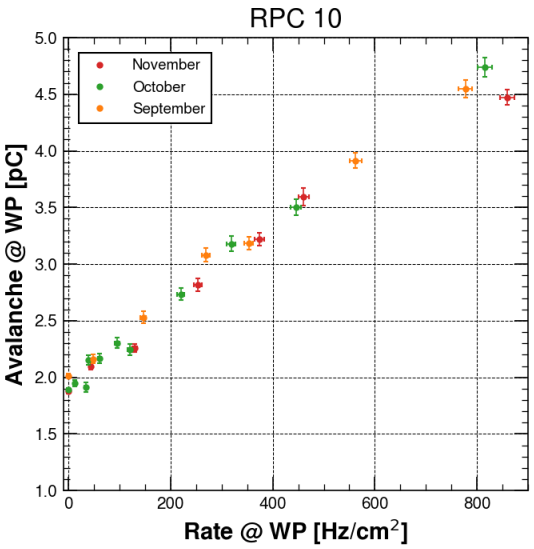

(c)

Figure 4.15: Avalanche charge as a function of the detector rate for RPC 7 (a), RPC 8 (b) and RPC 10 (c) operated with STD gas mixture in the four test period periods.

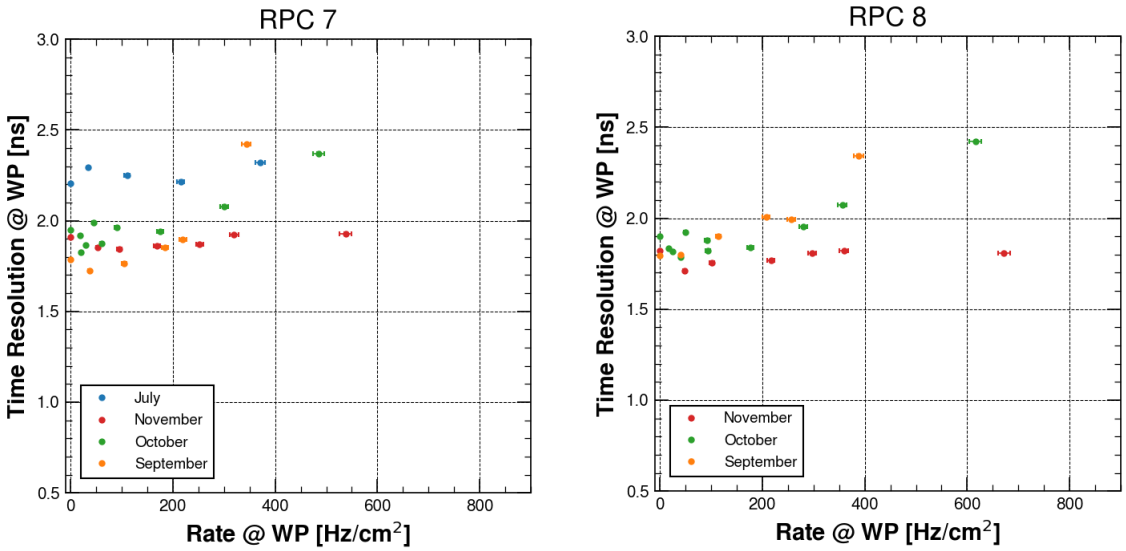

(a)

(b)

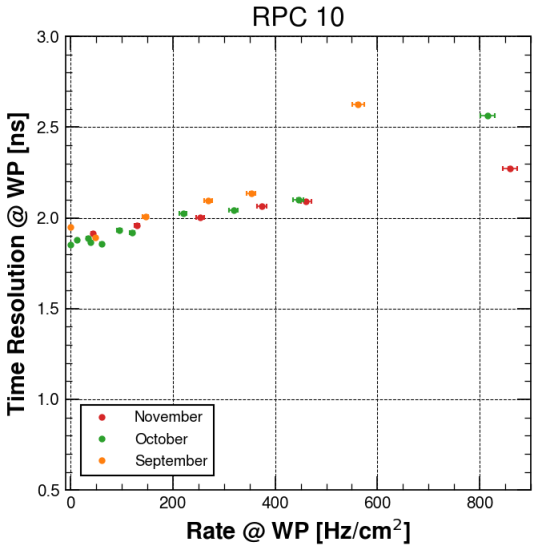

(c)

Figure 4.16: Time resolution as a function of the detector rate for RPC 7 (a), RPC 8 (b) and RPC 10 (c) operated with STD gas mixture in the four test period periods.

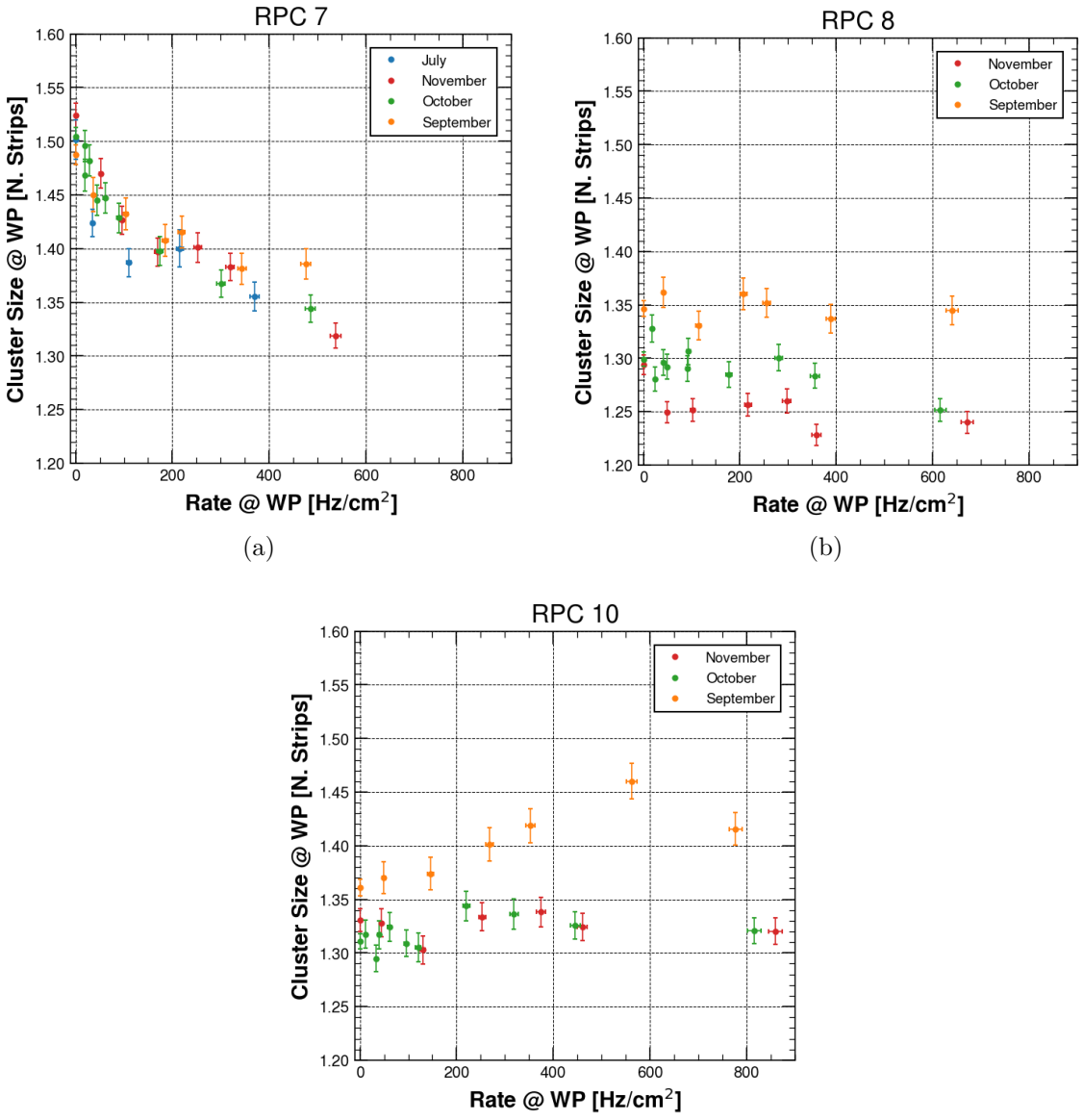

Figure 4.17: Cluster size as a function of the detector rate for RPC 7 (a), RPC 8 (b) and RPC 10 (c) operated with STD gas mixture in the four test period periods.

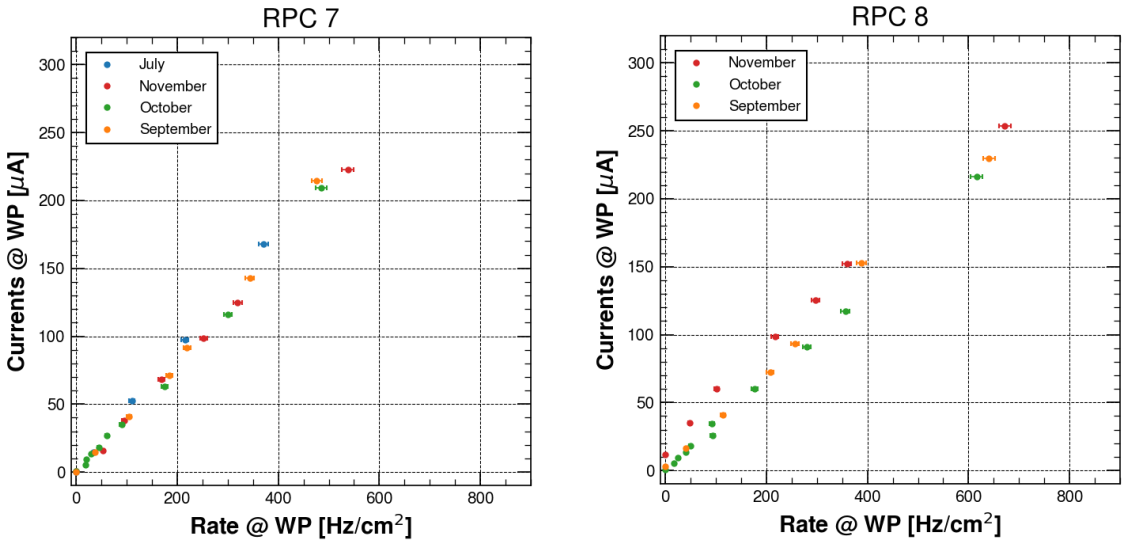

(a)

(b)

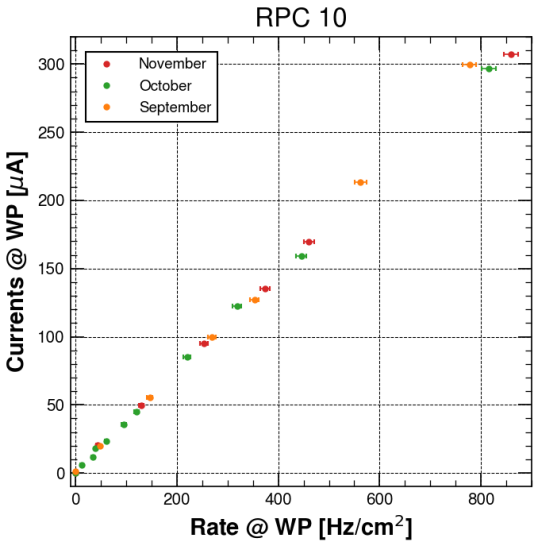

(c)

Figure 4.18: Currents as a function of the detector rate for RPC 7 (a), RPC 8 (b) and RPC 10 (c) operated with STD gas mixture in the four test period periods.

4.3.2 Addition of He or CO_2 to the STD gas mixture

From Section 3.3.2 and Section 3.3.3, two gas mixtures were selected in order to verify the detector performance under high background gamma rate in presence of the muon beam. In particular, the two He 30% and CO_2 30% gas mixtures with 0.3% SF_6 concentration were chosen. This allows to have a direct comparison with respect to the STD gas mixture, since it presents the same SF_6 concentration. Then the two best He 30% and CO_2 30% gas mixtures with 1% of SF_6 concentration were selected. Also the He 40% gas mixture with 1% of SF_6 concentration was tested. The latter gas mixture was already tested in the laboratory with a 0.3% SF_6 concentration. However, from the laboratory data, it is possible to notice that the behavior of the charge distribution changes significantly for He concentration greater than 30%, as it is possible to see from Figure 4.19a that shows the charge distribution for a He concentration of 20%, 30%, 40% and 50% with a SF_6 concentration of 0.3%. The SF_6 concentration was increased from 0.3% to 1%, in order to reduce the charge developed inside the detector gaps, as it is possible to see from Figure 4.19b.

Table 4.3 shows all the gas mixture tested at GIF++ with the respective GWP_{100}.

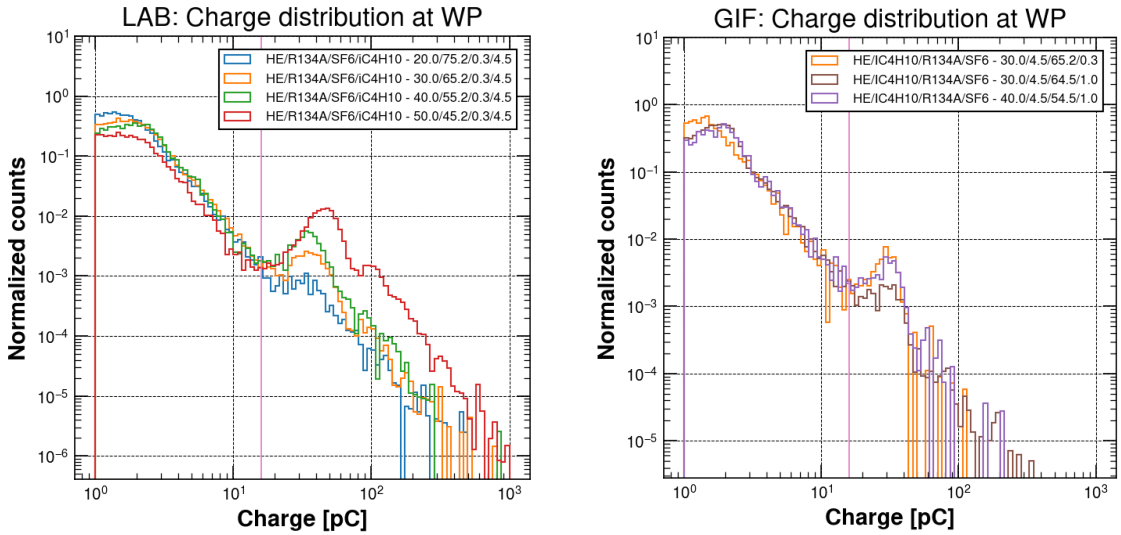

(a) (b)

Figure 4.19: Charge distribution for different He and SF_6 concentrations as substitute of R134a in the STD gas mixture.The vertical line represents the charge threshold (16 pC) that allows to distinguish an avalanche signal from a streamer signal. (a) Laboratory data with RPC 4 (General Tecnica, 2016); (b) Test beam data at source off with RPC 7.

For each gas mixture tested, the comparison of RPC performance is done with respect to the STD gas mixture features. Table 4.4, Table 4.6 and Table 4.8 report the STD gas mixture main features for the three RPCs. Detector performance at source off are

Table 4.3: GWP_{100} for He and CO_2 test beam gas mixtures.

	R134a [%]	**He** [%]	**CO_2** [%]	**SF_6** [%]	**iC_4H_{10}** [%]	**GWP_{100}**
STD	95.2	0	0	0.3	4.5	3384
He 30% SF_6 0.3%	65.2	30	0	0.3	4.5	2390
CO_2 30% SF_6 0.3%	65.2	0	30	0.3	4.5	2390
He 30% SF_6 1%	64.5	30	0	1	4.5	2896
CO_2 30% SF_6 1%	64.5	0	30	1	4.5	2896
He 40% SF_6 1%	54.5	40	0	1	4.5	2564

studied using only the muon beam with the source completely shielded ("source off", so with a gamma rate of 0 Hz/cm^2). The errors on the features are obtained with the error propagation starting from the fit errors. However, it is important to estimate the main detector features at a detector rate of about 600 Hz/cm^2, since this is the expected detector rate for HL-LHC Phase of ATLAS and CMS RPC systems [48, 49]. Data were collected with different source filters, so different detector rates, and then the main RPC features were studied as a function of the detector rate. For the working point, the maximum efficiency and the currents it is possible to use, for simplicity, a linear regression in order to extrapolate their values at 300 Hz/cm^2 and 600 Hz/cm^2. From data and from the fit errors, it is possible to see that the linear regression seems to be a good approximation (Figure 4.20), although the trend of the data could be described by other types of functions. Also in this case, the error was extrapolated from the covariance matrix as the mean standard deviation. However, these values are an underestimation of the uncertainty, since these do not consider some source of uncertainty, such as the effective voltage one or the one due to the linear approximation.

The main features at source off and at a detector rate of 300 Hz/cm^2 and 600 Hz/cm^2 for all the gas mixture tested were extrapolated in the same way. These features values are reported in Appendix A.1.

In order to effectively analyze the data, it is possible to consider the difference between the detector performance with the STD gas mixture and the performance of each gas mixture tested. These data are shown in Table 4.5, Table 4.7 and Table 4.9. In order to avoid an underestimate of the errors, they are computed for each difference as the sum between errors of the STD gas mixture features and the gas mixtures under test. These data are then summarized in Figure 4.21, in which each parameter is considered as a function of RPC and gas mixture.

Figure 4.22 and Figure 4.23 show the cluster size and the time resolution as a function of the rate. In this case it is not possible to extrapolate the features at a detector rate of 300 Hz/cm^2 and 600 Hz/cm^2 from a linear approximation, since the trend is clearly not linear.

Before analyzing the data, some considerations are necessary. First of all, the He 30% SF_6 0.3% gas mixture was tested only during the July test beam, in which only RPC 7 was ready to take data. Moreover, the ohmic currents of RPC 8 increased between the October and November test beam, from 0.8 μA to 11.7 μA for source off, probably due to

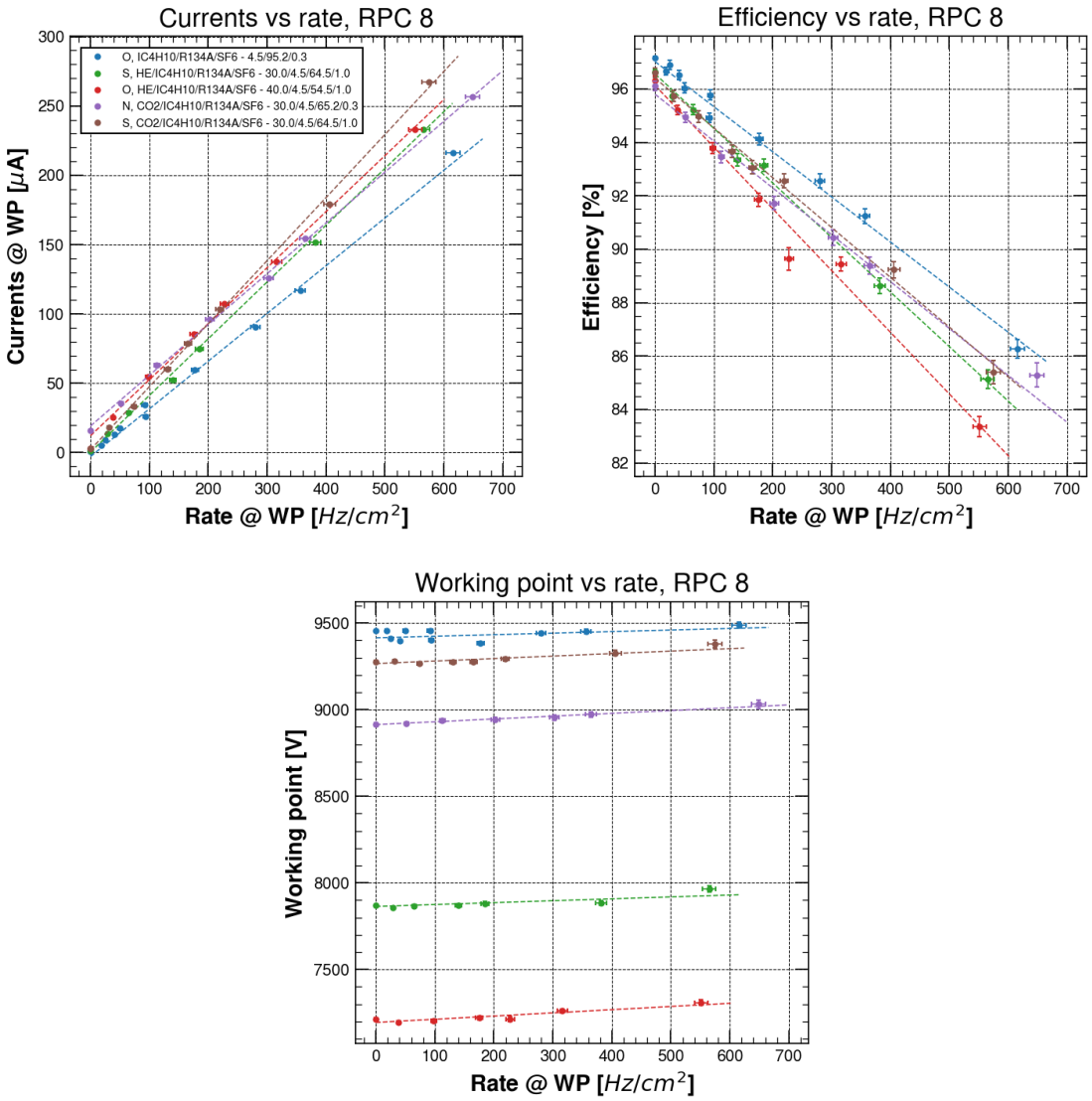

Figure 4.20: Example for RPC 8 of linear approximation for currents, maximum efficiency and working point as a function of the rate.

a too high gamma rate background for a few days.

It is possible to consider the working point. From Figure 4.21 (data also reported in Table 4.5, Table 4.7 and Table 4.9), it is possible to see that all the gas mixtures tested present a lower or compatible working point with respect to the STD gas mixture, for rate values of 0 Hz/cm^2, 300 Hz/cm^2 and 600 Hz/cm^2. In particular, the CO_2 30% SF_6 1% has the most similar working point with respect to the STD gas mixture and the He 40% SF_6 1% gas mixture has the lowest working point (about -2200 V). The bigger differences as the rate varies are for RPC 7, while for RPC 8 and 10 the differences are below 100 V. The only exception is the RPC 7 working point for the CO_2 30% SF_6 0.3% gas mixture that has the opposite behavior to that expected, since the difference decreases as the detector

rate increases. This could be produced by some statistical issue related to the estimation of the working point from the sigmoid fit. However, for all the gas mixtures it seems that the increase in the detector rate does not lead to problematic increases in the value of the working point.

Then it is possible to consider the maximum efficiency. From Figure 4.21, it is possible to see that all the gas mixtures that have 1% SF_6 concentration present the bigger efficiency drop, between -4% and -6% for a detector rate of 600 Hz/cm^2. Instead, the gas mixtures with the 0.3% SF_6 concentration present an efficiency drop between -2% and -3% for a detector rate of 600 Hz/cm^2. It is possible to see that this efficiency drop is related to the RPC resistivity, since bigger is the HPL resistivity, bigger is the maximum efficiency drop. The CO_2 30% SF_6 0.3% and the He 30% SF_6 0.3% gas mixture have the same behavior as what concern the maximum efficiency. Also the He 30% SF_6 1% gas mixture and He 40% SF_6 1% gas mixture present the same behavior. So, an increase of the 10% of He doesn't affect the detector efficiency drop. Also in this case, the CO_2 30% SF_6 1% gas mixtures and the He 30% SF_6 1% gas mixture have the same behavior. Therefore it is possible to affirm that for a concentration of the 30%, the CO_2 and the He affect in the same way the maximum efficiency.

The bigger efficiency drop for the SF_6 1% gas mixtures could be related to the currents increase, as it is possible to see from Figure 4.21. This current increase could bring to a bigger charge development inside the detector gap, which leads to a reduction of the efficiency due to the higher occupation of the detector. Another explanation of the bigger efficiency drop could be related to the loss of signal sensitivity due to the higher SF_6 concentration. In this case the higher currents must be more produced by the ionic part than the electronic part of the currents.

However, all the gas mixtures have higher values of the currents with respect to the STD gas mixture. If the He 30 SF_6 1% and the CO_2 30% SF_6 1% gas mixtures are compared, it is possible to see that the He gas mixture has lower currents with respect to the CO_2 gas mixture. Instead, for the same gas mixture but with the 0.3% SF_6 concentration, the currents are similar.

Then it is possible to consider the cluster size, shown in Figure 4.22. For RPC 7 the cluster size decreases as the detector rate increases, while for RPC 8 and 10 it seems constant. The different behaviors is probably caused by the different strips pitch: 2.1 cm for RPC 7 and 2.6 cm for RPC 8 and 10. In any case, the cluster size seems to be higher for the gas mixtures that have the 1% SF_6 concentration and 30% He or CO_2 concentration, while it seems lower for the He 40% gas mixture.

If the time resolution is considered, shown in Figure 4.23, it is possible to see that there is not a common behavior of the different gas mixtures and for the different RPCs. In general, the time resolution increases as the detector rate increases, remaining however below 2.6 ns.

Table 4.4: Main features for the STD gas mixtures and RPC 7 valued at source off, at a detector rate of 300 Hz/cm^2 and 600 Hz/cm^2.

Gas mixture	**RPC 7**	**Source OFF**	**300 Hz/cm^2**	**600 Hz/cm^2**	**Δ 300 Hz/cm^2**	**Δ 600 Hz/cm^2**
STD	Working point [V]	9680 ± 5	9973 ± 26	10304 ± 49	293 ± 31	624 ± 54
October	Maximum efficiency [%]	96.6 ± 0.1	90.8 ± 0.5	85.1 ± 0.9	-5.7 ± 0.6	-11 ± 1
	Currents at WP [μA]	0.3 ± 0.4	123 ± 6	246 ± 10	123 ± 6	245 ± 10

Table 4.5: Features difference between the STD gas mixture and He, CO_2 gas mixtures, evaluated at source off and at a detector rate of 300 Hz/cm^2 and 600 Hz/cm^2 for RPC 7.

Gas mixture	**RPC 7**	**Δ STD at OFF**	**Δ STD at 300 Hz/cm^2**	**Δ STD at 600 Hz/cm^2**
He 30% SF_6 0.3%	Working point [V]	-1928 ± 13	-1839 ± 82	-1765 ± 155
July	Maximum efficiency [%]	-0.4 ± 0.2	-2 ± 1	-3 ± 2
	Currents at WP [μA]	-0.2 ± 0.9	9 ± 13	21 ± 22
CO_2 30% SF_6 0.3%	Working point [V]	-552 ± 16	-597 ± 44	-666 ± 82
November	Maximum efficiency [%]	-0.6 ± 0.3	-1.4 ± 0.7	-2 ± 1
	Currents at WP [μA]	0 ± 2	3 ± 10	9 ± 17
He 30% SF_6 1%	Working point [V]	-1612 ± 11	-1523 ± 55	-1469 ± 105
September	Maximum efficiency [%]	-0.6 ± 0.2	-3 ± 1	-6 ± 3
	Currents at WP [μA]	-0.2 ± 0.6	14 ± 9	31 ± 15
CO_2 30% SF_6 1%	Working point [V]	-188 ± 17	-35 ± 45	90 ± 85
September	Maximum efficiency [%]	-0.5 ± 0.3	-2 ± 1	-4 ± 2
	Currents at WP [μA]	-0.1 ± 0.6	31 ± 10	65 ± 17
He 40% SF_6 1%	Working point [V]	-2304 ± 14	-2286 ± 31	-2302 ± 59
October	Maximum efficiency [%]	-0.8 ± 0.3	-2.8 ± 0.8	-5 ± 1
	Currents at WP [μA]	-0.1 ± 0.7	15 ± 8	31 ± 13

Table 4.6: Main features for the STD gas mixtures and RPC 8 valued at source off, at a detector rate of 300 Hz/cm^2 and 600 Hz/cm^2.

Gas mixture	**RPC 8**	**Source OFF**	**300 Hz/cm^2**	**600 Hz/cm^2**	**Δ 300 Hz/cm^2**	**Δ 600 Hz/cm^2**
STD	Working point [V]	9457 ± 4	9441 ± 31	9468 ± 54	-16 ± 34	11 ± 57
October	Maximum efficiency [%]	97.2 ± 0.1	92.0 ± 0.3	86.9 ± 0.6	-5.2 ± 0.4	-10.3 ± 0.6
	Currents at WP [μA]	0.8 ± 0.3	100 ± 3	204 ± 5	100 ± 3	203 ± 6

Table 4.7: Features difference between the STD gas mixture and He, CO_2 gas mixtures, evaluated at source off and at a detector rate of 300 Hz/cm^2 and 600 Hz/cm^2 for RPC 8.

Gas mixture	**RPC 8**	**Δ STD at OFF**	**Δ STD at 300 Hz/cm^2**	**Δ STD at 600 Hz/cm^2**
CO_2 30% SF_6 0.3%	Working point [V]	-545 ± 13	-481 ± 39	-456 ± 68
November	Maximum efficiency [%]	-1.1 ± 0.3	-1.4 ± 0.7	-1 ± 1
	Currents at WP [μA]	15 ± 1	28 ± 7	35 ± 11
He 30% SF_6 1%	Working point [V]	-1588 ± 8	-1544 ± 43	-1538 ± 77
September	Maximum efficiency [%]	-0.5 ± 0.2	-1.5 ± 0.5	-2.6 ± 0.9
	Currents at WP [μA]	0.5 ± 0.5	23 ± 5	42 ± 9
CO_2 30% SF_6 1%	Working point [V]	-181 ± 12	-132 ± 42	-116 ± 74
September	Maximum efficiency [%]	-0.6 ± 0.2	-1.1 ± 0.6	-2 ± 1
	Currents at WP [μA]	2.0 ± 0.5	38 ± 6	71 ± 10
He 40% SF_6 1%	Working point [V]	-2240 ± 11	-2185 ± 46	-2154 ± 81
October	Maximum efficiency [%]	-0.6 ± 0.2	-1.1 ± 0.6	-2 ± 1
	Currents at WP [μA]	2.0 ± 0.5	38 ± 6	71 ± 10

Table 4.8: Main features for the STD gas mixtures and RPC 10 valued at source off, at a detector rate of 300 Hz/cm^2 and 600 Hz/cm^2.

Gas mixture	**RPC 10**	**Source OFF**	**300 Hz/cm^2**	**600 Hz/cm^2**	**Δ 300 Hz/cm^2**	**Δ 600 Hz/cm^2**
STD	Working point [V]	9420 ± 4	9396 ± 12	9408 ± 21	-24 ± 16	-12 ± 25
October	Maximum efficiency [%]	97.3 ± 0.1	91.8 ± 0.6	87 ± 1	-5.5 ± 0.7	-10 ± 1
	Currents at WP [μA]	0.3 ± 0.5	111 ± 2	219 ± 3	111 ± 2	218 ± 3

Table 4.9: Features difference between the STD gas mixture and He, CO_2 gas mixtures, evaluated at source off and at a detector rate of 300 Hz/cm^2 and 600 Hz/cm^2 for RPC 10.

Gas mixture	**RPC 10**	**Δ STD at OFF**	**Δ STD at 300 Hz/cm^2**	**Δ STD at 600 Hz/cm^2**
CO_2 30% SF_6 0.3%	Working point [V]	-532 ± 14	-522 ± 27	-531 ± 44
November	Maximum efficiency [%]	-0.8 ± 0.3	-1 ± 1	-1 ± 2
	Currents at WP [μA]	0 ± 2	13 ± 6	23 ± 8
He 30% SF_6 1%	Working point [V]	-1552 ± 8	-1520 ± 30	-1516 ± 54
September	Maximum efficiency [%]	-0.3 ± 0.2	-1 ± 1	-1 ± 2
	Currents at WP [μA]	0.3 ± 0.7	13 ± 4	27 ± 7
CO_2 30% SF_6 1%	Working point [V]	-147 ± 14	-128 ± 23	-132 ± 40
September	Maximum efficiency [%]	-0.5 ± 0.2	-0.5 ± 0.8	-1 ± 1
	Currents at WP [μA]	1.4 ± 0.9	34 ± 4	68 ± 6
He 40% SF_6 1%	Working point [V]	-2239 ± 11	-2211 ± 19	-2214 ± 32
October	Maximum efficiency [%]	-0.6 ± 0.2	-1 ± 1	-2 ± 2
	Currents at WP [μA]	-0.2 ± 0.8	9 ± 3	20 ± 5

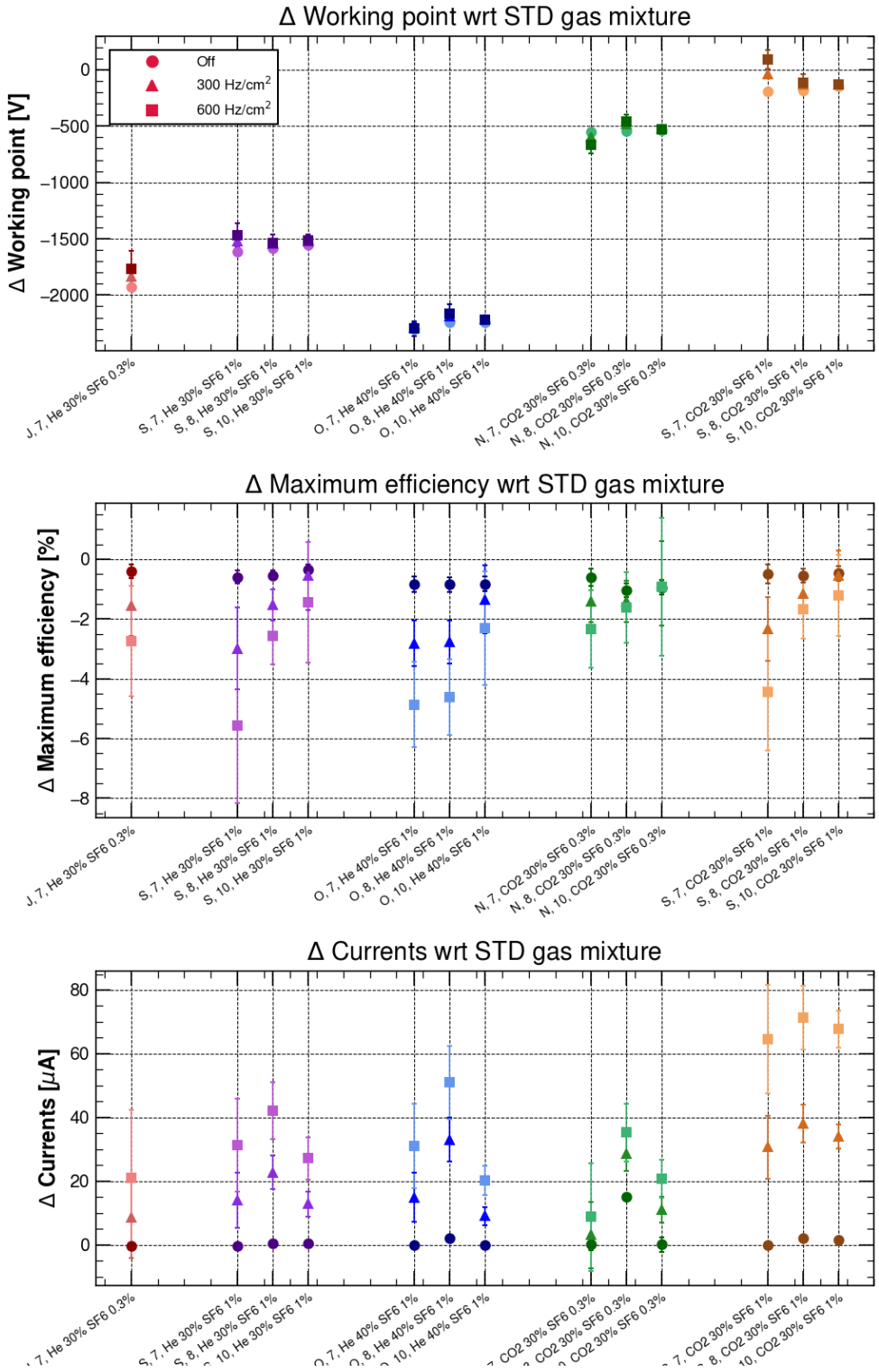

Figure 4.21: Difference between the STD gas mixture and the He, CO_2 gas mixtures as a function of the RPC and the gas mixture for the working point, efficiency and currents. On the x-axis, the letter represents the initial of the month in which the test beam started, followed by the RPC number.

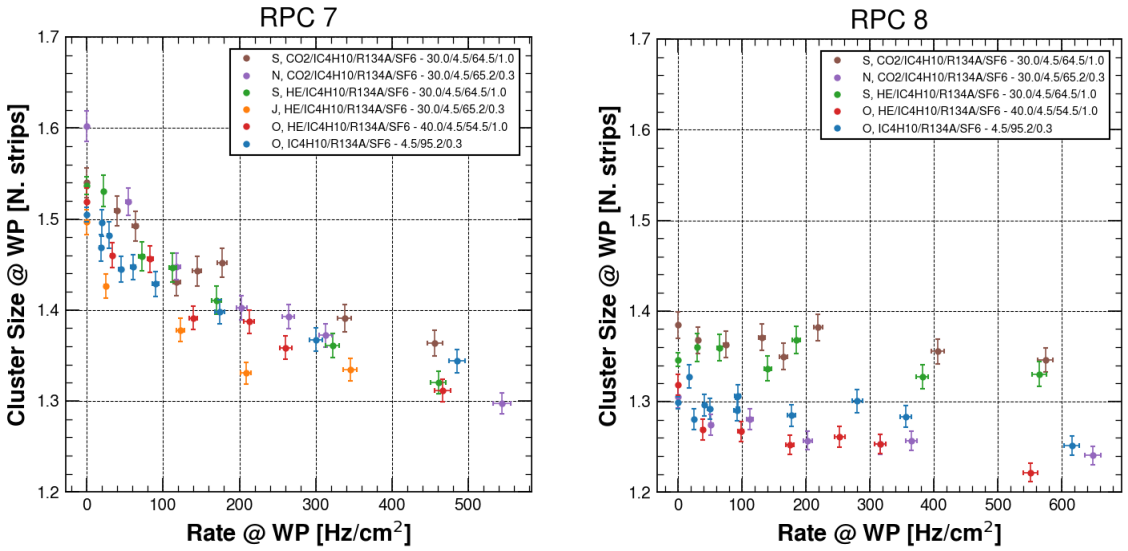

(a)

(b)

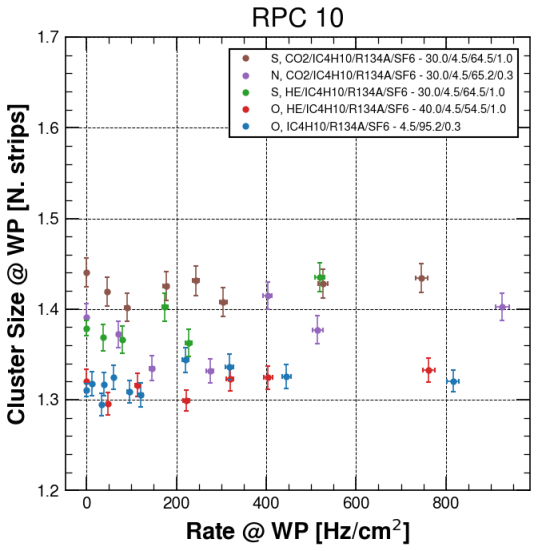

(c)

Figure 4.22: Cluster size difference between the STD gas mixture and the He, CO_2 gas mixtures for RPC 7 (a), RPC 8 (b), RPC 10 (c) in the different test beam periods.

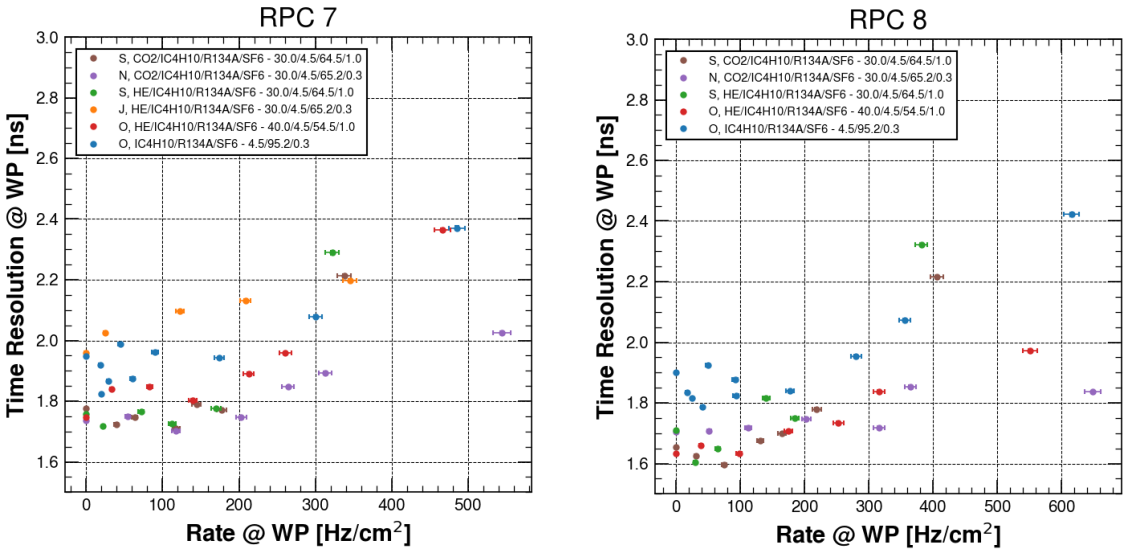

(a) (b)

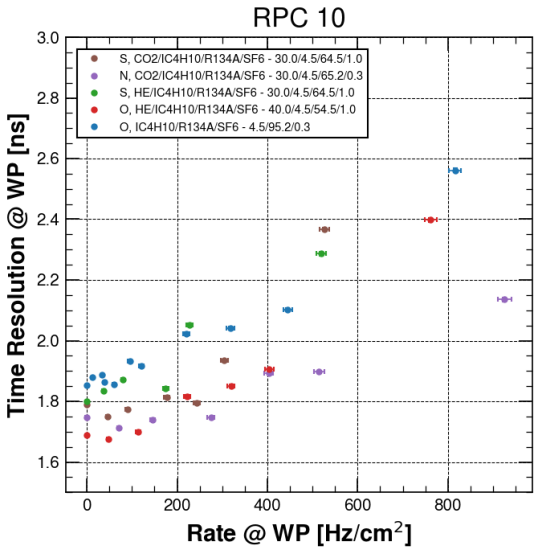

(c)

Figure 4.23: Time resolution difference between the STD gas mixture and the He, CO_2 gas mixtures for RPC 7 (a), RPC 8 (b), RPC 10 (c) in the different test beam periods.

4.3.3 HFO1234ze gas mixtures

From Section 3.3.5 the CO_2 69%-HFO gas mixture was selected in order to test it during the muon beam. In fact, it is possible to study the effect on RPCs performance of the HFO1234ze in a high gamma rate environment. Other two gas mixtures were tested, namely CO_2 50%, R-HFO, SF_6 1% and He 30%, R-HFO, SF_6 0.6%. These gas mixtures were selected from previous laboratory studies, and they are composed by a combination of R134a and HFO. Table 4.10 shows all the gas mixtures tested with the respective GWP_{100}.

Table 4.10: GWP_{100} for HFO1234ze test beam gas mixtures.

	R134a [%]	**HFO1234ze** [%]	**He** [%]	**CO_2** [%]	**SF_6** [%]	**iC_4H_{10}** [%]	**GWP_{100}**
STD	95.2	0	0	0	0.3	4.5	3384
CO_2 69%-HFO	0	25	0	69	1	5	762
CO_2 50%, R-HFO, SF_6 1%	22.25	22.25	0	50	1	4.5	1499
He 30%, R-HFO, SF_6 0.6%	32.45	32.45	30	0	0.6	4.5	1536

For each gas mixture tested, it is possible to consider the comparison with respect to the STD gas mixture features. The data are collected and analyzed in the same way as seen in Section 4.3.2. Table 4.11, Table 4.13 and Table 4.15 show the STD gas mixture main features for the three RPCs. Table 4.12, Table 4.14 and Table 4.16 show the difference between the features of the STD gas mixture and the features of each gas mixture tested, for source off and for a detector rate of 300 Hz/cm^2 and 600 Hz/cm^2. These data are then summarized in Figure 4.24, as a function of the RPCs and of the gas mixtures. All the raw parameters for each gas mixture are shown in Appendix A.2. Figure 4.25 and Figure 4.26 show the cluster size and the time resolution as a function of the rate.

First the working point is considered. From Figure 4.24 it is possible to see that all the gas mixtures have a working point higher with respect to the STD gas mixture. In particular, the CO_2 50%, R-HFO, SF_6 1% presents 800 V higher working point at 600 Hz/cm^2, while He 30%, R-HFO, SF_6 0.6% and CO_2 69%-HFO gas mixtures have 400 V higher working point at 600 Hz/cm^2. The behavior of RPC 7 seems different with respect to the other RPCs for these last two gas mixtures, since the working point has a higher increase as the detector rate increases. This effect could be related to the higher HPL resistivity of RPC 7.

If maximum efficiency is considered, shown in Figure 4.24, it is possible to see that the CO_2 69%-HFO and the CO_2 50%, R-HFO, SF_6 1% gas mixtures have a lower maximum efficiency at source off with respect to the STD gas mixture. When higher detector rates are considered, the efficiency drop increases faster in the CO_2 69%-HFO gas mixture, reaching difference values between -16% and -6%, depending on the detector. For the CO_2 50%, R-HFO, SF_6 1% the efficiency drop reaches difference values between -5% and -4%. Both gas mixtures have an high concentration of CO_2, respectively 69% and 50%, and a similar concentration of HFO, respectively 25% and 22.25%. Moreover, the CO_2 concentration difference is compensated in the CO_2 50%, R-HFO, SF_6 1% by the addition of R134a (22.25%). It is possible to affirm that the difference in the CO_2 and R134a ratio brings to a relevant difference in the maximum efficiency reached by the detector. In particular, the

presence of R134a allows to limit the efficiency drop for high detector rates. If the He 30%, R-HFO, SF_6 0.6% gas mixture is considered, it is possible to see that it has a compatible efficiency with respect to the STD one at source off. Moreover, this mixture has a lower efficiency drop with respect to the other two. This could be produced by the lower SF_6 concentration, as reported in Section 4.3.2, but also by the lower ratio between He and R134a concentration, since Section 3.3.4 shows that the behaviour of He and CO_2 are very similar for a concentration around 30%.

It is possible to consider the currents, reported in figure 4.24. All the gas mixture tested have higher currents with respect to the STD gas mixture. In particular, the CO_2 69%-HFO mixture reaches the higher currents difference, about 200 μA (+70% with respect to STD) while the He 30%, R-HFO, SF_6 0.6% reaches the lower currents difference, about 100μA (+30% with respect to STD). This 50% currents reduction is probably related to the difference between the CO_2/He and R134a ratio.

If the cluster size is considered, shown in Figure 4.25, it is possible to see that for RPC 7 it decreases for all the gas mixtures as the rate increases, while it remains stable for RPC 8 and 10. The only exception is the CO_2 69%-HFO mixture, for which the cluster size decreases also for these two RPCs. The difference between RPC 7 and RPC 8 and 10 is related to the difference in the strip pitch, respectively 2.1 cm and 2.6 cm. If He 30%, R-HFO, SF_6 0.6% and CO_2 50%, R-HFO, SF_6 1% mixtures are considered, it is possible to affirm that their charge lateral development for lower detector rate is between 2.1 cm and 2.6 cm, since it is possible to see a decrease for RPC 7 and not for RPC 8 and 10, and it decrease below 2.1 cm as the detector rate increases. However, if the CO_2 69%-HFO gas mixture is considered, the charge lateral development for lower detector rate must be higher than 2.6 cm and it must decrease below this value as the detector rate increases, since also RPC 8 and 10 see cluster size decrease.

If the time resolution is considered, shown in Figure 4.26, it is possible to see that it increases when the detector rate increases. This could be an effect of the higher detector occupancy for high rate, that could bring to a higher time resolution. However, all the gas mixtures have a lower time resolution with respect to the STD gas mixture.

Table 4.11: Main features for the STD gas mixtures and RPC 7 valued at source off, at a detector rate of 300 Hz/cm^2 and 600 Hz/cm^2.

Gas mixture	**RPC 7**	**Source OFF**	**300 Hz/cm^2**	**600 Hz/cm^2**	**Δ 300 Hz/cm^2**	**Δ 600 Hz/cm^2**
STD	Working point [V]	9680 ± 5	9973 ± 26	10304 ± 49	293 ± 31	624 ± 54
October	Maximum efficiency [%]	96.6 ± 0.1	90.8 ± 0.5	85.1 ± 0.9	-5.7 ± 0.6	-11 ± 1
	Currents at WP [μA]	0.3 ± 0.4	123 ± 6	246 ± 10	123 ± 6	245 ± 10

Table 4.12: Features difference between the STD gas mixture and HFO1234ze gas mixtures, evaluated at source off and at a detector rate of 300 Hz/cm^2 and 600 Hz/cm^2 for RPC 7.

Gas mixture	**RPC 7**	**Δ STD at OFF**	**Δ STD at 300 Hz/cm^2**	**Δ STD at 600 Hz/cm^2**
CO_2 69%-HFO	Working point [V]	336 ± 18	426 ± 58	498 ± 110
October	Maximum efficiency [%]	-1.4 ± 0.3	-9 ± 1	-16 ± 3
	Currents at WP [μA]	0.1 ± 0.5	87 ± 12	171 ± 21
CO_2 50%, R-HFO, SF_6 1%	Working point [V]	798 ± 19	823 ± 32	809 ± 61
November	Maximum efficiency [%]	-1.2 ± 0.3	-3 ± 2	-5 ± 3
	Currents at WP [μA]	0 ± 2	45 ± 22	85 ± 40
He 30%, R-HFO, SF_6 0.6%	Working point [V]	350 ± 15	541 ± 46	706 ± 87
September	Maximum efficiency [%]	-0.4 ± 0.3	-3 ± 1	-6 ± 2
	Currents at WP [μA]	-0.1 ± 0.8	50 ± 11	101 ± 19

Table 4.13: Main features for the STD gas mixtures and RPC 8 valued at source off, at a detector rate of 300 Hz/cm^2 and 600 Hz/cm^2.

Gas mixture	**RPC 8**	**Source OFF**	**300 Hz/cm^2**	**600 Hz/cm^2**	**Δ 300 Hz/cm^2**	**Δ 600 Hz/cm^2**
STD	Working point [V]	9457 ± 4	9441 ± 31	9468 ± 54	-16 ± 34	11 ± 57
October	Maximum efficiency [%]	97.2 ± 0.1	92.0 ± 0.3	86.9 ± 0.6	-5.2 ± 0.4	-10.3 ± 0.6
	Currents at WP [μA]	0.8 ± 0.3	100 ± 3	204 ± 5	100 ± 3	203 ± 6

Table 4.14: Features difference between the STD gas mixture and HFO1234ze gas mixtures, evaluated at source off and at a detector rate of 300 Hz/cm^2 and 600 Hz/cm^2 for RPC 8.

Gas mixture	**RPC 8**	**Δ STD at OFF**	**Δ STD at 300 Hz/cm^2**	**Δ STD at 600 Hz/cm^2**
CO_2 69%-HFO	Working point [V]	229 ± 12	296 ± 44	317 ± 78
October	Maximum efficiency [%]	-1.6 ± 0.2	-6 ± 1	-10 ± 2
	Currents at WP [μA]	0.9 ± 0.4	75 ± 8	145 ± 14
CO_2 50%, R-HFO, SF_6 1%	Working point [V]	852 ± 16	884 ± 53	883 ± 93
November	Maximum efficiency [%]	-1.7 ± 0.3	-2.8 ± 0.6	-4 ± 1
	Currents at WP [μA]	29 ± 1	86 ± 8	142 ± 13
He 30%, R-HFO, SF_6 0.6%	Working point [V]	310 ± 12	382 ± 47	402 ± 83
September	Maximum efficiency [%]	-0.9 ± 0.2	-1.5 ± 0.5	-2.1 ± 0.9
	Currents at WP [μA]	3.3 ± 0.6	41 ± 5	74 ± 9

Table 4.15: Main features for the STD gas mixtures and RPC 10 valued at source off, at a detector rate of 300 Hz/cm^2 and 600 Hz/cm^2.

Gas mixture	**RPC 10**	**Source OFF**	**300 Hz/cm^2**	**600 Hz/cm^2**	**Δ 300 Hz/cm^2**	**Δ 600 Hz/cm^2**
STD	Working point [V]	9420 ± 4	9396 ± 12	9408 ± 21	-24 ± 16	-12 ± 25
October	Maximum efficiency [%]	97.3 ± 0.1	91.8 ± 0.6	87 ± 1	-5.5 ± 0.7	-10 ± 1
	Currents at WP [μA]	0.3 ± 0.5	111 ± 2	219 ± 3	111 ± 2	218 ± 3

Table 4.16: Features difference between the STD gas mixture and HFO1234ze gas mixtures, evaluated at source off and at a detector rate of 300 Hz/cm^2 and 600 Hz/cm^2 for RPC 10.

Gas mixture	**RPC 10**	**Δ STD at OFF**	**Δ STD at 300 Hz/cm^2**	**Δ STD at 600 Hz/cm^2**
CO_2 69%-HFO	Working point [V]	330 ± 14	325 ± 31	341 ± 53
Octobe	Maximum efficiency [%]	-1.3 ± 0.2	-3 ± 1	-6 ± 3
	Currents at WP [μA]	0.7 ± 0.9	103 ± 11	199 ± 19
CO_2 50%, R-HFO, SF_6 1%	Working point [V]	812 ± 16	788 ± 26	798 ± 43
November	Maximum efficiency [%]	-1.4 ± 0.3	-3 ± 1	-4 ± 2
	Currents at WP [μA]	1 ± 3	71 ± 8	149 ± 12
He 30%, R-HFO, SF_6 0.6%	Working point [V]	362 ± 13	399 ± 24	407 ± 42
September	Maximum efficiency [%]	-0.8 ± 0.2	-1.0 ± 0.8	-2 ± 1
	Currents at WP [μA]	2.7 ± 0.9	49 ± 7	102 ± 10

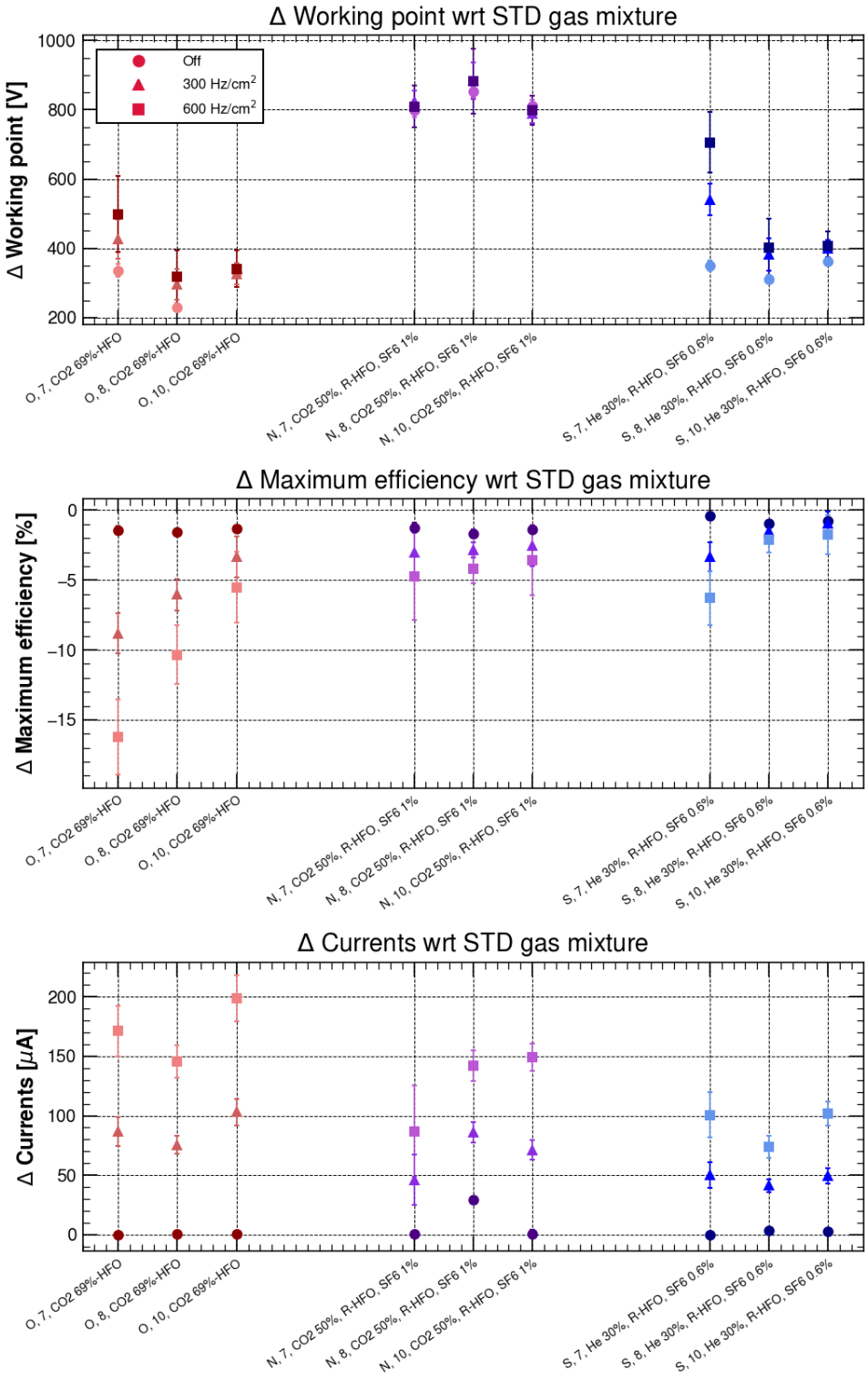

Figure 4.24: Difference between the STD gas mixture and the HFO1234ze gas mixtures as a function of the RPC and the gas mixture for the working point, efficiency and currents. On the x-axis, the letter represents the initial of the month in which the test beam started, followed by the RPC number.

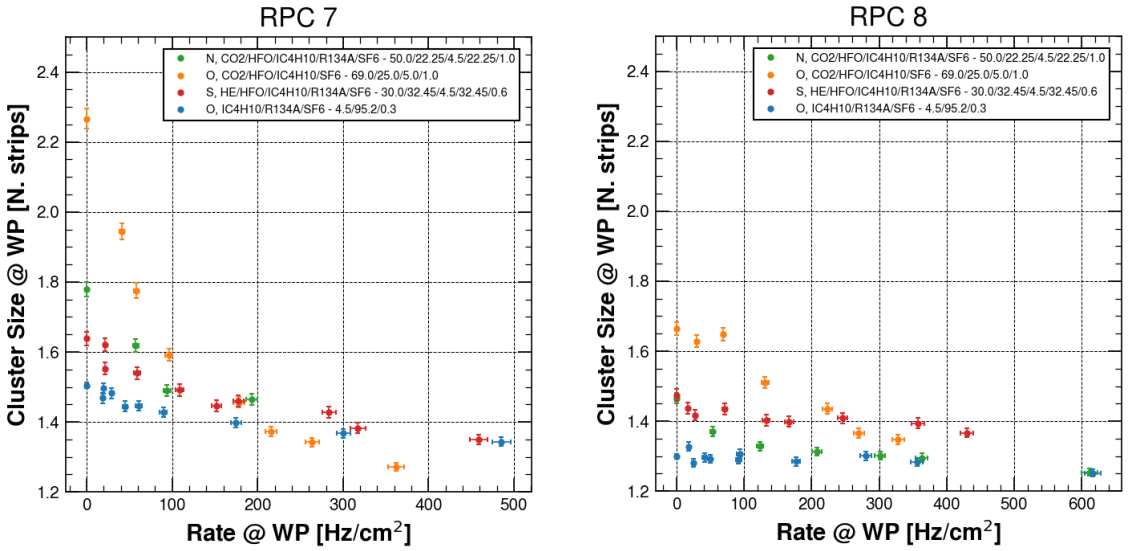

(a) (b)

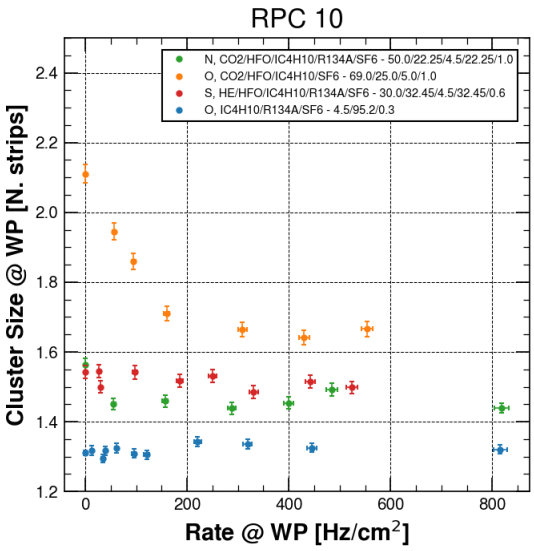

(c)

Figure 4.25: Cluster size difference between the STD gas mixture and HFO1234ze gas mixtures for RPC 7 (a), RPC 8 (b), RPC 10 (c) in the different test beam periods.

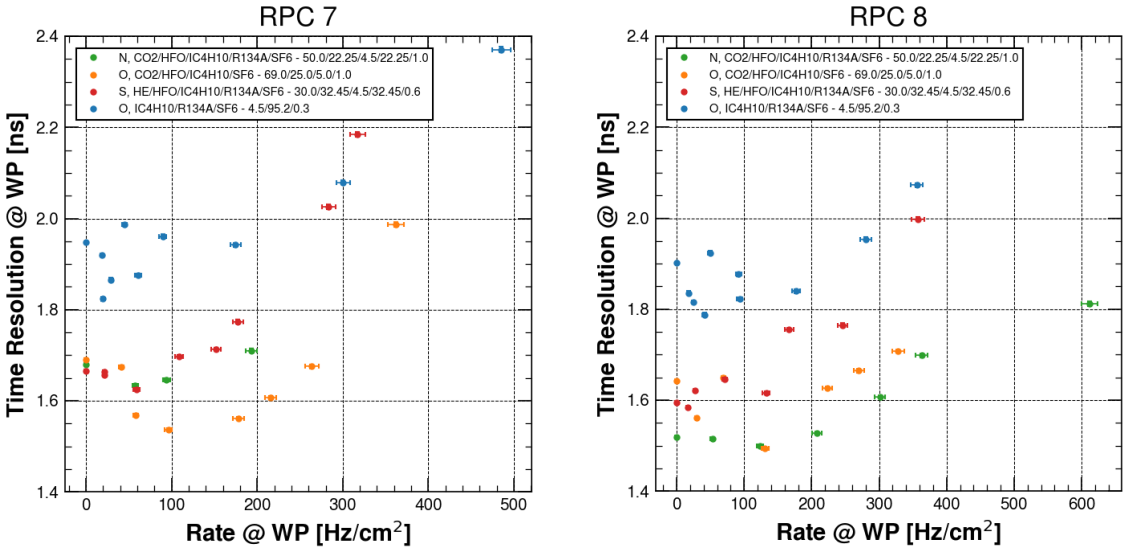

(a)

(b)

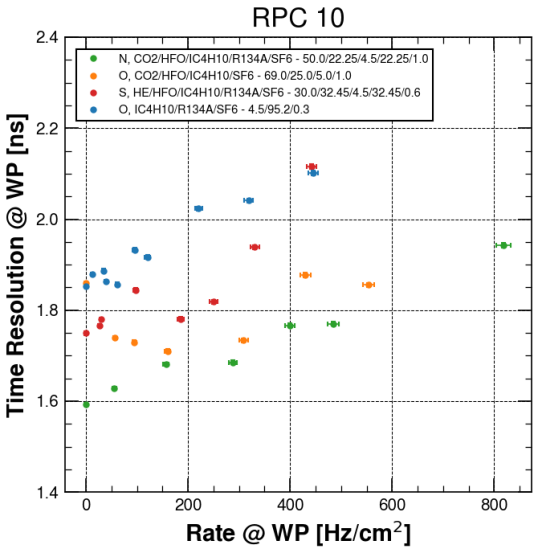

(c)

Figure 4.26: Time resolution difference between the STD gas mixture and HFO1234ze gas mixtures for RPC 7 (a), RPC 8 (b), RPC 10 (c) in the different test beam periods.

4.3.4 Novec 4710 gas mixtures

From Section 3.3.6, the Novec 4710 0.1% and 0.3% gas mixture were selected in order to test them during the muon beam. Table 4.17 shows all the gas mixtures tested during the test beam with the respective GWP_{100}.

Table 4.17: GWP_{100} for Novec 4710 gas mixtures.

	R134a [%]	**CO_2** [%]	**He** [%]	**iC_4H_{10}** [%]	**SF_6** [%]	**Novec 4710** [%]	**GWP_{100}**
STD	95.2	0	0	4.5	0.3	0	3384
Novec 0.1%	95.4	0	0	4.5	0	0.1	3250
Novec 0.3%	95.2	0	0	4.5	0	0.3	3194

For each gas mixture tested, the comparison with respect to the STD one features is considered. The data are collected and analyzed in the same way as seen in Section 4.3.2. Table 4.18, Table 4.20 and Table 4.22 show the STD mixture main features for the three RPCs. Table 4.19, Table 4.21 and Table 4.23 show the difference between the features of the STD mixture and the features of each gas mixture tested, for source off and for a detector rate of 300 Hz/cm^2 and 600 Hz/cm^2. These data are then summarized in Figure 4.27 as a function of the RPCs and of the gas mixtures. All the raw parameters for each gas mixture are shown in Appendix A.3. Figure 4.28 and Figure 4.29 show the cluster size and the time resolution as a function of the rate.

Concerning the working point, shown in Figure 4.27, it is possible to see that the Novec 0.1% mixture has a similar working point with respect to the STD. In particular, if the working point difference at a detector rate of 600 Hz/cm^2 is considered, this difference is lower than 100 V. Instead, the working point difference for the Novec 0.3% at source off is about 500 V higher with respect to the STD. Also in this case the increase of the working point difference between source off and at a detector rate of 600 Hz/cm^2 is around 100 V. So, both the gas mixture are compatible with the actual HV power supply used in LHC experiments.

The maximum efficiency is shown in Figure 4.27. Both gas mixtures have the same maximum efficiency with respect to the STD gas mixture, for all the detector rates. The only exception is the Novec 0.3% gas mixture with RPC 8, but the efficiency drop is not higher than -1.5%.

The currents are shown in Figure 4.27. It is possible to see that the Novec 0.1% gas mixture exhibits a better behavior. Its currents are for the most part compatible with respect to the STD gas mixture ones. However, for the Novec 0.3% mixture the currents increase significantly as the detector rate increases, even if the currents values at source off are compatible to the STD mixture. For the Novec 0.3% gas mixture the maximum difference increase in the currents is about 50 μA, which remains an acceptable value.

Concerning the cluster size, shown in Figure 4.28, it is possible to see that for RPC 7 the cluster size decreases as the detector rate increases. However, the cluster size seems to be stable for RPC 8 and RPC 10. This is probably due to the different strip pitch that is 2.1 cm for RPC 7 and 2.6 cm for RPC 8 and 10.

Figure 4.28 shows the time resolution. It is possible to see that the time resolution increases as the detector rate increases. The difference in the behavior between the Novec gas mixtures and the STD one are negligible.

Table 4.18: Main features for the STD gas mixtures and RPC 7 valued at source off, at a detector rate of 300 Hz/cm^2 and 600 Hz/cm^2.

Gas mixture	**RPC 7**	**Source OFF**	**300 Hz/cm^2**	**600 Hz/cm^2**	**Δ 300 Hz/cm^2**	**Δ 600 Hz/cm^2**
STD	Working point [V]	9680 ± 5	9973 ± 26	10304 ± 49	293 ± 31	624 ± 54
October	Maximum efficiency [%]	96.6 ± 0.1	90.8 ± 0.5	85.1 ± 0.9	-5.7 ± 0.6	-11 ± 1
	Currents at WP [μA]	0.3 ± 0.4	123 ± 6	246 ± 10	123 ± 6	245 ± 10

Table 4.19: Features difference between the STD gas mixture and Novec 4710 gas mixtures, evaluated at source off and at a detector rate of 300 Hz/cm^2 and 600 Hz/cm^2 for RPC 7.

Gas mixture	**RPC 7**	**Δ STD at OFF**	**Δ STD at 300 Hz/cm^2**	**Δ STD at 600 Hz/cm^2**
Novec 0.1%	Working point [V]	5 ± 12	40 ± 35	34 ± 65
October	Maximum efficiency [%]	0.1 ± 0.2	0.2 ± 0.7	0 ± 1
	Currents at WP [μA]	-0.1 ± 0.7	-3 ± 8	-8 ± 14
Novec 0.3%	Working point [V]	507 ± 12	587 ± 41	631 ± 76
October	Maximum efficiency [%]	0.1 ± 0.2	0.1 ± 0.9	0 ± 2
	Currents at WP [μA]	-0.1 ± 0.8	20 ± 8	37 ± 14

Table 4.20: Main features for the STD gas mixtures and RPC 8 valued at source off, at a detector rate of 300 Hz/cm^2 and 600 Hz/cm^2.

Gas mixture	**RPC 8**	**Source OFF**	**300 Hz/cm^2**	**600 Hz/cm^2**	**Δ 300 Hz/cm^2**	**Δ 600 Hz/cm^2**
STD	Working point [V]	9457 ± 4	9441 ± 31	9468 ± 54	-16 ± 34	11 ± 57
October	Maximum efficiency [%]	97.2 ± 0.1	92.0 ± 0.3	86.9 ± 0.6	-5.2 ± 0.4	-10.3 ± 0.6
	Currents at WP [μA]	0.8 ± 0.3	100 ± 3	204 ± 5	100 ± 3	203 ± 6

Table 4.21: Features difference between the STD gas mixture and Novec 4710 gas mixtures, evaluated at source off and at a detector rate of 300 Hz/cm^2 and 600 Hz/cm^2 for RPC 8.

Gas mixture	**RPC 8**	**Δ STD at OFF**	**Δ STD at 300 Hz/cm^2**	**Δ STD at 600 Hz/cm^2**
Novec 0.1%	Working point [V]	-6 ± 10	49 ± 44	53 ± 77
October	Maximum efficiency [%]	0.0 ± 0.2	-0.2 ± 0.5	-0.5 ± 0.8
	Currents at WP [μA]	0.8 ± 0.7	3 ± 4	2 ± 8
Novec 0.3%	Working point [V]	441 ± 9	481 ± 57	492 ± 102
October	Maximum efficiency [%]	0.1 ± 0.2	-0.6 ± 0.5	-1.3 ± 0.9
	Currents at WP [μA]	1.0 ± 0.7	23 ± 7	44 ± 11

Table 4.22: Main features for the STD gas mixtures and RPC 10 valued at source off, at a detector rate of 300 Hz/cm^2 and 600 Hz/cm^2.

Gas mixture	**RPC 10**	**Source OFF**	**300 Hz/cm^2**	**600 Hz/cm^2**	**Δ 300 Hz/cm^2**	**Δ 600 Hz/cm^2**
STD	Working point [V]	9420 ± 4	9396 ± 12	9408 ± 21	-24 ± 16	-12 ± 25
October	Maximum efficiency [%]	97.3 ± 0.1	91.8 ± 0.6	87 ± 1	-5.5 ± 0.7	-10 ± 1
	Currents at WP [μA]	0.3 ± 0.5	111 ± 2	219 ± 3	111 ± 2	218 ± 3

Table 4.23: Features difference between the STD gas mixture and Novec 4710 gas mixtures, evaluated at source off and at a detector rate of 300 Hz/cm^2 and 600 Hz/cm^2 for RPC 10.

Gas mixture	**RPC 10**	**Δ STD at OFF**	**Δ STD at 300 Hz/cm^2**	**Δ STD at 600 Hz/cm^2**
Novec 0.1%	Working point [V]	14 ± 11	46 ± 20	41 ± 33
October	Maximum efficiency [%]	0.1 ± 0.2	0 ± 1	0 ± 2
	Currents at WP [μA]	0 ± 1	4 ± 4	9 ± 7
Novec 0.3%	Working point [V]	492 ± 10	529 ± 20	536 ± 34
October	Maximum efficiency [%]	-0.1 ± 0.2	0.3 ± 0.9	0 ± 1
	Currents at WP [μA]	0 ± 1	18 ± 4	38 ± 6

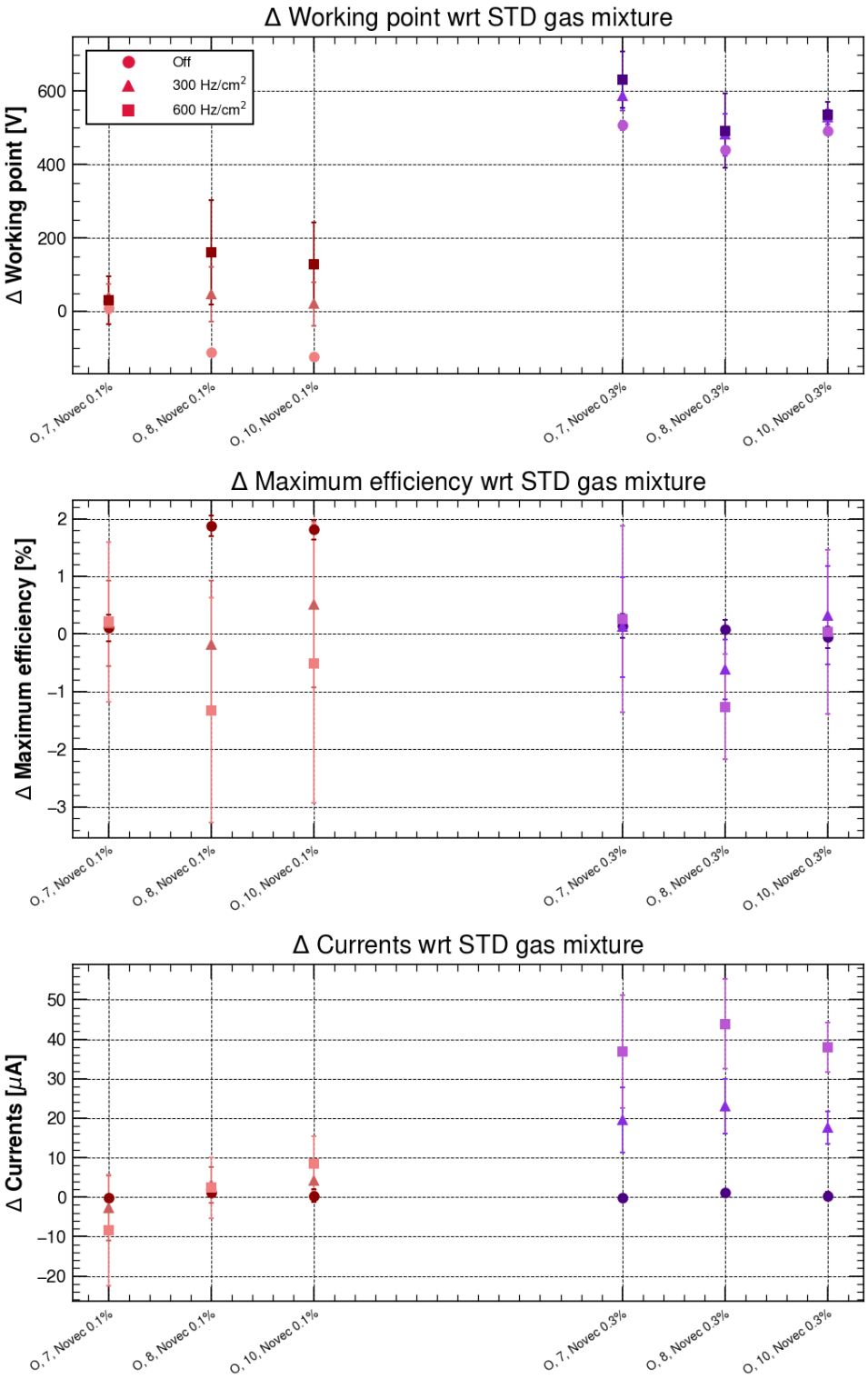

Figure 4.27: Difference between the STD gas mixture and the Novec 4710 gas mixtures as a function of the RPC and the gas mixture for the working point, efficiency and currents. On the x-axis, the letter represents the initial of the month in which the test beam started, followed by the RPC number.

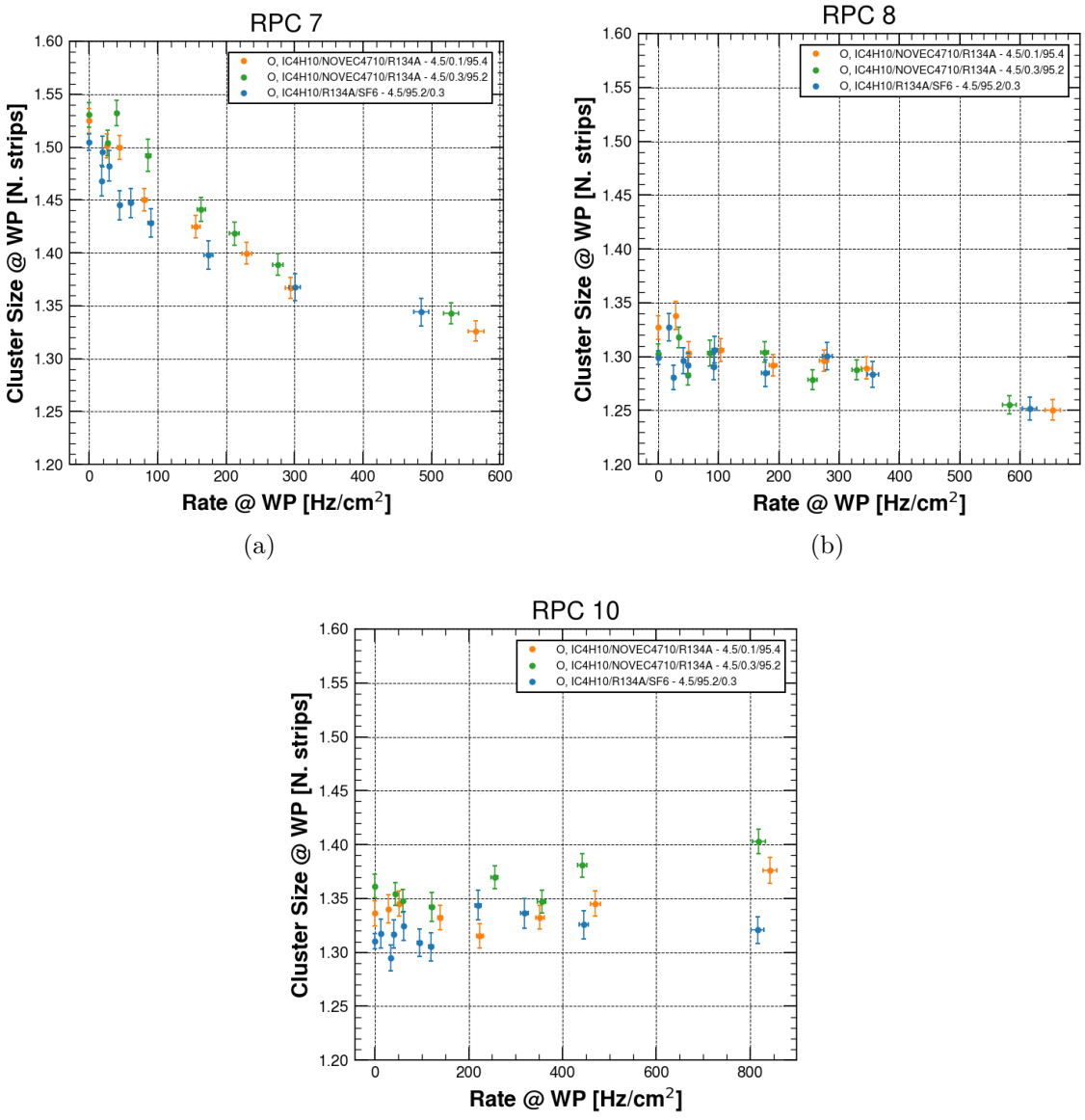

(a) (b)

(c)

Figure 4.28: Cluster size difference between the STD gas mixture and Novec 4710 gas mixtures for RPC 7 (a), RPC 8 (b), RPC 10 (c) in the different test beam periods.

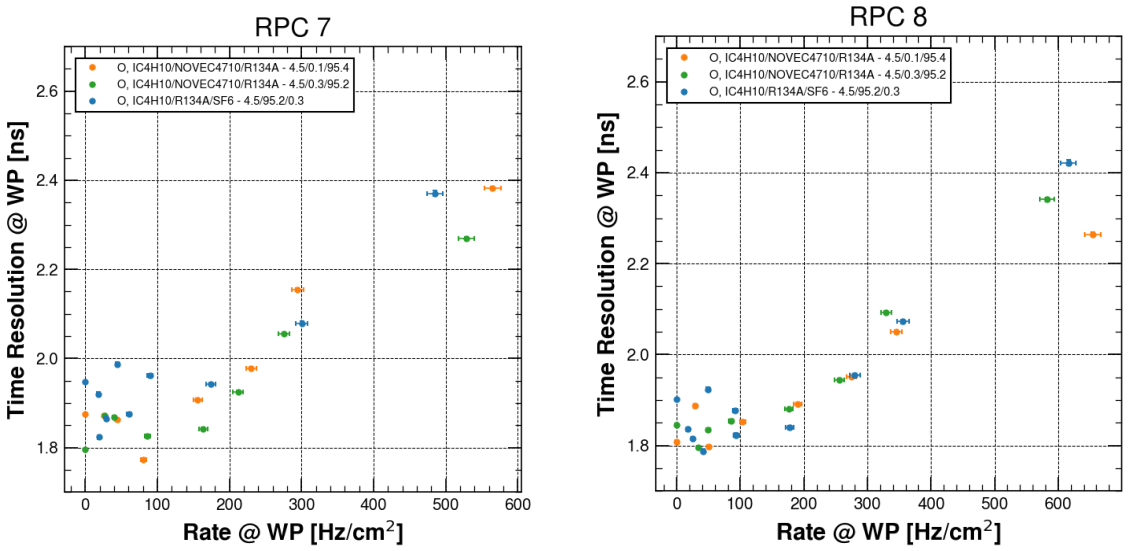

(a) (b)

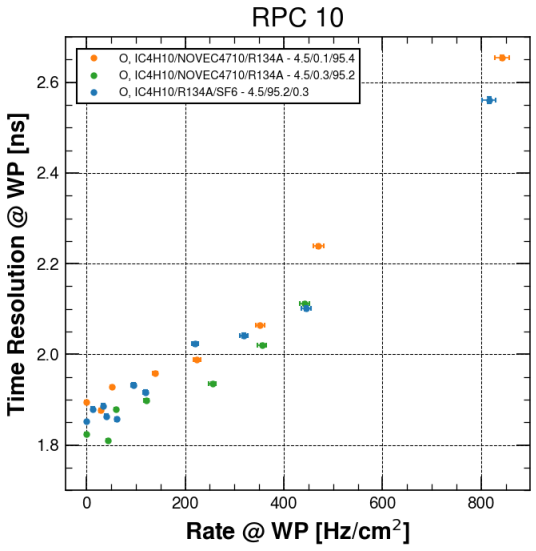

(c)

Figure 4.29: Time resolution difference between the STD gas mixture and Novec 4710 gas mixtures for RPC 7 (a), RPC 8 (b), RPC 10 (c) in the different test beam periods.

4.4 Summary results

It is possible to resume the results found in previous sections. Figure 4.30 shows the main features, computed with respect to the STD gas mixture, as a function of the RPCs and of the gas mixture.

It is possible to start considering the working point for the different gas mixtures. The majority of the tested mixtures have a lower or comparable working point with respect to the STD. The exceptions are all the HFO1234ze gas mixtures and the Novec 0.3% gas mixture. However, there are no critical increase in the working point as the detector rate increases.

Then it is possible to consider the maximum efficiency. The mixtures can be divided into three different groups.[5] The first group is characterized by an efficiency drop less than 4% with respect to the STD gas mixture and for a detector rate of 600 Hz/cm^2. In this group there are the two Novec mixtures and the He 30% and CO_2 30% mixtures with a 0.3% SF_6 concentration. The second group is characterized by an efficiency drop between 4% and 6% with respect to the STD. In this group are collected the He 30% and CO_2 30% mixtures with a 1% SF_6 concentration, the He 40% SF_6 1% mixture, the CO_2 50%, R-HFO, SF_6 1% mixture and the He 30%, R-HFO, SF_6 0.6% mixture. The last group is characterized by an efficiency drop greater than 6% with respect to the STD and it is represented by the CO_2 69%-HFO mixture.

Then, it is possible to consider the currents. Also in this case, the gas mixtures tested can be divided into three different groups[6]. The first group is characterized by a currents value below 30 μA with respect to the STD. In this group there are the Novec 0.1% mixture and the He 30% and CO_2 30% mixtures with a 0.3% SF_6 concentration. The second group is characterized by currents value between 30μA and 70μA with respect to the STD gas mixture. In this group are collected the Novec 0.3% gas mixture, the He 30% and CO_2 30% gas mixtures with a 1% SF_6 concentration and the He 40% SF_6 1% gas mixture. The last group is characterized by a currents value greater than 70 μA with respect to the STD and it is represented by all the HFO mixtures.

Table 4.24 shows a summary of the division into the different groups. There is a relationship between the currents increase and the efficiency drops. If the table is considered from left to right and from top to bottom, it is possible to see that the gas mixture presents an increasing of SF_6 and a decreasing of the R134a/HFO ratio. The best gas mixtures are the ones that remain in the group 1 both for the efficiency drop and the currents, so the Novec 0.1% gas mixture and the He 30% and CO_2 30% gas mixtures with a 0.3% SF_6 concentration. The worst gas mixture is the one that remains in group 3 both for the efficiency drop and the currents, so the CO_2 69%-HFO gas mixture. Also the other HFO1234ze gas mixtures are not among the best candidates, since they present high currents and a intermediate efficiency drop. In the intermediate values of efficiency drop

[5]For this cataloging the RPC 7 data are used, since its high resistivity makes it more sensitive to the efficiency drop. Then, from the results of the classification the division also for the other two RPCs can be extrapolated.

[6]Also in this case, the RPC 7 data are used and then, from the results of the classification, the division also for the other two RPCs can be extrapolated.

and currents there are the He 30% and CO_2 30% mixtures with a 1% SF_6, He 40% SF_6 1% mixture and the Novec 0.3% mixtures.

It is possible to conclude that an increase in the electronegative component of the gas mixture, such as SF_6 or Novec 4710, leads to an increase of the detector currents. This currents could be justified only in terms of an increase in the ionic part of the currents, since the electronegative gas should reduce the dimension of the electron multiplication. It is also possible to confirm that a 30% CO_2 concentration has the same behavior of a 30% He concentration, as concerning the currents and the efficiency drop, while the working point remain below the STD mixture values. The addition of HFO1234ze brings to a significant increase in the currents and in the efficiency drop. The latter could be limited if we add some R134a together with the HFO1234ze, even if the currents remain high.

Table 4.24: Summary of the division into the efficiency drop groups (top) and the currents groups (left). The difference values are computed with respect to the STD gas mixture values, between the values at source off and at a detector rate of 600 Hz/cm^2. For this cataloging we use the RPC 7 data, since its high resistivity makes it more sensitive to the efficiency drop. Then, from the results of the classification we extrapolate the division also for the other two RPCs.

Max. Eff. drop limit [%] @ 600 Hz/cm^2 / Currents limit [μA] @ 600 Hz/cm^2	Group 1 RPC 7: [-4, 0] RPC 8: [-1.2, 0] RPC 10: [-0.3, 0]	Group 2 RPC 7: [-6, -4] RPC 8: [-2.5, -1.2] RPC 10: [-2.6, -0.3]	Group 3 RPC 7: < -6 RPC 8: < -2.5 RPC 10: < -2.6
Group 1 RPC 7: [0, 30] RPC 8: [0, 40] RPC 10: [0, 20]	He 30% SF_6 0.3% CO_2 30% SF_6 0.3% Novec 0.1%		
Group 2 RPC 7: [30, 70] RPC 8: [40, 70] RPC 8: [20, 70]	Novec 0.3%	He 30% SF_6 1% CO_2 30% SF_6 1% He 40% SF_6 1%	
Group 3 RPC 7: > 70 RPC 8: > 70 RPC 10: > 70		CO_2 50%, R-HFO, SF_6 1% He 30%, R-HFO, SF_6 0.6%	CO_2 69%-HFO

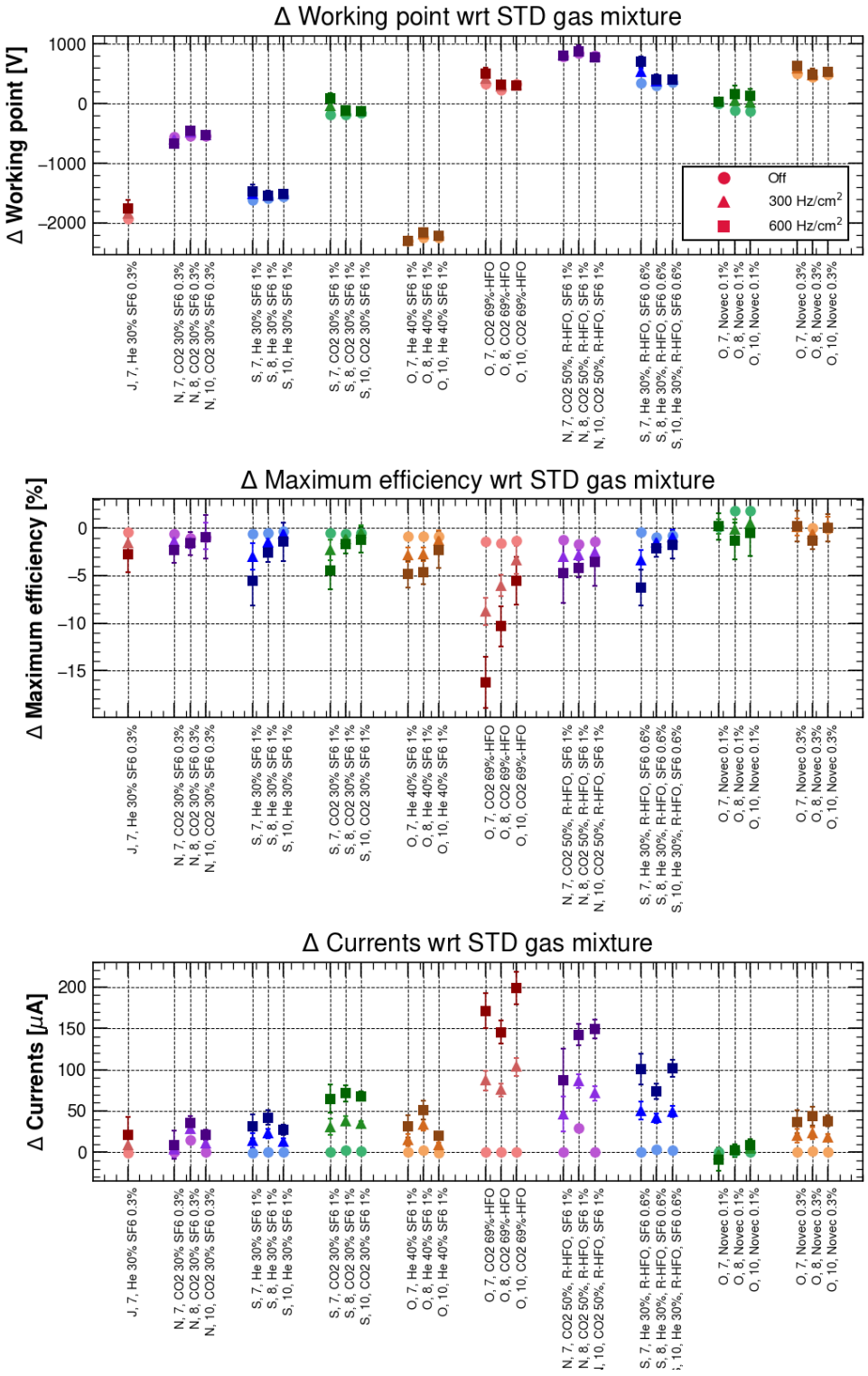

Figure 4.30: Features difference between the STD gas mixture and all the gas mixtures tested as a function of the RPC and the gas mixture. On the x-axis, the letter represents the initial of the month in which the test beam started, followed by the RPC number.

Chapter 5

Conclusion

This work was focused on the studies of alternative gas mixtures for RPCs detectors. Eighteen gas mixtures were tested in the laboratory environment and ten of them were selected to be tested at the GIF++. In both cases some alternatives to the R134a were tested, in particular He, CO_2 and HFO1234ze with different SF_6 concentrations. Novec 4710 was tested as a substitute of SF_6.

Concerning alternatives to R134a, the main results obtained are:

- The substitution of 30% R134a concentration with He or CO_2 does not imply any change in RPC performance with respect to the STD gas mixture. From the laboratory data it is possible to see that all the main RPC performances are the same for the two gas mixtures with less R134a, although they reach the best performance for different concentrations of SF_6: 0.45% for the He gas mixture and 0.8% for the CO_2 gas mixture. During the test beam period, these gas mixtures were tested with a concentration of SF_6 of 0.3% and 1%. In the first case, the performances under a high irradiation condition are similar to the STD gas mixture, while in the second case the efficiency drops and the currents are higher with respect to the standard gas mixture ones. Concerning the GWP, the He and CO_2 gas mixtures with 0.3% SF_6 concentration has a GWP of 2389, which is around 30% less than the standard gas mixture one of 3384.

- The substitution of 69% R134a concentration with CO_2 brings to a lower maximum efficiency reached by the detector. It is possible to affirm that the increase in the ratio between CO_2 and R134a brings to lower detector maximum efficiency and higher currents values. Also the streamer probability increase more than 10% with respect to the STD gas mixture, although its value is influenced by the specific detector characteristic, such as its resistivity. However, this gas mixture presents a GWP 53% less than the STD gas mixture.

- From the test beam data, it is possible to see that an increase of the SF_6 concentration, for example in the He 30% or CO_2 gas mixtures, produces also an increase of the currents and of the efficiency drops for a high irradiation condition.

- It is possible to substitute part of R134a with HFO1234ze only if another gas (He or CO_2) is added in order to reduce the working point of the gas mixture. All

HFO1234ze, without R134a, gas mixtures tested in the laboratory present a high CO_2 concentration, around 70%. From the comparison of the different gas mixtures tested, it is possible to see that the HFO1234ze gas mixtures present higher avalanche charges with respect to the standard gas mixtures. This effect is produced both by the high concentration of the CO_2 (as we can see from the comparison between the CO_2 69%-R134a and the STD gas mixture) and by the presence of the HFO1234ze (as we can see from the comparison between the CO_2 69%-R134a and the CO_2 69%-HFO gas mixture).

- From the test beam data, it is possible to see that HFO1234ze gas mixtures present higher currents and a bigger efficiency drops with respect to the other gas mixtures. In particular, It is possible to see that an increase of the SF_6 concentration together with a decrease of the ratio between R134a and HFO1234ze brings to an increase in the currents and in the efficiency drop with respect to the STD gas mixture, in a condition of gamma rates of about 600 Hz/cm^2.

Despite the excellent results of the He 30% gas mixture, it must be remembered that the use of He is currently prohibited in the experimental caverns, due to the presence of photomultipliers.

Concerning the substitution of SF_6 with Novec 4710, the main results obtained are:

- From the laboratory data, it is possible to see that a 0.1% Novec concentration instead of the 0.3% SF_6 concentration does not change the characteristics of the STD gas mixture. In particular, also the streamer probability is the same as the STD gas mixture, for both the Novec concentration. The Novec 0.1% gas mixture presents GWP 4% less than the STD gas mixture.

- When RPCs are irradiated at GIF++, it is possible to see that the currents values for the 0.1% Novec concentration do not increase significantly as the radiation increases. Instead, for a concentration of 0.3% of Novec they are higher with respect to the STD gas mixture and the increase more rapidly with increasing background radiation.

- Since Novec 4710 seems promising as a substitute of SF_6, the He 30% and CO_2 30% gas mixture were tested in the laboratory environment with a 0.35% Novec concentration. The detectors performances with these two gas mixtures are similar to the standard He 30% and CO_2 30% gas mixture. The only difference concerns the currents, that remain higher with respect to the STD gas mixture. In this case, the two gas mixtures present a GWP 34% lower than the STD gas mixture.

Even though the Novec 0.1% gas mixture looks great, it is known that it can react with water. For this reason, a study of the production of possible compounds is ongoing.

Appendix A

Raw test beam parameter for all the RPCs and gas mixtures

In the following sections are reported the raw test beam parameters used for the analysis in Chapter 4.

A.1 He and CO_2 gas mixtures

Table A.1: Main features for He, CO_2 gas mixtures valued at source off, at 300 and 600 Hz/cm^2 detector rate for RPC 7.

Gas mixture	**RPC 7**	**Source OFF**	**300 Hz/cm^2**	**600 Hz/cm^2**	**Δ 300 Hz/cm^2**	**Δ 600 Hz/cm^2**
STD	Working point [V]	9680 ± 5	9973 ± 26	10304 ± 49	293 ± 31	624 ± 54
October	Maximum efficiency [%]	96.6 ± 0.1	90.8 ± 0.5	85.1 ± 0.9	-5.7 ± 0.6	-11 ± 1
	Currents at WP [μA]	0.3 ± 0.4	123 ± 6	246 ± 10	123 ± 6	245 ± 10
He 30% SF_6 0.3%	Working point [V]	7752 ± 8	8134 ± 56	8539 ± 106	382 ± 64	787 ± 114
July	Maximum efficiency [%]	96.2 ± 0.2	89.3 ± 0.5	82.4 ± 0.9	-6.9 ± 0.7	-14 ± 1
	Currents at WP [μA]	0.1 ± 0.6	131 ± 7	267 ± 12	131 ± 8	266 ± 12
CO_2 30% SF_6 0.3%	Working point [V]	9128 ± 11	9376 ± 18	9638 ± 33	248 ± 30	511 ± 45
November	Maximum efficiency [%]	96.0 ± 0.2	89.4 ± 0.2	82.8 ± 0.4	-6.6 ± 0.4	-13.2 ± 0.6
	Currents at WP [μA]	0.4 ± 1	126 ± 5	255 ± 7	126 ± 6	255 ± 8
He 30% SF_6 1%	Working point [V]	8068 ± 6	8450 ± 28	8835 ± 55	382 ± 64	787 ± 114
September	Maximum efficiency [%]	96.0 ± 0.1	87.8 ± 0.9	80 ± 2	-8 ± 1	-16 ± 2
	Currents at WP [μA]	0.1 ± 0.2	137 ± 3	277 ± 5	137 ± 3	277 ± 5
CO_2 30% SF_6 1%	Working point [V]	9492 ± 12	9938 ± 19	10394 ± 36	446 ± 31	902 ± 48
September	Maximum efficiency [%]	96.1 ± 0.2	88.5 ± 0.6	81 ± 1	-7.6 ± 0.8	-15 ± 1
	Currents at WP [μA]	0.2 ± 0.3	154 ± 4	310 ± 7	153 ± 5	310 ± 7
He 40% SF_6 1%	Working point [V]	7376 ± 9	7687 ± 5	8002 ± 10	311 ± 14	626 ± 19
October	Maximum efficiency [%]	95.7 ± 0.2	88.0 ± 0.3	80.3 ± 0.5	-7.7 ± 0.5	-15.4 ± 0.7
	Currents at WP [μA]	0.2 ± 0.4	138 ± 2	277 ± 4	138 ± 3	276 ± 4

Table A.2: Main features for He, CO_2 gas mixtures valued at source off, at 300 and 600 Hz/cm^2 detector rate for RPC 8.

Gas mixture	**RPC 8**	**Source OFF**	**300 Hz/cm^2**	**600 Hz/cm^2**	**Δ 300 Hz/cm^2**	**Δ 600 Hz/cm^2**
STD	Working point [V]	9457 ± 4	9441 ± 31	9468 ± 54	-16 ± 34	11 ± 57
October	Maximum efficiency [%]	97.2 ± 0.1	92.0 ± 0.3	86.9 ± 0.6	-5.2 ± 0.4	-10.3 ± 0.6
	Currents at WP [μA]	0.8 ± 0.3	100 ± 3	204 ± 5	100 ± 3	203 ± 6
CO_2 30% SF_6 0.3%	Working point [V]	8913 ± 9	8960 ± 8	9012 ± 14	47 ± 17	100 ± 23
November	Maximum efficiency [%]	96.0 ± 0.2	90.6 ± 0.3	85.5 ± 0.6	-5.4 ± 0.5	-10.6 ± 0.8
	Currents at WP [μA]	15.8 ± 0.8	128 ± 4	238 ± 5	112 ± 5	222 ± 6
He 30% SF_6 1%	Working point [V]	7870 ± 4	7897 ± 12	7930 ± 23	27 ± 17	60 ± 27
September	Maximum efficiency [%]	96.6 ± 0.1	90.4 ± 0.2	84.3 ± 0.4	-6.2 ± 0.3	-12.3 ± 0.5
	Currents at WP [μA]	1.3 ± 0.2	123 ± 2	246 ± 4	122 ± 2	244 ± 4
CO_2 30% SF_6 1%	Working point [V]	9276 ± 9	9309 ± 11	9352 ± 20	33 ± 20	76 ± 29
September	Maximum efficiency [%]	96.6 ± 0.2	90.8 ± 0.2	85.2 ± 0.4	-5.8 ± 0.4	-11.4 ± 0.6
	Currents at WP [μA]	2.8 ± 0.2	138 ± 3	275 ± 5	136 ± 3	272 ± 5
He 40% SF_6 1%	Working point [V]	7218 ± 8	7256 ± 15	7314 ± 27	38 ± 23	96 ± 35
October	Maximum efficiency [%]	96.6 ± 0.2	89.4 ± 0.3	82.5 ± 0.6	-7.1 ± 0.5	-14.0 ± 0.8
	Currents at WP [μA]	2.9 ± 0.4	133 ± 4	254 ± 6	130 ± 4	251 ± 6

Table A.3: Main features for He, CO_2 gas mixtures valued at source off, at 300 and 600 Hz/cm^2 detector rate for RPC 10.

Gas mixture	**RPC 10**	**Source OFF**	**300 Hz/cm^2**	**600 Hz/cm^2**	**Δ 300 Hz/cm^2**	**Δ 600 Hz/cm^2**
STD	Working point [V]	9420 ± 4	9396 ± 12	9408 ± 21	-24 ± 16	-12 ± 25
October	Maximum efficiency [%]	97.3 ± 0.1	91.8 ± 0.6	87 ± 1	-5.5 ± 0.7	-10 ± 1
	Currents at WP [μA]	0.3 ± 0.5	111 ± 2	219 ± 3	111 ± 2	218 ± 3
CO_2 30% SF_6 0.3%	Working point [V]	8889 ± 10	8875 ± 15	8877 ± 24	-14 ± 24	-12 ± 33
November	Maximum efficiency [%]	96.4 ± 0.2	91.0 ± 0.8	86 ± 1	-5 ± 1	-10 ± 2
	Currents at WP [μA]	0.3 ± 2	124 ± 4	241 ± 6	124 ± 6	241 ± 7
He 30% SF_6 1%	Working point [V]	7868 ± 5	7877 ± 18	7892 ± 34	8 ± 22	24 ± 38
September	Maximum efficiency [%]	96.9 ± 0.1	91.3 ± 0.5	86 ± 1	-5.7 ± 0.6	-11 ± 1
	Currents at WP [μA]	0.6 ± 0.2	124 ± 2	246 ± 4	123 ± 2	245 ± 4
CO_2 30% SF_6 1%	Working point [V]	9273 ± 10	9268 ± 11	9277 ± 19	-5 ± 21	3 ± 29
September	Maximum efficiency [%]	96.8 ± 0.2	91.3 ± 0.2	86.0 ± 0.3	-5.5 ± 0.4	-10.8 ± 0.5
	Currents at WP [μA]	1.7 ± 0.4	145 ± 2	286 ± 3	143 ± 2	285 ± 3
He 40% SF_6 1%	Working point [V]	7181 ± 7	7185 ± 7	7194 ± 11	4 ± 14	13 ± 19
October	Maximum efficiency [%]	96.6 ± 0.2	90.5 ± 0.5	84.9 ± 0.8	-6.1 ± 0.6	-11.8 ± 0.9
	Currents at WP [μA]	0.1 ± 0.3	120 ± 1	239 ± 2	120 ± 1	239 ± 2

A.2 HFO1234ze gas mixtures

Table A.4: Main features for HFO1234ze gas mixtures valued at source off, at 300 and 600 Hz/cm^2 detector rate for RPC 7.

Gas mixture	**RPC 7**	**Source OFF**	**300** **Hz/cm^2**	**600** **Hz/cm^2**	**Δ 300** **Hz/cm^2**	**Δ 600** **Hz/cm^2**
STD	Working point [V]	9680 ± 5	9973 ± 26	10304 ± 49	293 ± 31	624 ± 54
October	Maximum efficiency [%]	96.6 ± 0.1	90.8 ± 0.5	85.1 ± 0.9	-5.7 ± 0.6	-11 ± 1
	Currents at WP [μA]	0.3 ± 0.4	123 ± 6	246 ± 10	123 ± 6	245 ± 10
CO_2 69%-HFO	Working point [V]	10016 ± 13	10399 ± 31	10803 ± 60	384 ± 45	787 ± 74
October	Maximum efficiency [%]	95.1 ± 0.2	82.0 ± 0.9	69 ± 2	-13 ± 1	-26 ± 2
	Currents at WP [μA]	0.4 ± 0.2	210 ± 6	417 ± 11	209 ± 7	416 ± 12
CO2 50%, R-HFO,	Working point [V]	10478 ± 14	10796 ± 6	11113 ± 11	318 ± 20	635 ± 25
SF_6 1%	Maximum efficiency [%]	95.3 ± 0.2	88 ± 1	80 ± 2	-7 ± 1	-15 ± 2
November	Currents at WP [μA]	1 ± 2	168 ± 16	330 ± 30	168 ± 18	330 ± 32
He 30%, R-HFO	Working point [V]	10030 ± 10	10514 ± 20	11010 ± 38	483 ± 30	980 ± 48
SF_6 0.3%	Maximum efficiency [%]	96.1 ± 0.2	87.5 ± 0.5	79 ± 1	-8.7 ± 0.7	-17 ± 1
September	Currents at WP [μA]	0.3 ± 0.4	173 ± 5	346 ± 9	173 ± 6	346 ± 9

Table A.5: Main features for HFO1234ze gas mixtures valued at source off, at 300 and 600 Hz/cm^2 detector rate for RPC 8.

Gas mixture	**RPC 8**	**Source OFF**	**300 Hz/cm^2**	**600 Hz/cm^2**	**Δ 300 Hz/cm^2**	**Δ 600 Hz/cm^2**
STD	Working point [V]	9680 $\pm$ 5	9973 $\pm$ 26	10304 $\pm$ 49	-16 $\pm$ 34	11 $\pm$ 57
October	Maximum efficiency [%]	96.6 $\pm$ 0.1	90.8 $\pm$ 0.5	85.1 $\pm$ 0.9	-5.2 $\pm$ 0.4	-10.3 $\pm$ 0.6
	Currents at WP [μA]	0.3 $\pm$ 0.4	123 $\pm$ 6	246 $\pm$ 10	100 $\pm$ 3	203 $\pm$ 6
CO_2 69%-HFO	Working point [V]	9687 $\pm$ 8	9737 $\pm$ 13	9786 $\pm$ 24	50 $\pm$ 21	99 $\pm$ 32
October	Maximum efficiency [%]	95.6 $\pm$ 0.2	85.9 $\pm$ 0.8	77 $\pm$ 2	-10 $\pm$ 1	-19 $\pm$ 2
	Currents at WP [μA]	1.7 $\pm$ 0.1	176 $\pm$ 4	349 $\pm$ 9	174 $\pm$ 5	347 $\pm$ 9
CO2 50%, R-HFO, SF_6 1%	Working point [V]	10310 $\pm$ 12	10326 $\pm$ 23	10351 $\pm$ 40	16 $\pm$ 35	41 $\pm$ 52
November	Maximum efficiency [%]	95.5 $\pm$ 0.2	89.1 $\pm$ 0.2	82.7 $\pm$ 0.4	-6.4 $\pm$ 0.4	-12.8 $\pm$ 0.6
	Currents at WP [μA]	30 $\pm$ 1	186 $\pm$ 5	346 $\pm$ 8	156 $\pm$ 6	316 $\pm$ 9
He 30%, R-HFO, SF_6 0.3%	Working point [V]	9767 $\pm$ 9	9824 $\pm$ 16	9871 $\pm$ 29	56 $\pm$ 25	103 $\pm$ 38
September	Maximum efficiency [%]	96.2 $\pm$ 0.2	90.4 $\pm$ 0.2	84.8 $\pm$ 0.4	-5.8 $\pm$ 0.4	-11.4 $\pm$ 0.5
	Currents at WP [μA]	4.1 $\pm$ 0.3	142 $\pm$ 2	277 $\pm$ 4	137 $\pm$ 3	273 $\pm$ 4

Table A.6: Main features for HFO1234ze gas mixtures valued at source off, at 300 and 600 Hz/cm^2 detector rate for RPC 10.

Gas mixture	**RPC 10**	**Source OFF**	**300** Hz/cm^2	**600** Hz/cm^2	**Δ 300** Hz/cm^2	**Δ 600** Hz/cm^2
STD	Working point [V]	9680 ± 5	9973 ± 26	10304 ± 49	−24 ± 16	−15 ± 25
October	Maximum efficiency [%]	96.6 ± 0.1	90.8 ± 0.5	85.1 ± 0.9	−5.5 ± 0.7	−10 ± 1
	Currents at WP [μA]	0.3 ± 0.4	123 ± 6	246 ± 10	111 ± 2	218 ± 3
CO_2 69%-HFO	Working point [V]	9750 ± 10	9722 ± 19	9746 ± 33	−28 ± 29	−4 ± 43
October	Maximum efficiency [%]	96.0 ± 0.2	88.5 ± 0.8	82 ± 1	−8 ± 1	−14 ± 2
	Currents at WP [μA]	0.9 ± 0.5	214 ± 9	418 ± 16	213 ± 10	417 ± 17
CO2 50%, R-HFO, SF_6 1%	Working point [V]	10232 ± 12	10185 ± 14	10203 ± 22	−47 ± 26	−29 ± 34
November	Maximum efficiency [%]	95.9 ± 0.2	89.3 ± 0.9	84 ± 1	−7 ± 1	−12 ± 2
	Currents at WP [μA]	1 ± 3	182 ± 7	368 ± 9	181 ± 10	367 ± 12
He 30%, R-HFO, SF_6 0.3%	Working point [V]	9782 ± 10	9795 ± 13	9812 ± 22	13 ± 22	29 ± 31
September	Maximum efficiency [%]	96.5 ± 0.2	90.9 ± 0.2	85.5 ± 0.4	−5.7 ± 0.4	−11.0 ± 0.5
	Currents at WP [μA]	2.9 ± 0.5	160 ± 5	321 ± 7	157 ± 5	318 ± 8

A.3 Novec 4710 gas mixtures

Table A.7: Main features for Novec 4710 gas mixtures valued at source off, at 300 and 600 Hz/cm^2 detector rate for RPC 7.

Gas mixture	**RPC 7**	**Source OFF**	**300 Hz/cm^2**	**600 Hz/cm^2**	**Δ 300 Hz/cm^2**	**Δ 600 Hz/cm^2**
STD	Working point [V]	9680 $\pm$ 5	9973 $\pm$ 26	10304 $\pm$ 49	293 $\pm$ 31	624 $\pm$ 54
October	Maximum efficiency [%]	96.6 $\pm$ 0.1	90.8 $\pm$ 0.5	85.1 $\pm$ 0.9	-6 $\pm$ 0.6	-11 $\pm$ 1
	Currents at WP [μA]	0.3 $\pm$ 0.4	123 $\pm$ 6	246 $\pm$ 10	123 $\pm$ 6	245 $\pm$ 10
Novec 0.1%	Working point [V]	9685 $\pm$ 7	10013 $\pm$ 9	10338 $\pm$ 16	328 $\pm$ 16	653 $\pm$ 24
October	Maximum efficiency [%]	96.7 $\pm$ 0.1	91.0 $\pm$ 0.3	85.4 $\pm$ 0.5	-6 $\pm$ 0.4	-11.3 $\pm$ 0.6
	Currents at WP [μA]	0.2 $\pm$ 0.3	120 $\pm$ 3	237 $\pm$ 4	120 $\pm$ 3	237 $\pm$ 5
Novec 0.3%	Working point [V]	10187 $\pm$ 7	10560 $\pm$ 14	10935 $\pm$ 27	373 $\pm$ 22	748 $\pm$ 34
October	Maximum efficiency [%]	96.7 $\pm$ 0.1	91 $\pm$ 0.4	85.4 $\pm$ 0.7	-6 $\pm$ 0.5	-11.3 $\pm$ 0.8
	Currents at WP [μA]	0.3 $\pm$ 0.4	143 $\pm$ 3	282 $\pm$ 4	142 $\pm$ 3	282 $\pm$ 5

Table A.8: Main features for Novec 4710 gas mixtures valued at source off, at 300 and 600 Hz/cm^2 detector rate for RPC 8.

Gas mixture	**RPC 8**	**Source OFF**	**300 Hz/cm^2**	**600 Hz/cm^2**	**Δ 300 Hz/cm^2**	**Δ 600 Hz/cm^2**
STD	Working point [V]	9680 ± 5	9973 ± 26	10304 ± 49	-16 ± 34	11 ± 57
October	Maximum efficiency [%]	96.6 ± 0.1	90.8 ± 0.5	85.1 ± 0.9	-5 ± 0.4	-10.3 ± 0.6
	Currents at WP [μA]	0.3 ± 0.4	123 ± 6	246 ± 10	100 ± 3	203 ± 6
Novec 0.1%	Working point [V]	9451 ± 6	9490 ± 13	9521 ± 23	39 ± 19	70 ± 29
October	Maximum efficiency [%]	97.2 ± 0.1	91.7 ± 0.1	86.4 ± 0.2	-5 ± 0.2	-10.8 ± 0.3
	Currents at WP [μA]	1.6 ± 0.4	104 ± 1	206 ± 2	102 ± 2	204 ± 3
Novec 0.3%	Working point [V]	9899 ± 5	9923 ± 27	9960 ± 48	24 ± 32	61 ± 53
October	Maximum efficiency [%]	97.2 ± 0.1	91.3 ± 0.2	85.6 ± 0.3	-6 ± 0.3	-11.6 ± 0.4
	Currents at WP [μA]	1.8 ± 0.4	123 ± 4	247 ± 6	122 ± 4	246 ± 6

Table A.9: Main features for Novec 4710 gas mixtures valued at source off, at 300 and 600 Hz/cm^2 detector rate for RPC 10.

Gas mixture	**RPC 10**	**Source OFF**	**300 Hz/cm^2**	**600 Hz/cm^2**	**Δ 300 Hz/cm^2**	**Δ 600 Hz/cm^2**
STD	Working point [V]	9680 ± 5	9973 ± 26	10304 ± 49	-24 ± 16	-12 ± 25
October	Maximum efficiency [%]	96.6 ± 0.1	90.8 ± 0.5	85.1 ± 0.9	-5 ± 0.7	-10 ± 1
	Currents at WP [μA]	0.3 ± 0.4	123 ± 6	246 ± 10	111 ± 2	218 ± 3
Novec 0.1%	Working point [V]	9434 ± 7	9442 ± 7	9449 ± 13	8 ± 14	16 ± 20
October	Maximum efficiency [%]	97.3 ± 0.1	92.1 ± 0.3	87.1 ± 0.6	-5 ± 0.5	-10.2 ± 0.7
	Currents at WP [μA]	0.5 ± 0.6	115 ± 3	227 ± 4	115 ± 3	227 ± 4
Novec 0.3%	Working point [V]	9913 ± 6	9925 ± 8	9944 ± 13	13 ± 14	32 ± 20
Octobe	Maximum efficiency [%]	97.2 ± 0.1	92.1 ± 0.2	87.3 ± 0.4	-5 ± 0.3	-10 ± 0.5
	Currents at WP [μA]	0.5 ± 0.6	129 ± 2	257 ± 3	128 ± 3	256 ± 4

Bibliography

[1] Heuer R. D. (2012), "The future of the Large Hadron Collider and CERN", *Philosophical Transactions of the Royal Society*, 370 (2012), pp. 986-994 (DOI: 10.1098/rsta.2011.0467).

[2] Evans L., Bryant P. (ed.) (2007), "The CERN Large Hadron Collider: Accelerator and Experiments", *Journal of Instrumentation*, 3 (2008), pp. 1-18.

[3] CERN, `https://home.cern/science/accelerators/accelerator-complex` (2021/11/07).

[4] ATLAS Collaboration (2012), "Observation of a new particle in the search for the Standard Model Higgs boson with the ATLAS detector at the LHC", *Physics Letters B*, 716 (2012), pp. 1-29 (DOI: 10.1016/j.physletb.2012.08.020).

[5] CMS Collaboration (2012), "Observation of a new boson at mass of 125 GeV with the CMS experiment at the LHC", *Physics Letters B*, 716 (2012), pp. 30-61 (DOI: 10.1016/j.physletb.2012.08.021).

[6] Mobs E., "The CERN accelerator complex. Complexe des accélérateurs du CERN.", General Photo (2019) `https://cds.cern.ch/record/2684277` (2021/11/07).

[7] ALICE Collaboration (2008), "The ALICE experiment at the CERN LHC", *Journal of Instrumentation*, 3 (2008), pp. 1-8.

[8] CMS Collaboration(2008), "The CMS experiment at the CERN LHC", *Journal of Instrumentation*, 3 (2008), pp. 1-25.

[9] ATLAS Collaboration (2008), "The ATLAS Experiment at the CERN Large Hadron Collider", *Journal of Instrumentation*, 3 (2008), pp.1-18.

[10] LHCb Collaboration (2008), "The LHCb Detector at the LHC", *Journal of Instrumentation*, 3 (2008), pp. 1-5, 126.

[11] Abbaneo D. *et alii* (2013), "Studies on the upgrade of the muon system in the forward region of the CMS experiment at LHC with GEMs", *Journal of Instrumentation*, 9 (2014), p. 2.

[12] `https://cerncourier.com/a/atlas-undergoes-some-delicate-gymnastics/` (2022/02/05).

[13] ALICE Collaboration, `https://alice-collaboration.web.cern.ch/menu_proj_items/Muon-Spect` (2021/11/07).

[14] Abbrescia M. *et alii*, (2018) *Resistive Gaseous Detectors. Designs, Performance, and Perspectives* (Weinheim: Wiley-VCH Verlag GmbH & Co., 2018).

[15] Keuffel J. W. (1948), "Parallel-plate counters and the measurement of very small time intervals", *Physical Review*, 73 (1948), 531.

[16] Keuffel J. W. (1949), "Parallel-plate counters", *Review of Scientific Instruments*, 20 (1949), 202 (DOI: 10.1063/1.1741489).
[17] Conversi M. (1982), "The development of the flash and spark chambers in the 1950's", *Journal de Physiques Colloques*, 43 C8 (1982), pp. 91-99.
[18] Leo W. R. (1994), *Techniques for Nuclear and Particle Physics Experiments. A How-to Approach* (Berlin, Heidelberg: Springer-Verlag 1994).
[19] Santonico R., Cardarelli R. (1981), "Development of Resistive Plate Counters", *Nuclear Instruments and Method*, 187 (1981), pp. 337-380.
[20] Cardarelli R. *et alii* (1996), "Avalanche and streamer mode operation of resistive plate chambers", *Nuclear Instrument and Method in Physics Research A*, 382 (1996), pp. 470-474.
[21] Raether, H. (1964), *Electron Avalanches and Breakdowns in Gases* (Washington: Butterworths, 1964).
[22] Abbrescia M. *et al.* (2001), "The resistive plate chambers for CMS and their simulation", *Nuclear Instrument and Method in Physics Research A*, 471 (2001), pp. 55-59.
[23] CMS Muon Technical Design Report CERN/LHCC/97-32, December 1997.
[24] Vitulo P. *et alii* (2000), "The bakelite for the RPCs of the experiment CMS", *Nuclear Instrument and Method in Physics Research A*, 456 (2000), p. 132.
[25] E Cerron Zeballos *et al.* (1996), "A new type of resistive plate chamber: The multigap RPC", *Nuclear Instrument and Method in Physics Research A*, 374 (1996), pp. 132-135.
[26] Ahn S. H. *et alii* (2000), "Temperature and humidity dependence of bulk resistivity of bakelite for resistive plate chambers in "CMS" ", *Nuclear Instrument and Method in Physics Research A*, 451 (2000), pp. 582-587.
[27] Mann M. E. (2021) `https://www.britannica.com/science/greenhouse-gas` (2021/12/04).
[28] Shine K. P. *et alii* (2005), "Alternatives to the Global Warming Potential for Comparing Climate Impacts of Emissions of Greenhouse Gases", *Climatic Change* 68 (2005), pp. 281-302 (DOI: 10.1007/s10584-005-1146-9).
[29] Official Journal of the EU (L 150/95), vol. 57, 20 May 2014, ISSN 1977-0677.
[30] `https://www.wartsila.com/encyclopedia/term/ozone-depletion-potential-(odp)` (2021/12/04).
[31] Koreshev V. *et alii*, "Operation of narrow gap RPC with tetrafluoroethane-based mixture", *Nuclear Instrument and Method in Physics Research A*, 456 (2000), pp. 46-49.
[32] Camarri P. *et alii*, "Streamer suppression with SF6 in RPCs operated in avalanche mode", *Nuclear Instrument and Method in Physics Research A*, 414 (1998), pp. 317-324.
[33] Liu Z. A. (*eds.*) (2018), *Proceedings of International Conference on Technology and Instrumentation in Particle Physics 2017. Volume I* (Singapore: Springer Nature, 2018).
[34] Guida R. *et alii* (2018), "Gas Systems for Particle Detectors at the LHC Experiments: Overview and Perspectives" in [33], pp. 97-101.
[35] Pfeiffer D. *et alii* (2017), "The radiation field in the Gamma Irradiation Facility GIF++ at CERN", *Nuclear Instrument and Method in Physics Research A*, 866 (2017), pp. 91-103.
[36] `http://www.fcon-inc.jp/en/en_MFC/Principle/Principle.html` (2022/01/03).
[37] Rigoletti G., `https://doi.org/10.5281/zenodo.5816688` (2022/01/03).
[38] Abbrescia M. *et alii* (1995), "Resistive plate chambers performances at cosmic rays fluxes", *Nuclear Instrument and Method in Physics Research A*, 359 (1995), pp. 603-609

(DOI: 10.1016/0168-9002(94)01698-4).

[39] Abbrescia M. *et alii* (2016), "Eco-friendly gas mixtures for Resistive Plate Chambers based on tetrafluoropropene and Helium", *Journal of Instrumentation*, 11 (2016) (DOI: 10.1088/1748-0221/11/08/P08019).

[40] Colucci A. *et alii* (1998), "Measurement of drift velocity and amplification coefficient in C2H2F4-Isobutane mixtures for avalanche operated Resistive Plate Counters", ATL-MUON-98-265 (1998).

[41] Incandela J. *et al.* (1988), "The performance of photomultipliers exposed to helium", *Nuclear Instrument and Method in Physics Research A*, 269 (1988), pp. 237-245.

[42] Proto G. *et alii* (2021), "Characterization of new eco friendly gas mixtures based on HFO for RPCs", *Journal of Instrumentation*, 16 (2021) (DOI: 10.1088/1748-0221/16/02/C02001).

[43] Rigoletti G. *et alii* (2019), "Studies of RPC detector operation with eco-friendly gas mixtures under irradiation at the CERN Gamma Irradiation Facility", *PoS EPS-HEP2019*, 164 (2020).

[44] 3M™ Novec™ 4710 datasheet. `https://multimedia.3m.com/mws/media/1132124O/3m-novec-4710-insulating-gas.pdf` (2021/01/12).

[45] Magatti D. (2021), *Characterization of RPC detectors operated with new eco friendly gas mixtures*, master thesis in physics, Università degli Studi di Milano-Bicocca, 2021, supervisor: Croci G., Mandelli B., Perelli E., pp. 35-39.

[46] Rigoletti G., Mandelli B., Guida R. (2020), "Characterization of RPC detectors with LHC-like background radiation and new eco-friendly gas mixtures", *Journal of Instrumentation*, 15 (2020) (DOI: 10.1088/1748-0221/15/11/C11003).

[47] Guida R., Mandelli B. (2017), "A portable gas recirculation unit for gaseous detectors", *Journal of Instrumentation*, 12 (2017) (DOI: 10.1088/1748-0221/12/10/T10002).

[48] Kumari P. *et al.* (2020), "Improved-RPC for the CMS muon system upgrade for the HL-LHC", *Journal of Instrumentation*, 15 (2020) (DOI: 10.1088/1748-0221/15/11/C11012).

[49] Alberghi G. L. *et al.* (2018), "Status of the present ATLAS RPC system and overview towards HL-LHC", *ATL-MUON-PROC-2018-006* (2018).

[50] Mandelli B. (2011), *Optimization of the RPC gas recirculation system for the CMS experiment*, master thesis in physics, Università degli Studi di Pavia, 2011, supervisor: Vitulo P., Garrido M. C., Guida R..

[51] Rigoletti G. (2019), *Performance studies on Resistive Plate Chambers detectors operated with new environmentally friendly gas mixtures at CERN GIF++ facility*, Università degli Studi Milano-Bicocca, 2019, supervisor: Paganoni M., Guida R..

Acknowledgements

Intendo ringraziare il prof. Paolo Vitulo che mi ha permesso di intraprendere questo percorso nel migliore dei modi. Estendo questo ringraziamento anche a Roberto Guida e Beatrice Mandelli, che mi hanno seguito in questi mesi di lavoro.

Ancora una volta, ringrazio i miei genitori, Marta e Sergio, che hanno continuato a sostenermi e incoraggiarmi. Estendo questo ringraziamento anche alla nonna Angela e alla nonna Teresa, a Flavio, Ornella, Chiara, Paolo e Marco.

Figure 1: Incipit of checkmate.

For the sake of brevity, Figure 1 shows the most important people who helped me in this work. Tuttavia questi ringraziamenti non possono essere esaustivi, in quanto gli amici che hanno collaborato a questo percorso di studi sono parecchi e, per brevità, non potrò citarli tutti. Ringrazio quindi anche coloro che non compaiono in questa pagina e che hanno contribuito, in un modo o nell'altro, a questi due anni.